Devitrification Behaviour of Alkaline-Earth Silicate Fibre

Ruihua Li

A thesis submitted in partial fulfilment of the requirements of

Sheffield Hallam University

for the degree of Doctor of Philosophy

July 1997

ACKNOWLEDGEMENTS

I wish to acknowledge my supervisors Dr. John Young and Dr. Robin Acheson for their support throughout the project especially for reviewing the draft for this thesis and making many comments and corrections that improved its completeness and readability.

I would like to express my appreciation to Dr. Ian Wadsworth for his help at the initial stage of this project.

I'm grateful to the following technical staff: Gerry Gregory of MRI, and Derek Latimer and Roy Gunson of School of Engineering, for their generous support in the experimental area.

My thanks are due to the final-year, undergraduate project students who have contributed to this project: Graham Brown, Hoiling Wang and Ian Platts.

I would also like to thank Dr. Gary Jubb and Dr. Iain Alexander of Morgan Materials Technology for providing the fibre materials and valuable discussions.

My sincere thanks go to all my friends in Sheffield Hallam University. Their understanding, friendship, and good cheer made my stay a pleasant memory.

Carrying out the research for and writing this thesis has proved to be very enjoyable and challenging. I thank my family and friends for their patience, love and support during the over-long period of writing up. Their constant encouragement has been invaluable.

ABSTRACT

The alkaline-earth silicate fibres are a new generation of man-made insulation materials. The materials are amorphous on manufacture and have been shown to be soluble in physiological solutions and to be cleared from the lung in animal exposure trials.

This reported study provides a thorough investigations of the devitrification behaviour of Superwool X-607 (Morgan Materials Technology), and two further compositions, code names A2 and B3.

Thermal exposures were made within the region extending from 700 to 1250°C and 10 minutes to 3240 hours in clean furnace environments. The devitrified microstructures and products were identified using X-ray powder diffraction and analytical electron microscopy. Details are provided of the development of specimen preparation techniques to enable fibre cross-sections to be analyzed in the TEM.

The devitrification products are presented as a function of exposure temperature and time for all 3 compositions. The amorphous glass separated into a silica-rich phase and an alkaline-earth silicate rich phase and the development of these amorphous phases is presented and discussed. The subsequent devitrification of these separated phases into associated silica crystalline phases and alkaline-earth silicate crystalline phases, and, in each case, the subsequent phases and transformations with increasing thermal exposure are also presented and discussed.

For the crystalline silica phases, the following unusual transformation situation was identified in all 3 compositions: amorphous silica $\rightarrow$ α-quartz $\rightarrow$ α-cristobalite $\rightarrow$ tridymite. In comparison with established understanding of silica phase transformations, the following anomalies were identified and explained: a) the formation of quartz as the primary crystalline silica phase at temperatures $\geq$1000°C, and b) the subsequent formation of α-cristobalite, the low-temperature form, other than β-cristobalite, the high-temperature form, which was the only silica phase identified in the devitrified aluminosilicate fibres.

For the alkaline-earth silicate phases, two forms of wollastonite solid solution were characterised. The low-temperature form, containing more Mg^{2+}, transforms to the high-temperature form and diopside at temperatures above 900°C. The low-temperature anomaly, ie the formation of the immature high-temperature form below 900°C is possibly due to a secondary phase separation. Pseudowollastonite was found to be metastable in the investigated temperature region. It is suggested that the detailed transformation process among these alkaline-earth silicate phases has been identified for the first time.

This thesis also includes a detailed review of published studies concerning this materials systems as well as recommendations for further work.

CONTENTS

Refractory ceramic fibres are used extensively in insulation, fire protection, refractory and engineering applications due to their good high-temperature performance including low thermal conductivity, low thermal capacity, good resistance to thermal shock, good resistance to chemical corrosion and cheaper installation and maintenance costs in comparison with more traditional materials[1]. These products have included aluminosilicate fibres, possibly with additional oxide components to stabilise the fibres for higher temperature use, and now include the alkaline earth silicate fibre which have been developed in response to the need for fibres which present a reduced health risk when inhaled.

These fibres are vitreous as manufactured but can devitrify in high temperature use. Studies[2, 3, 4, 5, 6, 7, 8] of the devitrification of aluminosilicate refractory ceramic fibres have identified the formation of cristobalite and concern has arisen that inhalation of cristobalite-containing dust, say during subsequent repair, refurbishment, or disposal of furnace linings, could cause lung disease[9, 10, 11, 12]. Detailed and systematic investigations of both the materials-related and health-related aspects of the devitrification in aluminosilicate fibres have been reported by Young et al[13, 14], Sara[15] and Laskowski, et al.[16]. However, little is known about the devitrification behaviour of the new generation of alkaline-earth silicate fibres which in their as-manufactured state have been shown by in vivo and in vitro studies to be much safer[17]. Further, data from the manufacture emphasises the properties of the as-manufactured fibres and does not address of changes occurring to the fibres during their intended use.

The main aim of this project has been to provide knowledge and understanding of the detailed devitrification behaviour of this new generation of alkaline earth silicate fibres with a view to informing the development of these materials in relation to their engineering properties and safety in use. A related aim was the development of a better understanding of the devitrification process and products in such fibrous systems. The study focused primarily on the devitrification behaviour of Superwool X-607 but included analysis of two products, coded A2 and B3 chosen to provide understanding of related compositions. Detailed objectives were the determination of devitrification products, microstructures and processes as a function of thermal exposure temperatures. These were chosen to include also realistic usage conditions of the fibres in clean furnace environments.

The study involved thermal exposure of the fibrous materials over the following ranges of temperature from 700 to 1250°C and time from 10 minutes to 3240 hours using laboratory muffle furnaces and a purpose built vertical tube furnace. Devitrification products were identified using, in particular, a combination of X-ray diffractometry (XRD), electron diffraction (ED) and energy dispersive spectroscopy (EDS) and microstructure studied using transmission electron microscopy (TEM) and scanning electron microscopy (SEM). Techniques were developed to provide the necessary thin fibre cross-sections for detailed TEM studies.

This thesis provides a detailed reviews of reported work relevant to this study (chapter 2) and describes the experimental apparatus and techniques (chapter 3).

Chapter 4 is a presentation and analysis of the experimental results and chapter 5 contains a detailed discussion and interpretation of the findings together with recommendations for further work. The major conclusions from this investigation are defined in chapter 6.

2.1 Refractory Ceramic Fibres

Asbestos has been used extensively for many applications since the late 19th century. It is a relatively inexpensive material with useful chemical and physical properties, such as good chemical stability, fire resistance, mechanical strength, high fibre length to diameter ratio, flexibility and good friction and wear characteristics, which make it very durable. Such properties make it ideally suited for many applications, such as high temperature thermal insulation and fire protection, making brakes and clutches, as a reinforcing agent for various composites, etc. Unfortunately, asbestos exposure can cause asbestosis and lung cancer[18, 19], and hence concern about the safety of asbestos has led to extensive legislation in most countries. Many inorganic fibrous materials are used as substitutes for asbestos in certain applications[20, 21]. Among them, refractory ceramic fibres (RCFs) are in widespread use as refractory insulation and find application as dry seals and fire protective components.

The development, manufacture and properties of "specialised" high-performance ceramic fibres have been reviewed by Bracke et al[22]. These fibrous materials include whiskers and continuous filament forms and single crystal, polycrystalline and multiphase microstructures. They are made by a range of different routes including vapour deposition, chemical transformation, and crystallisation. However, the bulk of fibrous materials produced for use in high temperature insulation are vitreous aluminosilicate fibres, usually prepared as wool.

Standard grade aluminosilicate fibre has an arithmetic-mean fibre diameter of typically 2-3 μm[23]. They have good resistance to high temperatures. They are made either, by melting a combination of the oxides of aluminum and silicon in approximately equal proportions, or by melting calcined kaolin. Figure 2-1 is a schematic diagram illustrating the manufacture of the fibres. The melt stream is delivered for fiberisation by passing the melt through graphite bushes at the bottom of the melting furnace[24]. Fiberisation is achieved by blowing or spinning. In the blowing process, the melt stream is dispersed by a high-pressure air or steam jet which disperses the molten stream into droplets that gain momentum from the jet and elongate and attenuate them into fibre. In the spinning process, the melt stream drops onto the periphery of one or a number of vertical rotating discs. The molten material bonds to the disc surface and melt droplets are ejected and attenuated by centrifugal action. Other oxides such as zirconia and chromia are sometimes added to the melt to alter the physical properties of the resulting RCFs, especially its high temperature resistance[1]. Generally, these fibres have low thermal conductivity, low thermal capacity, high thermal shock resistance, and good resistance to chemical corrosion, except from hydrofluoric and phosphoric acids and concentrated alkalis. Applications for RCFs include the insulation of furnaces, heaters, kiln linings and other high-temperature equipment, fire protection, and refractory and engineering products.

It is still not clear what the causative mechanism is that relates some forms of asbestos with disease, but some researchers believe that the mechanism is mechanical and size related [25]. It has been noted that the lower end of the fibre diameter range of ceramic fibres extends into the respirable region. The adverse effects of exposure to

asbestos has led to some concern about the potential for other fibrous materials to cause similar diseases in exposed humans. In the as-manufactured state most RCFs are vitreous but they can devitrify on heating. Results of studies concerning the occurrence of cristobalite in furnace-exposed linings, the dust release from furnace-exposed materials and the industrial hygiene of furnace stripping operations have been published [2, 3, 4, 8]. Concern has arisen that changes in physical and chemical properties of traditional aluminosilicate refractory ceramic fibres during high temperature applications, may pose a health hazard through the subsequent release and inhalation of cristobalite dust [9, 10, 11, 12]. Accordingly there is a demand for inorganic fibres that will pose as little risk as possible, ideally no risk, and for which there are objective grounds to believe them safe.

2.2 Alkaline-Earth Silicate Refractory Ceramic Fibre

2.2.1 Development of the Fibre

Although the biological activity of inorganic fibres is influenced by chemical composition, the toxicity of fibres that are durable in tissues is primarily dependent on diameter. One approach to greater safety is to produce fibres of non-respirable size using non-melt processing[26]. The risk of asbestos-linked disease appears to depend very much on the length of exposure. The shorter the time a fibre is resident in the body the less damage it can do. If fibres are soluble in physiological saline solution, provided the dissolved components are not toxic, the fibres should be safer than those which are not so soluble. Another approach to make safer fibre has therefore been to

make fibres which are soluble in lung fluids. European patent specifications disclose a selection of fibres characterised by their level of saline solubility[27]. The refractoriness of these fibres varies considerably and the maximum service temperature of any of these fibres was only 815°C. There was thus a demand for physiologically soluble fibres having a service temperature of greater than 815°C. Alkaline-earth silicate based ceramic fibre has been developed by Morgan Materials Limited to meet this demand[17]. They have low thermal conductivity characteristics similar to existing ceramic fibre products, but are sufficiently soluble in physiological fluids that their residence time in the human body is short, so that damage would not occur or at least be minimised. Their solubility in physiological solutions and clearance in the most extreme animal exposure trials make this fibre an outstanding material for thermal insulation.

The composition range of the alkaline-earth silicate fibre patented by Morgan Materials is as follows (mass %)[17]:

SiO_2	>58%	(for MgO ≤10%) and
SiO_2	>58% + 0.5 (%MgO -10)	(for MgO ≥10%)
CaO	0%—42%	
MgO	0%—31.33%	
Al_2O_3	0%— <3.97%	

This composition range is represented on the SiO_2 - CaO - MgO phase diagram in figure 2-4. The compositions are essentially free of fluxing components such as alkali metals and boron oxide.

Superwool® Blanket Grade X-607, A2 and B3 fibres, which have been investigated in this project, are developed from this system. Superwool X-607 was the first commercial product coming into the market in 1993. A2 and B3 fibres are development products in this alkaline-earth silicate fibre system. As will be introduced in section 3.2 they have very different compositions from Superwool X-607, A2 with higher MgO concentration and B3 higher CaO concentration.

2.2.2 Physical and Chemical Properties of Alkaline Earth Silicate Fibre [17, 28]

The alkaline-earth silicate fibres made in the composition range defined above have a shrinkage of less than 3.5% when exposed to 1000°C for 24 hours and/or 800°C for 24 hours. Superwool® Grade X-607 products, which is already available on the market, normally contains fibres showing a range of lengths and diameters. Table 1 shows typical diameter distributions for two production runs. Fibre diameters were measured using a Calai particle analyser with shape analysis software and 40,000 fibres were analysed for each run. The fibres displayed a distribution of diameters and a significant proportion of fibres were of respirable diameter (< 3μm). The product is claimed to retain a soft fibrous texture at temperatures up to 1000°C in clean oxidising conditions.

Traditional refractory alumino-silicate ceramic fibres (RCF) are about 200 times more soluble than chrysotile asbestos and Superwool is over 100,000 times more soluble.

This means that any fibre of Superwool fibre which does reach the lung will not survive and will thus have little chance of causing any damage. Being substantially more soluble than traditionally RCFs, Superwool may be expected to be a potentially safer fibre.

2.2.3 Manufacture and Product Forms of the Fibre[28]

Alkaline-earth silicate fibres can be produced by using spinning and blowing methods. The melt is formed by electrical discharge melting of the constituent raw materials in an electric resistance furnace. The molten mixture is made into a fibre by subsequent spinning and blowing. The manufacturers have found that the Al_2O_3 content in the fibre composition is important. The maximum Al_2O_3 content lies somewhere between 2.57 and 3.97 mass %. It was found that with increasing alumina levels the first phase to crystallise was a calcium aluminate and this possibly forms a liquid phase that assists flow and hence shrinkage. The use of calcium oxide in making alkaline-earth silicate fibres is inconvenient and can be hazardous. Therefore the manufacturers use wollastonite to substitute calcium oxide and part of the silica in the composition.

Alkaline-earth silicate fibres are available in a wide range of forms, including: blanket, textile yarn, cloth, rope and etc. Blanket fibre is generally made by a process of sucking air-borne fibre onto a conveyor to form a blanket. The blanket fibres are secured by adding a binder to lock the fibres together, or needling the blanket. In needling, needles are passed through the thickness of the blanket to push and draw

fibres to lie transverse to the blanket and so tie the fibres together. The binders used are usually organic resins, such as phenolic resins, and burn off on firing.

2.2.4 Applications of Alkaline-Earth Silicate Fibre[28]

Maximum service temperatures are dependent on applications. Superwool is ideal for a wide variety of industrial and building applications up to 1000 °C. Examples of applications are:

- Furnace linings.
- General purpose high temperature industrial insulation.
- Re-usable insulation blankets for stress relieving of welds in the field.
- Removable insulating blankets for steam and gas turbines.
- Insulation wrap on investment casting moulds.
- Flexible high temperature pipe insulation.
- Fire protection.
- Insulation of electrical appliances, boilers, fire-places, etc..

2.3 Phase Equilibria in the Relevant Systems

2.3.1 Silica

The classic paper by Fenner[29] established the relationship between the several forms of silica and laid a sound foundation for all silicate systems. Because of the great importance of silica as a refractory material and ceramic raw material, the

relationships among the various crystalline phases of silica have been studied in great depth over the past century.

As shown in the equilibrium phase diagram, figure 2-2 there are two forms of quartz, referred to as high- and low-quartz. Tridymite and cristobalite also have high and low temperature forms, but the low forms are metastable and do not appear on an equilibrium phase diagram. Coesite and stishovite originate in very high-pressure environments. It should be noted that the nomenclature used in this thesis is that of α for a lower temperature form and β for a higher temperature form of a given crystalline phase. The transformation from α-quartz to β-quartz traditionally has been placed at 573°C at 1 bar. The transition from β-quartz to β_2-tridymite at 1 bar occurs at 867°C, and β_2-tridymite inverts to β-cristobalite at 1470°C. β-cristobalite melts to silica liquid at 1727°C.

2.3.2 CaO-SiO_2

Day and Shepherd[30] reported on the lime-silica series of minerals. This work was extended by Rankin and Wright[31] and was later modified by Greig[32] in the high-silica region. Bowen, Schairer and Posnjak[33] showed that there is no solid solution with an excess of SiO_2 or an excess of lime in the compound $CaSiO_3$. They reported a correction to the composition of the eutectic between pseudowollastonite, which is the high temperature form of $CaSiO_3$, and tridymite. They also showed that the inversion temperature between high and low-temperature forms of $CaSiO_3$ must be 1150° C or even lower. Osborn and Schairer [34] determined this inversion temperature

more accurately at 1125±10° C. The equilibrium diagram for $CaO-SiO_2$ is given as figure 2-3.

2.3.3 $CaO-MgO-SiO_2$

The occurrence of liquid immiscibility in alkaline earth silicate systems was established by Greig[32]. Investigations on a portion of this system was carried out by Bowen[35], who determined the phase relationships in the ternary system diopside-forsterite-silica. Ferguson and Merwin[36] studied the whole system. They identified four ternary compounds - diopside ($CaO{\cdot}MgO{\cdot}2SiO_2$), akermanite ($2CaO{\cdot}MgO{\cdot}2SiO_2$), monticellite ($CaO{\cdot}MgO{\cdot}SiO_2$) and a compound $5CaO{\cdot}2MgO{\cdot}6SiO_2$ in the system. Schairer and Bowen[37] showed that the compound $5CaO{\cdot}2MgO{\cdot}6SiO_2$ did not exist, in the system but instead a low-temperature form of $CaSiO_3$, wollastonite - diopside solid solution appeared. (this issue will be addressed in more detail in the following section). This was confirmed by Osborn[38]. X-ray diffraction data obtained by the powder method, for 19 compounds which are stable and metastable at room temperature in the system $CaO-MgO-SiO_2$ have been presented by Clark[39]. Additional phase equilibrium data has been contributed by Ricker and Osborn[40] and a revised equilibrium diagram of the ternary system $CaO-MgO-SiO_2$ was presented as shown in figure 2-4.

2.3.4 $CaSiO_3$-$CaMgSi_2O_6$

The relationship between the principal forms of $CaSiO_3$, ie wollastonite in its low temperature form and pseudowollastonite in its high temperature form (see section 2.4 for more detailed information), and $CaMgSi_2O_6$ (diopside) have been discussed by Allen et al[41] , who studied the system by means of heating curves and microscopic examination. Later Ferguson and Merwin in two papers on the system CaO-MgO-SiO_2 and on wollastonite and related solid solutions in the ternary system CaO-MgO-SiO_2 , discussed the relationships between $CaSiO_3$ and $CaMgSi_2O_6$ [36] . Schairer and Bowen[37] made a detailed re-examination of the relationships between $CaSiO_3$ and $CaMgSi_2O_6$ and a phase diagram was produced, as shown in figure 2-5. In the system $CaSiO_3$- $CaMgSi_2O_6$, the low temperature form of $CaSiO_3$ (wollastonite) can take up to 21% $CaMgSi_2O_6$ into solid solution (wollastonite solid solution), while little or no $CaMgSi_2O_6$ enters into solution in the high temperature form (pseudowollastonite). As a consequence, the inversion temperature of the wollastonite solid solutions to pseudowollastonite increases from 1125±10°C in pure wollastonite to a maximum of 1368±2°C and wollastonite solid solutions persist upto the liquidus. There is a eutectic at 1358±2°C and at 62 mass % diopside. At the eutectic, crystals of pure diopside and of wollastonite solid solution with the maximum soluble amount of diopside (21%) are in equilibrium with liquid. The crystals of diopside in this system are always pure $CaMgSi_2O_6$. There is no solid solution of $CaSiO_3$ in diopside. At temperatures below the eutectic, wollastonite solid solution crystals contain less diopside than at the eutectic and precipitation therefore occurs at lower temperatures.

Investigations by Osborn[38] showed that wollastonite solid solutions occurring in the system $CaSiO_3$-$CaMgSi_2O_6$-$CaAl_2Si_2O_8$ had the same compositional range as those in the system $CaSiO_3$- $CaMgSi_2O_6$.

2.3.5 $CaO-Al_2O_3-SiO_2$

Figure 2-6 shows the equilibrium diagram for the ternary system $CaO-Al_2O_3-SiO_2$[42] . It is worth noting that the eutectic temperature in this system can be as low as 1170°C at low Al_2O_3 concentrations, which suggests small amounts of Al_2O_3 in alkaline-earth silicate fibre might not only greatly affect the devitrification behaviour of the fibre but also affect the refractoriness of the fibre.

2.4 Potential Devitrification Products

2.4.1 Crystalline Silica

2.4.1.1 Silica Polymorphs

The traditional view, after Fenner[29], is that there are three distinct families of silica structures which are stable at ambient pressure: quartz, tridymite and cristobalite, all of which have both high and low temperature modifications. In each case the structure is built from SiO_4 tetrahedra which are linked by sharing each of their corners with another tetrahedron. In the three dimensional framework thus formed, every silicon atom has four oxygen atoms and every oxygen has two silicon atoms as nearest neighbours. Figure 2-7 shows the modifications, transformations and crystal structures of silica. In the high-low transformations, only slight distortions of structure occur, with no breaking of Si-O bonds. Research over the past several decades has sought out the mechanisms that control these transitions. The transformations between the three mineral species however involves a major rearrangement of the silica tetrahedra and the breaking of Si-O bonds. Although quartz is believed to be the stable phase at temperatures below about 867°C, both tridymite and cristobalite can be cooled to low temperatures, where they are

metastable due to the high activation energy for reconstructive transformation. The structures of the different forms and transformation relationships have been discussed in detail by Griffen [43].

2.4.1.2 Quartz

The pioneering work of Bragg[44] and Gibbs[45] firmly established the topological conformation of the silica framework for α-and β-quartz. Single crystal high temperature studies have allowed measurement of the structural changes that accompany the α-β quartz transition using X-rays[46, 47]and neutrons[48]. Low-temperature refinements of α-quartz have been reported[49, 50]. Quartz has also been approached through Rietveld refinement of standard X-ray[51] and synchrotron X-ray[52] powder diffraction data. The structure of α-quartz is most easily envisioned as a distortion of the high-temperature β modification. In β-quartz, paired helical chains of silica tetrahedra spiral in the same sense around 6_4 or 6_2 screw axes parallel to c. When β-quartz is cooled below 573°C, the expanded β-quartz framework collapses to the denser α-quartz configuration. Detailed studies of the α-β quartz transition have been reviewed by Dolino[53] and by Heaney and Veblen[54]. Anomalous behaviour near the critical temperature has been detected by different analytical techniques[55, 56]. Young suggested that macroscopic Dauphine twin domains are replaced by fine-scale microtwins as α-quartz transforms to β-quartz on the basis of high-temperature X-ray diffraction experiments[46] His suggestion was supported by Van Tendeloo et al[57] and Malov and Sonyushkin[58], who observed the α-β quartz transition in situ by transmission electron microscopy. Bachheimer [59] provided experimental verification for the occurrence of at least one stable intermediate phase by simultaneous monitoring of thermal expansion, elastic compliance and birefringence about the transition. These observations are consistent with hysteresis effects reported in Raman experiments[60] and Neutron diffraction studies[61].

2.4.1.3 Tridymite

The anomalous thermochemical properties of tridymite has prompted some researchers to suggest that tridymite is not a pure silica polymorph with a true stability field within the silica system. In response to these ideas, Hill and Roy [62] successfully synthesised tridymite from transistor-grade silicon and high purity silica gel using only H_2O and D_2O as fluxes; confirmation of these results by subsequent researchers, e.g. Sato[63] , has convinced most scientists of the legitimacy of tridymite as a stable phase of silica. Tridymite has several energetically almost degenerate modifications. Determination of the structures of the low-temperature polymorphs of tridymite has proved one of the greater challenges in the crystal structure analysis of minerals. The idealised tridymite structure[43] comprises hexagonal sheets of SiO_2 tetrahedra arrayed in six-fold rings, with adjacent tetrahedra directed in opposite directions. Successive sheets are stacked in an "ABAB..." sequence parallel to [001], analogous to "hexagonal close packing" in metals. The actual behaviour appears to be crucially dependent on both the starting materials and its thermal history. The tridymite structure is very tolerant to ionic substitutions[64, 65]. Large cations, most notably Na, K and Ca, can be accommodated within [001] structural channels, residing between successive sheets of silicate tetrahedra, with 9 nearest-neighbour oxygen atoms. Charge balance is attained by the partial replacement of silicon by a lower-valence cation (e.g., Al or Mg). Not only do samples vary chemically, but the layer structure is amenable to a high degree of stacking disorder and defects, and to the possibility of long-range superstructures. Coexistence and structural intergrowth of several tridymite polymorphs and cristobalite has been observed[66, 67, 68].

X-ray powder diffraction patterns of tridymite have long been debated[69 , 70, 71, 72]. Deviations in the diffractograms of tridymite due to texture effect, stacking disorder

and intergrowth of different modifications which complicate identification and indexing, have been discussed by Graetsch and Florke[73]. Varying degrees of stacking disorder will cause line broadening, differing reflection profiles, peak shifts and changes in the intensity of X-ray powder patterns of tridymite.

2.4.1.4 Cristobalite

Cristobalite is the highest-temperature polymorph of silica. The crystal structure is related to that of tridymite: the ideal structures differ only in the stacking sequence of otherwise identical layers of SiO_4 tetrahedra. The "ABCABC" stacking sequence of tetrahedral sheets gives a maximum topological symmetry of Fd3m. Although cristobalite shows macroscopic cubic symmetry at high temperatures, the true microscopic symmetry is probably much lower, indicated by the observation of diffuse intensity in diffraction patterns [74].

Theoretically the high-temperature β-cristobalite phase cannot be preserved by quenching because the α-β transition is displacive in nature. Beginning with the work of Florke[75], and Hill et al[76], it was realised that the phase relationships between the two forms of cristobalite were complex. The temperature of the α-β inversion in cristobalite is variable and depends on the structure of the starting material, any prior thermal history[77], chemical effects such as the incorporation of foreign ions, such as Na^+, Ca^{2+} and Al^{3+} and also the degree of disorder of the crystalline structure, for example tridymite stacking faults caused by low crystallisation temperatures and/or impurity ions[77]. The inversion temperatures displayed by different specimens range from 120 to 272°C[78] with a hysteresis as large as 40°C[79]. For a single sample, the transition temperature even differs on heating and cooling. When cooling from high temperature, β-cristobalite transforms reversibly to low-temperature or α-cristobalite near 250°C by a process of long- range ordering of a cooperative tilt system in the

tetrahedral network. This produces a spontaneous strain as large as -1.0% and -2.2% for the a- and c-directions respectively[80].

The β to α transformation of cristobalite may be suppressed by one or a combination of the following mechanisms:

a) Stress depression: Wagstaff[81] found β-cristobalite crystals which had nucleated and grown within a vitreous silica matrix. The large difference in thermal expansion induced a strain energy large enough to retain β-cristobalite metastably at room temperature.

b) Chemical stabilisation[82 83 84] : The presence of foreign ions in the interstices inhibits the contraction of the structure during the β-α transition of cristobalite, stabilising the cubic β-cristobalite to low-temperature.

c) Stacking disorder stabilisation: Florke[80, 85] found that tridymite stacking faults in cristobalite caused by a low crystallisation temperature and /or impurity-ions, lowered the α-β phase transition temperature.

β-cristobalite has also been observed stabilised to room temperature in devitrified Standard™ and High-duty™ grade fibres by Young et al [13] and Lascowski et al[16]. This was shown by X-ray powder diffractometry data and differential scanning calorimetry data.

2.4.2 $CaSiO_3$

2.4.2.1 Modifications

Table 2-2 shows the different modifications of $CaSiO_3$ and their related crystallographic information[86].

There are three modifications of calcium metasilicate:

Pseudowollastonite (β-$CaSiO_3$) which is the high-temperature form,

Wollastonite, also referred to as wollastonite Tc, and

Parawollastonite, also known as wollastonite-2M.

Wollastonite and parawollastonite have closely related properties. They are both commonly identified as the low temperature form, α-$CaSiO_3$, and are only only stable below 1125°C±10°C[37].

2.4.2.2 Structures

2.4.2.2.1 Wollastonite

The crystal structures of wollastonite-Tc and wollastonite-2M are well established, and are related in a polytypic manner. Direct structure imaging of wollastonite by high-resolution electron microscopy at 500 kV has been demonstrated by Smith[87] both experimentally and theoretically. The distinguishing features of the X-ray powder diffraction patterns of wollastonite-Tc and wollastonite-2M have been identified by Heller and Taylor [88]. It is claimed that the distinction can be made by noting the separation between the strong 3.83 Å line and the one adjacent on the low-angle side; this has a d-spacing of 4.05Å in wollastonite and 4.37Å in wollastonite-2M.

The triclinic nature of the wollastonite-Tc structure was first confirmed by Peacock[86] and further detailed work on wollastonite-Tc has been carried out by a number of workers[89, 90]. The structure of wollastonite was determined by Mamedov and Belov[91] and refined by Buerger and Prewitt[92] . The structure of wollastonite-Tc is characterised by chains of SiO_4- tetrahedra which extend parallel to the y-axis and

have a three cell repeat (b=7.32 Å). This repeat unit can be considered as consisting of a pair of tetrahedra joined apex to apex as in the $[Si_2O_7]$ group, alternating with a single tetrahedron with one edge parallel to the chain direction. The chains are held together by interstitial Ca^{2+} which is in a distorted six fold co-ordination. Figure 2-8a shows a z-projection of the structure of triclinic wollastonite as determined by Mamedov and Belov[91] from two-dimensional film data.

The cell parameters of wollastonite-2M were obtained by Barnick [93]. Three-dimensional X-ray single-crystal work has confirmed that wollastonite-2M is related to wollastonite-Tc by a simple stacking modification[94]. The triclinic form can be distinguished from the monoclinic form by the slight inclination of the optic axial plane to the plane normal to the y-axis, which was confirmed by asymmetry in the single-crystal X-ray diffraction pattern. It was shown that wollastonite-2M has the same type of chain structure as wollastonite-Tc [95] (figure 2-8b).

Polymorphism of wollastonite is very common. This can be achieved in various ways. If A is the normal wollastonite-Tc unit cell and B is a unit cell related to the original one by a mirror reflection on (100), or by rotation on a screw axis around [010], or by translation or glide parallel to [010], all with (100) as the composition plane, then for the different polymorphs the following stacking sequences of A and B could occur[96]:

1T: A A A A

2M: A B A B

4T: A A A B A A A B

4M: A A B B A A B B

∞T: A B A A B B B

As the units might be distorted in the packing, a slightly triclinic symmetry can also be expected for the 2M and 4M arrangement. A "fibrous" wollastonite was considered by Jeffery[97] to consist of complex intergrowth of both triclinic and monoclinic forms

with packing mistakes, or alternatively with a twinning relationship. Parawollastonite may be produced by stacking faults in every second triclinic unit cell of wollastonite, whereas twin lamella may be produced by faults in every adjacent triclinic unit cell[98].

Different superstructures of wollastonite from the regional metamorphic Lepontine zone (Souththern Alps) and other localities were found by Wenk[96]. Besides well ordered normal 1T, 2M and 4T-wollastonite, other disordered intermediate states were found. It was also noticed that the superstructure occurred only in strained rocks with well developed lineation and strong preferred orientation and hence could could be explained as a deformation effect.

Polymorphism and stacking disorder in wollastonite were also investigated by Jefferson and Bowen[99]. A wollastonite crystal was reported to give X-ray diffraction patterns of 4M polytype with triclinic distortion, a possible explanation being that this may represent a fine intergrowth of 1T and 2M forms. Some wollastonites give patterns in which reflections on k even layers are sharp, but in which there is streaking parallel to a* on k odd layers, sometimes with maxima on the streaks. Such patterns are attributed to stacking disorder. Further transmission electron microscopic evidence of polytypism in wollastonite are presented by Wenk et al[100] and Hutchison and McLaren [101]. The latter confirmed that simple stacking faults and twinning both occur.

2.4.2.2.2 Pseudowollastonite

On the basis of investigations made by Clark[39], Jeffery et al, Liebau[102] and Hilmer[103], Yamanaka et al[104] studied a single crystal of pseudowollastonite and the presence of polytype structures was elucidated by X-ray photographs. A four-layer polytype was found to be predominant, but in a few cases they also found a six-layer polytype, a

mixed structure of four- and six-layer polytypes and disordered structure. The structure of the four-layer polytype consisted of four Ca-octahedra layers and ternary rings of three tetrahedra of Si_3O_9 interposed between the layers (Figure 2-9). Ca atoms in the unit cell occupy seven independent positions: two on inversion centres and five at general positions. These Ca octahedra in a layer are compressed in the c-direction, while tetrahedra of the rings are elongated in the same direction. Thus distances between Ca and two bridging O atoms in the tetrahedra are short enough for Ca atoms to co-ordinate these O atoms. All Ca atoms have an eightfold co-ordination in the structure, though they seemingly occupy octahedral sites.

2.4.2.3 Inversion

It has been noted that when pure pseudowollastonite was cooled, even very slowly, it did not revert to wollastonite owing to the sluggish nature of the silicate transformation[105]. If powdered glass of composition $CaSiO_3$ is crystallised at any temperature, the product always consists almost exclusively of pseudowollastonite, but lumps of the same glass will crystallise readily to wollastonite with only a trace of pseudowollastonite present at temperature between 800-1100°C[37]. The inversion temperature between wollastonite and pseudowollastonite has been determined to be 1125±10°C[34].

The change may be so sluggish, close to the inversion temperature, that a longer period of heating would affect some inversion at a still lower temperature. Buckner et al[106] found an anomalous two-phase region, with both wollastonite and pseudowollastonite present between about 1115°C and 1135°C, in duplicate runs starting with both wollastonite and pseudowollastonite. On the basis of this data, the temperature of the reversion of pseudowollastonite to wollastonite was taken to be at least as low as 1120°C. Wollastonite was not converted completely to

pseudowollastonite even when exposed at 1142°C for 169 hours. They found that the lowest temperature at which pseudowollastonite, in addition to wollastonite, was crystallised from glass to be 1117°C. Wollastonite held at 1117°C for 71 hours remained wollastonite, but yielded small amounts of pseudowollastonite at 1120°C. The inversion temperature was raised to 1368°C as a consequence of diopside entering into solid solution in wollastonite in amounts up to 21 mass % , while little or no diopside enters into solution in the high temperature form[38].

2.4.3 Diopside

The structure of diopside was first determined by Warren et al[107]. It contains typical pyroxene chains: SiO_4 tetrahedra are linked by sharing two out of four corners to form continuous chains of composition $(SiO_3)_n$. The pyroxene chains are linked laterally by Ca and Mg ions (figure 2-10). The Mg ions are in octahedral co-ordination with oxygen atoms which themselves are linked to only one silicon atom, while the larger Ca ions are surrounded by eight oxygen atoms, two of which are shared by neighbouring tetrahedra in the chains. Mg atoms lie principally between the apices of SiO_4 chains, whereas Ca atoms lie principally between their bases. The neighbouring chains are staggered in the z-direction, so that a monoclinic cell with a=9.73, b=8.91, c=5.25 Å, and β=105°50' results; its space group being C2/c. The melting point of synthetic diopside was first determined by Day et al[108]; a more precise determination by Adams[109] gave the value 1391.2°±1.5°C.

2.4.4 Wollastonite Solid Solution

Studies using X-ray diffraction and high resolution electron microscopy [110, 111] have confirmed that the single-chain silicates such as wollastonite constitute a system with a basic structure which may, in principle, be adapted in an almost limitless number of

ways to accommodate different conditions of pressure, temperature and chemical substitution[112, 113]. Although normally fairly close in composition to $CaSiO_3$, the wollastonite structure can accept considerably amounts of Fe and Mn, and lesser amounts of Mg, all replacing Ca. With the entry of Mn and Fe into the structure there is a distinct decrease in cell volume[114, 115, 116].

Wollastonite solid solutions occurring in the system $CaSiO_3$-$CaMgSi_2O_6$-$CaAl_2Si_2O_8$ (anorthite) have the same compositional range as those in the system $CaSiO_3$- $CaMgSi_2O_6$[38]. It was found that the wollastonite solid solution crystals appearing in the system $CaSiO_3$-$CaMgSi_2O_6$-$CaAl_2Si_2O_8$ exhibited two distinct crystal habits. The most usual type appearing in equilibrium with liquid were small (0.01 to 0.03 mm), equant or elongated slightly parallel to the b-direction. A second type were large (0.1 to 0.3 mm in length) lath-shaped crystals, elongated parallel to the b-direction. If the runs were short (1 to a few hours), the first type was generally the only form appearing in equilibrium with other ternary liquids. If the runs were longer (from several days to a month), the first type disappeared as the second type appeared. If the same material was used and the temperature was raised to a value at which pseudowollstonite appeared and then lowered to a temperature at which wollastonite solid solution is the stable form, only large laths of wollastonite solid solution appeared. These results suggested that the small crystals of wollastonite solid solution were not a stable form. Posnjak[38] examined the crystals of wollastonite solid solution and they gave a typical wollastonite X-ray powder pattern with the lines slightly displaced owing to solid solution. Shinno[117] found a new phase of the diopside composition with the wollastonite structure, which he called Mg-

wollastonite. This Mg-wollastonite was found to appear throughout the whole range of the system $CaSiO_3$- $CaMgSi_2O_6$. The X-ray and infra-red absorption data of the wollastonite-diopside solid solutions (Mg-wollastonite) were presented[118]. Mg-wollastonite containing between 100% and 85% $CaSiO_3$ was described as stable, while between 80% and 0% $CaSiO_3$ as metastable. In the stable Mg-wollastonite, linear contractions of cell dimensions were observed due to the replacement of Ca by Mg, but no remarkable change occurred in the infrared absorption spectra. In the metastable Mg-wollastonite, an anisotropic contraction of the cell dimensions and linear changes in the wavenumber of the absorption bands were observed. Costantini et al[119] observed wollastonite-diopside solid solution when investigating the mechanism of the devitrification process of glasses in the system $(1+x)CaO.\ (1-x)MgO.2SiO_2$, $(0 \leq x \leq 1.0)$. X-ray powder diffraction patterns for samples from a differential thermal analysis (DTA) run stopped just after the exothermal crystallisation peak were analysed. They noticed that the diffraction peaks of the wollastonite phase progressively shifted towards high Bragg angles as CaO was substituted by MgO (x increased from 0.2 to 0.8). In these patterns diffraction peaks of diopside were absent. Sample $x = 0.2$ showed diffraction peaks for both wollastonite and diopside after heat treatment at 1100°C for 10 hours.

2.5 Phase Separation and Devitrification

2.5.1 Glasses

Glasses are kinetically frozen-in thermodynamically non-equilibrium states[120]. Classically, the term glass refers to any non-crystalline solid formed by cooling from the melt. By non-crystalline, it is meant that the molecules of the material are arranged in a chaotic or "amorphous" way so as to give rise to the characteristic diffuse X-ray pattern of a liquid. By solid, it is meant that the substance is macroscopically hard or rigid. Glasses at present are obtained not only by the undercooling of melts, but also by a variety of other methods, e.g., vapour deposition methods and solution methods[121], although as far as this thesis is concerned only oxide glasses made by cooling from a melt will be considered. The glass will have varying structures and properties depending upon the rate at which it was cooled through the glass transition. The conceptual picture of the random network was widely accepted as the best structural model for glasses[122]. There exist thermodynamic driving forces in glasses for crystallisation towards the respective equilibrium state.

2.5.2 Phase Separation in Glasses

Glasses are regarded as homogeneous materials. However, it is known that some binary or multicomponent systems exhibit miscibility gaps in their phase diagrams, the system existing in equilibrium, or metastable equilibrium, as two liquid phases of

different compositions. The process whereby the homogeneous liquid separates into two liquids as it is brought into the two-liquid region is known as phase separation. Most alkali and alkaline-earth silicate systems exhibit a region of liquid-liquid immiscibility in which two phases, one alkali or alkaline-earth ions-rich and the other silica rich, coexist. Much of the early work was concerned with stable immiscibility in which liquid separation occurs at temperatures above the liquidus, as shown in figure 2-11. It was not until the electron microscope was applied to the study of the microstructure of glass that metastable liquid immiscibility in oxide systems was found to be a common phenomenon. Metastable miscibility gaps occur below the liquidus (figure2-11) but above the glass transition. The chemical composition, quantity and sizes of regions of inhomogeneity are dependent on the initial glass composition, cooling rate, or time of holding of the glass at the given temperature. Thus a wide range of inhomogeneous structures can be obtained.

Phase separation has been observed in many glasses and melts[123]. It influences a variety of glass properties[123]. Thus there have been much research activity on the subject. Detailed reviews on phase separation in glass forming systems have been published by Hammel[124], Porai-Koshits[125], Charles[126], Zarzycki[127], James[128], Uhlmann and Kolbeck[129], Vogel[130], Seward[131], Mazurin and Porai-Koshits[123]. The origin of immiscibility, kinetics of phase separation, influence on the properties, etc., have been discussed in detail in these reviews and therefore only a brief review of the theories of nucleation, growth, spinodal decomposition and intersecting growth, which are important for the understanding of this thesis, will be presented here.

Thermodynamically, phase separation takes place because the system can reduce its free energy by separating into two or more phases. Theoretically there are two types of transformation mechanisms by which the final structure is attained. One is by a nucleation and growth mechanism, and the other spinodal decomposition.

Classical homogeneous nucleation and growth theory considers the existence of a nucleation barrier[122]. Once a stable nucleus has formed, growth is usually diffusion controlled. The separating phase at constant temperature maintains a constant composition with respect to time. During the initial stage, the nuclei tend to develop as randomly distributed spherical particles with low connectivity. The interface between the dispersed phase and matrix is relatively sharp during the growth period. During the early stages of the growth of isolated spherical droplets, produced by nucleation in the metastable region of the immiscibility gap, the droplets grow by long range diffusion at a rate controlled by temperature. At a later stage of growth, when the matrix is approaching its equilibrium composition a coarsening process begins to dominate, in which the smaller particles tend to dissolve and the larger particles grow at their expense.

According to spinodal decomposition theory[132, 133]., the work of formation of a nucleus approaches zero at the spinodal and within the spinodal no nucleation barrier exists. Phase separation is spontaneous, limited only by the mobility of the molecular species. When temperature is constant, the separating phase shows a continuous, irreversible variation in extremes of composition with time until equilibrium compositions are reached. The interface is initially diffuse, the second phase tends to be nonspherical in shape but uniformly distributed in size and shapes, and showing high connectivity.

Following the work by Cahn[132], the highly interconnected microstructure of many phase separated glasses observed by electron microscopy was taken by some authors as evidence for spinodal decomposition. However, it was realised that morphology alone is not sufficient to decide on the mechanism of separation. Haller [134] has demonstrated that an interconnected microstructure can also be produced by classical nucleation, to form a high density of small discrete spherical particles followed by radial growth of these particles until they touch, the area of contact enlarging by a rearrangement process. This model predicts that the nucleation density determines the final morphology of the structure. The larger the nucleation density, the closer the spherical particles approach each other before matrix depletion slows down the diffusion process. Hence for a given composition, high nucleation density may produce a highly interconnected microstructure, whereas a low nucleation density may yield isolated droplets and low connectivity. Haller's theory[134], known as the intersecting growth theory, received support from Seward et al[135] who made an electron microscope study of the $BaO\text{-}SiO_2$ system in the region of the miscibility gap. The work of MacDowell and Beall[136] on phase separation in $Al_2O_3\text{-}SiO_2$ glasses also supported this model.

The factors which affect the phase separation process and morphology have been studied in great detail[123]. The mean composition and the heat-treatment temperature define the compositions and volume fractions of coexisting phases. Mazurin et al [137] investigated the effect of previous thermal history on the morphology of a phase-separated glass. Slow cooling of the melt leads to a droplet structure more often than sharp decrease in temperature and subsequent isothermal holding. Haller and

Macedo[138] studied a 7 mass % Na_2O, 25 mass % B_2O_3, 68 mass% SiO_2 glass to prove that the type of a structure also depended on how the heat-treatment temperature was achieved, ie by cooling from a higher a temperature or by heating the previously quenched glass from room temperature. Roskova[139] demonstrated in greater detail that for all compositions of sodium silicate and sodium borosilicate glasses within the spinodal region and lying in the vicinity of the spinodal, the cooling from higher temperature resulted in the development of a droplet structure, whereas the interconnected structure was associated with heating from room temperature. Porai-Koshits and Averjanov[140] demonstrated that the tendency of a given glass to develop the interconnected structure increased with decreasing temperature in a 12.5 mass% Na_2O-87.5 mass % SiO_2 system.

2.5.4 Devitrification of Glasses

Glasses generally form as a result of the large energy barrier to homogeneous nucleation. The stabilisation of the non-equilibrium glass always precedes the crystallisation of the undercooled melt. An understanding of the devitrification mechanism is of particular significance in many aspects of glass science and technology. It is important to understand the factors affecting the stability of a glass for practical applications where the formation of nuclei and their subsequent growth to crystals must be avoided, such as in optical fibres, laser glasses, optical switching glasses, etc, as well as in the preparation of glass-ceramics with desired microstructures by controlled nucleation and crystallisation. Since the first Symposium on Advances in Nucleation and Crystallisation in Glasses in 1961[141],

seventeen international congresses have been dedicated to glass sciences. In these conferences, nucleation and crystallisation in glass forming systems have been one of the main issues[142, 143, 144, 145, 146]. Other excellent reviews and more recently published articles are available, e.g. Uhlmann[147], and Gutzow[148]. Only relevant key issues will therefore be reviewed in this thesis.

Crystallisation is generally viewed as a two-step process[149]. It includes nucleation and crystal growth. Nucleation may be either homogeneous or heterogeneous. Assuming an activated process, the rate of nucleation increases to a maximum value as the undercooling is increased. With further undercooling the rate decreases exponentially as the portion of atoms with sufficient thermal energy to make the jump across the melt-crystal interface is decreased (figure 2-12). The temperature dependency of the growth rate of crystals in a supercooled melt follows a curve which is similar in shape to that for nucleation.

As far as the devitrification products are concerned, a phase diagram only represents the ideal situation whereby phase changes are allowed an infinite time in which to occur, so that the given material will always attain the ultimate condition or equilibrium state. Given that the driving force for a number of possible transformations is appreciable, the kinetics will determine which phases are formed. A common type of non-equilibrium behaviour is the formation of a metastable phase which has a lower energy than the mother phase, but is not the lowest-energy equilibrium phase[150]. The transformation which involves the minimum reduction in free energy is kinetically most favourable, as the smaller ΔG implies a greater

structural or chemical similarity to the parent. In general, high temperature forms have a more open structure than low-temperature forms and consequently are more nearly like the structure of a glassy starting material. It is exemplified by a number of systems. For example, when silica glass crystallises, cristobalite may be the phase formed, even within the temperature range over which quartz or tridymite is stable[151]. Ferguson and Merwin[36] observed that when calcium-silicate glasses were cooled to a temperature below 1125°C, at which wollastonite is the stable form, the high-temperature modification, pseudowollastonite, was found to crystallise first and then slowly transform into the more stable wollastonite.

Phase separation and crystallisation are independent phase transformation processes. Whether liquid phase separation or crystallisation takes place in the system depends on the interrelation between the rates of formation of the two phases. However, in most multi-component systems crystallisation may be accompanied by processes of liquid phase separation and vice versa. The separation of the initially homogeneous phase into two or more different liquid phases may substantially affect the course of the subsequent crystallisation process. Theoretically, amorphous phase separation could influence crystal nucleation in several ways[129]:-

(a) the supersaturation with respect to crystallisation in the different liquid phases may be quite different that in the initial homogeneous phase;

(b) the viscosity in the evolving new phases may differ;

(c) in the bulk of the melt, new interfaces are created which may favour nucleation;

(d) nucleation sites may be distributed differently in the newly formed phases.

James[128] has discussed several mechanisms for the enhancement of crystal nucleation associated with the interfaces between the liquid phases.

2.5.4 Devitrification in Alkaline-Earth Silicate Fibres

Three different fibres, Superwool 607, A2 and B3 (see Section 3.2), have been studied in this project. The compositions of these fibres lie in the SiO_2 - $CaO{\cdot}SiO_2$ - $CaO{\cdot}MgO{\cdot}2SiO_2$ phase triangle and are not far from the two liquid region. Crystalline SiO_2, $CaSiO_3$ and $CaMgSi_2O_6$ would be expected as final devitrification products. However, the detailed devitrification process and the resulting microstructure will depend on the thermal exposure conditions.

Philips and Roy[152] studied three compositions M1, M2 and M3 (table 2-3) near, but outside, the stable liquid immiscibility region in this ternary system and found that composition M1 lead to clear glass and no separation could be obtained; composition M2 contained some crystals on quenching and M3 formed a clear glass which did separate metastably after being heat treated at sub-solidus temperatures. Electron micrographs showed that phase separation developed with time at 825°C.

Subsequent devitrification of the alkaline-earth silicates rich glassy phase by appropriate thermal treatment would be expected to result in the formation of crystalline silica, $CaSiO_3$ and $CaMgSi_2O_6$. Much research has been carried out on the devitrification behaviour of silica phases in bulk silicate glasses and in aluminosilicate fibres, but until this investigation, very little work has been carried out on alkaline-earth silicate systems. More than half century ago, Osborn and his colleagues noted that two different forms of wollastonite solid solution existed in the $CaSiO_3$ -

$CaMgSi_2O_6$ system[38], one of which was not stable on extended heat treatment. Detailed composition analysis and phase transformation studies were not possible, due to the unavailability of modern analytical techniques. In the 1970's, Shinno found a range of wollastonite solid solution in this system[117, 118]. He concluded that Mg-wollastonite was metastable, but the phase transformation mechanism was ambiguous. More recently, Costanini et al also noted the interesting crystallisation behaviour of this system[119], but no further studies were performed.

Alkaline-earth silicate fibres, have been developed as a replacement for traditional ceramic fibres. Although the fibre diameters are in the respirable range, the manufacturers claim they are safer to use by virtue of their relatively high solubility in lung fluids[17]. The devitrification products formed during high temperature service have however, not been fully established or the mechanism by which they form, and the issue of silica from after-use inhalation remains. Clearly the understanding of microstructural development in this system, as a function of temperature and time, would make a useful contribution to our knowledge of these materials and their development as safe ceramic fibres with improved materials performance in use. This was the objective of the work reported in this thesis.

3.1 Experimental Design

The aim of this project has been twofold: to gain a thorough knowledge of the devitrification behaviour of selected compositions of the new generation of the alkaline-earth silicate fibres and to contribute to the understanding of this particular glass forming system. The detailed objectives have been (a) identification of devitrification products as a function of exposure temperature and time in clean furnace environments, (b) determination of the microstructures of devitrified fibres and (c) developing an understanding of the devitrification process. The experimental program for the project is shown by figure 3-1.

The study has been mainly focused on the Superwool® X-607 which is the first commercial alkaline-earth silicate fibre product to be released onto the market. Investigations of A2 and B3 fibres which are industrial probe type of fibres of different compositions were undertaken for comparison purposes and broaden the understanding of the devitrification behaviour of this alkaline-earth silicate fibre system.

Choice of the exposure temperatures and times was based on (a) information from phase diagrams, (b) the manufacturer's specified service temperature for the fibres, and (c) a wider range of temperature chosen to aid understanding of the phase development and transformation. The fibres were thermally exposed in magnesia crucibles and in clean furnace environments for time ranging from a few minutes to

thousands of hours and at temperatures ranging from 700°C to 1250°C These exposures were achieved using a combination of a specially-designed vertical tube furnace for short exposures and muffle furnaces.

As-manufactured and thermally exposed fibres were analysed using a range of complementary analytical techniques. X-ray diffractometry (XRD) was employed to identify the devitrification products. The microstructures of as-manufactured and heat-exposed fibres were analysed using analytical transmission electron microscopy incorporating electron microscopy, electron diffraction and X-ray microanalysis. To enable the detailed microstructural analysis necessary to determine the various phases and their distribution within the fibres, techniques involving ion beam thinning and ultramicrotomy were developed to reliably prepare electron-transparent samples of fibre cross-sections. Scanning electron microscopy (SEM) was used to determine the surface structure and phases in fibres and, in particular, in shot particles. Thermal analysis also contributed to the phase characterisation of the devitrified fibres.

3.2 Materials

3.2.1 Origin[28, 153]

Three different grades of alkaline-earth silicate fibre were provided by Morgan Materials Technology Ltd: Superwool® Grade X-607, A2 and B3. The fibres were manufactured by the spinning process. Superwool® Grade X-607 (hereafter called

'Superwool fibre') was supplied in blanket form. The lubricant introduced during manufacture had been removed by heating to about 650°C for about 30 minutes This material has a classification or indicative maximum service temperature of 1050°C (manufacturer's data). A2 and B3 fibres were supplied in their as-manufactured wool form. These man-made mineral fibres are categorised as insulation wool according to IPCS classification (International Programme on Chemical Safety)[154]. The compositions of the fibres were analysed using X-ray fluorescence spectrometry (XRF) and the results are presented in table 3-1. Figure 3-2 shows their positions in the triangle SiO_2-CaO·SiO_2-CaO·MgO·2SiO_2 in SiO_2-CaO-MgO phase diagram and detailed information about their properties and applications has been introduced in Section 2.2 and is also available in the product information sheet[28].

3.2.2 Handling and Safety[154]

These fibrous products are mechanical irritants to skin, eyes and the upper respiratory system but studies of animals exposed to high concentrations of Superwool did not show chronic health effects. As with any dust, pre-existing upper respiratory and lung diseases may be aggravated. It is therefore recommended that disposable gloves and laboratory coats be worn when handling the fibres, that clothing should be loose around the neck and wrists and that precautions should be taken to avoid breathing dusts. All the processes including fibre loading and removal from crucibles, fibre grinding, preparing XRD samples should be carried out in a circulatory fume cupboard. Air flow of the cupboard should be checked before use. Work areas should be regularly cleaned. An 'asbestos-grade' vacuum cleaner for spillage should

be to hand. After handling, any exposed skin areas should be washed with water and work clothing should be washed separately. All surfaces coming into contact with fibres should be wiped down with a damp cloth. The fume cupboard should be emptied and wiped down with a damp cloth after use. Paper lining from cupboard and disposable gloves, together with any other disposable materials should be put into double sealed and labelled bags for disposal.

3.3 Thermal Exposure

3.3.1 Extended Exposures

A number of Carbolite muffle furnaces were used to provide extended thermal exposures at set temperatures of 700°C, 750°C, 800°C , 900°C, 1000°C, 1100°C, 1200°C and 1250°C. Superwool fibre was exposed in its original blanket form and A2 and B3 fibres were exposed in their original wool form. As will be explained in section 3.3.2.2, fibre was not ground before thermal exposure.

Fibres were exposed in silica crucibles at temperatures up to 900°C. Silica crucibles devitrify at temperatures exceeding 900°C and therefore magnesia crucibles were utilised at the higher temperatures. Pyrotenex type k internal sheath thermocouples and a 5-channel recording thermometer type KM1242 were used to constantly monitor furnace temperatures. The monitoring thermocouple was positioned in the centre of the furnace and up to 6 crucibles surrounded the thermocouple in each

furnace. The deviation in temperature as measured in these crucibles was within ±2°C of the set temperature.

The fibres in their crucibles were introduced into the furnaces at the set temperatures under atmospheric conditions. As the sample was introduced into the furnace, the temperature fell slightly below the set value but took only 2-3 minutes to regain. This time was considered negligible in comparison with the heat treatment times which ranged from 30 minutes to thousands of hours. Fluctuation in temperature due to power failure, heating elements failure etc. were identified from the record of the monitored furnace temperatures. Identified problems resulted in the corresponding furnace being switched off and the particular furnace exposure being abandoned. Thermal exposure was repeated using as-manufactured fibres only after the furnace was serviced and a stable temperature reading was achieved. The crucibles were allowed to air cool upon removal from the furnace and the fibres were emptied from the crucible after it had cooled naturally to room temperature.

3.3.2 Short Term Exposure

3.3.2.1 Furnace Design

A vertical tube furnace was designed and developed for short term (less than 30 minutes) exposure of fibre. Figure 3-3 illustrates the design of the furnace. Platinum was chosen as the crucible material because of its high thermal conductivity and low thermal mass and platinum wire bound to the thermocouple sheath was used to manually lift and lower the crucible. An alumina tube was

designed to support the crucible after it was lowered to the exposure position in the furnace. Following the required exposure, the crucible was removed from the furnace and allowed to cool naturally to room temperature before removing the fibres from the crucible. With the furnace in operation at 1000°C it was shown that the temperature variation over a distance of 1.5 cm in the hottest zone of the tube was less than 1°C. The crucible was suspended in the centre of the hot zone and the resulting temperature gradient over the sample was therefore assumed negligible.

The temperature of the fibre within a crucible was monitored by a Pt/Pt-13% Rh thermocouple connected to a PC-based data acquisition system (figure 3-4). The thermocouple was embedded in the centre of the fibre in the crucible and its output voltage was amplified and linearised by signal conditioning modules, then digitised by a plug-in board and processed by WorkBench PC™ software to convert the input voltage to the measured temperature. The sampling rate could be up to 1000Hz.

3.3.2.2 Materials and Thermal Behaviour

When the crucible was first introduced into the hot furnace a temperature gradient exists from the crucible wall to the centre of the fibre sample. Figure 3-5 shows a typical temperature-time trace for a short exposure. The exposure time was measured between the crucible being loaded into (point A) and lifted out (point B) of the furnace (figure 3.5). The time taken to establish a uniform

temperature inside the crucible depended on the packing density of fibres. Fibres in their original wool or blanket forms have lower packing density and a faster thermal response than ground fibres. Figure 3-6 shows that it took approximately 7 minutes for ground fibres to reach the furnace temperature of 900°C while less than 2 minutes was required for the fibre blanket to reach the same temperature. This response suggests that fibres should be exposed in their wool or blanket form, rather than in their ground form, to give the fastest response.

The embedded thermocouple enabled further characteristics of the thermal response of the fibres to be identified. Figure 3-7 shows the thermal response curves for fibre A2 after it had been introduced into the furnace as a wool at temperatures of 900°C, 960°C and 1000°C. An exothermic peak corresponding to the crystallisation of the fibres was detected at both 960°C and 1000°C while no peak was observed at 900°C. This implies that the crystallisation temperature of the original fibre is between 900°C and 960°C. It also suggests that the sensitivity of this temperature monitoring system is high and is able to detect temperature variations within the fibre sample in the crucible. For ground fibres, as shown in figure 3-8, the exothermic peak was observed at 900°C and 1000°C. This suggests that the process of grinding results in devitrification of the fibre at a lower temperature and a change in the crystallisation behaviour.

The desire to look at the material in its as-used state and to minimise long thermal response times supported experiments where the thermal response was studied for the wool/blanket form of fibres rather than following fibre grinding.

3.4 Materials Characterisation

3.4.1 X-Ray Powder Diffractometry

3.4.1.1 X-Ray Diffractometer

Analysis of the devitrified products to determine the identity and development of the phases was carried out using a Philips multi-purpose X-ray powder diffractometer system. This system has a type PW 1710 controller, type PW 1830 X-ray generator fitted with a copper tube and type PW 1820 goniometer with graphite monochromator. The system was PC-controlled using the Philips APD version 3.0 software. Diffraction data plots were obtained under the following conditions: Cu Kα radiation operating at 35kV and 45mA, 2θ range from 10 to 60° at a scanning rate of 0.008 of 2θ per second, 1°Divergence slit, 0.20 receiving slit and 1° scatter slit. When lines of interest are obscured by overlapping peaks or when a complex background is present, profile fitting was used to eliminate these interferences before the analysis. The software enabled a database of standard diffraction files to be stored. Lines corresponding to a particular phase could then be superimposed onto an experimental diffraction pattern for comparison purpose.

3.4.1.2 Qualitative Analysis

For qualitative analysis, data plots were analysed and interpreted using Phillips Automated Powder Diffractometer (APD) Version 3.0 software. The information in a diffraction pattern includes the d-spacings of the peaks, their associated intensities and other significant features of the total diffraction pattern such as line profiles. The measured d-spacings reflect the geometry of the crystal lattice, i.e., the size and shape of the unit cell, and the intensity of the peaks is related to the specific atoms in a crystal and their arrangement in the unit cell. The diffraction profile is related to the size and perfection of the crystallites under study and to various instrumental parameters.

The phase identification process involves a detailed comparison of the measured data for the material studied with published standard data i.e. data in the JCPDS Powder Diffraction File (PDF) published by the International Centre for Diffraction Data (ICDD). Crystalline phases were identified when a satisfactory agreement was achieved.

For cristobalite key features distinguishing the α-cristobalite and β-cristobalite forms in XRD patterns are the additional diffraction peaks for α-cristobalite and the differing values for d-spacings and intensities. Table 3-2 (standard data) shows the d-spacings of crystallographic planes and the associated relative intensities of the diffraction peaks for the two cristobalite forms.

To help identify the cristobalite form in the devitrified fibres standard α-cristobalite was manufactured. The starting material was a high-purity synthetic fused silica tube and XRF analyses showed 99.99% SiO_2. The tube was ground using an agate pestle and mortar and the resulting powder was selected using a 37 μm mesh sieve. The powder was then devitrified at 1400°C for 165 hours in a platinum crucible in a muffle furnace. Figure 3-9 shows the XRD traces of the amorphous silica starting material and the resulting α-cristobalite product. The measured d-spacings and the associated relative intensities for the α-cristobalite had an excellent match when compared with standard JCPDS card no. 39-1425.

For the wollastonite, 3 different sets of diffraction data, two for monoclinic and another one for triclinic forms, were found from JCPDS cards. Table 3-3 summarises the crystallographic and diffraction data for these wollastonite phases. As will be reported in Chapter 4 the best match of the measured and standard data for the d-spacings and relative intensities of the wollastonite formed in devitrified fibre was found to be monoclinic as presented in JCPDS no 27-88.

For the other potential crystalline products, the distinguishing peaks used for their identification are (220), (004) and (222) for tridymite (T); (100) and (101) for α-quartz (Q); (006), (112), ($\bar{1}$22), (2$\bar{2}$2), (114) for pseudowollastonite (PW), and (021), ($\bar{2}$20), ($\bar{2}$21) and ($\bar{3}$11) for diopside (D). Table 3-4 displays these major diffraction peaks, their intensities and d-spacing data and associated crystallographic planes. The main peaks of these different crystalline phases are identified in figure 3-10, which is

the X-ray powder diffraction pattern of Superwool fibre devitrified at 1000°for 3240 hours.

Crystalline phases may sometimes form solid solutions. When an atom substitutes for another in a given structure, the size difference between the two types of atoms may cause the lattice parameters to increase or decrease, or in some cases, some parameters to increase and others to decrease. X-ray powder diffraction patterns are related to composition through (a) the unit cell parameters, and (b) the reflected intensities. The d-value is a direct function of the lattice parameters and solid solution formation may therefore cause significant shifts in the measured d-values. As indicated in Section 2.4.4, wollastonite may form Mg-wollastonite and resulting shifts in the d-spacings have been reported by Posnjak[38], Shinno[117, 118], and Costantini et al[119].

3.4.1.3 Semi-Quantitative Analysis

In order to determine the exposure temperature and time for the onsets of the different crystalline products and the relative changes in the mass of a particular phase with varying exposure conditions, semi-quantitative analysis of the thermally exposed fibres was carried out using XRD. Quantitative analysis by XRD is based on the fact that the intensity of a diffraction peak from a particular phase in a mixture of phases depends on the concentration of that phase in the mixture. The internal-standard method [155, 156] is the most general of any of the XRD methods for quantitative phase analysis.

For an internal-standard analysis[156], a diffraction line from the phase to be determined is compared with a line from a reference material of known and fixed proportion within the XRD sample, the internal standard. The basic equation can be expressed as:

$$\frac{Ii}{Ir} = KiWi \tag{3-1}$$

where Ii = integrated peak intensity for analysis peak chosen for the phase to be quantified, Ir = integrated peak intensity for analysis peak chosen for the standard material, Ki = calibration constant for phase I, and Wi = weight fraction of phase I in the sample discounting the standard material. The internal standard material chosen for this work was BaF_2 (Purity 99.9%, Fluorochem Limited). BaF_2 gives only 2 reflections in the angular range of interest. As shown by figures 3-10 and 3-11 its strongest peak, (111), is conveniently located providing only minimal interference with the diffraction peaks from the phases to be analysed.

To carry out a complete quantitative analysis of the devitrified products, standard reference materials for each phase are needed. As will be found in the results part of this thesis, among the main crystalline phases formed in the devitrified fibres, wollastonite always crystallised in the form of a solid solution and an appropriate reference material would be a phase pure wollastonite solid solution containing the same amount of Mg^{2+}. Efforts to find a wollastonite which could meet this requirement failed and the chance of finding this kind of wollastonite from natural or commercial sources is felt to be very small and the best way would probably be

chemical synthesis using alkaline-earth oxides and silica. This work has not been undertaken and therefore, only changes in relative peak intensities for different phases in the devitrifying fibres will be used to show phase development and transformation. This method will be called semi-quantitative analysis.

The relative peak intensities were expressed as the ratio of the integrated intensity of a particular phase to the intensity of the strongest peak from BaF_2, (111). Profile fitting was used for accurate determination of peak positions, backgrounds, and intensities. The counts collected for the peaks were fitted and numerically integrated to extract the peak area.

To establish which diffraction lines were to be used for each phase, including the internal standard, the aim was to select the strongest peak for each phase consistent with avoiding any overlaps with peaks from other phases. For diopside and wollastonite, due to overlapping peaks, it was not possible to use the strongest peak for each phase. In such cases, by consulting the appropriate JCPDS cards, the second or third strongest peak had to be chosen. The chosen diffraction peaks for semi-quantitative analysis were therefore: (101) for α-quartz; (101) for α-cristobalite; (002) for wollastonite and $(\bar{2}20)$ for diopside.

Like all instrumental methods of analysis, X-ray powder diffractometry is subject to a variety of random and systematic errors, for example the relative intensities in a given pattern are very dependent on particle orientation and the peak positions are sensitive

to specimen height. The effect of specimen height was minimised by careful preparation and mounting of the specimen.

3.4.1.4 Sample Preparation

An agate mortar and pestle were used for general grinding. Working in a fume cupboard, as-manufactured and thermally-exposed fibres were ground to fine powders and compacted into a front loading diffractometer specimen holder. There were essentially two major concerns: (a) to obtain a completely random orientation of fibres and (b) to obtain a smooth flat surface which meets tangentially with the focusing circle of the diffractometer. When necessary, the accuracy of intensity data were improved by repacking and reanalysing the sample a number of times and averaging the results. For semi-quantitative analysis, the devitrified fibres were crushed and mixed with 20 wt % BaF_2 for measurement purposes.

3.4.2 Transmission Electron Microscopy

3.4.2.1 Transmission Electron Microscope

A Philips CM20 analytical transmission electron microscope was employed for microstructure analysis. Either a W or LaB_6 filament was used and normally the microscope was operating at 200kV accelerating voltage. Information such as bright and dark field images, selected area electron diffraction patterns, X-ray energy dispersive spectra and X-ray mapping of the as-manufactured and devitrified products were obtained and analysed.

3.4.2.2 Transmission Electron Microscopy

Transmission electron microscopes (TEMs) ideally have the ability to form images of features within materials with a resolution, currently, of about 0.15 nm. Conventional methods of image formation in the TEM are bright-field (BF) and dark-field (DF) imaging. Additionally, modern microscopes offer the possibility to determine the crystal structure of features using different electron diffraction techniques.

Electron diffraction patterns have many similarities to those formed by X-ray diffraction techniques. The great advantage, though, is that in the TEM the volume analysed can be extremely small (a few tens of nm^3) as this volume is, in principle, determined by the diameter of the incident electron beam and the thickness of the specimen. Thus, for example, the structure of tiny crystalline particles embedded in a glassy matrix can be determined and ultimately the material of the particles can be identified.

The analysis of selected area electron diffraction (SAED) pattern relies on the well known Bragg equation. In the corresponding diffraction pattern it can be shown that the distance g_{hkl} between an (hkl) diffraction spot and the transmitted spot is given by:

$$g_{hkl} = \frac{\lambda L}{d_{hkl}} \qquad (3\text{-}2)$$

where λL is a constant dependent upon the microscopes lens currents and the accelerating voltage, and d_{hkl} the interplanar spacing of diffracting (hkl) planes. The angle between any two diffracting vectors is identical to the angle between the corresponding planes in real space. Thus, the angles between the planes can be determined. Knowing the indices and angles between planes, the direction in the crystal along which the electron beam travels can be determined.

Further, the modern analytical transmission electron microscope (ATEM) normally includes energy-dispersive X-ray Analysis (EDXA) which can be used to analyse the chemical content of TEM specimens. When a high-energy electron beam is incident on a TEM specimen, X-rays are produced following inelastic scattering of the beam electrons by the sample atoms. As the energy levels of the electrons in atoms of different elements are not the same, the energies of the X-ray emissions are different for the various elements in a specimen. These characteristic emissions allow the presence of a particular element to be established. Further, a quantitative chemical determination of the electron-irradiated area can be carried out by analysing the integrated intensity of the various characteristic peaks.

To investigate the microstructures of the as-manufactured and heat-exposed fibres and to unambiguously determine the various phases and their distribution within the fibres, it has been necessary to select analytical transmission electron microscopy with the associated techniques of electron diffraction and X-ray microanalysis.

3.4.2.3 Sample Preparation

3.4.2.3.1 Introduction

The necessary TEM analysis necessitated the preparation of specimens which would enable the detailed microstructure analysis of fibre cross-sections. The specimens had to be uniformly and adequately thin (a) to allow representative cross-sections to be selected from a number of sections viewed in the specimen and (b) to enable the separate identification and analysis of single grains or phase separated regions in selected cross-sections. Requirement (b) was particularly stringent as individual grains or phase separated regions could approach dimensions on nanometer scales and too great a specimen thickness (I) made it difficult to isolate and analyse distinct regions as opposed to regions overlapping with depth and (ii) degraded the spatial resolution, notably for Energy Dispersive X-ray Analysis (EDXA), which again limited the ability to analyse distinct regions in the selected fibre cross-sections. Requirement (a) demanded pre-alignment and parallel packing of fibres and the preparation method chosen had to be reliable and time efficient to cope with the overall number of specimens required by this investigation. The project also demanded a significant number of specimens associated with differing values of investigated variables and the reliability and time taken to prepare specimen were also key issues.

Methods of specimen preparation based on ultramicrotomy (UM) and ion beam thinning (IBT) are described and critically compared in the following sections.

3.4.2.3.1 Ion Beam Thinning

The procedure initially involved making a 3 mm fibre/resin disc having a high fibre packing density and low porosity. The disc was then ground, polished and dimpled to achieve a thickness of about 15 μm at the centre and, finally, ion beam thinned until a perforation was formed.

The procedure is illustrated in detail in figure 3-12: The first stage was to make a 3 mm diameter fibre/resin disc having a high fibre packing density and low porosity. Two-component Gatan's G-1 resin was confirmed to be an ideal embedding medium because of its short curing time, high strength and stability during the preparation process and also under electron beam exposure. It forms extremely strong bonds with the fibres and no additional wetting process was needed. The as-manufactured or thermally exposed fibre was crushed to fine powder with pestle and mortar. Figure 3-13 shows the crushed fibre. The crushed fibre was then mixed on a glass slide with Gatan's G-1 epoxy and hardener (figure 3-12a). The mixture was vacuum degassed for about 30 min to reduce the density of air bubbles, then transferred to a 3 mm diameter stainless steel tube and again vacuum degassed (figure 3-12b). The epoxy was cured for 30 min at a temperature of 100°C before the tube was sliced into a series of 250-500μm thick discs (figure 3-12c) using a wiresaw. The discs were ground to a thickness of about 50 μm with one side polished with 0.25 μm-grade diamond paste (figure 3-12d).

Dimpling of the discs was achieved by grinding, coarse polishing and fine polishing.

6μm diamond paste was used to dimple grind the disc down to a central thickness of 20μm and the sample was then thoroughly cleaned in methanol in an ultrasonic bath. 1μm diamond paste was used to dimple and coarse polish the sample to a central thickness of 15 μm and to remove scratches and other mechanical damage resulting from grinding. Fine polishing to produce a smooth surface was achieved using a new, clean, felt polishing wheel and 0.05μm γ-alumina suspension (figure 3-12e).

Traditionally, it is difficult to get thin foil of fibre cross sections for TEM using ion beam thinning methods because the medium used to support the fibres tends to be preferentially sputtered away. Gatan's newly developed Model 691 Precision Ion Polisher PIPS™ has been designed to address this problem. In this system, the ion beams are incident at glancing angles to the specimen and because the argon ion beams strike the sample at low angles, the fibres shield the supporting epoxy and this minimises the rate of epoxy removal.

The dimpled disc was first loaded on the specimen post with the dimple downwards and thinned using 3 keV argon ion beams. During thinning the fitted automatic terminator at perforation was not used due to semitransparency of the epoxy and the specimen was viewed with the attached microscope and the process terminated when the perforation was first seen (figure 3-12f). The perforated disc was then reloaded with the dimple upwards and ion-beam polished for 5 minutes at 2 kev. The disc was carbon coated before analysis in the microscope.

The low magnification TEM micrograph (figure 3-14) shows a representative view of fibre packing density in the fibre/resin disc in an ion beam thinned specimen. The resulting specimens showed (a) the use of PIPS™ did reduce the preferential thinning of the resin matrix, (b) full views of fibre cross-sections with no fragmentation, and (c) good adhesion of cross sections to the resin matrix. Drawbacks were (a) Specimen made using this method did give some thin fibre cross sections near the edge of perforation but the number was limited, (b) random alignment of fibres which made it difficult to obtain for analysis sufficient well-aligned cross-sections close to the perforation, and (c) the length and complexity of the process to prepare a single specimen from an initial sawn disc.

3.4.2.3.2 Method Employing Ultramicrotomy

Ultramicrotomy (UM) has been extensively used for the preparation of TEM specimens from biological materials and increasingly from a wider range of materials including polymers [157], metals [158], surface coatings [159], metal multilayers [160], particles[161] and whiskers [162, 163]. The challenge and uniqueness of the work reported here was to develop the method, as described by Reid [164], to meet our analytical requirements for fibre alignment, high fibre packing density and specimen uniformity and thinness.

The procedure developed to prepare the fibre specimen using UM was as follows:

The fibres to be analysed were first powdered using a pestle and mortar. The crushed fibres were initially wetted in an epoxy primer solution of 1% γ-glycidoxypropyl trimethoxysilane in 50% methanol and 50% water and then dried. This process, reported by Swab and Klinger [165] for multilayer optical coatings, strengthened the interfacial bond between fibres and resin and limited fibre pullout during ultramicrotomy.

Embedding: an important consideration in embedding was the need to maximise the parallel alignment and packing together of fibres to ensure as many as possible ultimately had their cross section parallel to the block face. A four-component Spurr resin (Agar Scientific Ltd) was chosen as the embedding medium and the fibres were initially dispersed in this medium. This resin was chosen for its low initial viscosity which is essential for fibre dispersion, extrusion and alignment and good sectioning properties after polymerisation and the proportions of the four components were chosen to produce a block of suitable hardness. Generally, the harder the block the better the results although too much hardener will reduce the lifetime of the resin. It was preferred to use fresh resin i.e. the resin made up immediately before use. Also some of the components were subjected to oxidation and degraded after supplied for a period of time and the proportion is supposed to be adjusted. To this end, typically 20% by mass of fibre powder was added and dispersed in the fresh resin mixture. The following 2-step embedding process was followed:

First, a pasteur pipette was used to extrude and inject the fibre/resin mixture into a plastic tube of 1 mm internal diameter and then the loaded tube was laid horizontally

and left for about 1 hour before curing the fibre/resin mixture in an oven for 8 hours at 70°C. The extrusion provided initial fibre alignment, the horizontal resting of the loaded tube provided fibre packing and further alignment through sedimentation, and the subsequent curing of the loaded tube and removal of the outer plastic sheath left a fibre/resin cylinder. Second, the cured fibre/resin cylinder was mounted with its end up to the mould face of a standard specimen mould (Agar Aids). The mould was then filled with fresh resin and cured at 70°C for 8 hours. (figure 3-15a). Figure 3-16 is the SEM micrograph of the cross section of the fibre/resin cylinder.

Trimming of the specimen cutting face: Using a Reichart OmU3 Ultramicrotome attached with a freshly made glass knife, the cutting face of the block containing the embedded fibres was trimmed down to a facet in order to provide a minimum area to the knife and thus maximise the cutting force per unit length (figure 3-15b).

Ultra thin sectioning and section retrieval for TEM examination: Ultra thin sectioning was achieved using the ultramicrotome equipped with a 45° diamond knife. Sections were collected on the surface of the distilled water in the collection trough attached to the knife. The rate of thermal feed, the cutting speed and the knife returning speed were carefully controlled to obtain required section thickness. This thickness was monitored using the binocular microscope to view the interference colours as the thin section floated onto the water surface. Ribbons of sections which were grey in colour indicating a thickness around 60 nm [166]. These were then collected on a carbon film on 200 mesh copper grids and dried prior to viewing in the transmission electron microscope.

Figure 3-17 shows a typical section of as-manufactured fibre imaged in the Philips CM20 transmission electron microscope. Analysis demonstrated that the specimens produced routinely by the ultramicrotomy method were thin enough to allow the detailed identification and analysis of the various components of the microstructures by analytical transmission electron microscopy and, once the resin block was made for a particular starter powder further TEM specimens could be quickly prepared. The most dramatic result of UM was the extensive electron transparent regions of uniform thickness observed. It provided an adequate ability to select good cross sections of this thickness. Such large regions of uniform thickness are also beneficial for the rapid identification of chemical and structural inhomogeneties within the fibre. The fibre cross-sections tended to crack and fragment during sectioning but this did not prove a problem in analysis as the microstructures in fragments can be individually analysed and the location of the fragments in the cross-sections can be readily seen. Fibre cross-sections were firmly adhered to resin and no pullout of fibres was observed.

While methods based on both ultramicrotomy and ion beam thinning procedures can be applied to the preparation of the required TEM samples of ceramic fibres it was concluded that the method based on UM with associated development of embedding to provide pre-alignment and closer fibre packing was superior in terms of the quality of samples and reliability and time efficiency of operation. Therefore, in this project it was decided to use UM as the main method to prepare the required TEM specimens.

3.4.3 Scanning Electron Microscopy

3.4.3.1 Scanning Electron Microscope

To determine the development of structures of fibre surface and shot particles with thermal exposure temperature and time, A Philips XL40 scanning electron microscope with EDS attachment was used. The microscope was operating at 20 kV and secondary electron imaging, and back-scattered electron imaging, microanalysis (including X-ray energy dispersive analysis, semi-quantitative composition analysis and X-ray mapping were carried out. The results from micrographs and chemical analysis were analysed.

3.4.3.2 Scanning Electron Microscopy

The main advantages of scanning electron microscopy (SEM) are the high lateral resolution (1~10nm), large depth of focus and the numerous types of electron-specimen interactions that can be used for imaging or chemical analyses purposes. The most often used signals produced during the interactions are from secondary electrons (SE) and back scattered electrons (BSE). The topographic contrast observed in most SE images give a crisp three-dimensional appearance while BSE images carry atomic number or material contrast. The X-rays emitted during electron-beam-solid interactions can be used for elemental identification. One commonly used technique is energy-dispersive spectrometry (EDS, in this thesis "EDS" will also be applied to the spectra produced using this technique.). Besides, in

contrast to transmission electron microscopy, specimens of largely varying sizes can be examined without elaborate specimen preparation.

3.4.3.3 Sample Preparation

For analysis of the surfaces of fibres and shot particles, the samples were carbon coated to prevent electron charging.

To explore the microstructural development inside shot particles, the particles were separated from fibres and embedded in Spurr resins to make a specimen block. The specimen block was carefully polished with its cross section finished to 1 μm diamond. Carbon was coated on the polished surface.

3.4.4 Differential Scanning Calorimetry

Differential scanning calorimetry (DSC) is a well-established primary thermal analysis technique, which fundamentally combines heating/cooling curves with calorimetry. A DSC profile is a record of the thermal events which occur when a material is heated or cooled over a defined temperature range. Therefore, it can be used to determine the temperature and enthalpy corresponding to a phase change and hence crystalline transitions etc.

To distinguish the α and β-cristobalite in the devitrified alkaline-earth silicate fibres, DSC measurements were performed using a computer controlled and monitored Mettler type TA3000 DSC30 system. Approximately 20mg of powdered fibre sample

was compacted and sealed in the standard aluminium crucible and heating scans were undertaken from 25°C to 400°C at a rate of 10°C per minute.

4.1 Introduction

The present chapter is structured as follows: In section 4.2 the as-manufactured Superwool, A2 and B3 fibres are characterised; section 4.3 presents experimental results concerning the devitrification products for Superwool fibre; section 4.4 summarises the results for the devitrification behaviours of A2 and B3 fibre; section 4.5 is devoted to results for microstructure evolution as a function of temperature and time in the devitrifying Superwool fibre, and the features of microstructure development in A2 and B3 fibres are presented in section 4.6.

4.2 As-Manufactured Fibre

The as-manufactured Superwool was in the form of a blanket which showed a slightly bluish colour. The fibres looked like cotton-wool and they were entangled without any obvious ordered arrangement. Figure 4-1 is the X-ray powder diffraction pattern of crushed fibre blanket and it is shown that the as-manufactured Superwool fibre is amorphous in nature. The secondary electron (SE) image shown in figure 4-2 indicated that the as-manufactured Superwool fibre blanket consisted of fibres, shot (unfiberised particle) and flakes.

The fibres had a range of diameters as shown in figure 4-3, and they had smooth surfaces. The EDS spectrum in figure 4-4 showed the fibre matrix was composed of

Si, O, Mg and Ca. Semi-quantitative analyses suggested that the composition by mass was 5.8% MgO, 25.9% CaO and 68.3% SiO_2.

Shot particles were separated from the fibres. As shown in figure 4-5 these shot particles had a distribution of diameters from tens of microns to larger than 1 millimeter. Figure 4-6 shows the surface of a shot particle. The degree of opalescence of shot particles increased with the increase in particle size and they changed with increase in size from nearly transparent bluish to cream colour.

XRD studies proved they were amorphous while TEM micrograph revealed the inhomogeneity inside the particles. As shown by figure 4-7a to e, the microstructure in shot particles was characteristic of the bright spherical regions of inhomogeneity (the separated phase) embedded in surrounding dark matrix (the matrix). The density and dimension of the separated phase varied with the sizes of the shot particles. The separated phase with lower density and bigger diameter was found in the big-sized shot particles. The dimension of the separated phase ranged from 20nm to 150nm.

The diffuse electron diffraction patterns from both the separated phase and the matrix gave decisive evidence of liquid-liquid phase separation. As shown by figure 4-8, which was the diffraction pattern from the separated phase, neither spots nor distinct rings, which are characteristic of crystalline material were found.

Figure 4-9a and 4-9b show typical EDS spectra from the separated phase and the matrix respectively. From these results, it was concluded that the brighter circular

separated phase represented droplets of silica phase while the surrounding matrix was rich in alkaline-earth ions. Figure 4-10 shows X-ray mapping of the element O, Si, Ca and Mg in fragments of a shot particle, and further indicate that the separated phase was the silica rich component and the matrix the alkaline earth ions rich.

Due to the various diameters, the fibres exhibited different initial microstructure. When their diameters were less than 10μm, as shown by the TEM micrograph (figure 11), they had a homogeneous structure while fibres with larger diameters (≥ 10 μm), had similar microstructures to the shot particles.

X-ray powder diffraction studies of as-manufactured A2 and B3 fibres also indicated that they were amorphous. Figure 4-12 is a representive TEM micrograph of the cross section of an A2 fibre and figure 4-13 of a B3 fibre. Both of them showed uniform amorphous structure.

4.3 Devitrification of Superwool Fibres

4.3.1 Identification of Devitrification Products

The devitrification products observed in the fibres were identified using XRD and the methods described in section 3.4.1.

Figure 4-14 shows X-ray diffraction patterns for Superwool fibre following thermal exposure at 1100°C for exposure times extending from 10 minutes to 3024 hours. The d-spacings and relative intensities of quartz formed in Superwool matched the standard data (JCPDS card no. 33-1161) for the low temperature form, denoted as α-quartz. The letter "Q" will be assigned to α-quartz. Analysis of the X-ray diffraction peaks assigned to cristobalite indicated a small increase from tabulated standard d-spacing (JCPDS) values for the low temperature form, or α-cristobalite phase. Figure 4-15 compares the diffraction pattern of the cristobalite formed in the exposed fibre with that of the synthesized α-cristobalite standard. It was noted that the cristobalite peaks were broader and they were accompanied by a small broad peak identified as tridymite (004) at 21.765° 2θ. The relative intensities of the peaks were a good match to the standard data of α-cristobalite (JCPDS card no. 39-1425) even though there was a small deviation in the d-spacings. It is further noted that α-cristobalite is distinguished from β-cristobalite by the peaks (111) and (102) at 2θ angle 28.44° and 31.465° which are not observed in the β form. Figure 4-16 is the DSC traces of devitrified fibre and synthesized α-cristobalite standard. The cristobalite standard gives an exothermic peak at 258°C and the devitrified fibre at 251°C. The exothermic peak is characteristic of the low-temperature form of cristobalite which transforms to the high-temperature form[63]. The difference in the transformation temperature is due to the disorder or stacking faults in the cristobalite structure. Therefore, the cristobalite phase was identified as α-cristobalite or the low temperature form and is denoted by "C" in graphs and photos in the following sections.

The d-spacing and relative intensity data of diopside formed in Superwool exhibited a good match with the standard data for diopside given by the JCPDS card 11-654. Diopside will be denoted as "D" in the graphs or photos. For wollastonite, as indicated in figure 4-14 two different forms were found to exist under different exposure conditions. The form with the smaller d-spacing was identified as wollastonite 1 (W1), and the other as wollastonite 2 (W2). It was noted that the measured d-spacings of wollastonite 1 and wollastonite 2 remained constant following initial crystallisation. Figure 4-17 was the diffraction pattern after 5 hours' exposure at 1100°C and this showed the typical diffraction pattern for wollastonite associated with wollastonite 1. Figure 4-18 showed the diffraction pattern for Superwool fibre exposed for 3024 hours at 1100°C and thus showed the typical diffraction pattern identified as wollastonite 2 together with the peaks for diopside and α-cristobalite.

The best match with standard data for wollastonite 1 and wollastonite 2 was found from JCPDS card no. 27-88. While the diffraction patterns for both wollastonites were very similar to the standard data, the diffraction peaks in both cases shifted to higher Bragg angles, i.e. lower d-spacings and the relative intensities, I/I_0, showed small changes. Assuming that both wollastonite 1 and wollastonite 2 have the structure corresponding to JCPDS card 27-88, a set of unit cell parameters were determined for each wollastonite using the following method.

Equation 4-1 expresses the relationship between the d-spacing and cell parameters for crystals with monoclinic structure:

$$\frac{1}{d^2} = \frac{1}{a^2} \cdot \frac{h^2}{\sin^2 \beta} + \frac{1}{b^2} \cdot k^2 + \frac{1}{c^2} \cdot \frac{l^2}{\sin^2 \beta} - 2hk \cdot \frac{\cos \beta}{ac \sin^2 \beta} \qquad (4\text{-}1)$$

The d-spacings, for wollastonite 1 were measured from the X-ray diffraction data shown in figure 4-17 d_{400}=3.7771, d_{002}=3.453, d_{320}=2.9304 and d_{202}=3.0341, and for wollastonite 2 from figure 4-18 d_{400}=3.8179, d_{002}=3.5004, d_{320}=2.9661 and d_{202}=3.0765. Using these data and the equation 4-1 cell parameters for wollastonite 1 and 2 were obtained and are presented in table 4-1.

Using these results and equation 4-1, d-spacing values for wollastonite 1 and wollastonite 2 were calculated. Table 4-2 presents the calculated d-spacing values for wollastonite 1 and wollastonite 2 together with d-spacing data and relative intensity data for wollastonite-2M from JCPDS card 27-88. For wollastonite 1 and wollastonite 2 relative intensity profiles were similar to those for wollastonite-2M, however, both of them showed variations.

4.3.2 Devitrification Behaviour At Different Temperatures

4.3.2.1 1100°C

The X-ray diffraction patterns of figure 4-14 illustrated the development of wollastonite 1, wollastonite 2, diopside, quartz and cristobalite phases as a function of time for Superwool fibre devitrifying at 1100°C. Wollastonite 1 was the initial crystalline phase and its peaks were resolved at the exposure time of 10 minutes. At this stage its peaks were broad but they narrowed and increased in intensity with

increasing exposure time very quickly. It was noticed that a small peak existed between 2θ values of 31.5 and 32°. This peak was also observable in the 5h XRD pattern but disappeared at 20h and at longer exposure times. The peaks of wollastonite 1 in the 5h XRD pattern were sharper than those in the 10 minutes' XRD pattern. The 20h XRD pattern showed the formation of both quartz and cristobalite. At the same time, trace amounts of wollastonite 2 and diopside developed. The onset of wollastonite 2 can be seen in the small humps on the left side of the (002) and (320) peaks of wollastonite 1 and the formation of diopside can be seen by reference to the $(\bar{3}11)$ peak. At this stage, 5 different crystalline phases, wollastonite 1, wollastonite 2, diopside, α-quartz and α-cristobalite, coexisted. After 48 hours, as shown by the 48h XRD pattern, peaks associated with α-quartz started decreasing in intensity while those for cristobalite continued to increase. After a duration of 96 hours, the (101) and (111) peaks of quartz became very weak while cristobalite related peaks became stronger. After 168 hours, peaks corresponding to quartz vanished.

Semi-quantitative results for the development with time of the silica phases in Superwool devitrified at 1100°C are illustrated further in figure 4-19. The integrated intensities of the (101) peak of α-quartz and the (101) peak of α-cristobalite were used for analysis. Even though the (101) peak of α-cristobalite overlapped the tridymite peak (004) and may have introduced some experimental error in calculating the integrated intensity of α-cristobalite. Quartz was observed after 7 hours and increased in relative concentration with time to a maximum intensity 30 hours

exposure. It then started decreasing in intensity until it could no longer be detected after 180 hours. Cristobalite formed after 10 hours' exposure and its peak intensity increased with increasing exposure time up to 180 hours. Afterwards its intensity remained relatively constant with further increases in exposure time.

Figure 4-20, again based on semi-quantitative results, shows the development of wollastonite 1, wollastonite 2 and diopside in devitrifying Superwool fibre as a function of time at 1100°C. The (002) peak of wollastonite and the ($\bar{2}$20) peak of diopside were used for analysis. The intensity of the wollastonite 1 peak increased with exposure time, reaching a maximum after a duration of about 10 hour. Afterwards, the relative intensity of wollastonite 1 started decreasing with further increase in exposure time. Simultaneously with this decrease, wollastonite 2 and diopside started forming and their intensities increased with increasing exposure time. This continued until wollastonite 1 was no longer observed after an exposure time of 1680 hours. It is clearly shown by figure 4-20 that wollastonite 2 and diopside develop while there is a corresponded decrease in the wollastonite 1. It was also noted that the rates of increase in intensities for wollastonite 2 and diopside decreased corresponding to the decrease in the peak intensity of wollastonite 1.

Therefore, wollastonite 2, diopside and cristobalite were the final devitrification products obtained at 1100°C.

4.3.2.2 1250°C

Figure 4-21 shows the x-ray powder diffraction patterns of Superwool fibre after exposure at 1250°C. Cristobalite was the initial crystalline silica phase formed. The diffraction peak for cristobalite was accompanied by a small tridymite peak (004) at 21.765° as observed in the diffraction patterns for the Superwool fibre exposed at 1100°C. After extended exposure, more prominent growth of the tridymite peak (004) was observed.

Wollastonite 1, wollastonite 2 and diopside were all identified for the shorter exposure times with the wollastonite 1 peaks more prominent than wollastonite 2 peaks. As with the situation at 1100°C, wollastonite 1 decomposed to wollastonite 2 and diopside, with increasing exposure time and after 4 hours no wollastonite 1 was left while wollastonite 2 and diopside developed mature peaks.

4.3.2.3 1200°C

Figure 4-22 is the X-ray powder diffraction patterns of Superwool fibre after exposure at 1200°C. The development of different crystalline phases at this temperature showed similar tendencies to that at 1100°C. The '5 minutes' XRD pattern showed the formation of wollastonite 1 and trace amounts of quartz. The formation of cristobalite was observed after 10 minutes' exposure, and a subsequent increase in exposure time yielded more quartz and cristobalite.

Figure 4-23 shows the development and transformation of quartz and cristobalite at 1200°C. After half an hour the relative intensity of the quartz peak reached a maximum and a significant reduction in relative peak intensity of was identified subsequently. After 2 hours, no quartz was detectable. Cristobalite was identified after an exposure of 10 minutes and its intensity reached a maximum value after about 2 hours or so. This time is consistent with disappearance of the quartz peak. These results imply that cristobalite formed at the expense of quartz.

Figure 4-24 shows the development of wollastonite 1 and wollastonite 2 with exposure time at 1200°C. After 10 minutes exposure, wollastonite 1 had already reached its maximum intensity and further exposure led to a decrease in its peak intensity. At the same time the peak intensity of wollastonite 2 increased with time. After 24 hours, no wollastonite 1 remained, which suggested that the increase in wollastonite 2 is at expense of wollastonite 1.

4.3.2.4 1000°C

Figure 4-25 shows the X-ray powder diffraction patterns of Superwool after thermal exposure at 1000°C. As shown, quartz was the first crystalline silica phase to form. After 168 hours, trace amounts of quartz were detected by the appearance of the (101) diffraction peak and there was no sign of cristobalite at this stage. After 336 h, in addition to the increased intensity of quartz, small amounts of cristobalite were detected from the first appearance of the (101) peak. After 672 hours, both quartz and cristobalite showed increased intensity with time. The development of relative

peak intensities for quartz and cristobalite were plotted individually in figure 4-26 for the range of exposure times. Cristobalite increased in its peak intensity after its initial formation at 1000°C and an exposure time exceeding 168 hours. Quartz showed an initial increase then a subsequent decrease in its peak intensity ratio after an exposure time of 1500 hours at this temperature.

Wollastonite 1 was again the first alkaline earth silicate phase to form. Trace amounts of pseudowollastonite were detected after 1 hour exposure at 1000°C as identified by Pw. The pseudowollastonite peaks developed slowly with increasing exposure time and reached a maximum intensity after about 24 hours' exposure. Afterwards, the peak intensity started to decrease and after 168 hours it effectively disappeared. Wollastonite 2 and diopside were not detected until after 672 hours' exposure. At the same time, the intensities of the wollastonite 1 peaks started decreasing, and this trend continued with increasing exposure time. After 3192 hours wollastonite 1 still coexisted with wollastonite 2 and diopside. The 1000°C transformation rate from wollastonite 1 to wollastonite 2 and diopside was therefore much lower than those observed at 1100°C and 1250°C.

4.3.2.5 900°C

Figure 4-27 shows some typical X-ray powder diffraction patterns of Superwool fibre after exposure at 900°C. Wollastonite 1 was detected after 1 hour's exposure and remained the main crystalline phase up to the longest exposure time of 2688 hours. As indicated in the figure the same tiny peak of pseudowollastonite, positioning

between 31.5 and 32°, as observed under certain circumstances at 1000°C was also detected. Figure 4-28 shows the development of the relative peak intensities of (002), $(\bar{2}02)$ and (320) of wollastonite 1 with time. The diffraction intensities reached their maximum after about 5 hours' exposure and then remained fairly constant. Figure 4-29 shows the d-spacings of the (320), (002) and $(\bar{2}02)$ peaks of wollastonite with increasing time. The reference lines show the d-spacings for these peaks from JCPDS card no. 27-88. While the positions of the measured peaks, or the d-spacings of wollastonite 1, kept fairly constant with increasing exposure time, they did show a significant deviation from the standard JCPDS data.

4.3.2.6 Temperatures below 900°C

Figure 4-30 shows the development of the crystalline products from the amorphous matrix after a range of exposure times at 850°C. After 1 hour, the fibre maintained an amorphous state. After 2 hours, several crystalline peaks emerged. These peaks were assigned to wollastonite 2 and diopside. After 5 hours, peaks related to wollastonite and diopside, such as W1 and W2 (002), W2(202), W1 and W2(320), D$(\bar{3}11)$ were resolved. When the exposure time increased to 7 hours, W1(400) was resolved and the (002) and (320) peaks of wollastonite 1 increased significantly in intensity. It was noted that, besides the peaks belonging to wollastonite 1, wollastonite 2 and diopside, several unidentified peaks, marked as U1, U2, U3 and U4 on the 15h XRD pattern, had formed. These peaks were first detected after 5 hours exposure, increased in intensity with increasing exposure time and decreased.

After 120 hours all these peaks disappeared. After 10 hours, the peaks assigned to wollastonite 2 were relatively intense and sharp. The intensity of the diopside related peaks increased up to 20 hours and then started decreasing as shown by the D(-220) and D(-311) peaks. As to the development of wollastonite 1, its peaks were detected after 2 hours' exposure and the peak intensities increased with increasing exposure time. With increasing exposure time from 5 hours to 20 hours, the intensity of the (202) peak of wollastonite 2 decreased and that of wollastonite 1 increased. It appeared that there was a transformation between these two peaks. The intensities of peaks associated with wollastonite 2 and diopside increased up to 20 hours then showed a tendency to decrease while the peaks related to wollastonite 1 continued to increase in intensity with increasing exposure time. Another feature was that the (002), (202) and (320) peaks wollastonite 1 and wollastonite 2 peaks emerged before the (400) peak.

For an exposure temperature of 800°C, superwool fibre gave amorphous diffraction pattern until an exposure time of at least 96h had been exceeded (figure 4-31). After 96 hours, the main peaks associated with wollastonite 1, wollastonite 2 and diopside were resolved. In addition, there existed unidentified peaks, as observed in the XRD patterns for 850°C which disappeared after 672 hours' exposure. With increasing exposure time, it was noted that the peak intensity of wollastonite 1 increased while the peak intensities of wollastonite 2 and diopside decreased.

At 750°C, superwool remained amorphous to beyond 840 hours' exposure. After 1680 hours' exposure, as shown in figure 4-32, the main peaks associated with

wollastonite 1, wollastonite 2 and diopside were resolved. In addition, unidentified peaks were again resolved and the peaks were showing improved development at 2016 hours.

Figure 4-33 shows the XRD diffraction patterns of Superwool fibre after exposure for 1680 hours at 750°C, 800°C and 850°C respectively. While the peaks in the diffraction pattern after 1680 hours exposure at 750°C were broad and immature, the peaks related to wollastonite 1, wollastonite 2 and diopside could be easily identified. For exposure at 800°C or 850°C, the unidentified peaks (u) disappeared after 20 hours or 672 hours' exposure respectively while in the case of 750°C these peaks remained even after 1680 hours' exposure. It was noticed that there was a tendency for the peak intensity ratio or peak height ratio, of the wollastonite 1 to wollastonite 2 peaks to increase dramatically with increasing temperature. When looking at diopside peaks, their relative intensities decreased with increasing temperature. The results suggest that a transformation from wollastonite 2 and diopside to wollastonite 1 took place and the transformation rate increased with increase in exposure temperature.

4.3.3 Temperature and Time Dependence of Devitrification Products

The qualitative analysis of X-ray powder diffractometry data for thermally exposed Superwool indicated the presence of wollastonite, diopside, quartz, cristobalite and tridymite products. Results for the production of these various products under

various thermal exposure conditions are summarised in figure 4-34. A logarithmic scale for exposure time is employed to represent the large range in the times involved.

The schematic plots in figure 4-34 illustrate the exposure temperatures and times related to 8 different regions where different phase combinations formed. In the region denoted by '♦', the XRD patterns for the exposed fibres are characterised by a broad, amorphous hump. In the region denoted by 'O', peaks for wollastonite 1, wollastonite 2 and diopside plus some unidentified peaks and the amorphous hump were identified. The unidentified peaks emerged and disappeared with increasing exposure temperature and time. In the region denoted by '▲', the XRD patterns showed wollastonite 1 peaks on an amorphous hump. Although wollastonite 1 was the main crystalline phase, as confirmed by TEM and XRD, a small amount of psedowollastonite was detected under certain exposure conditions. Increase in exposure temperature and time to the region denoted by '◊', resulted in the formation of cristobalite and quartz in addition to wollastonite 1 and amorphous glass. As noted in section 4.3.2, at the early stage quartz was the only crystalline silica phase identified, however, cristobalite formed immediately afterwards. There should therefore possibly be a very narrow further band where quartz was the only crystalline silica phase present and where the range of products was quartz, wollastonite 1 and residual glass. It is worthy of note that the α-cristobalite peak is always accompanied by a small broad peak of tridymite, which is identified as a distinct phase only after significant growth. In the '●' region, wollastonite 1, wollastonite 2, diopside, cristobalite and quartz were observed. In the '□' region, crystalline phases of

wollastonite 1, wollastonite 2, diopside and cristobalite were resolved. In the '□' region, no wollastonite 1 was detected and the crystalline phases identified were wollastonite 2, diopside and cristobalite. In the 'Δ' region, in addition to wollastonite 2, diopside and cristobalite being observed, significant growth of tridymite related peaks took place.

4.4 Devitrification Characteristics of A2 and B3 Fibres

4.4.1 Devitrification of A2 Fibres

Figure 4-35 shows the X-ray diffraction patterns for A2 fibres after thermal exposure at 750°C for 24, 48, 168 and 1008 hours respectively. After 24 hours' exposure, the diffraction pattern of the fibres shows a typical amorphous hump. After 48 hours, several small peaks emerged from the amorphous background at around 2θ 30°. These peaks are identified as main peaks of diopside. This crystalline phase continued to develop with increasing exposure time. Diffraction patterns of fibres after 168 and 1008 hours' exposures show more developed diopside patterns. Crystallisation resulted in the formation of diopside as the primary crystalline phase.

Figure 4-36 shows X-ray diffraction patterns for A2 fibres after exposed at 800°C for 1, 5, 24, 168 and 672 hours. At 1 hour's exposure, the fibre remained amorphous. At 5 hours, main peaks of diopside were initially resolved at about 2θ 30°. At 24 hours, the resultant diffraction pattern showed developed diopside peaks. At 168 hours,

while diopside continued to develop, two small peaks near 2θ 23 and 25° appeared in the diffraction pattern. There were identified as wollastonite peaks. At 672 hours, diopside and wollastonite are the two crystalline phases observed.

Figure 4-37 shows X-ray diffraction patterns of A2 fibres devitrified at 900°C for 48, 336 and 1344 hours. At 900°C, at 48 hours, the diffraction pattern is similar to that for the fibres exposed at 800°C for 672 hours. At this stage diopside is the main crystalline phase and this is accompanied by a trace amount of wollastonite. At 1344 hours' exposure, as shown in the figure, no obvious change was detected in the X-ray diffraction pattern of the fibres.

Figure 4-38 shows X-ray diffraction patterns of A2 fibres after devitrification at 1000°C at 48, 168, 336, 672 and 1344 hours. The diffraction patterns show that after 48 hours and at 168 hours' exposure, diopside and wollastonite were the only two crystalline phases identified. At 336 hours, the main diffraction peaks of cristobalite at 2θ=21.98° and of quartz at 2θ=20.85° and 26.65° appeared. The intensities of both quartz and cristobalite increased with increasing exposure time as shown in the figure. The intensities of the two diffraction peaks for wollastonite decreased in intensity with increasing thermal exposure time.

Figure 4-39 shows the X-ray diffraction patterns of A2 fibres after thermal exposure at 1100°C for 48, 96, 168, 336, 672 and 1344 hours. At this temperature, diopside was observed throughout the range of exposure times. Wollastonite peaks were

detected up to 168 hours' exposure. Cristobalite peaks developed with increasing exposure time from 48 to 168 hours while quartz peaks decreased in intensity with increasing time. At 168 hours' exposure, the main cristobalite peak is accompanied by the typical tridymite hump on its left hand side and no quartz was detected.

At 1250°C, as shown by figure 4-40, cristobalite existed in addition to diopside throughout the range of exposure times from 48 hours to 1344 hours. Initially, the main cristobalite peak was accompanied by the small, broad tridymite peak on its left hand side and the intensity of this peak grew with increasing exposure time.

Figure 4-41 shows diffraction patterns of A2 fibres after thermal exposure at different temperatures for 48 hours. At 750°C only the main peaks for diopside appeared above the amorphous hump. Exposure at 800° resulted in much stronger diopside peaks. At 900°C and 1000°C diopside and a small amount of wollastonite were formed. At 1100°C diopside, wollastonite, quartz and cristobalite were observed and exposure at 1250°C resulted in the formation of diopside, cristobalite and a small amount of tridymite.

The diffraction patterns for diopside formed in A2 fibre throughout the range of exposure temperatures and times investigated were a very good match with the data in the JCPDS card 11-654. Identification of the particular polymorph of wollastonite was difficult due to the low intensities of the two characteristic peaks. However, wollastonite 2M, the orthorhombic form, provided the most satisfactory match for all

of the exposure conditions. Cristobalite was identified as α-cristobalite due to its characteristic peaks at 2θ=28.44° and 31.465°. The quartz was also determined in its low temperature form by its diffraction peaks at 20.85° and 26.65°. Figure 4-42 summarises the devitrification products identified by XRD as a function of exposure temperature and time. From this figure , it is apparent that the primary devitrification product was diopside. This crystalline phase was found to be present throughout the full range of temperatures and exposure times with the exception of the glass-only region. Wollastonite was the second crystalline phase to form, being first resolved at an exposure of 96 hours at 800°C. Subsequent increases in exposure temperature and exposure time resulted in the decompositioning of this wollastonite phase. Crystalline silica products were not observed until the fibres had been exposed to a temperature of 1000°C. At this temperature and a duration of 336 hours, two crystalline forms of silica, quartz and cristobalite formed. An increase in temperature to 1100°C yielded both of these crystalline silica polymorphs after the short exposure duration of 48 hours. Once formed cristobalite continued to develop with increasing temperature and time. The quartz, after initial formation increased in diffraction intensity with increasing time and then gradually disappeared. Diopside and cristobalite were the only crystalline phases identified after exposure at 1250°C for a short duration. Diopside, cristobalite and tridymite then existed up to the limits of exposure duration and temperature.

4.4.2 Devitrification of B3 Fibre

Figure 4-43 shows the X-ray diffraction patterns for B3 fibres exposed for 672 hours at different temperatures. Diopside, pseudowollastonite, two forms of wollastonite, quartz, cristobalite and tridymite are identified in these devitrified B3 fibres. At 800°C, diopside, pseudowollastonite and wollastonite were detected. The d-spacings and relative intensities of pseudowollastonite formed in B3 fibre were a good match to the standard data for pseudowollastonite given by JCPDS card no.31-300. Each wollastonite peak has a small shoulder on its right side. They are identified as the diffraction peaks of another form of wollastonite, wollastonite 'a'. The wollastonite with larger d-spacings, or smaller 2θ, will be called wollastonite 'b' and denoted as Wb in the figures. Wollastonite 'b' has the same d-spacings and relative intensities as wollastonite 2 which was identified in devitrified superwool fibre. Wollastonite 'a', denoted as Wa, has d-spacings smaller than those of wollstonite 'b' but larger that those of wollastonite 1 formed in devitrified Superwool fibre. Increasing the exposure temperature to 900°C, wollastonite 'a' increased in its diffraction peak intensities while wollastonite 'b' decreased. Their corresponding peaks overlap with each other and form broad combination peaks. No distinguishing diopside peaks were found. These results suggest that wollastonite 'b' and diopside transformed to wollastonite 'a' when increasing exposure temperature from 800 to 900°C. At 1000°C, the crystalline phases were pseudowollastonite, wollastonite 'b' accompanied by small wollastonite 'a' peaks, diopside, cristobalite and quartz. Wollastonite 'a' had been transforming to wollastonite 'b' and diopside. With further increases in temperature to 1100°C, X-ray diffraction patterns of the exposed fibre showed sharp wollastonite

'b' peaks together with diopside and cristobalite peaks. No wollastonite 'a' was detected. Pseudowollastonite decreased in its diffraction intensities with increasing exposure temperature and at 1100°C only trace amounts of pseudowollastonite can be detected from the diffraction pattern. At 1250°C, in addition to sharp wollastonite 'b' and diopside peaks, dramatic growth of tridymite related peaks was observed. No pseudowollastonite was observed.

Figure 4-44 shows X-ray diffraction patterns for B3 fibre after thermal exposure at 800°C for 5, 15, 24, 48, 96, 168 and 336 hours. After 5 hours' exposure, B3 fibres remained amorphous. After 15 hours, primary crystalline phases of pseudowollastonite, diopside and wollastonite appeared. This wollastonite was identified as wollastonite 'b'. At the same time, some unidentified peaks (X_1, X_2 etc) emerged. The intensity of diopside peaks increased with time up to 48 hours and then started decreasing. Pseudowollastonite continued to develop after it crystallised out. For wollastonite, the (400) and ($\bar{2}$02) peaks at around $2\theta = 23°$ and 27° started developing after 48 hours, while the (002), (202) and (320) peaks at around 25.5°, 29° and 30° developed as soon as the fibre started devitrifying. Unknown peaks X_1-X_5, developed with increasing time up to 48 hours and then decreased in intensity. They disappeared after 336 hours' exposure. It appeared that the development of the (400) and ($\bar{2}$02) peaks of wollastonite 'b' was related to the decrease of these unidentified phases. At the same time, small shoulders turned up on the right hand side of wollastonite 'b' peaks in the diffraction pattern, implying the formation of wollastonite 'a'. Wollastonite 'b' decreased in its intensity and diopside disappeared

as wollastonite 'a' appeared, suggesting that wollastonite a formed at the expense of wollastonite 'b' and diopside.

Figure 4-45 shows diffraction patterns for B3 fibres thermally exposed at 900°C after 2, 15, 24, 168, 336, 672, 1344 and 2688 hours. At this temperature and throughout the exposure times investigated no diopside peaks were detected. Both wollastonite 'a' and 'b' formed, their diffraction peaks overlapping with each other and formed short, broad wollastonite peaks. Pseudowollastonite peaks appeared after 2 hours and existed afterwards.

Figure 4-46 shows X-ray diffraction patterns for B3 fibres devitrified at 1000°C for 48, 96, 168, 336, 672 and 1848 hours respectively. With increasing exposure time from 48 to 1848 hours, the intensities of the pseudowollastonite peaks decreased. As to wollastonite, both wollastonite 'a' and 'b' appeared. XRD patterns showed that at 168 hours wollastonite 'b' and diopside increased in their intensities while wollastonite 'a' decreased with increasing time. This suggested that wollastonite 'a' started decomposing to wollastonite 'b' and diopside as wollastonite 1 transformed to wollastonite 2 and diopside in devitrifying Superwool fibres. After 1848 hours, wollastonite 'b' showed stronger sharp peaks and accompanied by tiny wollastonite 'a' peaks. As to the silica phase, after 96 hours traces of quartz and cristobalite were identified in the diffraction pattern. The intensity of cristobalite peaks increased with increasing exposure time up to 1848 hours. The quartz peaks increased in intensity with time up to 672 hours and then decreased at 1848 hours' exposure.

Figure 4-47 shows X-ray diffraction patterns of fibres exposed at 1100°C for 48, 96, 336 and 672 hours. At 48 hours' exposure, cristobalite, wollastonite 'b', diopside and a small amount of pseudowollastonite were detected from the diffraction patterns. As shown in this figure, with increasing exposure time up to 672 hours, no obvious change in the diffraction pattern was observed.

Figure 4-48 shows X-ray diffraction patterns of fibres exposed at 1250°C for 48, 96, 168, 336, 672 and 1008 hours. At 48 hours, wollastonite 'b', cristobalite, tridymite and diopside were identified in the diffraction pattern. At this stage the characteristic peak of tridymite was small and broad. The tridymite peaks were particularly strong at exposure temperatures of 672 and 1008 hours. At the same time, the intensities of the cristobalite peaks decreased. The (004) peak of tridymite overlapping with the main peak of cristobalite (101), gave a broad, combined peak at about 22° after extended exposures.

Figure 4-49 summaries the devitrification products observed for B3 fibre as a function of exposure temperature and time. Pseudowollastonite, diopside and wollastonite 'b' were primary crystalline forms. Their main peaks were resolved after 15 hours' exposures ('▲' region). The development of wollastonite phases was associated with some unidentified peaks. Increasing the exposure temperature and time to the 'O' region, resulted in wollastonite 'a' being formed with wollastonite b and pseudowollastonite. At the same time diopside disappeared. A further increasement of temperature and time '◆' region) resulted in the formation of quartz and cristobalite. In the '□' region, wollastonite 'a' gradually transformed to wollastonite

'b' and diopside, and quartz transformed to cristobalite after formation. After being exposed at 1100°C only very small peaks of pseudowollastonite were left, and no wollastonite a was detected. After exposure at 1250°C no pseudowollastonite was detected. Intially wollastonite 'b', diopside and cristobalite were formed. Further exposure at this temperature resulted in the formation of tridymite.

4.5 Microstructure Development in the Devitrifying Superwool

4.5.1 Phase Separation

The series of TEM micrographs shown by figure 4-50a to e illustrate the effects of increasing thermal exposure time on the development of the microstructure of Superwool fibre at 750°C. After 4 hours'exposure, worm-like phase regions with structure of about 15 nm in size developed (figure 4-50a). After 24 hours, this type of structure remained with the typical size of the brighter separated phase increasing to about 25 nm (figure 4-50b). For the purposes of this thesis, the brighter separated phase will be identified as "the separated phase" and the remainer phase "the matrix". After 168 hours' exposure, the separated phase showed a developed microstructure in the form of closed worm-like regions and some spheres (figure 4-50c). These spheres, around 40 nm in diameter, are possibly the ends of worm-like inclusions. After 336 hours' exposure, apart from the increased dimensions of the separated phase, the structures of both the separated phase and the matrix showed high interconnectivity (figure 4-50d). The

average dimension of the elongated or branching regions of the separated phase size was typically about 60nm. Increasing the exposure time to 504 hours, resulted in the structure shown by figure 4-50e. The separated phase coarsened and remained highly interconnected with dimensions of typically 80 nm.

After thermal exposure, the circular silica particles observed in the as-received shot particles (figure 4-7) started combining with each other to form larger particles. Figure 4-51 shows the typical structure of a shot particle exposed at 750°C for 504 hours. The structure includes mainly 'kidney bean' like discrete silica particles distributed in an alkaline-earth silicates rich matrix.

The structural changes observed in Superwool fibre at 800°C with increasing thermal exposure time are illustrated by figures 4-52a to h. After 1 hour's exposure, a separated phase in the form of granule and interconnected worm was distributed in the darker matrix phase (figure 4-52a). Figure 4-52b shows, after 5 hours' exposure, that high density mainly discrete round and kidney-bean like particles of about 50 nm size formed. At this stage the separated phase appeared in the form of separated granules rather than being interconnected. With longer heat treatment the granules combine with one another to form a partially interconnected worm-like structure. Figure 4-52c shows, after 24 hours' exposure, that the fibre was characterised by this type of coarsening channelised structure. After 48 hours, the interconnected channel structure coarsened and remained highly interconnected (figure 4-52d). A skeleton-like structure was also observed in a cross section of fibre after exposure for 48 hours (figure 4-52e). EDS analysis showed that this phase was silica (figure 4-52f) and it is

believed that these silica fractions formed during the ultramicrotomy sectioning process when the alkaline-earth silicates phase fell apart. This implies that a clear boundary exists between the two separate phases.

Figure 4-52g shows an extensive cross section of fibre after 96 hours' exposure. The structure suggests that phase separation took place homogeneously throughout the fibre from its surface to its centre. Figure 4-52h shows this microstructure at a higher magnification. The micrographs indicated that at this stage the channel structure of the separated phase started to dissociate into discrete spherical particles. It showed a distinct interface between the two separated phases. At this stage, the separated phase existed in a mixed form of channellised and isolated particles with dimensions ranged from 120nm to 160nm. The change from a channel structure to discrete particles was gradual and it was difficult to distinguish a time period when the worm-like dispersed phase existed from another when only isolated particles were seen. Figure 4-53a and figure 4-53b are typical EDS spectra respectively for the separated phase and the matrix. They indicate that the brighter separated phase is silica (figure 5-53a) and the glass matrix is the alkaline-earth silicate rich phase (figure 4-53b).

For the shot particles, figure 4-54 shows that after 48 hours' exposure at 800°C the coarser 'kidney bean' like silica particles formed from the spherical silica particles observed in the unexposed shot particles.

As indicated by the results of X-ray powder diffractometry, Selected Area Electron Diffraction (SAED) studies with the TEM confirmed that the exposed samples

investigated in this section were still amorphous in nature. Figures 4-55 shows SAED pattern corresponding to the darker areas in figure 4-52h. The pattern shows diffuse rings which are typical of amorphous materials.

4.5.2 Devitrification Products

Figure 4-56 shows that after 168 hours' at 800°C the alkaline-earth silicates started to crystallise from the alkaline-earth rich regions. Figure 4-57 is the SAED pattern taken from the crystallised regions in figure 4-56. At this stage silica remained amorphous.

Figure 4-58a shows the microstructure of a Superwool fibre thermally exposed at 900°C for 168 hours. Figure 4-58b is an image at higher magnification. They suggest the fibre has a "uniform" phase structure from its surface to its centre. The microstructure consists of two different types of region, one brighter "structureless" region and the other darker needle-like region. With reference to the XRD results for these exposure conditions (section 4.3.1) the crystalline phase formed in this fibre identified as wollastonite 1. Figures 4-59a and b are typical EDS spectra corresponding respectively to the wollastonite 1 and amorphous silica phases. Semi-quantitative analysis showed that the composition of wollastonite 1 is SiO_2:58.05%, CaO: 34.97% and MgO: 6.97% (wt) and confirmed that the wollastonite 1 is a Mg-containing wollastonite solid solution.

SAED patterns of wollastonite 1 were taken in different directions by rotating the specimen. The d-spacings of the planes producing the diffraction spots were

calculated using equation 3-2 and the angles between the planes were determined by measuring the angle between corresponding diffraction vectors. Using equation 4-1, the cell parameters of wollastonite 1 were obtained as a=15.206Å, b=7.170Å, c=6.891Å and β=95.46° as displayed in table 4-1. Figure 4-60 shows a typical SAED patterns. This pattern is indexed as (200)x(001) along which the electron beam travelling in the [0$\bar{2}$0] direction in the crystal (see section 3.4.2.2 for method of analysis). Figure 4-61 is a TEM micrograph of a fibre cross section for a fibre exposed for 1344 hours' at 900°C. This shows mature devitrified wollastonite 1. Figure 4-62 is the corresponding SAED pattern. Analysis of this diffraction pattern showed that the wollastonite 1 had the same cell structure as that formed in the fibre after 168 hours' exposure at this temperature, which confirmed the XRD finding that once wollastonite 1 formed the structure of did not change with increasing exposure time. Figure 4-63 shows a fraction of a broken cross section of fibre after exposure for 1344 hours' and shows fragments of wollastonite 1 crystals attached to the silica particles.

Figure 4-64 is a microstructure of the fibre thermally exposed at 1000°C for 168 hours. It shows a similar structure to that observed in the fibres after exposed at 900°C. Analysis of the SAED patterns and EDS spectra indicated the primary crystalline phase was wollastonite 1 as observed in the fibres exposed at 900°C. Figure 4-65 shows the associated (200)x(001) electron diffraction pattern and figure 4-66 shows a fibre several silica particles near the fibre edge. It is believed that the wollastonite 1 component had fallen apart during the process of preparing the TEM

specimens. The lower left hand corner of the micrograph shows that there are a bit wollastonite 1 was still attached to the silica balls.

Figure 4-67a and b are respectively the TEM bright field and dark field images of a crystalline particle observed in the Superwool fibre after thermal exposure at 1250°C for 168 hours. The EDS spectrum (figure 4-68) showed this particle was silica. Further electron diffraction studies showed it was α-cristobalite which is consistent with the XRD and DSC results. Figure 4-69 shows its (001)x(100) diffraction pattern.

The crystalline particles in the cross section of figure 4-70 were also confirmed as α-cristobalite by SAED and EDS analyses and the formation of wollastonite 2 in the same fibre was confirmed by TEM.

The wollastonite 2 particles are identified by 'W' in figure 4-71. Figure 4-72 is the EDS spectrum from the particles marked as W in this figure and semi-quantitative analyses showed their composition to be: SiO_2=53.51%, CaO=45.45% and MgO=2.04% (mol). Figure 4-73 is the related electron diffraction pattern. Analyses of SAED patterns gave the cell parameters of a=15.337Å, b=7.210Å, c=7.022Å and β=95.31°. The particles marked as 'C' in figure 4-71 were identified as α-cristobalite.

Large diopside crystallites were also observed in the Superwool fibre after thermal exposure at 1250°C for 168 hours. Figure 4-74 shows a diopside particle and figure

4-75 is its corresponding EDS spectrum. Figure 4-76 is its electron diffraction pattern identified as (110)x($\bar{1}$10).

For Superwool fibres thermally exposed at 1250°C for 1344 hours, in addition to the α-cristobalite, wollastonite 2 and diopside, tridymite crystallites were identified among the cristobalite particles. Figure 4-77a and b show respectively the bright field image and correspoding dark field image for a cross section of Superwool fibre thermally exposed at 1250°C for 1344 hours. The brighter particle in the dark field image was identified as tridymite and figure 4-78 is its corresponding (200)x(020) electron diffraction pattern.

4.5.3 Development of Fibre Surface Structure

The development of the surface structure of fibres after thermal exposure was analysed using the high resolution XL40 SEM. When TEM analysis showed the structural changes taking place in the fibres the fibres exposed at 800°C and 900°C for the investigated exposure times (section 4.5.2), the SEM showed relatively smooth surfaces, due to its relative low spatial resolution. For example, figures 4-79 and 4-80 are the secondary electron (SE) images of fibres exposed at 800°C for 3864 hours and at 900°C for 2688 hours respectively and these show fibres with smooth surfaces. At 1000°C, after 672 hours' exposure, the surfaces of the fibres also remained smooth (figure 4-81). Further exposure resulted in the development of fibre surface structure. Figure 4-82 is an SE image of the fibres after 2352 hours' exposure

at this temperature which shows that a rougher surface had developed. Figure 4-83 is the SE image of the fibre after thermal exposure at 1100°C for 336 hours. This shows that surface structure had formed on a scale of .

Back-scattered electron (BSE) images in figures 4-84a to e show the rapid development of surface structure on Superwool fibres as the exposure time is increased from 0.5, 24, 168, 672, to 1344 hours at 1250°C. As soon as the thermal exposure commenced two distinct regions developed on the fibre surfaces (figure 4-84a). The brighter regions correspond to alkaline-earth silicates due to their higher average atomic number and the darker regions to silica. The sizes of the regions increased with increasing thermal treatment time (figure 4-84b). When the heat treatment time was increased to 168 hours, the fibre showed bright discrete alkaline-earth silicate particles embedded in dark silica phase (figure 4-84c). This type of structure developed further with increasing time (figure 4-84d). After 1344 hours, mature individual alkaline silicates particles with regular crystal shapes developed(figure 4-84e) and it appeared that they were connected by silica crystallites. The average size of the fibre (figure 4-84f) appeared to decrease with extended thermal exposure (fibre shrinkage).

4.5.4 Structure Development in the Shot Particles

Figures 4-85 to 87 show surface structures on shot particles following thermal treatment at different temperatures. Figure 4-85 is an SE image of the surface

structure after exposure at 1100°C for 336 hours. This shows that small lumps sized at about 1 μm had evolved. Figure 4-86 is a SE image of a shot particle exposed at 1200°C for 336 hours. Particles of about 4 μm in size were diaplayed. Figure 4-87a to c are BSE images which shows the rapid development of surface structure on the shot particles after exposure at 1250°C for 24, 672, and 1344 hours respectively. After 24 hours, particles of about 4 μm in size had developed (figure 4-87a); After 672 hours, the fibre surface structure was characterised by large bright crystalline particles distributed in dark silica "sea" (figure 4-87b); and after 1344 hours' exposure, bright crystalline particles with regular shapes developed. The size of these alkaline-earth silicate crystallites was typically 10 μm.

Figure 4-88 to 91 show BSE images of the microstructures of cross sections of shot particles which had undergone thermal exposure at different temperatures: figure 4-88 shows the structure in the shot particle after thermal exposure at 1000°C for 3192 hours; figure 4-89 shows the structure of the shot particle after thermal exposure at 1100°C for 3024 hours, and figure 4-90 shows the structure after thermal exposure at 1200°C for 672 hours. All three images, identify three distinct phases, white, grey and black, though this is not as obvious in figure 4-88 as in figure 4-89 and 4-90 due to the finer structure in figure 4-88. The grey phase was always combined with, or contained in, the white phase. The size of these phases increased rapidly from figure 4-88 to 90 and the connectivity of white phase decreased from figure 4-88 to 90. In figure 4-90 the white phase and grey phase together were more or less discrete particles distributed in black matrix.

Figures 4-91a to f show the development of structure within shot particles at 1250°C as a function of exposure time from 0.5, 1, 24, 168, 672 to 1344 hours. They also show the existence of three different phases, which exhibited different contrasts in the BSE images, respectively white, grey and black respectively. These particles coarsened rapidly with increasing exposure time. Figures 4-92a to c are EDS spectra corresponding to the three different phases in figure 4-91f. They indicated that the white phase is calcium silicate with a small amount of magnesium (figure 4-92a), the grey phase is magnesium calcium silicate (figure 4-92b) and the darkest one silica (figure 4-92c). Compared with XRD (section 4.3.1), these three phases were identified as wollastonite 2, diopside and cristobalite.

4.6 Microstructural Development of Fibre A2 and B3

4.6.1 Microstructural Features of Exposed A2 Fibres

Figure 4-93 is a TEM micrograph showing the cross section of A2 fibre after exposure at 750°C for 24 hours. The microstructure is characteristic of a high density of bright, discrete circular particles with a typical size of 25 nm distributed in a dark matrix. Increasing the thermal exposure to 48 hours resulted in an increase of size in the separated bright particles to about 45nm and a decrease in their density compared with those after 24h' exposure (figure 4-94).

Figure 4-95 shows the microstructure of A2 fibre after being exposed at 800°C for 48 hours. The structure is characterised by circular particles distributed in a lamellar-structured crystalline phase. Figure 4-96 shows the EDS spectrum of the circular particles, which suggests they are silica. Figure 4-97 is a SAED pattern corresponding to the crystalline phase in figure 4-95. The SAED pattern, together with EDS analysis, confirm the phase was diopside..

Figure 4-98 is a BSE image of an A2 shot particle after exposure at 1250°C for 1344 hours. It exhibits two coexisting phases, one white and the other black. Figure 4-99a and 4-99b are EDS spectra of these two phases in figure 4-98, suggesting that the white phase is diopside and the black one silica.

4.6.2 Microstructural Features of Exposed B3 Fibres

Figure 4-100 shows a TEM micrograph of the microstructure of B3 fibre after exposure at 750°C for 24 hours. The separated phase showed an internnected worm-like structure with a typical size of about 18 nm. Extended exposure resulted in the break up of this internnected structure and figure 4-101 shows that after 336 hours the separated phase developed as big spherical particles whose size ranged from 60 to 100 nm. At this stage SAED analyses showed both the separated phase and the matrix were still amorphous. EDS analyses showed the spherical particles were silica rich and the matrix were alkaline-earth silicate rich.

5.1. Experimental Aspects

The alkaline-earth silicate fibres are a new generation of refractory materials. They are vitreous when manufactured but can devitrify during high temperature use. To better understand their microstructural behaviour in use, experimental conditions for their thermal exposure in a "clean" environment were established. The as-manufactured fibres were thermally exposured at temperatures ranging from 700°C to 1250°C over time scales extending to thousands of hours using laboratory furnaces whose temperatures were carefully monitored. For short term exposure ranging from 10 mins, a specially designed tube furnace which was built as part of the project was used. This tube furnace was also used to determine the thermal response of the fibres.

Qualitative X-ray Diffraction (XRD) methods were employed to identify the devitrification products and semi-quantitative internal standard method was developed for the analysis of the devitrification products in relation to their maturity and transformation. The internal standard chosen was BaF_2, which proved to work well.

Special techniques involving ion beam thinning or ultramicrotomy were developed to reliably and efficiently prepare electron transparent fibre samples for TEM analysis. The ultramicrotome method proved most appropriate, and this was used to prepare the majority of the TEM samples in this study. While most published work on glass-glass phase separation and crystallisation are based on replica technique of TEM specimen preparation. This method provided a large number of fibre sections which

were thin enough for direct observation of microstructure and composition analysis under transmission electron microscopy. While fracturing the fibre cross sections was observed, the small fractions were big enough for analysis. Successful TEM studies have been carried out to identify the product crystalline phases and subsequently the evolution of fibre microstructure as a function of temperature and time.

Studies based on the SEM have greatly supported and contributed to the structural characterisation of the transforming fibres and to the understanding of the phase transformation and morphological development in the devitrifying fibres.

5.2 Glass-Glass Phase Separation

Transmission electron microscopy and X-ray diffraction studies indicated that the opalescence encountered in the as-manufactured Superwool fibre blanket and during the initial, relatively low temperature subsolidus heat treatment of the fibres was due to glass-glass phase separation. This phase separation occurred homogeneously throughout the volume of the glass fibres or shot particles rather than at surfaces.

During the fiberising process, the glass melt was rapidly quenched and the microinhomogeneous structure found in the as-manufactured shot particles indicated that phase separation took place during the fiberising process. When the homogeneous melt cools through the miscibility gap, the supercooled melt began to separate. This unmixing process continued until it was halted either by the

intervention of crystallisation or by the high viscosity attained by the system as it passed through the glass transition region. In the case of shot particles, crystallisation did not occur. The resulting glass was therefore a "phase separated" glass, a solid composed of two glassy phases. The extent of the phase separation depended on the time the system remained within the miscibility gap at high enough temperatures for the kinetic processes of separation to proceed. The rate of quenching of the material strongly depended on the size of the shot particles or fibres. The shot particles, as the fibres, had a range of diameters and the larger diameters led to lower quenching rates and therefore, phase separation had a longer time over which to develop. The separated silica phase was observed to increase in size with increase in shot diameter.

In Superwool, A2 and B3 fibres, when the fibre diameters was less than about 10μm, the fibres were rapidly quenched to room temperature during the fiberising process and formed a homogeneous, or near-homogeneous, glass. This glass was subsequently phase separable since, upon heating to a temperature where molecular transport could take place, phase separation could occur (although at these temperatures it will also be competing with the crystallisation process). Phase separation was observed with the TEM in these fibres after thermal exposure. The dimensions and morphologies of the phase separated phase largely depended on the compositions and thermal exposure conditions.

In Superwool fibre, worm-like structure with high connectivity seemed to be more easily produced by heat treatment at 750°C. The phase separated structure of the fibres treated at 800°C exhibited a smaller degree of connectivity, the difference in

behaviour probably reflecting a difference in the density of the separated phase particles. The effects of temperature on the characteristics of phase separation have been extensively investigated[137, 138,139]. It is generally observed that lower heat treatment temperatures within a miscibility gap lead to smaller and more numerous second phase particles .i.e. a small particle diameter and increased density of particles. According to Haller's intersecting theory[134], these particles approached each other to form an interconnected structure. The size of any interconnected microstructures showed a dependence on heat treatment temperature, a lower temperature, say 750°C giving a finer scale of structure. The limited size of the particles provides good equilibriation of temperature throught the volume of the material and therefore at lower temperatures a slower rate of coarsening. During thermal exposure, phase separation developed as a function of time and, in shot particles the separated silica phase showed coarsening with increase in time.

After thermal exposure of the A2 and B3 fibres under the same conditions, for example 750°C for 24 hours, the separated silica phase was observed as discrete particles, while in Superwool fibre the separated phase showed much higher interconnectivity. This is due to their different compositions. Reference to the phase diagram in figure 3-2, shows that if these fibrous glasses separate to alkaline-earth silicate phase and silica phase, the composition of the Superwool fibre gives a much higher volume fraction of separated silica phase. The higher density of separated silica particles therefore more readily approached each other and formed the interconnected structure.

The observed morphology of phase separation depended not only on the original composition of the fibre and, the time and temperature of the heat treatment but also on details of the thermal history of the fibres. Both discrete particles and interconnected structures can be produced. Coarsening has been shown to be an important process in phase separation and can involve changes in the morphology as well as the scale of the structure. It was shown in this fibrous glass system that slow cooling of the melt led to droplet structure while a sharp decrease in temperature during the fiberising process and subsequent isothermal heating led to a more highly interconnected structure. It is highly probable that a predominant role is played by the value of the melt viscosity. Similar phenomena were observed by Roskova[139] in sodium silicate and sodium borosilicate glasses.

So far very little research has been reported on phase separation in this particular material system. This study allowed the direct observation of phase separation and its development in the glassy fibre. Also, it is suggested that the initial phase separation in this fibrous system is a key to understanding the whole devitrification process. The influence of phase separation on crystallisation in general has been extensively studied[141,142,148] and the effects of phase separation on crystallisation in this fibre system will be considered in section 5.3.

5.3 Devitrification Behaviour Of Superwool Fibre

5.3.1 Development Of Alkaline-Earth Silicates

The development of alkaline-earth silicates in Superwool as a function of furnace exposure temperature and time are summarised in figure 5-1. This figure is constructed from figure 4-34.

As discussed in details in the last section, in the '◆' region phase separation took place. Both the silica rich and alkaline-earth rich regions were amorphous.

With increased thermal exposure time at and below 850°C i.e.in the 'Δ' region, the main peaks of wollastonite 2 (W2') and diopside (D') emerged and developed with increase in exposure time. Some unidentified peaks were detected in the XRD patterns and how they were involved with the overall phase development remain unclear. Further exposure resulted in the appearance of main peaks of wollastonite 1. In this region of temperature and time, all these alkaline-earth silicate phases showed very immature structures, however the gradual transformation from wollastonite 2' and diopside to wollastonite 1' as a function of increasing exposure time was identified. The transformation rate increased with increasing exposure temperature from 750°C to 850°C and these results strongly suggested that in this temperature range the wollastonite 2 is an unstable phase; it formed initially and slowly transformed to wollastonite 1 after extended exposure.

Increase in the exposure time at temperatures above 850°C led to the '*' and '●' region where wollastonite 1 was the main crystalline alkaline-earth silicate phase. After its formation, wollastonite increased in its diffraction intensity rapidly and soon reached its maximum. The results also showed that the d-spacings of wollastonite did not change with increase in exposure time. A small amount of pseudowollastonite was detected in addition to wollastonite 1 in the '●' region. At 900°C, wollastonite was stable against extended exposure and persisted even after 3000 hours' exposure. At temperatures higher than 900°C wollastonite 1 only existed in a limited time period.

With further increase in exposure temperature and time to '◇' area, wollastonite 1 decomposed into wollastonite 2 and diopside, and therefore, three phases of alkaline-earth silicate, wollastonite 1, wollastonite 2 and diopside, coexisted. The XRD results clearly demonstrated the transformation from wollastonite 1 to wollastonite 2 and diopside at exposure temperatures above 900°C. The decomposing rate of wollastonite 1, or the rate of formation of wollastonte 2 and diopside, largely depended on the exposure temperature and increased rapidly with the exposure temperature.

In '▲' region , which is at the top of the diagram, only wollastonite 2 and diopside were detected. This suggested that at the limit of the exposure time investigated and temperatures higher than 900°C, wollastonite 2 and diopside were the final alkaline-earth silicate products.

Both TEM and XRD studies confirmed the formation of two different forms of wollastonite solid solution in the thermally exposed Superwool fibre. It was noticed that the d-spacing of wollastonite 1 and wollastonite 2 remained fairly constant following crystallisation. Both TEM and SEM analysis revealed that wollastonite 1 and 2 are magnesium-containing wollastonites and are wollastonite-diopside solid solutions. Wollastonite 1 contained more Mg^{2+} in its structure as reflected in the greater shift in d-spacing in companion with standard wollastonite pattern. 'Doublet' X-ray diffraction peaks observed during their transformation suggested that these two wollastonites have similar structures but have unit cells of a differing size due to different concentrations of Mg^{2+}. Assuming wollastonite 1 and wollastonite 2 both have the monoclinic structure, i.e., parawollastonite structure, the recalculated d-spacings based on experimental results for the cell constants are a good match with experimental results. Cell parameters of wollastonite 1 and wollastonite 2 deduced from both XRD and TEM analyses are smaller than those on the JCPDS card for wollastonite due to the substitution of Ca^{2+} by Mg^{2+}, though the position of Mg^{2+} in the structure is not clear.

Wollastonite 1 was the low temperature form and stable at and below 900°C while wollastonite 2 formed after extended exposure at temperatures higher than 900°C. However, investigations showed that wollastonite 2 and diopside did form preferentially below 900°C and then transformed to wollastonite 1. At temperatures below 900°C phase separation had time to develop and it is possible that secondary phase separation occurred in the alkaline-earth silicate rich region, i.e., the

composition in the alkaline-earth silicate rich regions was not uniform. Secondary phase separation led to a change in the chemical composition of the region, caused the emergence of regions of nonuniformity similar in composition to wollastonite 2 and diopside, and accelerated the nucleation and growth of these crystals. These nonuniform regions kinetically favoured the formation of diopside and wollastonite 2 phases and, due to the relatively low temperatures involved, the wollastonite and diopside phases showed deformed or imperfect structures.

It is believed that these two types of wollastonite are similar to those observed by Osborn[38]. He did not mention the low temperature anomaly discussed in the last paragraph. Shinno[117] claimed that W85 (85%wollastonite, 15%diopside wt.%) -W0 (0%wollastonite, 100%diopside wt.%), which he defined as Mg-wollastonite, was a metastable phase in all temperature ranges while W100-W85 was the stable phase. He suggested a transformation occurred from Mg-wollastonite to diopside rather than the Mg-wollastonite1 to Mg-wollastonite 2 and diopside which we observed. After closely monitoring the development of alkaline-earth silicate phases in this system, we found that both wollastonite forms had their own stable temperature range. Costantini[119] reported the shift in XRD traces for wollastonites containing different amounts of Ca. The stability and transformation behaviour were mentioned in their paper.

The diopside identified in these devitrified fibres did not take extra Ca^{2+} and Mg^{2+} ions into its structure and its d-spacing matched the standard data in JCPDS cards.

5.3.2 Development of Crystalline Silica Phases

Figure 5-2 summarises the temperature and time dependence for the development of silica phases in the Superwool fibre. This diagram is also constructed from figure 4-34.

Crystalline silica phases were not detected until the fibre was exposed at 1000°C for 48 hours. Before that in the '✧' temperature and time region the separated silica phase remained amorphous.

The figure shows a narrow temperature and time band (solid triangle) in which quartz was the only crystalline silica. This suggested that quartz was the primary crystalline silica phase. As discussed in section 4, quartz was identified in its low-temperature form in the devitrifying alkaline-earth silicate fibres.

Increase in exposure temperature and time to '*' region, resulted in quartz starting to transform to cristobalite. XRD, TEM and thermal analysis identified the formation of α-cristobalite, the low temperature form and, these α-cristobalite peaks were accompanied by a small broad peak of tridymite. The tridymite peak is due to structural intergrowth of a small amount of tridymite and cristobalite. There was no proof that all the cristobalite formed from the transformation of quartz owing to a lack of quantitative analysis and it is possible that a small amount of cristobalite could transform straight from amorphous silica. However, the maximum rate of increase

of cristobalite corresponded to the maximum amount of quartz and this implies that at least most of cristobalite transformed from quartz. Further there is agreement between the time for cristobalite to grow to its maximum and for the quartz to disappear. The transformation rate from quartz to cristobalite was strongly dependent on the temperature. At the same temperature, the transformation rate depended on the amount of quartz formed.

At 1200°C or 1250°C after extended exposure, in the 'O' region, cristobalite was the main crystalline silica phase identified while significant growth of tridymite related peaks was confirmed by both TEM and XRD results.

When silica glass crystallises, it is often observed that cristobalite forms even within the temperature range over which quartz or tridymite is stable[13, 16, 149]. The reason is believed to be the similarity of the open structure of cristobalite to that of amorphous silica. However, the results showed that in this fibrous system quartz was the initial crystalline silica phase to form. At and above 1000°C, quartz formed and then transformed to cristobalite. As pointed out in section 2.4.1, quartz is only thermodynamically stable below 867°C[43]. Golubkov[167] suggested that there exist two different types of amorphous silica structure, one quartz like and another cristobalite like. In this fibrous system, after phase separation alkaline-earth silicates crystallised while the separated silica phase was retained to be amorphous below 1000°C. We presume that the structure of the separated amorphous silica evolved to be more quartz like in the wide '✧' range of the diagram. Therefore, with further increase in exposure temperature and time the system kinetically favoured the formation of

quartz. As quartz is not a thermodynamically stable phase at or above 1000 °C, it gradually transformed to cristobalite.

Also, the high-temperature form of cristobalite was identified as the primary and main crystalline phase[13, 16] in devitrified aluminosilicate fibres. The different devitrification products possibly reflected a different devitrification mechanism in these two different fibrous systems. For examples, the aluminosilicate fibre unlike the alkaline-earth silicate fibre was ground to its powder form before thermal exposure. The difference in thermal response of as-manufactured fibres in their unground and ground form as demonstrated in section 3.3.2, the damage to the fibre surface, any contamination of the fibre and, possibly any strain release from the rapidly quenched fibre during the grinding process may have affected or even changed the devitrification mechanism. Further, a difference may arise due to the formation of cristobalite, directly from amorphous silica or via the quartz intermediate.

5.3.3 Devitrification Process in Superwool Fibre

The discussions in section 5.3.1 and 5.3.2 indicate that the devitrification process in superwool fibre may be represented by the schematic diagram shown in figure 5-3. Initially phase separation took place in the homogeneous glass to produce two glassy phases, one alkaline-earth ions rich and the other silica rich. Crystallisation then took place in the two separated phases: wollastonite 1, wollastonite 2 and diopside crystallised from amorphous, alkaline-earth rich glass and quartz, cristobalite and

tridymite from the amorphous silica phase. At 900°C, wollastonite 1 was the stable phase. At higher temperature after extended exposure, the primary phase wollastonite 1 transformed to wollastonite 2 and diopside, i.e. Wollastonite 1→ Wollastonite 2 + Diopside. Wollastonite 2 and diopside were the final, alkaline-earth silicate products at and above 1000°. Wollastonite 2 and diopside did form in an immature form after extended exposure at temperatures below 900°C. However they slowly transformed to wollastonite1, i.e., Wollastonite 2' + Diopside' → Wollastonite 1'.

It was not until exposure temperatures exceeded 1000°C that α-quartz crystallised out from amorphous silica phase. The subsequent increases in exposure temperature and time yielded more quartz and it then transformed to cristobalite. At 1250°C after extended exposure, in addition to wollastonite 2, diopside and cristobalite, prominent growth of tridymite was then observed.

5.4 Devitrification Behaviour of A2 and B3 Fibres

5.4.1 Devitrification Behaviour of A2 Fibre

Phase separation took place in A2 fibre as discussed in section 5.2 and figure 5-4 shows from this information the development of the alkaline earth silicate products in the devitrifying A2 fibre.

Diopside was the initial and main crystalline product obtained from the alkaline-earth silicate component ('○'and '●' regions). In the '○' region, a trace of wollastonite was also detected. Diopside was the final devitrified alkaline-earth silicate product obtained at the hightest temperatures and times investigated ('●' regions). Silica phases showed the same behaviour to that observed in the Superwool fibre.

Figure 5-5 shows the devitrification process observed for A2 fibre. Phase separation took place initially. Diopside was the initial crystalline phase, though a trace of wollastonite did form as an intermediate product at certain temperatures and times. Subsequent increase in exposure temperature and time led to its disappearance. In terms of phase diagram, the A2 fibre sits on the line of SiO_2 and $CaO{\cdot}MgO{\cdot}2SiO_2$ in the equilibrium diagram and, therefore as expected diopside and cristobalite were the final equilibrium products.

In the A2 fibre, diopside was the initial crystalline phase and existed as the main devitrification product throughout the exposure temperatures and times investigated. Shinno[117, 118] claimed that the crystallisation of diopside from glass included two processes: crystallisation of Mg-wollastonite from the glass and then the transformation of Mg-wollastonite to diopside. In this fibrous material, the XRD results suggested that the majority of diopside crystallised directly from the amorphous alkaline-earth silicate glass. The trace of wollastonite detected might be the Mg-wollastonite defined by Shinno[118] which then transformed to diopside after longer exposure.

5.4.2 Devitrification Behaviour of B3 Fibre

Figure 5-6 shows the temperature and time dependence of the development of alkaline-earth silicates in the thermally exposed B3 fibre.

Again, as observed in the case of Superwool fibre two different forms of wollastonite, wollastonite 'a' and 'b', formed in the thermally exposed B3 fibre. As with wollastonite 1 in Superwool fibre, the results showed that wollastonite 'a' was the more stable phase at ≤900°C whereas wollastonite 'b', similar to wollastonite 2, was stable at temperatures above 900°C. At high temperatures after extended exposure, wollastonite 'a' started decomposing to wollastonite 'b' and diopside until wollastonite 'a' was no longer detected. Due to the limited amount of diopside formed, only part of the wollastonite crystallised out as wollastonite 'a' and the remainder crystallised out as wollastonite 'b' even in the stable temperature range of wollastonite 'a'. Both wollastonites coexisted in fibres devitrified at 900°C. At temperatures below 900°C, immaturally wollastonite b, diopside and pseudowollastonite initially formed. At the same time, a few unidentified peaks emerged which only only existed in a limited time range. With increasing exposure time, wollastonite b and diopside started transforming to wollastonite a.

In Superwool fibre only a trace of pseudowollastonite was detected in a limited temperature-time range from 900°C to 1200°C. With a higher concentration of CaO and SiO_2 in its original composition, B3 fibre demonstrated the typical crystallisation behaviour of pseudowollastonite. Its d-spacing matched JCPDS data which

confirmed Osborn's view that pseudowollastonite didn't take extra Mg^{2+} into its structure to form solid solution[38]. As with Superwool, pseudowollastonite only existed in a certain range of temperature and time. The XRD patterns of B3 fibre, after 672 hours' exposure at different temperatures, showed a tendency for pseudowollastonite to decrease in peak intensity with increasing in exposure temperature. After devitrification at 1100°C only trace amounts of pseudowollastonite were detected while, after 1250°C no pseudowollastonite was detected. At similar temperatures, for example 1000°C, the diffraction intensity of pseudowollastonite increased with exposure time up to 168 hours and then started to decrease. In B3 fibre with increasing exposure time from 336 hours to 1848 hours at 1000°C, wollastonite 'a', pseudowollastonite decreased in their intensities while wollastonite 'b' and diopside increased. Therefore, it was likely that pseudowollastonite had transformed to wollastonite 'b'.

These results suggest that pseudowollastonite was not stable in the temperature range investigated. The amount of pseudowollastonite decreased with increasing exposure temperature. As indicated by figures 4-47 and 48, at 1100°C only trace amounts of pseudowollastonite was identified, and at 1250°C no pseudowollastonite was detected. Owing to the high concentration of SiO_2 and CaO in the glass composition, and then in the phase separated alkaline-earth silicate rich regions, the system kinetically favoured the formation of pseudowollastonite as a metastable phase in the low temperature region. The formed pseudowollastonite gradually transformed to more stable wollastonite with increasing exposure temperature. The stable

temperature region for wollastonite was greatly increased due to the formation of wollastonite solid solution[37]. It was proved to be higher than the highest exposure temperature investigated, 1250°C. Bowen[35] identified that powdered $CaSiO_3$ glass crystallised to form pseudowollastonite while bulk $CaSiO_3$ glass crystallised to form wollastonite. No investigation was carried out to show if the pseudowollastonite formed from its powdered glass was stable against extended exposure. These fibrous materials had dimensions comparable to those of powders. This investigation suggested at around 900°C pseudowollastonite is one of the primary crystalline phases, however it was not stable against extended exposure.

As with the A2 fibre, the devitrification behaviour of the silica phases in B3 was similar to that observed in Superwool fibre. The development of tridymite at 1250°C was best demonstrated in B3 fibres. Because the original composition of B3 fibre was richer in silica and therefore the transformation appeared more prominent. As shown by figure 4-47, there was a significant reduction in the height of the cristobalite diffraction peak corresponding to the formation of tridymite, which implies a transformation from cristobalite to tridymite.

The complicated devitrification process for B3 fibre is illustrated by figure 5-7. As with Superwool and A2 fibres, phase separation took place at the initial stage of devitrification. When the fibre was exposed at 900°C both Pseudowollastonite, wollastonite 'a' and 'b' crystallised out. With further increase in exposure temperature, the wollastonite 'a' decomposed to wollastonite 'b' and diopside. After exposure at lower temperature (800°C), wollastonite b, diopside, pseudowollastonite

and some unidentified peaks appeared and with an increase in exposure time, wollastonite 'b' and diopside started transforming to wollastonite 'a'. Pseudowollastonite increased initially in diffraction intensity with increasing thermal exposure temperature and time, and then, most likely transformed to the more stable wollastonite b phase. Regarding the crystallisation of silica phases, as in Superwool and A2 fibres, quartz crystallised from the separated amorphous silica and then transformed to cristobalite. The latter then transformed to tridymite after extended exposure. Therefore, as in the Superwool fibre, wollastonite, diopside, cristobalite and tridymite were the final devitrification products.

5.5 Practical Implications and Recommendation for Further Work

The results obtained in this investigation were obtained in a "clean" laboratory environment. It is emphasised that the range of devitrification products may change significantly as a result of "contamination" by a particular industrial environment. It would therefore it will be of value to investigate the effects of different exposure environments on the devitrification process and products.

This investigation has confirmed the formation of silica phases including amorphous silica, α-quartz, α-cristobalite and tridymite in the thermally exposed alkaline-earth silicate fibres. In the devitrifying Superwool, A2 and B3 fibres, similar transformation behaviour between these phases was observed ie amorphous silica→α-quartz→α-

cristobalite→tridymite. The formation mechanism of α-quartz at temperatures ≥1000°C, which is not in its stable temperature region, remains to be clarified. It is accepted that β-cristobalite, the high-temperature form, was the only silica phase identified in the devitrified aluminosilicate fibres. The formation of metastable α-quartz here may hold the key to the formation of α-cristobalite, the low-temperature form, in the devitrified alkaline-earth silicate fibres. More detailed microstructural studies will help to understand the different crystallisation and transformation process in these silicate fibres.

The formation of these silica phases was observed at temperatures within the conditions of use recommended by the fibre manufacturers. These findings are important both for engineering and health perspectives. From an engineering perspective, the formation of cristobalite has an adverse effect on the mechanical properties of the fibres due to its large expansion coefficient[77,78], resulting in brittleness. The health effects of silica dusts have paralleled many developments of occupational medicine and industrial toxicology. Studies of the biological behaviour of these silica-contained devitrified fibres are important both practically and scientifically.

Wollastonite solid solutions containing different concentrations of Mg^{2+} were identified in the devitrified Superwool and B3 fibres. The structure of the wollastonite solid solutions, and the position of Mg^{2+} in the structure are yet to be studied and clarified. Microstructural evidence of transformation between the

wollastonite solid solution and diopside in Superwool and B3 fibres is yet to be provided using high resolution transmission electron microscopy.

Wollastonite 1 and wollastonite 'a' were identified as the low-temperature forms of wollastonite solid solution and wollastonite 2 and wollastonite 'b' as the high-temperature forms. However, the results showed that wollastonite 2 and wollastonite 'b' did form below 900°C. It is yet to be confirmed that if this low-temperature anomaly is due to a secondary phase separation which may have taken place in the alkaline-earth ions rich area. Also, Some mysterious peaks were observed in Superwool and B3 fibres at temperatures between 750°C to 850°C. To identify these unknown peaks and understand the role they played during the crystallisation of the alkaline-earth silicate phases will also help to clarify the crystallisation process.

In the thermally exposed Superwool and B3 fibres, pseudowollastonite, wollastonite solid solutions, diopside were identified. While in A2 fibre diopside was the main alkaline-earth silicate phase formed. The different microstructures of these devitrified fibres will possibly have different biological effects. Also in the recommended service temperature range of Superwool fibre by the manufacturer, the alkaline-earth silicates crystallised out in the form of deformed or imperfect structure between 750 to 850°C. In another word they are structurally active. Are they biologically active as well?

- Conditions for the thermal exposure of the fibres over a wide range of temperature and time in a "clean" environment have been reliably established.

- Specimen preparation methods involving ion beam thinning and ultramicrotomy have been developed to produce electron-thin specimens of fibre cross sections for examination in the transmission electron microscope. Analytical electron microscopy revealed the microstructural evolution of the phase products in the devitrifying fibres.

- Qualitative and semi-quantitative X-ray diffractometry were successfully employed to analyse the devitrification products in the heat treated Superwool, A2 and B3 fibres in relation to the formation, maturing and transformation of its crystalline phases.

- Microstructural analyses revealed that metastable phase separation in the initial glassy fibres and shot particles was the first stage of devitrification in the alkaline-earth silicate fibres. The phase separated microstructures depended not only on the composition, thermal exposure temperature and time, but also on the thermal behaviour in relation to fibre or particle size.

- For the phase separated fibres, wollastonite solid solutions, diopside and pseudowollastonite (only in Superwool and B3 fibres) crystallised from the

alkaline-earth silicate rich regions while quartz, cristobalite and tridymite came from the silica rich regions. The formation of these phases and the phase transformations were defined as a function of furnace exposure temperature and time.

- Two forms of wollastonite solid solutions were identified in the devitrified alkaline-earth silicate fibres. The low temperature form, containing relatively more Mg^{2+} ions transforms to the high temperature form and diopside at temperatures above 900°C after extended exposure. It is suggested that the detailed transformation process among these wollastonites, diopside and pseudowollastonite has been identified for the first time.

- The formation of an immature high temperature form of wollastonite solid solution and diopside below 900°C with extended thermal exposure is possibly due to secondary phase separation which may have taken place in the alkaline-earth rich regions of the separated glass.

- Pseudowollastonite is a metastable phase in the temperature range (750 to 1250°C) investigated. It forms in certain exposure temperature and time range and then transformed to wollastonite.

- The formation of silica phases including α-quartz, α-cristobalite and tridymite in the devitrified fibres is confirmed. These silica phases exhibit an unusual

transformation process: amorphous silica → quartz → cristobalite → tridymite, and it is proposed that a quartz like amorphous silica had formed in the silica rich region of the separated glass which is responsible for the formation of quartz as the primary crystalline silica phase.

- In the investigated temperature and time region, wollastonite, diopside, α-cristobalite and tridymite were the final devitrification products of Superwool and B3 fibres, and diopside, α-cristobalite and tridymite of A2 fibre.

1. Young, J. (1991), "Properties, Application and Manufacture of Man-made Mineral Fibres", In Liddell, D. and Miller, K. (Eds), *Mineral Fibres and Health,* CRS Press, Boca Raton, F1., USA, pp37-53, 1991.

2. Gaodu, A. N., Pitak, N. V., Vol'fson, R. E., and Drizheruk, M. E.(1977), " Crystallisation in Heated Aluminosilicate", *Inorganic Materials,* 13 (12) 1802-1804.

3. Old, L.E., Miller, W.C. and Pallo, J.M., (1980), " High Temperature Aluminium-Silicate Fibres Stabilized with Cr_2O_3", *Ceram. Bull.*, 59(7)739-741.

4. Belyakova, N.P., Kutukov, V.F., Ustyantsev, V.M. and Trebnikova, M.G. (1981) " Phase Transition in Materials Based on High-Alumina Fibre", *Inorgan. Mater.*, 17, 948-951.

5. Hickling, H., Tohomas, D.G. and Briggs, J. (1981). "High-Temperature Behaviour of Alumina-Silicate Ceremic Fibres", *Sci. Ceram.* 11, 397-403, 1981.

6. Jager, A., Stadler, Z. and Wernig, J.(1984), " Investigations on Microstructural Changes Undergone by Ceramic Fibres at Elevated Temperatures, Particularly as Regards the Formation of Cristobalite", 61 (3) 143-147.

7. Vine, G., Young, J., and Nowell, I. (1984), "Health Hazards Associated with Aluminosilicate Fibre Products", *Ann. Occup. Hyg,.* 28 (3) 356-359.

8. Dietrichs, P., Dhupia, G.S. and Kronert, W. (1986), " Interaction of Reducing and Corrosive Environments with Ceramic Fibres in the System Al_2O_3-SiO_2 ", *J. Physique*,47(2)C, 581-585, 1986.

9. Proceedings of International Symposia Concerning Man-made Mineral Fibres, WHO Regional Office for Europe, Copenhagen, 1976, 1982 and 1986.

10. Davies, J.M.G., Addison, J., Bolton R. E., Donaldson, K. Jones, A.D. and Wright A. (1982), "The Pathogenic Effects of Fibrous Ceramic Aluminosilicate Glass Administered to rats by inhalation or Peritoneal Injection", *Biological Effects of Man-made Mineral Fibres,* Vol.2, PP303-322, Proceedings of WHO/IARC conference copenhagen.

11. Gantner, B.A. (1986), "Respiratory Hazard from Removal of Ceramic Fibre Insulation from High-Temperature Industrial Furnaces", *Am. Ind. Hyg. Assoc. J.* 47 (8) 530-534.

12. Hesterberg, T.W, Mast, R. McConnell E.E., Chevalier, J., Bernstein, D.M., Bunn W.B., Anderson, R.,(1990) *In Mechanisms of Fibre Carcinogenesis, Plenum Press*, NATO ASI Series, 531-538.

13. Young, J., Rea, M. S. and Briggs, G.(1989), " The Non-Formation of α -Cristobalite in Devitrified Commercial-Grade Aluminosilicate Refractory Ceramic Fibre", *British Ceram Trans. J.*, 88, 58-62.

14. Young, J., Laskowski, J.J., Acheson,R. and Forder, S.D. (1991), "Health Related Aspects of the Heating of Refractory Ceramic Fibre", In Brown, R.C., Hoskins, J.A. and Johnson, N.F. (Eds), *Mechanisms of Fibre Carcinogenesis,* Plenum Press, New York, USA, pp 189-197.

15. Sara, E.A. (1993), "In Vitro Toxicologocal Testing of Devitrified Fibres from a Heat Treatment Furnace in the Steel Industry, *Private communication.*

16. Laskowski, J.J., Young, J., Gray, R., Acheson, R. and Forda, S.S. (1994). " The Identity Development and Quantification of Phases in Devitrified, Commercial-grade, Aluminosilicate Refractory Ceramic Fibres: an X-ray Powder Differactometry Study.", *Anal. Chim. Acta.*, 286(1), 9-23.

17. Patent(1993), Saline Soluble Inorganic Fibres, *Morgan Crucible Co plc, WO* 93/15028 A1 930805.

18. Wagner, J.C., (1976), "Asbestos Carcinogenesis", *Am. Chem. Soc. Monogr.*, 17, 260.

19. Asbestos: vol. 1, properties, applications and hazards, edited by Michaels, L, Schissick, S., Chichester: John Wiley and Son, 1979.

20. Hodgson, A. A., (ed), Alternatives to Asbestos: the Pros and Cons, Chichester: John Wiley and Son, 1989.

21. Alternatives to Asbestos Products, London, HMSO, 1986.

22. Bracke, P., Schurmans, H. and Verhoest, J., Inorganic Fibres and Composite Materials, Pergamon International Information Corporation, 1984.

23. Morganite Thermal Ceramics Ltd., 1990 data.

24. Miller, W. C., Rrefractory Fibres, in Kirk-Othmer Encyclopaedia of Chemical Technology, 3rd ed., Vol.20, grayson, M., Mark, H. F., Othmer, D. F., Overberger, C. G., and Seaborg, G. T., Eds., John Wiley and sons, New York, 1982, 65.

25. Brown, R.C., Hoskins, J.A. and Young, J.A. (1992), "Not Allowing the Dust to Settle", *Chemistry in Britain*, 910-915.

26. Birchall, J.D. (1983), "The Preparation and Properties of Polycrystalline Aluminium Oxide Fibres", *Trans. J. Br. Ceram. Soc.* 82, 143-145.

27. European Patent 0412878 and 0459897.

28. Morgan Thermal Ceramics, Product Information, Superwool®Blanket (Grade X-607).

29. Fenner, C.N. (1913)" The Stability Relations of the Silica Minerals", *Am. J. Sci.*, 36, 333-384.

30. Day, A. L. and Shepherd, E. S.(1906), " The Lime-Silica Series of Minerals", *J. Am. Chem. Soc.* 28 (9) 1089-1114.

31. Rankin, G. A. and Wright, F. E.(1915), "The Ternary System $CaO-Al_2O_3-SiO_2$", *Am. J. Sci.*, (4th series), 39 (229) 1-79.

32. Greig, J. W.(1927), "Immiscibility in Silicate Melts", *Am. J. Sci.*,, 13 (73) 1-44; (74) 133-154.

33. Bowen, N. L., Schairer, J. F. and Posnjak, E.(1933) , " The System $CaO-FeO-SiO_2$", *Am. J. Sci.*, (5th series), 26 (153) 193-284.

34. Osborn, N.L., and Schairer, J.F.(1941), " The Ternary System Pseudowollastonite-Akermanite-Gehlenite", *Am. J. Sci.*, 239, 715-763.

35. Bowen, N. L.(1914) , "The Ternary System Diopside-Forsterite-Silica", *Am. J. Sci.*, (4th series), 38 (225) 207-64.

36. Ferguson, J. B. and Merwin, H. E.(1919), "Wollastonite and Related Solid Solutions in the Ternary Systen $CaO-MgO-SiO_2$", *Am. J. Sci.*, (4th series), 48, (484) 165-89.

37. Schairer, J. F. and Bowen, N. L.(1942), "The Binary System $CaSiO_3$-Diopside and Relations Between $CaSiO_3$ and Akermanite", *Am. J. Sci.*, 240 (10) 725-42.

38. Osborn, E.F.(1942), "The System $CaSiO_3$-Diopside-Anorthite", *Am. J. Sci.*, 240(11), 751-788.

39. Clark, C. B.(1946), "X-Ray Diffraction for Compounds in the System CaO-MgO-SiO_2", *J. Am. Ceram. Soc.*, 29 (1) 25-30.

40. Ricker, R. W. and Osborn, E. F.(1953), " Additional Phase Equlibrium Data for the System CaO-MgO-SiO_2", *J. Am. Ceram. Soc.*, 37 (3) 133-139.

41. Allen, E. T., White, W. P. and Wright, F. E. (1906), " On Wollastonite and Pseudowollastonite-Polymorphic Forms of Calcium Metasilicate", *Am. J. Sci.*, (4th series), 21, 89-108.

42. Osborn, J.F. and Arnulf Muan (1960), revised and redrawn "Phase Equlibrium Diagrams of Oxide Systems", Plate 1, published by the American Ceramic Society and Edward Orton, Jr., Ceramic Foundation.

43. Griffen, D.T. (1992), Silicate Crystal Chemistry, Oxford University Press, Oxford, UK.

44. Bragg, W.L. and Gibbs, R.E. (1925), "The Structure of α and β Quartz", Proc. Roy. Soc. Lond. A109, 405-27.

45. Gibbs, R.E.(1925), "The Variation with Temperature of the Intensity of Reflection of X-rays From Quartz and its Bearing on the Crystal Structure", *Proc. Roy. soc. Lond.*, A107,561-570.

46. Young, R.A.(1962), "Mechanism of the Phase Transition in Quartz", U.S. Air Force, Office of Scientific Research, Contract No. AF49(638)-624.

47. Kihara, K. (1990), "An X-ray Study of the Temperature Dependence of the Quartz Structure", *Eur. J. Min.* 2, 63-77.

48. Wright, A.F. and Lehmann, M.S. (1981), "The Structure of Quartz at 25 and 590°C Determined by Neutron Diffraction", *J. Sol. State Chem.*, 36, 371-380.

49. Le Page Y., Calvert, L.D. and Gabe, E.J.(1980), "Parameter Variation in Low-Quartz Between 94 and 298K", *J. Phys. Chem. Solids*, 41, 721-725.

50. Lager, G.A., Jorgensen, J.D. and Rotella, F.J.(1982), "Crystal Structure and Thermal Expansion of α-quartz at Low Temperatures", *J. Appl. Phys.*, 53, 6751-6756.

51. Thompson, P. and Wood, I.G. (1983), "X-ray Rietveld Refinement Using Debye-Scherrer Geometry", *J. Appl. Cryst.* 16, 458-472.

52. Will, G., Bellotto, M., Parrish, W. and Hart M. (1988), "Crystal Structures of Quartz and Magnesium Germanate by Profile Analysis of Synchrotron-Radiation High-Resolution Powder Data", *J. Appl. Cryst.*, 21, 182-191.

53. Dolino, G. (1990), " The α-inc-β Transitions of Quartz: a Century of Research on Displacive Phase Transitions", *Phase Transitions*, 21, 59-72.

54. Heaney, P.J. and Veblen, D.R. (1991), "Observations of the α-β Phase Transition in Quartz: a Review of Imaging and Diffraction Studies and Some New Results", *Am. Min.* 76, 1018-1032.

55. Helgeson, H.C., Delany, J.M., Nesbitt, H.W. and Bird, D.K.(1978), "Summary and Critique of the Thermodynamic Properties of the Rock-Forming Minerals", *Am. J. Sci.*, 278-A:1-229.

56. Ghiorso, M.S., Carmichael, I.S.E. and Moret, L.K. (1979), "Inverted High-Temperature Quartz", *Contrib. Min. Petrol.*, 68, 307-323.

57. Van Tendeloo, G., Van Landuyt, J. and Amelinckx, S. (1976), "The α-β Phase Transition in Quartz and $AlPO_4$ as Studied by Electron Microscopy and Diffraction", *Phys. Status Solidi.* 33, 723-735.

58. Malov, Y.V. and Sonyushkin, V.E. (1976), "Direct Electron-Microscope Investigation of the α-β Transition Process in Quartz", *Sov. Phys. Crystal.* 20, 644-645.

59. Bachheimer, J.P. (1980), "An Anomaly in the β Phase near the α-β Transition of Quartz", *J. Physique-Lett*, 41, L559-L561.

60. Shapiro, S.M. and Cummins, H.Z. (1968), "Critical Opalscence in Quartz", *Phys. Rev. Lett.*, 21, 1578-1582.

61. Dolino, G., Bachheimer, J.P., Berge, B., Zeyen, C.M.E., Van Tendeloo, G., Van Landuyt, J. and Amelinckx, S. (1984), "Incommensurate Phase of Quartz: III. Study of the Coexistence State between the Incommensurate and the α-Phase of Neutron Scattering and Electron Microscopy", *J. Physique*, 45, 901-918.

62. Hill, V. G. and Roy, Rustum (1958), "Silica Structure Studies: V, The Variable Inversion in Cristobalite", *Journal of the American Ceramic Society,* 41 (12) 532-537.

63. Sato, M. (1963), "X-Ray Study Of Tridymite:(1): Tridymite M And Tridymite S", *Min. J. (Japan)* 4, 115-130.

64. Smith, J. V. and Steele, I.M. (1984), "Chemical Substitution in Silica Polymorphs", *Neues Jahrb Min. Mon.* 3, 137-144.

65. Schneider, H. (1986), " Chemical Composition of Tridymite and Cristobalite from Volcanic and Meteoritic Rocks", *Neues Jahrb Min. Mon.,* 10, 433-444.

66. Nukui, A., and Florke, O.W. (1987), "Three Tridymite Structural Modifications and Cristobalite Intergrown in One Crystal", *Am. Mineral.*, 72,167-169.

67. Carpenter, M.A. and Wennemer, M.(1985), "Characterisation of Synthetic Tridymites by Transmission Electron Microscopy", *Am. Mineral.*, 70, 517-528.

68. Ashworth, J.R. (1989), "Transmission Electron Microscopy of Coexisting Low-Tridymite Polymorphs", *Mineral. Mag.*, 53, 89-97.

69. Hill, V.G. and Roy, R. (1958), "Silica Structure Studies, VI, on Tridymite." *Trans. Br. Ceram. Soc.,* 57, 496-510.

70. Sato, M. (1964), "X-ray Studies of Tridymite: Unit Cell Dimensions and Phase Transition of Tridymite, Type S." *Mineral. J.* 4, 215-225.

71. Florke, O.W. and Langer, K.(1972), "Hydrothermal Recrystallisation and Transformation of Tridymite", *Contr. Mineral. Petrol.* 36, 221-230.

72. Hoffmann, W., Kockmeyer, M., Lons, J., Vach, Chr.(1983), "The Transformation of Monoclinic Low-Tridymite MC to a Phase with an Incommensurate Superstructure", *Fortsch. Mineral.*, 61, 96-98.

73. Graetsch, H. and Florke, O.W. (1991), "X-ray Powder Diffraction Patterns and Phase Relationship of Tridymite Modifications", *Z. Krist.*, 195, 31-48.

74. Hua, G. L., Welberry, T. R., Withers, R. L. and Thompson, J. G.(1988), " An Electron Diffraction and Lattice-Dynamical Study of the Diffuse Scattering in α -Cristobalite, SiO_2", *J. Appl. Cryst.,* 21, 458-465.

75. Florke, O.W.,(1955)" Structural Anomalies of Tridymite and Cristobalite, " *Ber. Dtsch. Keram. Ges.*, 32(12), 369.

76. Hill, V. G. and Roy, Rustum (1958), "Silica Structure Studies: V, The Variable Inversion in Cristobalite", *J. Am. Ceram. Soc.*, 41 (12) 532-537.

77. Hill, V.G. and Roy, R., (1958)," Silica Structure Studies: V, The Variable Inversion in Cristobalite, " *J. Am. Ceram. Soc.*, 41(12)532.

78. Sosman, R. B. (1965), *The phases of silica*, Rutgers Univ. Press, New Brunswick, NJ.

79. Phadke, A. V. and Kshirsagar, L.K. (1986) "Thermo-Analysis Of Low Cristobalite From Pune, Maharashtra, India: Paragenetic Significance". *Z. Geol. Wiss.* 14, 559-567.

80. Florke, O.W., (1957)" X-ray Mineral Analysis and Thermal Expansion Behavior of Cristobalite and Tridymine and the Composition of Silica Materials", *Ber.* , 34(11)343.

81. Wagstaff, F. E.(1968), "Crystallisation Kinetics of Internally Nucleated Vitreous Silica", *J. Am. Ceram. Soc.*, 51 (8) 449-452.

82. MacDowell, J.R., (1969)"Alpha- and Beta-Cristobalite Glass-Ceramic Articles and Methods," U.S. Pat. No. 3445 252, May 20.

83. Perrotta, A. J., Grubbs, D. K., Martin, E. S., Dando, N. R., Mckinstry, H. A. and Huang, C. Y.(1989), " Chemical Stabilization of -Cristobalite", *J. Am. Ceram. Soc.*, 72 (3) 441-447.

84. Saltzberg, M. A., Bors, S. L., Bergna, H. and Winchester, S. C.(1992), " Synthesis of Chemically Stabilized Cristobalite", *J. Am. Ceram. Soc.*, 75 (1) 89-95.

85. Florke, O.W., (1957)" X-ray Mineral Analysis and Thermal Expansion Behavior of Cristobalite and Tridymine and the Composition of Silica Materials", *Ber.* , 34(11)343.

86. Peacock, M. A.(1935), " On Wollastonite and Parawollastonite, *Am. J. Sci.*, 5(30) 495-529.

87. Smith, D. J., Jefferson , D. A. and Mallinson, L. G.(1981), "The Ultrastructure of Pyroxenoid Chain Silicates. II. Direct Structure Imaging of the Minerals Rhodonite and Wollastonite", *Acta Cryst.*, A37, 273-280.

88. Heller, L., Taylor, H. F. W. (1956), *Crystallographic Data for the Calcium Silicates*, London, Her Majesty's Stationary Office, P1-8.

89. Dornberger-Schiff, K.,Liebau, F. and Thilo, E., (1954), "Uber die Kristallstruktur des $(NaAsO_3)_x$ des Maddrellschen Salzes und des β-Wollastonite", *Naturwiss*, 41, 551.

90. Buerger, M.J. (1956), "The Arrangement of Atoms in Crystals of the Wollastonite Group of Metasilicates.", *Proc. N.A.S.* 42, 113-116.

91. Mamedov, Kh. S. and Belov, N. V.(1956), "Crystal Structure of Wollastonite (Kristallocheskaia Structura Vollastonta) ", *Dokl. Akad. Nauk SSSR*,107, 463-466.

92. Buerger, M. J. and Prewitt, C. T.(1961), "The Crystal Structures Of Wollastonite and Pectolite", *Proc. Nat. Acad.* Sci. *USA*, 47, 1884-1888.

93. Barnick, A.W.,(1936)"Strukturuntersuchung des Naturlichen Wollastonits", Mitt. Kaiser-Wilhelm-Inst. *Silikatforsch.* No. 172; abstracted in *Strukturbericht,* 4, 207-209.

94. Ito, T.(1950), *X-ray Studies on Polymorphism*, Maruzen, Tokyo, 93-110,

95. Trojer, F. J.(1968), "The Crystal Structure of Parawollastonite", *Z. Krist.,* 127, 291-308.

96. Wenk, H. -R. (1969), "Polytypism of Wollastonite", *Contr. Mineral. and Petrol.,* 22, 238-247.

97. Jeffery, J.W. and Heller, L.(1953), "Preliminary X-ray Investigation of Pseudowollastonite", *Acta Crystallography,* 6, 807-808.

98. Hutchison, J. L. and Mclaren, A.C. (1977) "Stacking Disorder in Wollastonite and Its Relationship to Twinning and the Structure of Parawollastonite", *Contr. Min. Petr.*, 61, 11-13.

99. Jefferson, D. A. and Bowen, N.L.(1973), "Polytypism and Stacking Disorder", *Nature Phys. Sci.,* 245, 43-44.

100. Wenk, H. -R., Müller, W. F., Liddell, N. A. and Phakey, P. P., Electron Microscopy in Mineralogy, Chapter 5.5: *Polytypism in Wollastonite.*

101. Hutchison, J. L. and McLaren, A.C., (1976) "Two-dimensional Lattice images of stacking disorder in wollastonite". *Contr. Min. Petr.*, 55, 303-309.

102. Liebau, F., "Zur Kristallchemie der Silikate, Germanate und Fluoberyllate des Formeltype ABX_3", *Neues Jahrb. Mineral.*, 94, 1209, 296.

103. Hilmer, W., (1958), Zur Struktur Bestimmungen Non Stronticsmgermanat. *Naturwiss*, 95, 238.

104. Yamanaka, T. and Mori, H.(1984), " The Structure and Polytypes of β-$CaSiO_3$ (Pseudowollastonite)", *Acta Cryst.*, B37, 1010-1017.

105. Allen, E. T., White, W. P. and Wright, F. E. (1906), " On Wollastonite and Pseudowollastonite-Polymorphic Forms of Calcium Metasilicate", *Am. J. Sci.*, (4th series), 21, 89-108.

106. Buckner, D.A. and Roy, R.(1960), "Note on a Subsolidus Study of the System $CaSiO_3$-$SrSiO_3$", *J. Am. Ceram. Soc.*, 43(1), 52-53.

107. Warren, B.E. and Biscoe, J., (1931), " The Crystal Structure of the Monoclinic Pyroxenes", *Zeit. Krist.*, Vol.80, 391.

108. Day, A.L. and Sosman, R.B., " The Nitrogen Thermometer from Zinc to Palladium", *Am. J. Sci.* 4th Series, 39, 93, 2910.

109. Adams, L.H. (1914)" Calibration Table for Copper-constantan and Platinum-Platinrhodium Thermoelements", *J. Am. Chem. SoC.*, 36, 65.

110. Aikawa, N. (1979), "Oriented Intergrowth of Rhodonite and Pyroxmangite and Their Transformation Mechanism", *Mineral. J. Jpn*, 9, 255-269.

111. Jefferson, D. A., Pugh, N. J., Alario-Franco, M., Mallinson, L. G., Millward, G. R. and Thomas, J. M., (1980), "The Ultrastructure Of Pyroxenoid Chain Silicates, 1. Variation Of The Chain Configuration In Rhodonite", *Acta Cryst.* A36, 1058-1065.

112. Liebau, F. (1972), *Handbook of Geochemistry*, Vol. II, Ch. 14. Berlin:Springer-Verlag.

113. Ohashi, Y. and Finger, L. W. (1975) "Stepwise Cation Ordering in Bustamite and Disordering in Wollastonite", *Ann. Rep. Carnegie Inst. Washington*, 74, 564-569.

114. Rutstein, M. S. and White, W. B.(1971) "Vibrational Spectra of High-Calcium Pyroxene and Pyroxeoids", *Amer. Min.*, 56, 877-887.

115. Peacock, D. R. and Prewitt, C. T. (1963), "Comparison of the Crystal Structures of Bustamite and Wollastonite", *Am. Mineral.* 48, 589-596.

116. Ohashi, Y. and Finger, L. W.,(1976) "Stepwise Cation Ordering in Bustamite and Disordering In Wollastonite", *Carnegie Inst. Washington, Ann. Rept. Dir. Geophys. Lab.*, 1975-76, 746-753.

117. Shinno, I. (1970) "A Consideration on the Crystallisation Process of Diopside", *Jnl. Jap. Assoc. Miner. Petrol. Econ. Geol.*, 63, 4146-159.

118. Shinno, I. (1974), "Unit Cell Dimensions and Infrared Absorption Spectra of Mg-Wollastonite in the System $CaSiO_3$-$CaMgSi_2O_6$", *Miner. J.*, 7(5) 456-471.

119. Costantini, A., Branda, F. and Buri, A.(1995), "Thermal Properties and Devitrification Behaviour of (1+x)CaO·(1-x)MgO·2SiO_2 Glasses", *J. Mater. Sci.* 30, 1561-1564.

120. Gutzow, I. And Schmelzer, J., *The Vitreous State, Thermodynamics, Structure, Rheology and Crystallisation*, Springer, 1995, P3.

121. Strawbridge, I., "Glass Formation by the Sol-Gel Process", *Chemistry of Glasses*, Editor: Paul, A., p51-85.

122. Kingery, W.D., Bowen, H.K., Uhlmann, D.R. (1972), *Introduction to Ceramics*, John Wiley And Sons, P95-98,

123. Mazurin, O. V. and Porai-Koshits (1984), *Phase Separation in Glass*, Elsecier Science publishers B. V.

124. Hammel, J.J.(1971), "Nucleation in Glass- a Review", *Advances in Nuleation and Crystallisation in Glasses,* Edited by Hench, L. l.and Freiman, S.W., The American Ceramic Society, Ohio, P1-9.

125. Porai-Koshits, E. A., Ed. *The Structure of Glass*, Vol. 8, Consultants Bureau, New York, 1973.

126. Charles, R. J. (1973), "Immiscibilty and its Role in Glass Processing", *Am. Ceram. Soc. Bull.* 52(9), 673-680.

127. Zarzycki, J., "Phase-Separated Systems", *Discuss. Faraday Soc.*, 50(1970)122-34.

128. [1]James, P. F. (1975), "Review: Liquid-Phase Separation in Glass-Forming Systems", *J. Mater. Sci.*, 10, 1802-1825.

129. Uhlmann, D. R. and Kolbeck, A. G.(1976), "Phase Separation and the Revolution in Concepts of Glass Structure", *Phys. Chem. Glasses,* 17(5)146-58.

130. Vogel, W. (1985), "6, Microphase Separation", in *Chemistry of Glass, Translated by Kreidl, N.* p69-95.

131. Seward III, T. P., "Mestable Phase Diagrams and Their Application to Glass-Forming Ceramic Systems", in *Phase Diagrams: matrials Science & Technology,* edited by Allen M. Alper, Vol.1: Theory, Principles, and Techniques of Phase Diagrams, 1970, 295-338.

132. Cahn, J.W.(1968), "Spinodal Decomposition", *Trans. of the Metallurgical Society of AIME,* 242, 166-80.

133. Cahn, J.W. and Charles, R.J.(1965), "The Initial Stages of Phase Separation in Glasses", *Phys. Chem. Glasses,* 6(5), 181-191.

134. Haller, W.(1965), "Rearrangement Kinetics of The Liquid-Liquid Immiscible Microphases In Alkaliborosilicate Melts", *J. Chem. Phy.* 42, 686-693.

135. Seward III, T. P., Uhlmann, D. R. and Turnbull, D.(1967), "Phase Separation in the System BaO-SiO2", *J. Am. Ceram. Soc.,* 51 (5) 278-285.

136. Macdowell, J. F. and Beall (1969), "Immiscibility and Crystallisation in Al_2O_3-SiO_2 Glasses", *J. Am. ceram. Soc.,* 52(1)17-25.

137. Mazurin, O. V., Roscova, G. P. and Averjanov, V. I. (1975), Fiz. Khim. Stekla 1110.

138. Haller, W., and Macedo, P. B. (1968), "The Origin of Phase Connectivity In Microheterogeneous Glasses", *Phys. Chem. Glasses.* 9. 153

139. Roscova, G. P., (1975), Influence of Heat treatment Conditions on the Structure and Properties of Phase -Separated Sodium Silicate Glasses, Avtoreferat Kandidat. Diss. Inst. Khimii Silikatov, Leningrad.

140. Porai-koshits, E.A., and Averjanov, V. I. (1969), "Primary and Secondary Phase Separation of Sodium Silicate Glasses", *J. Non-cryst. Solids,* 1. 29.

141. Advances in Ceramics, Vol.4, Nucleation and Crystallisation in Glasses, Editor: J.H.Simmons, D.R.Uhlmann and G.H. Beall, Washington D.C., 1982.

142. Advances in Glasses, Proceedings of VI Int. Congress on Glass, Editor: Frederick, R. Matson and Guy E. Rindone, 1963, Plenum Press.

143. 10th Int. Congress on Glasses, Editor: M. Kunugi, M. Tashiro and N. Saga, Kyoto, 1974.

144. XIVth Int. Congress on Glass, Insdoc, New Delhi, 1986.

145. Xvth Int. Congress on Glass, Editor: O.V. Mazurin, Leningrad, 1989.

146. XVIth Int. Congress on Glass, Editor: S.E. de Ceramica Vidrio, Industrias Graficas CARO, 1992.

147. Uhlmann, D. R., (1977) "Glass Formation", *J. Non-cryst. Solids*, 25, 43-85.

148. Gutzow, I., Toschev, S., Marinov, M. and Popov, E., "Non-Steady State Nucleation and Mechanism of Crystal Growth in a Model Glass" *Krist. Tech.* 3(1968)337-54.

149. Bergeron, C.G., (1972), "General Aspects of the Crystallisation of Glass", Introduction to Glass Science, Editors: Pye, L.D., Stevens, H.J. and LaCourse, W.C.,P173-196.

150. Gutzow, I. And Schmelzer, J., The Vitreous State, Thermodynamics, Structure, Rheology and Crystallisation, Springer, 1995.

151. Kingery, W.D., Bowen, H.K., Uhlmann, D.R.(1972), *Introduction to Ceramics*, John Wiley and Sons.

152. Philips, B. and Roy, R.(1964), "Controlled Phase Separation due to Metastable Liquid Immiscibility in Simple silicate systems", *Phys. Chem Galsses* 5(6), 172-175.

153. Manufacturer's data

154. Materials Safety Data Sheet, Morgan Thermal Ceramics, 1993.

155. Cullity, B. D., Elements of X-ray Diffraction, Addison-Wesley, Reading, MA, 2nd edn., 1978.

156. Klug, H. P. and Alexander, L. E., X-ray Diffraction Procedures, Wiley, New York, 2nd Edn., 1974.

157. Sawyer, L. C. and Grubb, D. T. (1987) *Polymer Microscopy*, Chapman and Hall, London, 85-95.

158. Thomas, G. (1962) *Transmission Electron Microscopy of Metals*, Wiley, New York, 182.

159. Swab, P. and Linger, R. E. (1988), " Preparation of Multilayer Optical Coatings for TEM Cross-Sectional Microanalysis by Ultramicrotomy". *Mat. Res. Soc. Symp. Proc.* 115, 229-234.

160. Howell, D.A., Heckman, J.W. & Crimp, M.A. (1995), " Prepration 0f Metal Multilayer TEM Cross-Sections Using Ultramicrotomy". *J. Micros.* 180, 182-185.

161. Chowdhury, A.J.S., Freundlich, A. and Sheppard, T. (1990) , "The Role of Ultramicrotomy in the Microstructural Studies of Rapidly Solidified Aluminium Alloy Powders". *Mat. Res. Soc. Symp. Proc.* 199, 181-188.

162. Ulan, J. G., Schooley, C. and Gronsky, R. (1990), " Microtomy of Large Particle Zeolites for TEM". *Mat. Res. Soc. Symp. Proc.* 199, 153-156.

163. Bradley, S.A., Dietz, N.L. and Karakek, K.R. (1988), " Sample Preparation Technique for Examination of Sic Whisker Cross Sections". *Mat. Res. Soc. Symp. Proc.* 115, 115-118.

164. Reid, N. Ultramicrotomy, *Practical methods in Electron Microscopy*, vol 3, A. M. Glauert, ed (Elsevier, Amsterdam, 1974).

165. Swab, P. and Linger, R. E. (1988) , "Preparation of Multilayer Optical Coatings for TEM Cross-Sectional Microanalysis by Ultramicrotomy". *Mat. Res. Soc. Symp. Proc.* 115, 229-234.

166. Peachey, L.D. (1958) , "Thin Sections, I. A Study of Section Thickness and Physical Distoration Produced During Microtomy". *J. Biophys. Biochem. Cytol.* 4, 233.

167. Golukov, V.V.(1991), "Structure and Structural Transitions in Vitreous Silica", *Fiz. Khim. Stekla*, 18,, 1, 57-59.

Table 2-1 Diameter Distributions of Fibres

	Mean	Median	100%<	%>5μm	%<1μm
Run1	5.1μm	3.4μm	30μm	33%	13%
Run 2	4.1μm	2.7μm	25μm	25%	19%

Table 2-2 Modifications of $CaSiO_3$

	Wollastonite-2M[51]	Wollastonite-Tc[45]	Pseudowollastonite[55]
Nomenclature	Parawollastonite	Wollastonite	Pseudowollastonite
Stability	Low-temperature Form	Low-temperature Form	High-temperature Form
Structure	Monoclinic	Triclinic	Triclinic
a(Å)	15.43	7.94	6.853
b(Å)	7.32	7.32	11.895
c (Å)	7.07	7.07	19.674
α	90°	90°02'	90.12°
β	95°24'	95°22'	90.55°
γ	90°	103°26'	90.55°

Table 3-1 Compositions of Fibres Studied (mass%)

mass%%	SiO_2	CaO	MgO	Al_2O_3	Fe_2O_3
Superwool	67.49	26.03	5.43	0.33	0.25
A2	61.97	21.67	15.16	0.76	0.13
B3	60.16	35.20	3.72	0.62	0.15

Table 3-2 Crystallographic Data for Cristobalite

Name	JCPDS No.	Crystall. system	d-spacing (Å)	2 θ (°)	Intensity %	Plane
α-cristobalite	39-1425	Tetragonal	4.04	21.985	100	101
			3.136	28.44	8	111
			2.841	31.465	9	102
			2.487	36.085	13	200
β-cristobalite	27-605	Cubic	4.11	21.6053	100	111
			2.518	35.6278	12	220

Table 3-3 Crystallographic Data of Parawollastonite and Wollastonite

Name	JCPDS Card No.	Crystall. system	d-spacing (Å)	2 θ (°)	Int.%	Plane
Wollastonite-2M	10-489	Monoclinic	3.83	23.15	80	400
			3.52	25.305	80	002
			3.31	26.85	80	$\bar{2}02$
			3.09	28.87	30	202
			2.97	29.99	100	320
			2.80	31.97	10	$\bar{3}12$
Wollastonite-	27-88	Monoclinic	3.839	23.15	18	400
			3.517	25.305	23	002
			3.318	26.85	29.1	$\bar{2}02$
			3.158	28.235	11	$\bar{1}12$
			3.09	28.87	22	202
			3.022	29.535	9	$\bar{2}12$
			2.977	29.99	100	320
Wollastonite-1A	29-372	Triclinic	3.838	23.1569	60	200
			3.510	25.3552	70	$\bar{2}01$
			3.312	26.8987	80	$\bar{1}02$
			3.228	27.6123	40	$0\bar{2}1$
			3.195	27.9032	40	$2\bar{1}1$
			3.167	28.1550	40	021
			3.08	28.9674	70	102
			2.976	30.0031	100	$\bar{2}20$

Table 3-4 Crystallographic Data of Quartz, Tridymite, Diopside and Pseudowollastonite

	JCPDS	Cryst.	d-spacing	2 θ	Int. %	Plane
α-Quartz	33-1161	Hexagonal	4.257	20.850	22	100
			3.342	26.65	100	101
Tridymite-O	42-1401	Orthorhombic	4.28	20.735	93	220
			4.08	21.765	100	004
			3.800	23.39	68	222
			3.242	27.49	48	420
			2.961	30.16	11	224
			2.852	31.34	9	600
Pseudo-wollastonite	31-300	Triclinic	3.282	27.15	50	006
			3.235	27.55	100	112
			3.219	27.69	100	$\bar{1}22$
			2.816	31.75	70	$2\bar{2}2$
			2.798	31.96	60	114
Diopside	11-654	Monoclinic	3.35	26.585	11	021
			3.23	27.595	25	$\bar{2}20$
			2.991	29.85	100	$\bar{2}21$
			2.893	30.885	30	$\bar{3}11$

Table 4-1 Comparison of Parameters of Wollastonites

	wollastonite-2M	wollastonite 1 by XRD	wollastonite 1 by EM	wollastonite 2 by XRD	wollastonite 2 by EM
a(Å)	15.426	15.177	15.206	15.337	15.337
b(Å)	7.32	7.207	7.170	7.284	7.210
c(Å)	7.066	6.937	6.891	7.031	7.022
β(°)	95.4	95.46	95.46	95.29	95.31

Table 4-2 Diffraction Data of Wollastonites

Woll-2M		Woll.1		Woll.2			
2θ(°)	d(Å)	2θ(°)	d(Å) ±0.001	2θ(°)	d(Å) ±0.001	Int.%	h k l
11.515	7.679	11.705	7.554	11.58	7.636	10	2 0 0
16.255	5.449	16.535	5.357	16.355	5.415	2	-2 0 1
18.775	4.723	19.11	4.641	18.865	4.700	2	1 1 1
20.3	4.371	20.645	4.299	20.42	4.346	6	-2 1 1
21.16	4.195	21.51	4.128	21.275	4.173	3	3 1 0
23.15	3.839	23.535	3.777	23.28	3.818	18	4 0 0
23.825	3.732	24.22	3.672	23.97	3.710	8	-3 1 1
25.305	3.517	25.78	3.453	25.425	3.500	23	0 0 2
26.19	3.400	26.625	3.345	26.335	3.382	5	4 1 0
26.85	3.318	27.335	3.260	27.005	3.299	29	-2 0 2
27.475	3.244	27.96	3.189	27.605	3.229	2	4 0 1
27.815	3.205	28.275	3.154	27.96	3.188	3	-1 2 1
28.235	3.158	28.75	3.103	28.385	3.142	11	-1 1 2
28.87	3.090	29.425	3.033	29	3.076	22	2 0 2
29.535	3.022	30.065	2.970	29.705	3.005	9	-2 1 2
29.99	2.977	30.48	2.930	30.15	2.962	100	3 2 0
31.565	2.832	32.095	2.787	31.74	2.817	3	-5 1 0
31.97	2.797	32.495	2.753	32.15	2.782	6	-3 2 1
32.855	2.724	33.425	2.679	33.06	2.707	5	-4 0 2

to be continued

Table 4-2

Woll-2M		Woll.1		Woll.2			
2θ(°)	d(Å)	2θ(°)	d(Å) ±0.001	2θ(°)	d(Å) ±0.001	Int.%	h k l
35.025	2.560	35.625	2.518	35.23	2.545	5	6 0 0
35.135	2.552	35.76	2.509	35.315	2.539	5	5 1 1
35.45	2.530	36.08	2.487	35.645	2.517	3	-1 2 2
36.265	2.475	36.915	2.433	36.44	2.464	15	1 2 2
38.22	2.353	38.865	2.315	38.435	2.340	9	-5 2 0
38.355	2.345	39.1	2.302	38.55	2.334	8	0 0 3
38.505	2.336	39.2	2.296	38.71	2.324	7	6 0 1
39.065	2.304	39.805	2.263	39.285	2.292	11	-2 0 3
40.72	2.214	41.47	2.176	40.925	2.204	3	3 2 2
41.305	2.184	42.02	2.149	41.51	2.174	16	5 2 1
41.605	2.169	42.33	2.134	41.88	2.155	3	-6 0 2
44.74	2.024	45.515	1.991	45.015	2.012	5	-5 2 2
45.725	1.983	46.585	1.948	45.94	1.974	4	6 0 2
47.315	1.920	48.145	1.889	47.6	1.909	2	8 0 0
48.01	1.894	48.895	1.861	48.24	1.885	2	5 2 2
48.33	1.882	49.17	1.852	48.61	1.872	4	7 2 0
49.055	1.856	49.905	1.826	49.36	1.845	4	-7 2 1
49.785	1.830	50.625	1.802	50.05	1.821	15	0 4 0
50.15	1.818	51.03	1.788	50.45	1.808	3	-4 3 2
50.4	1.809	51.315	1.779	50.67	1.800	2	8 0 1
50.825	1.795	51.805	1.763	51.07	1.787	4	3 2 3

to be continued

Table 4-2

Woll-2M		Woll.1		Woll.2			
2θ(°)	d(Å)	2θ(°)	d(Å) ±0.001	2θ(°)	d(Å) ±0.001	Int.%	h k l
51.95	1.759	53	1.726	52.225	1.750	6	0 0 4
52.215	1.751	53.25	1.719	52.51	1.741	4	-2 0 4
53.07	1.724	54.045	1.695	53.41	1.714	10	-5 2 3
53.28	1.718	54.225	1.690	53.63	1.708	10	-7 2 2
56.655	1.623	57.665	1.597	56.96	1.615	3	0 4 2
57.315	1.606	58.4	1.579	57.61	1.599	6	7 2 2
57.46	1.603	58.485	1.577	57.79	1.594	8	-2 4 2
58.58	1.575	59.64	1.549	58.89	1.567	2	2 4 2
59.52	1.552	60.68	1.525	59.875	1.544	2	-3 2 4
60.1	1.538	61.18	1.514	60.49	1.529	2	-9 2 1
60.21	1.536	61.31	1.511	60.58	1.527	3	10 0 0
60.5	1.529	61.62	1.504	60.91	1.520	2	-7 2 3
60.94	1.519	62.035	1.495	61.3	1.511	2	-4 4 2
62.32	1.489	63.435	1.465	62.685	1.481	2	6 4 0
62.765	1.479	64.045	1.453	63.08	1.473	5	3 2 4
63.085	1.473	64.26	1.448	63.42	1.466	3	4 4 2
63.565	1.463	64.73	1.439	64	1.454	2	-9 2 2
63.75	1.459	64.925	1.435	64.2	1.450	4	-10 0 2
65.035	1.433	66.255	1.410	65.415	1.426	2	-2 4 3
68.93	1.361	70.295	1.338	69.305	1.355	4	10 0 2

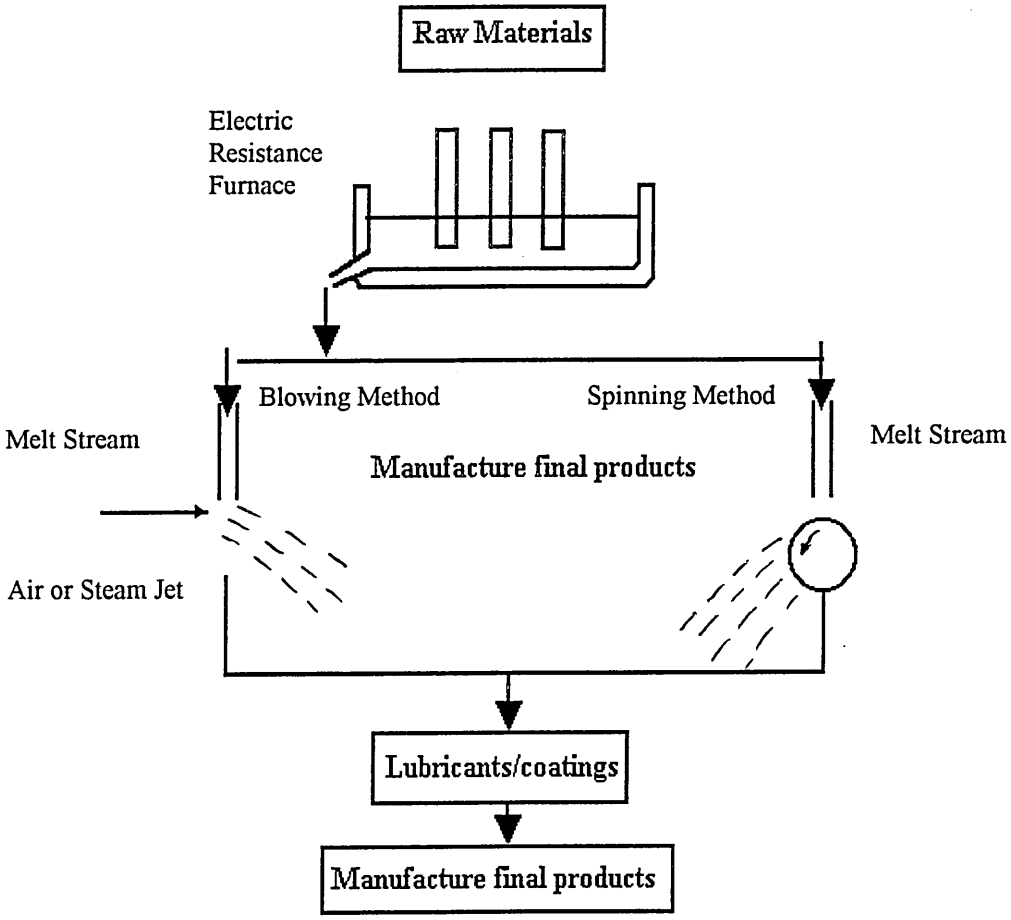

Figure 2- 1 Diagram illustrating manufacturing process for ceramic fibre[1].

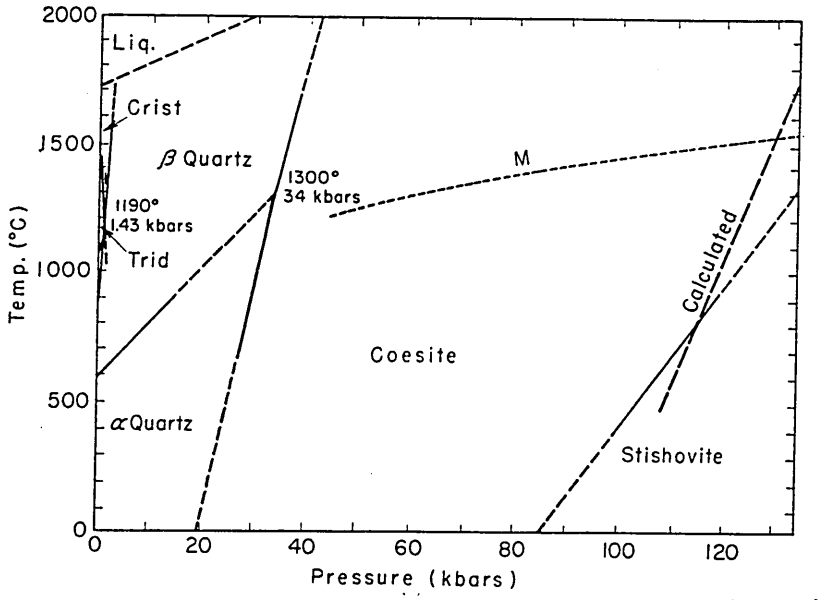

Figure 2- 2 Phase diagram of the silica system[29].

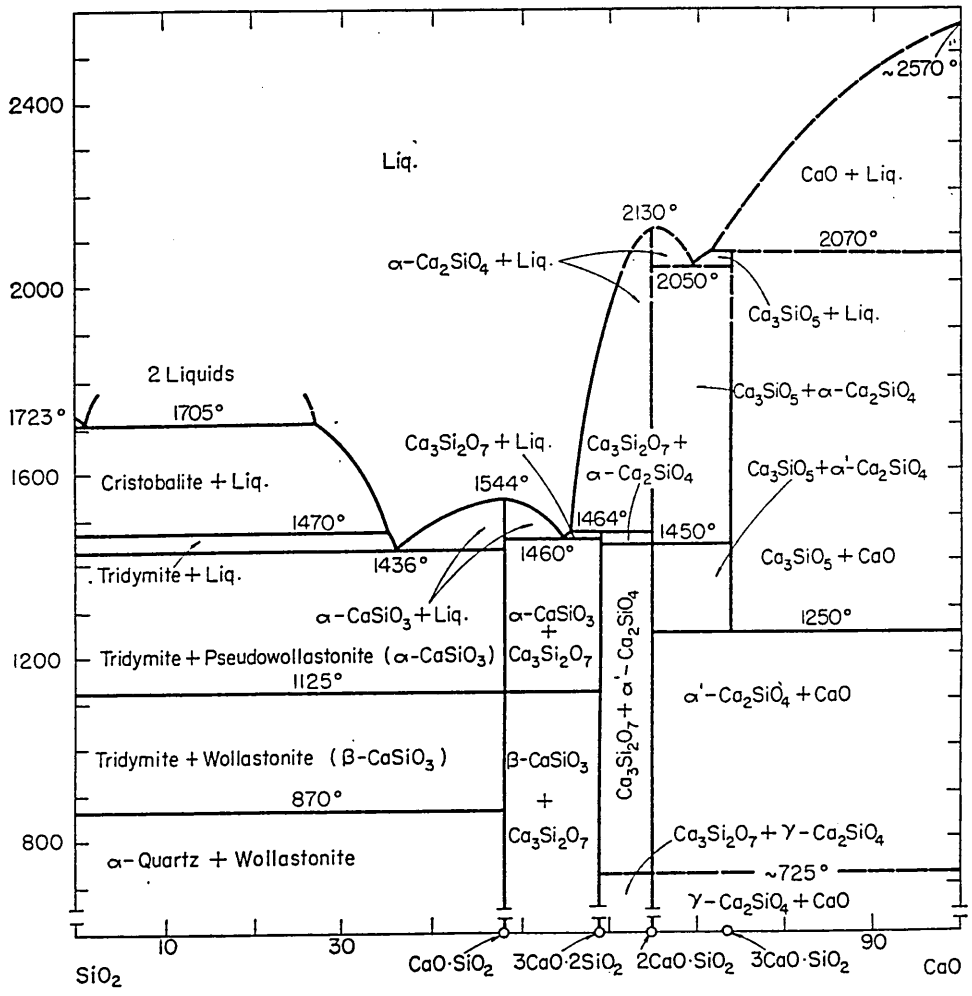

Figure 2- 3 Phase diagram of $CaO-SiO_2$ system[30].

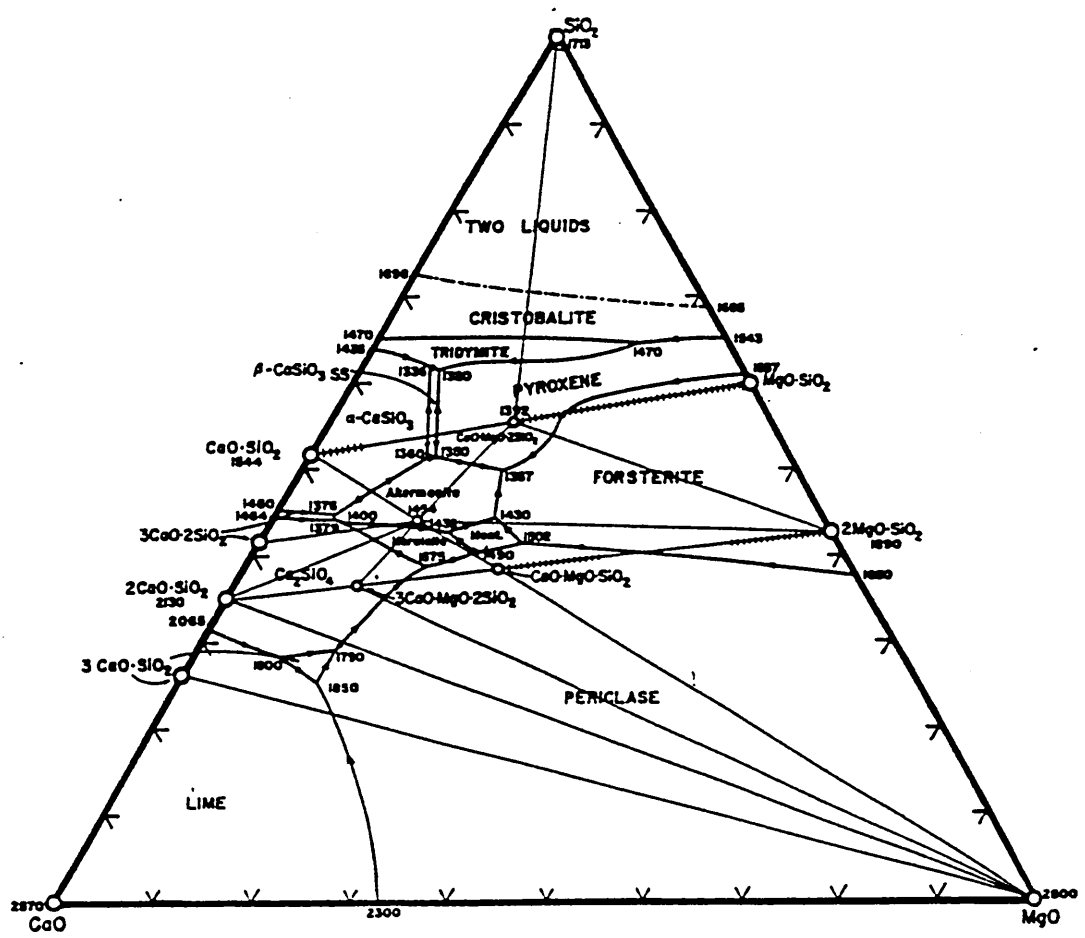

Figure 2- 4 Phase diagram of the system CaO-MgO-SiO_2[36, 40].

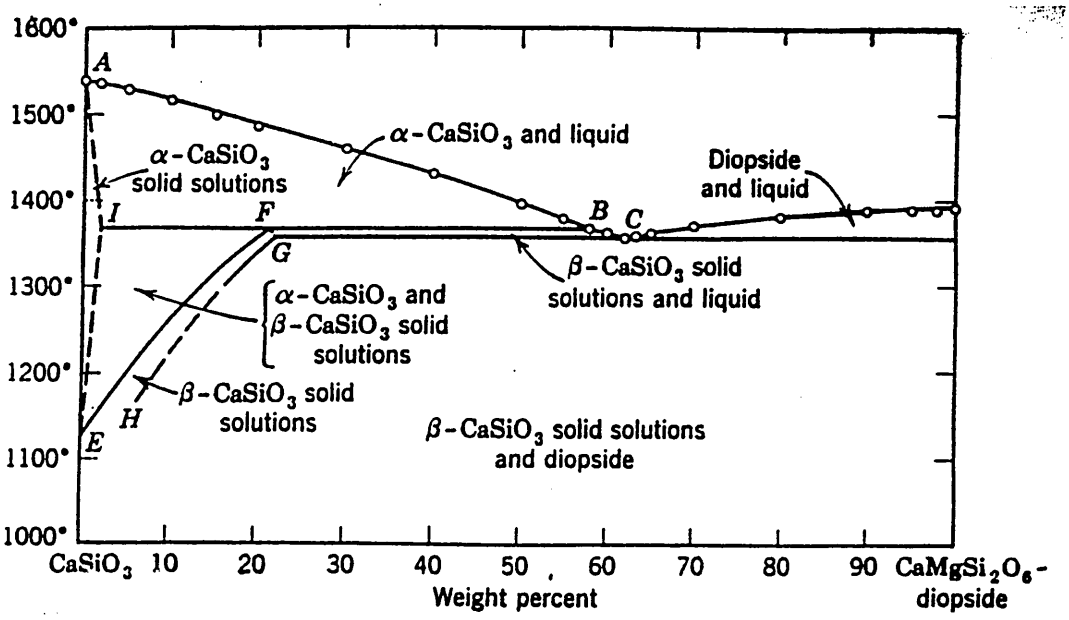

Figure 2- 5 Phase diagram of the binary system $CaSiO_3$-$CaMgSi_2O_6$[37].

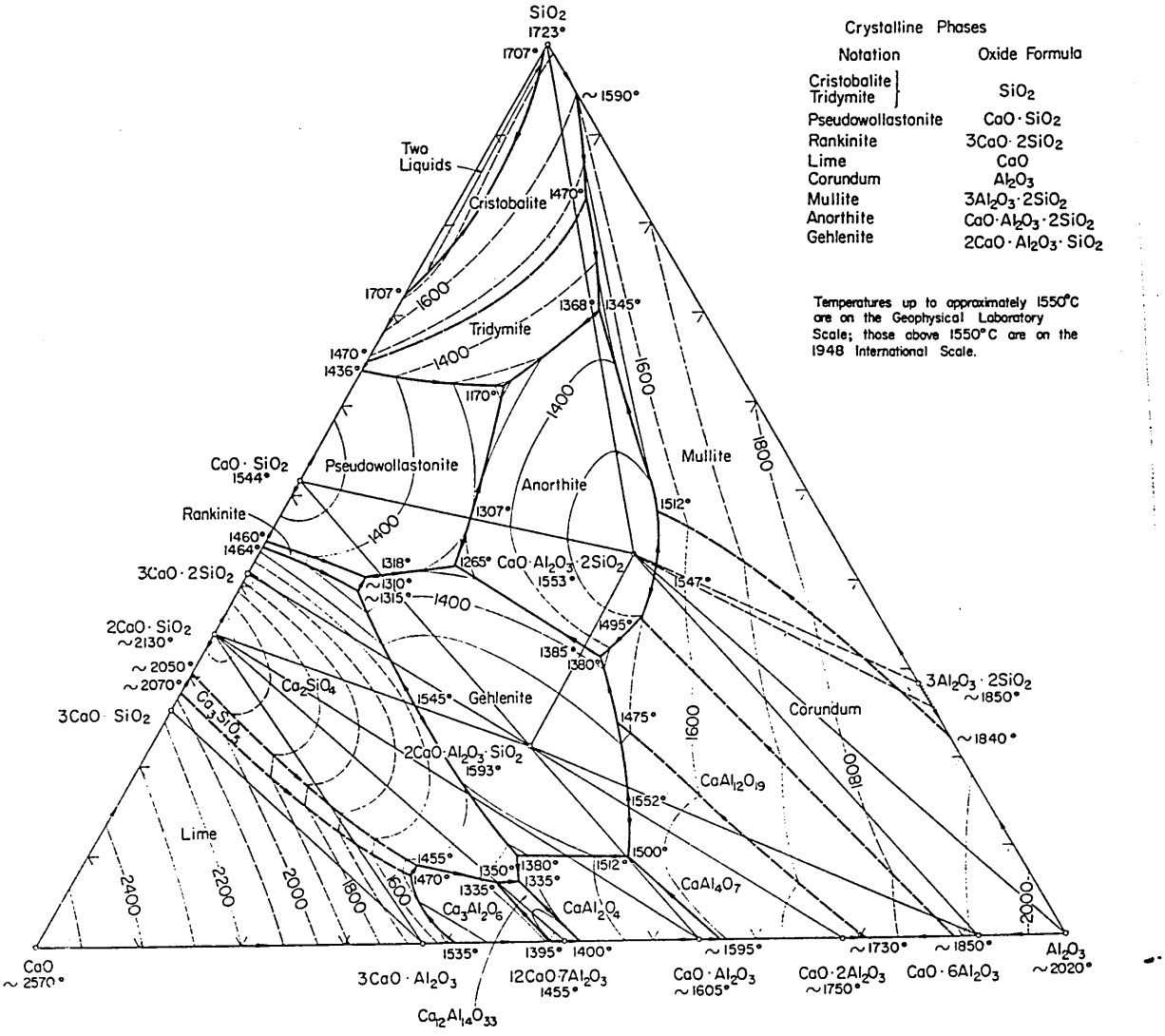

Figure 2- 6 Phase diagram of the system $CaO-Al_2O_3-SiO_2$[31].

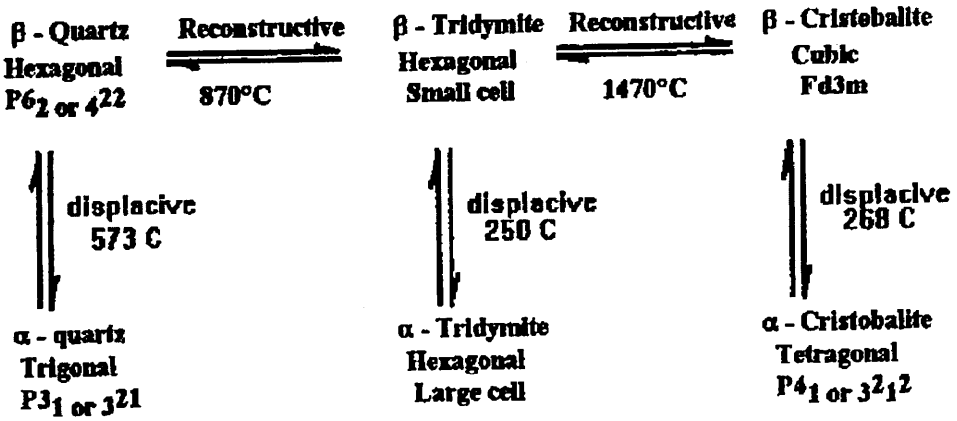

Figure 2- 7 Modifications of silica[43]

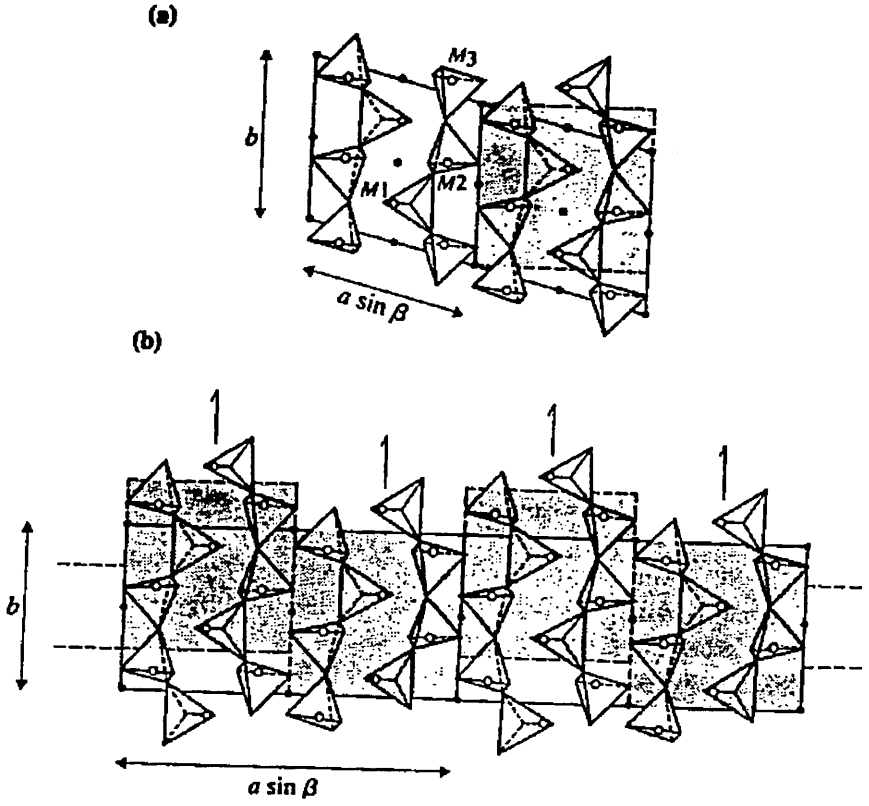

Figure 2-8 a. Project of the structure of wollastonite-Tc along Z axis. Shaded area has paeudomonoclinic symmetry; b. Stacking of pseudomonoclinic units with ±b/4 displcements to produce the structure of wollastonite-2M[93].

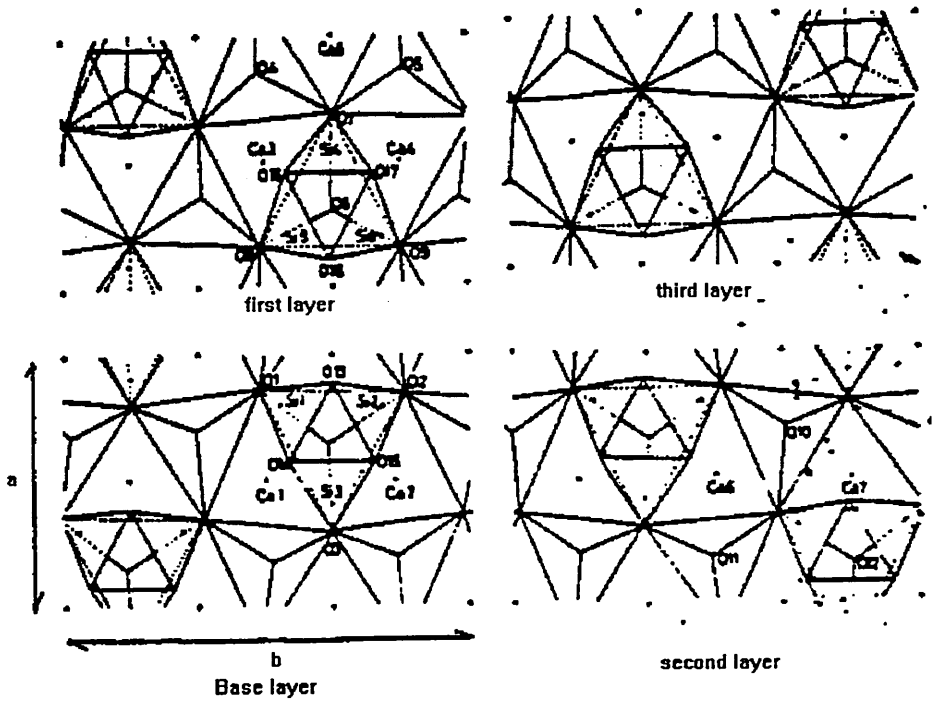

Figure 2-9 Projection of the four-layer type of psudowollastonite[106].

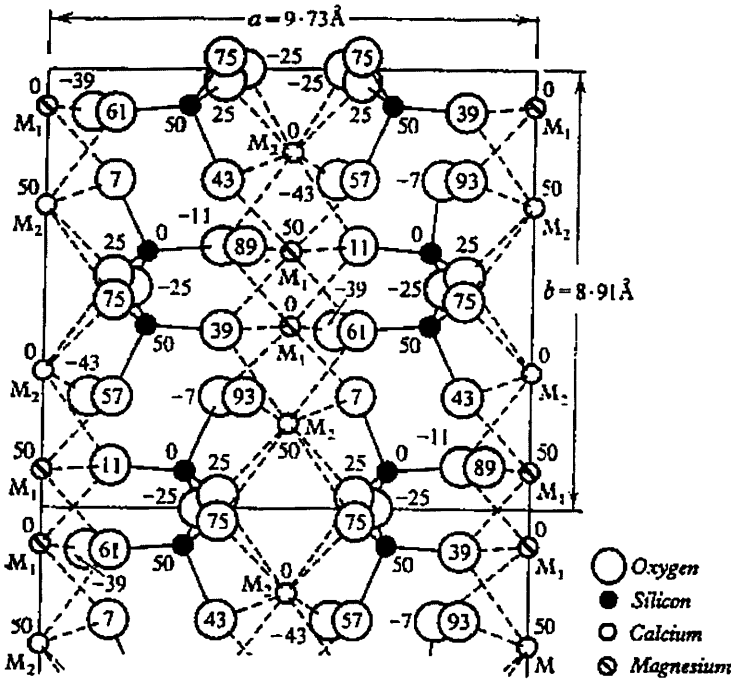

a

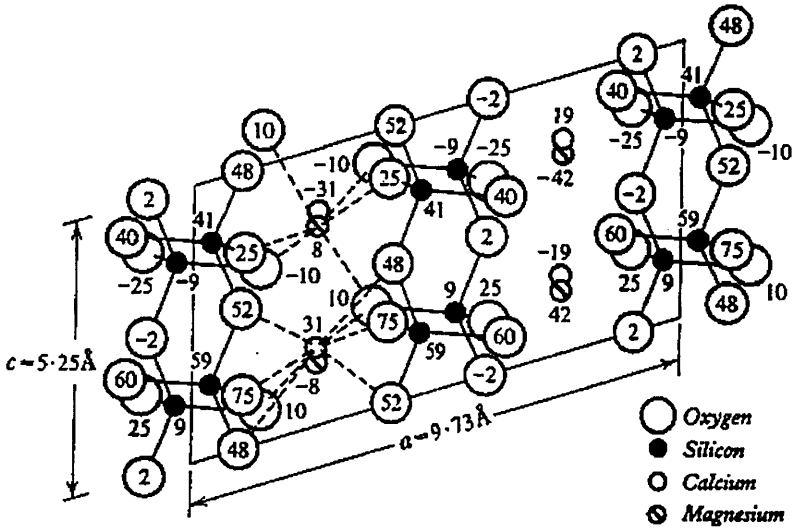

b

Figure 2-10 Structure of diopside. a. as viewed along the Z direction. atoms overlying one another have been slightly displaced; b. as viewed along the Y direction[109].

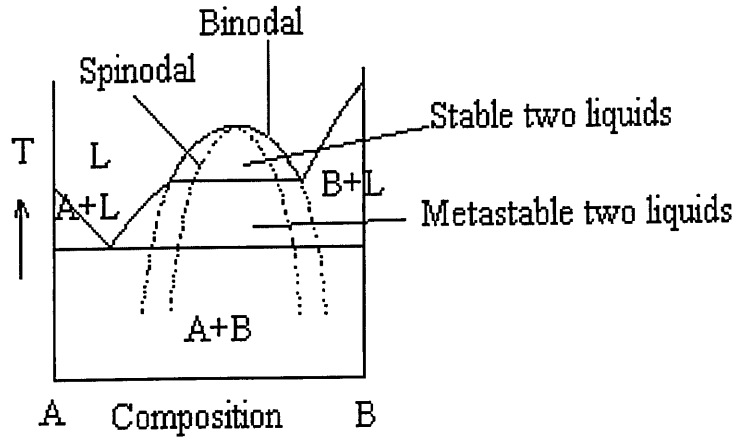

Figure 2- 11 Schematic binary phase diagrams showing both stable and metastable immiscibility[131].

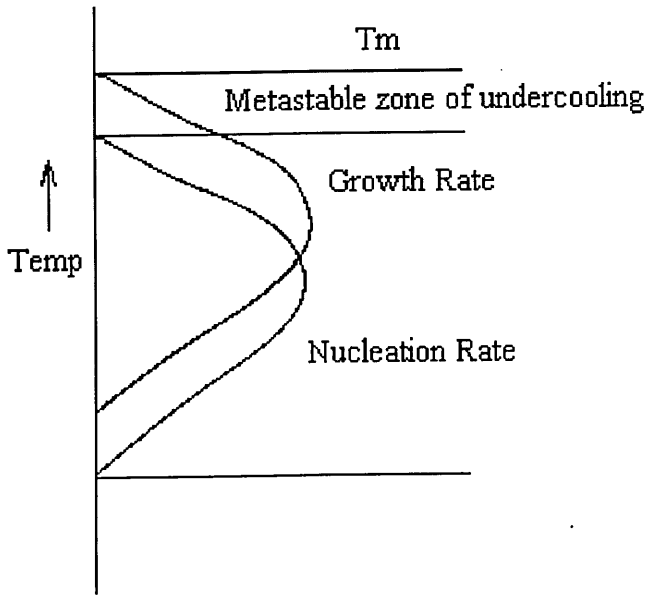

Figure 2-12 Schematic variation with temperature of homogeneous nucleation rate and growth rate.

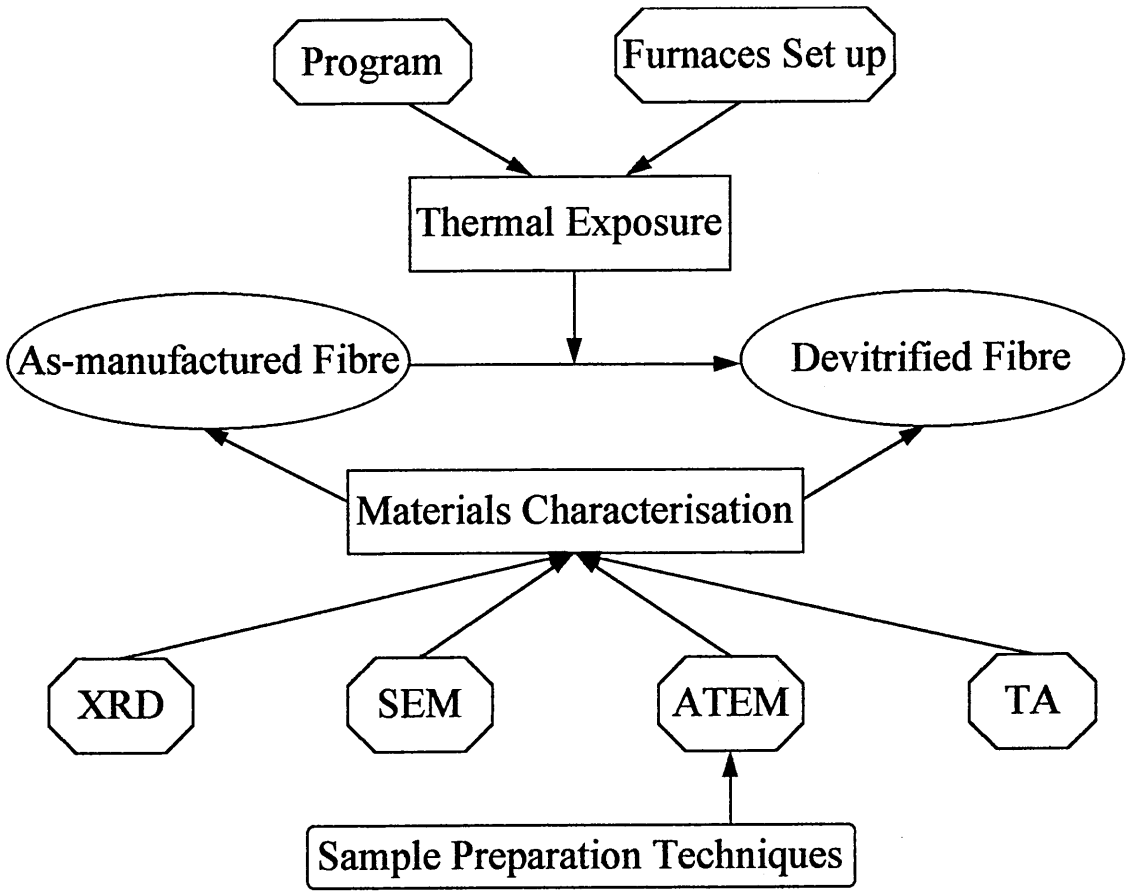

Figure 3-1 Experimental program

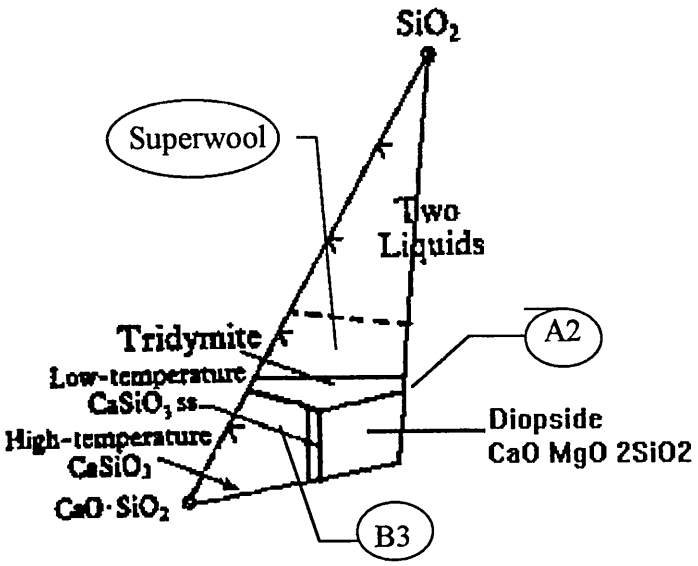

Figure 3-2 Phase diagram showing compositions of the fibres.

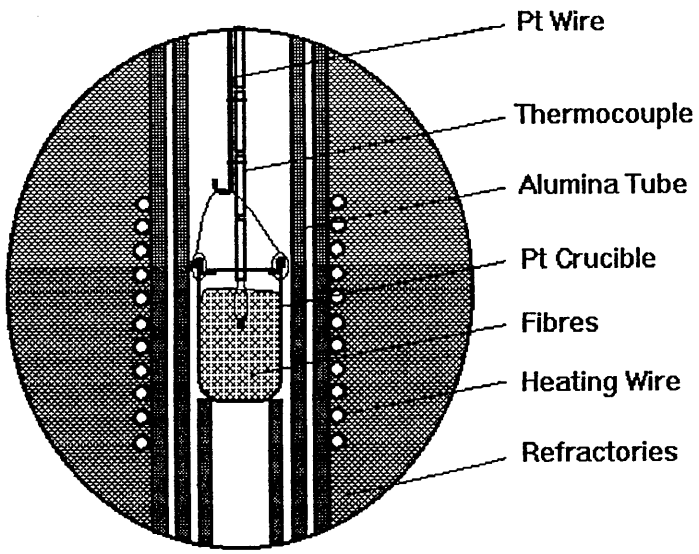

Figure 3-3 Design of the short term exposure furnace.

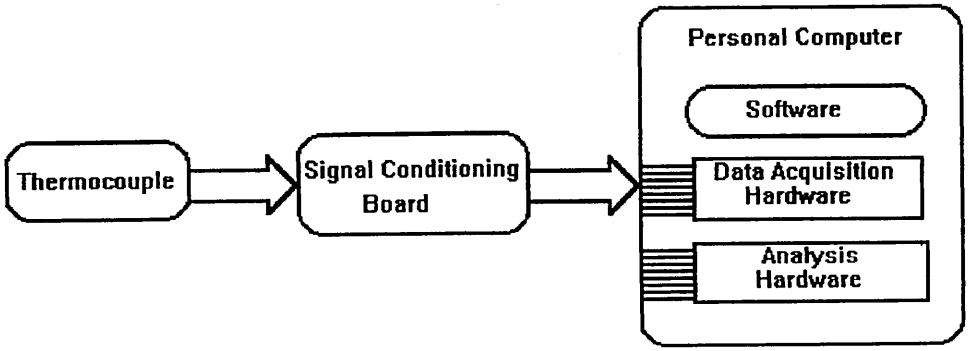

Figure 3-4 A PC-based temperature data acquisition system.

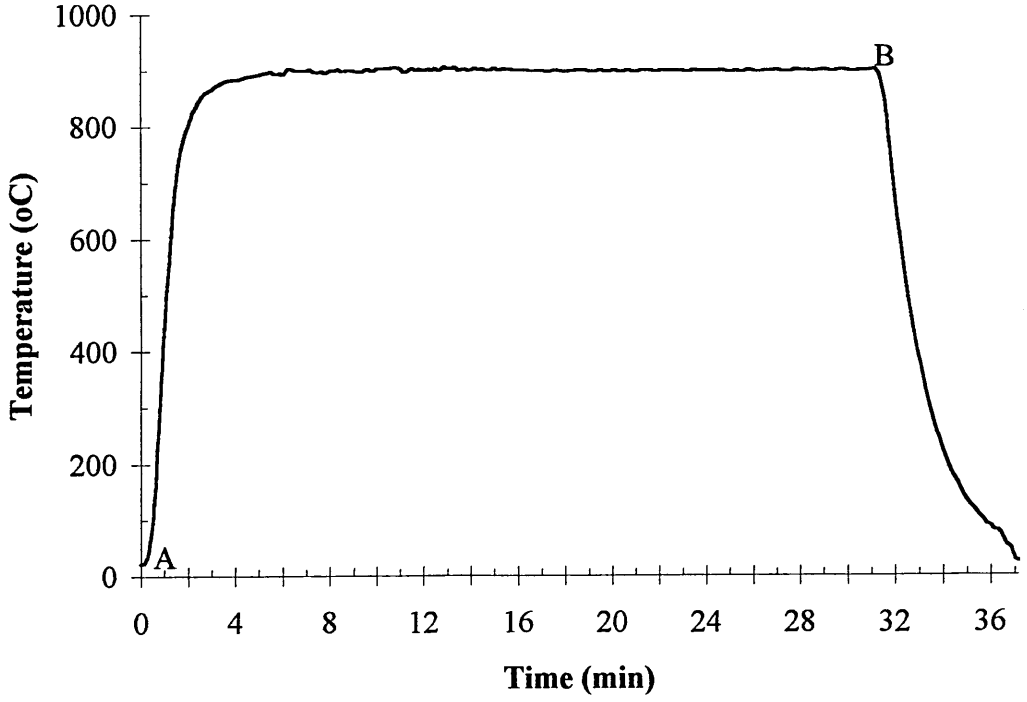

Figure 3- 5 Typical temperature-time trace of thermal exposure.

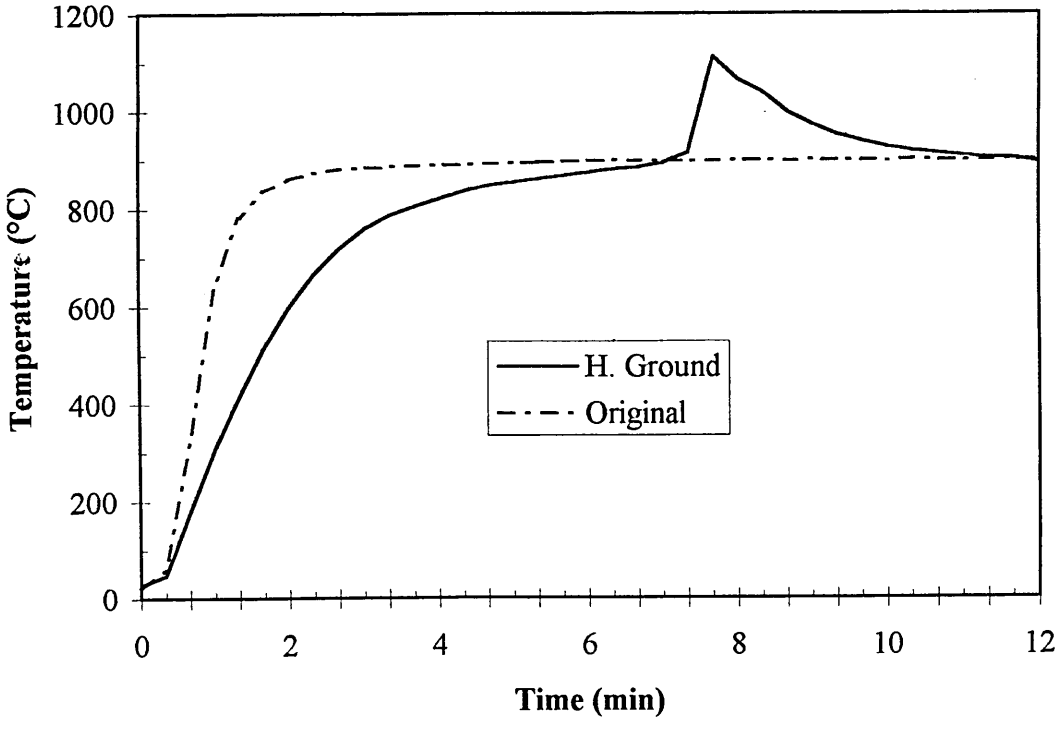

Figure 3- 6 Thermal response for original blanket state and ground fibres exposed in the furnace set at a temperature of 900°C.

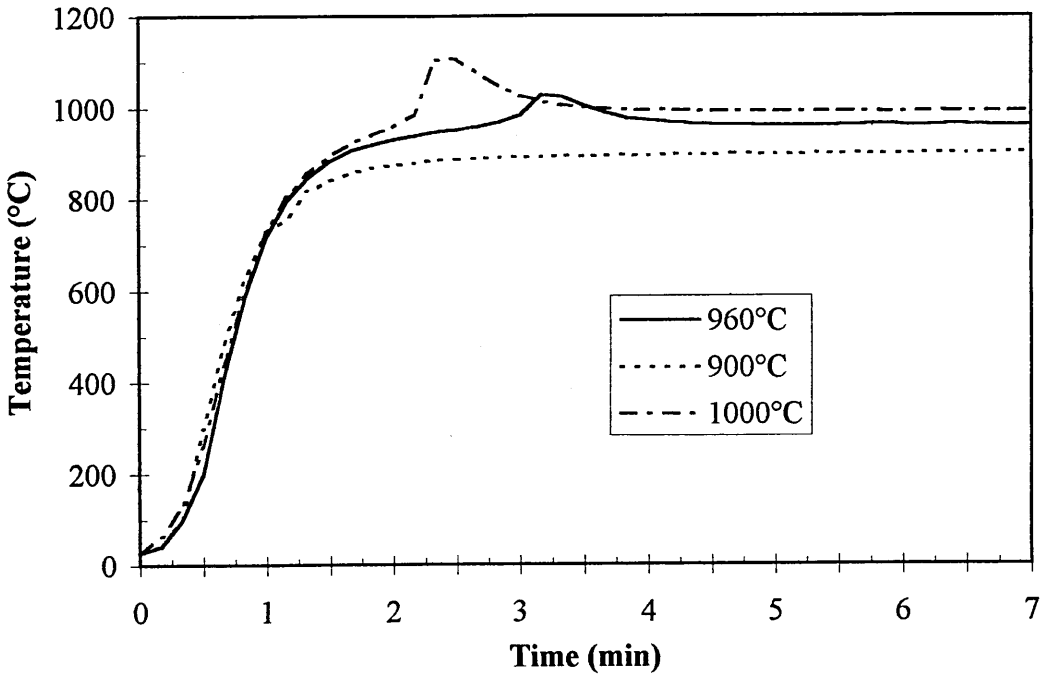

Figure 3-7 Thermal behaviour of original fibre A2.

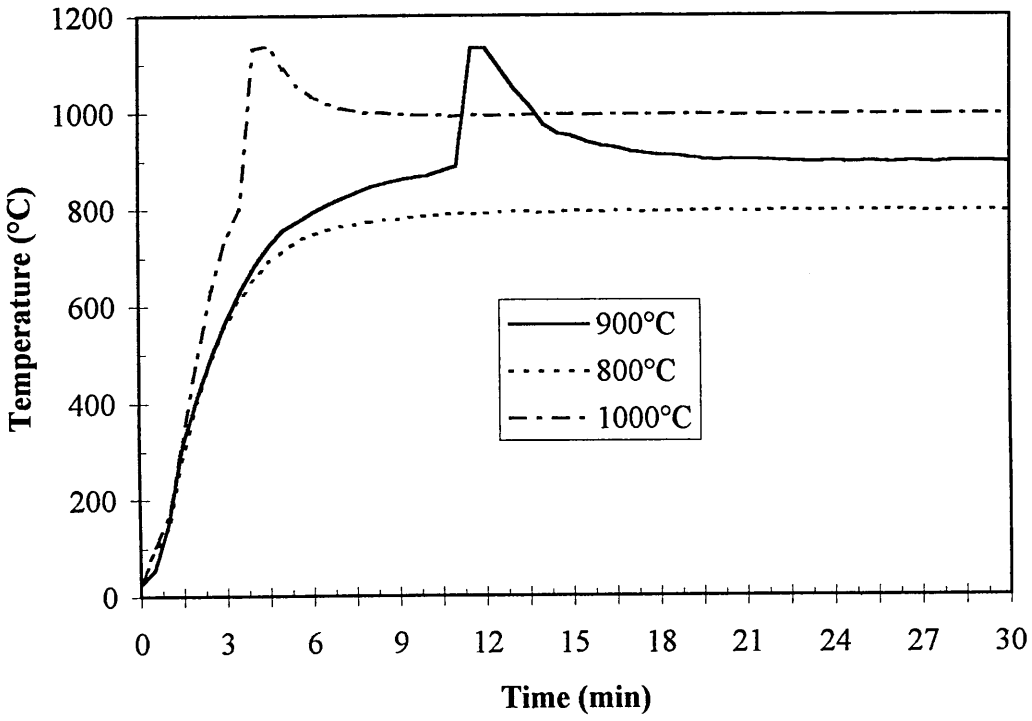

Figure 3- 8 Thermal behaviour of ground fibre A2.

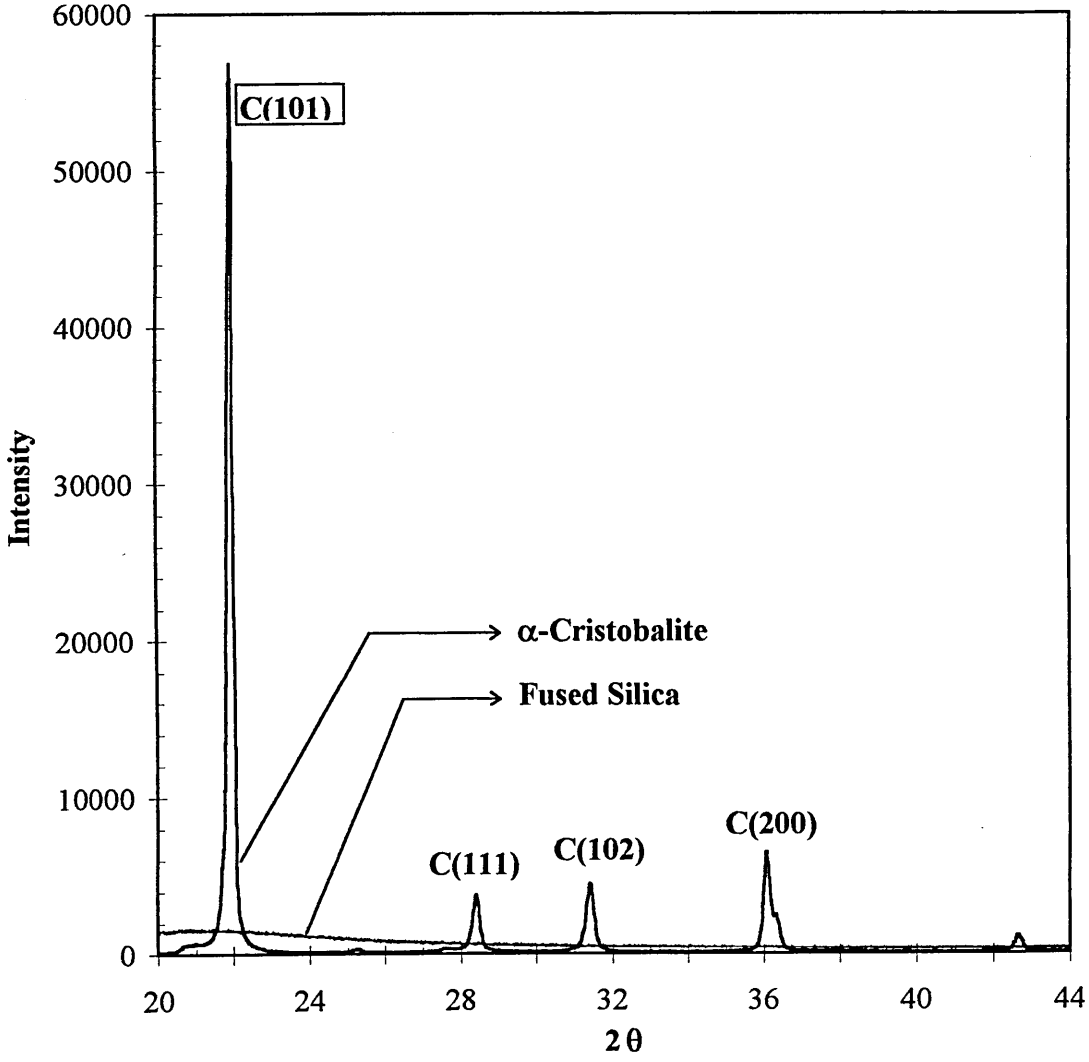

Figure 3-9 X-ray diffraction patterns of fused silica and α-cristobalite standard.

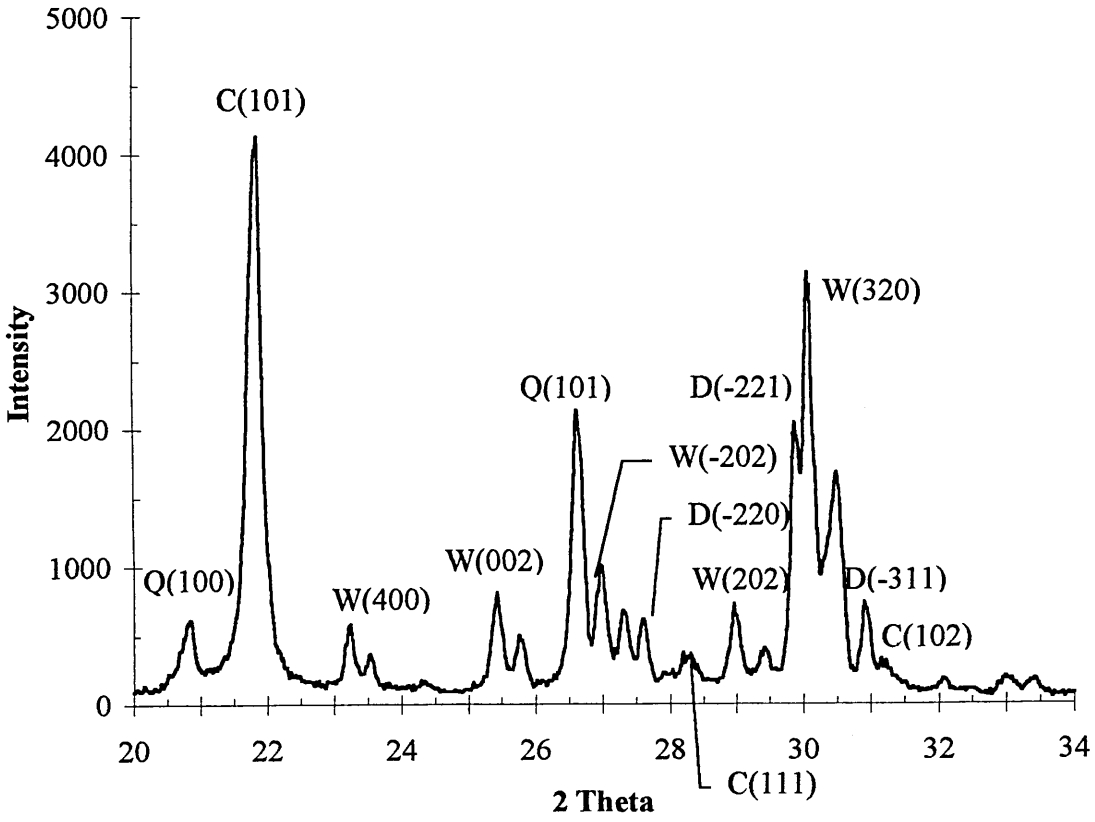

Figure 3-10 X-ray powder diffractometry plot for devitrified fibre showing analysis peaks.

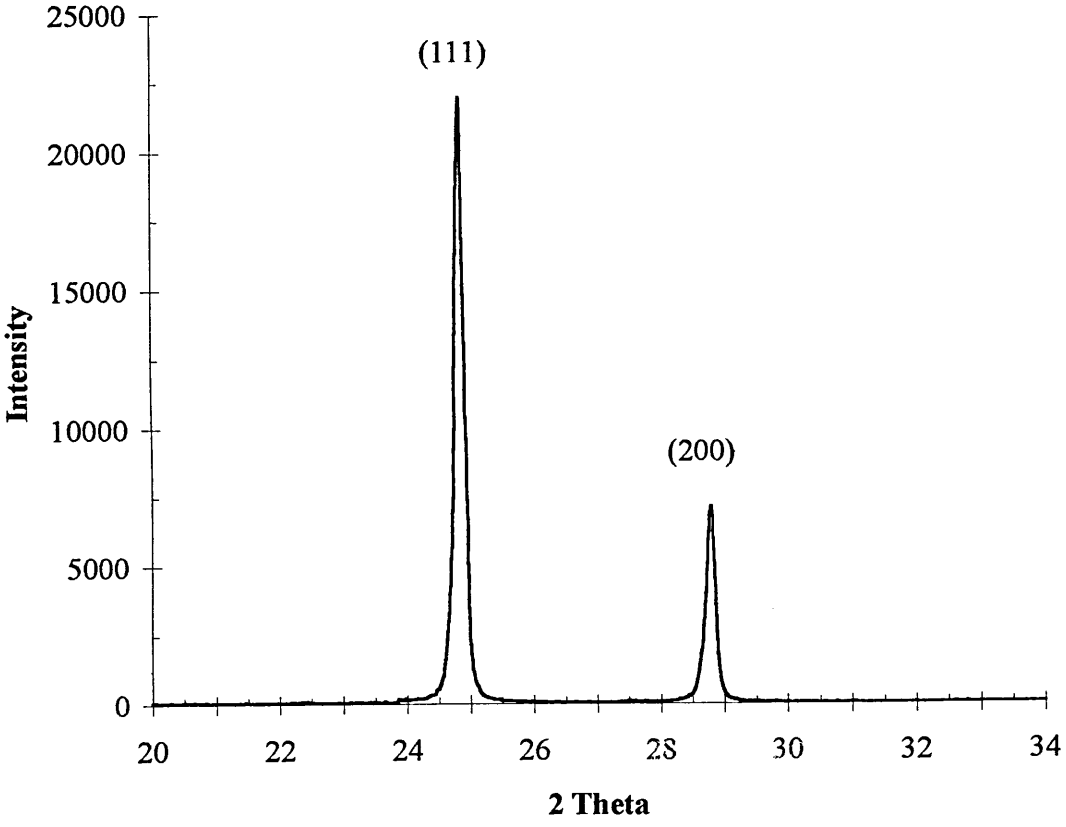

Figure 3-11 X-ray powder diffraction pattern of barium fluoride.

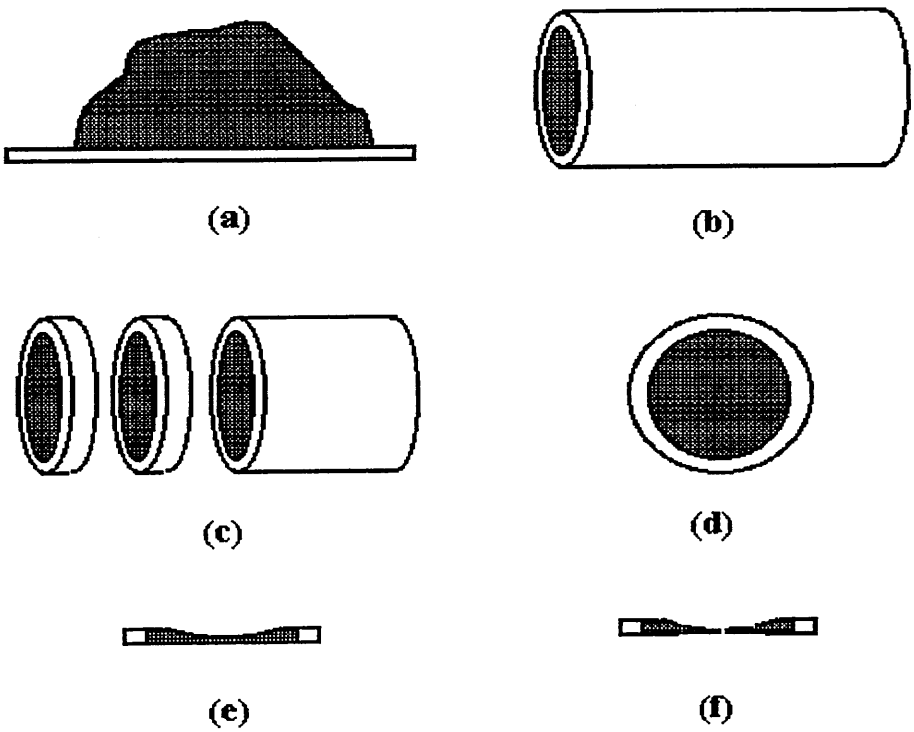

Figure 3- 12 Procedure for the preparation of fibre specimens by ion beam thinning. a, mixed components; b, mixture packed into the 3 mm i.d stainless steel tube; c, the sliced tube; d, initial ground and polished disc; e, dimpled disc and f, ion beam perforated disc.

Figure 3-13 Crushed as-manufactured fibre

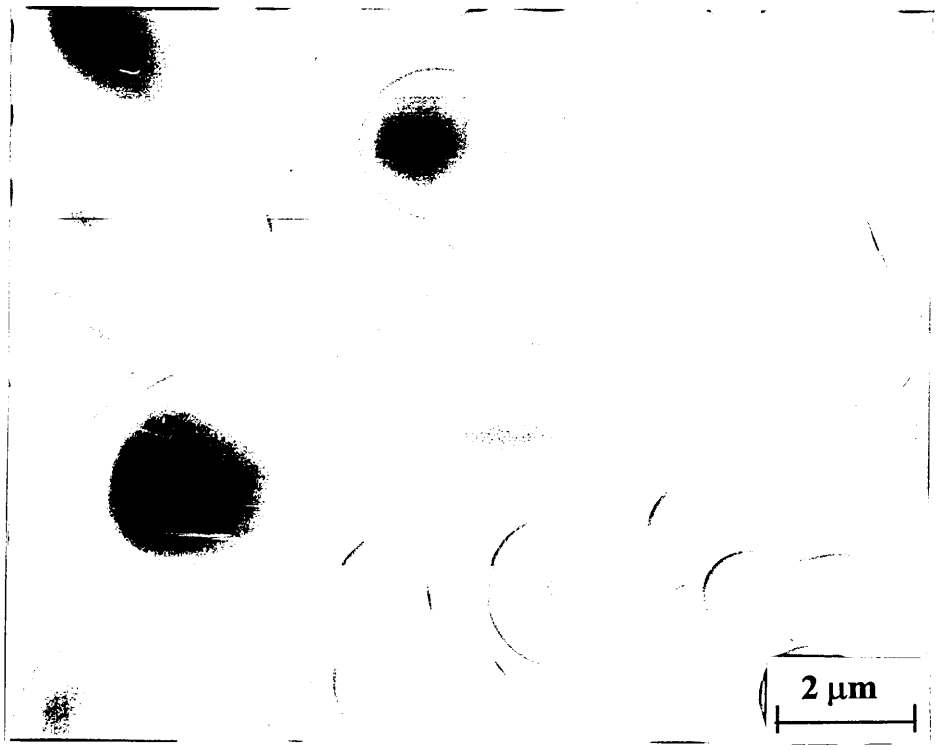

Figure 3- 14 TEM micrograph showing fibre packing and alignment in a specimen prepared by ion beam thinning.

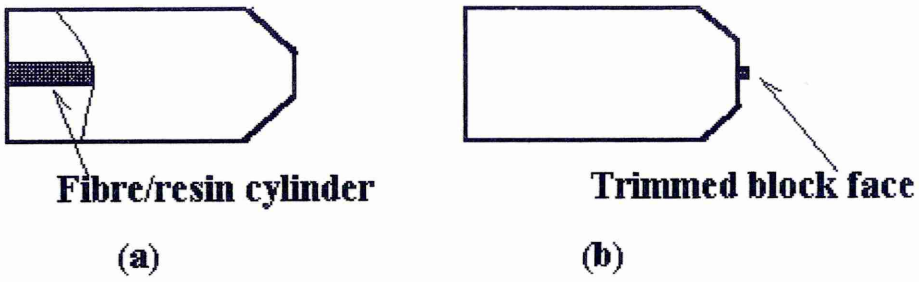

Figure 3-15 Specimen block for ultramicrotomy

Figure 3-16 Polishing surface of the cross section of fibre/resin cylindar.

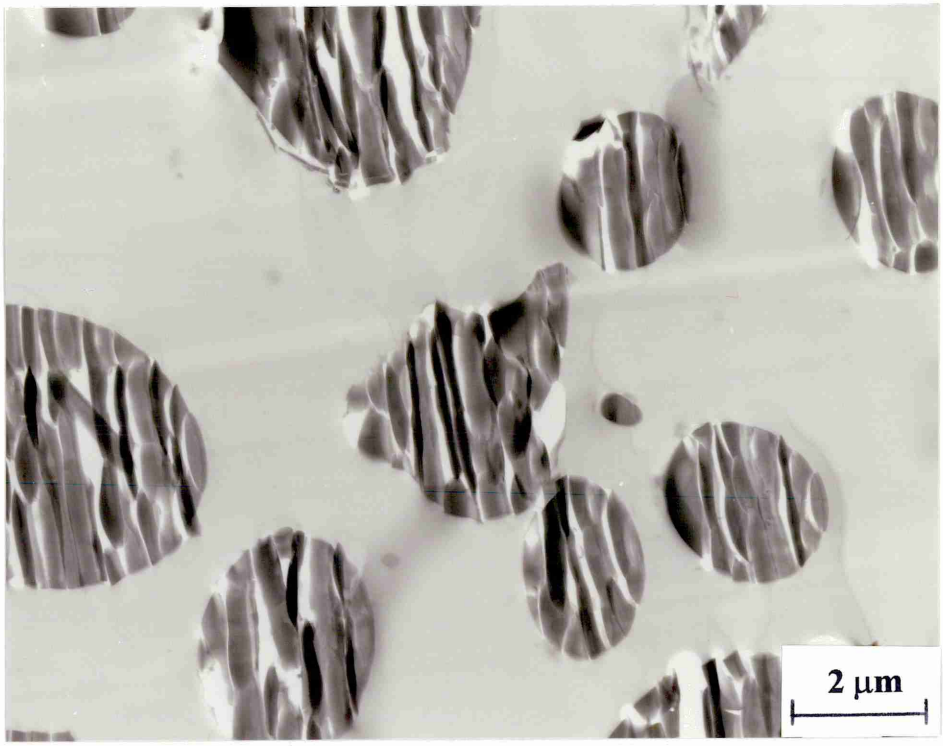

Figure 3-17 TEM micrograph showing representative cross-sections of as-manufactured fibres prepared by the ultramicrotomy method.

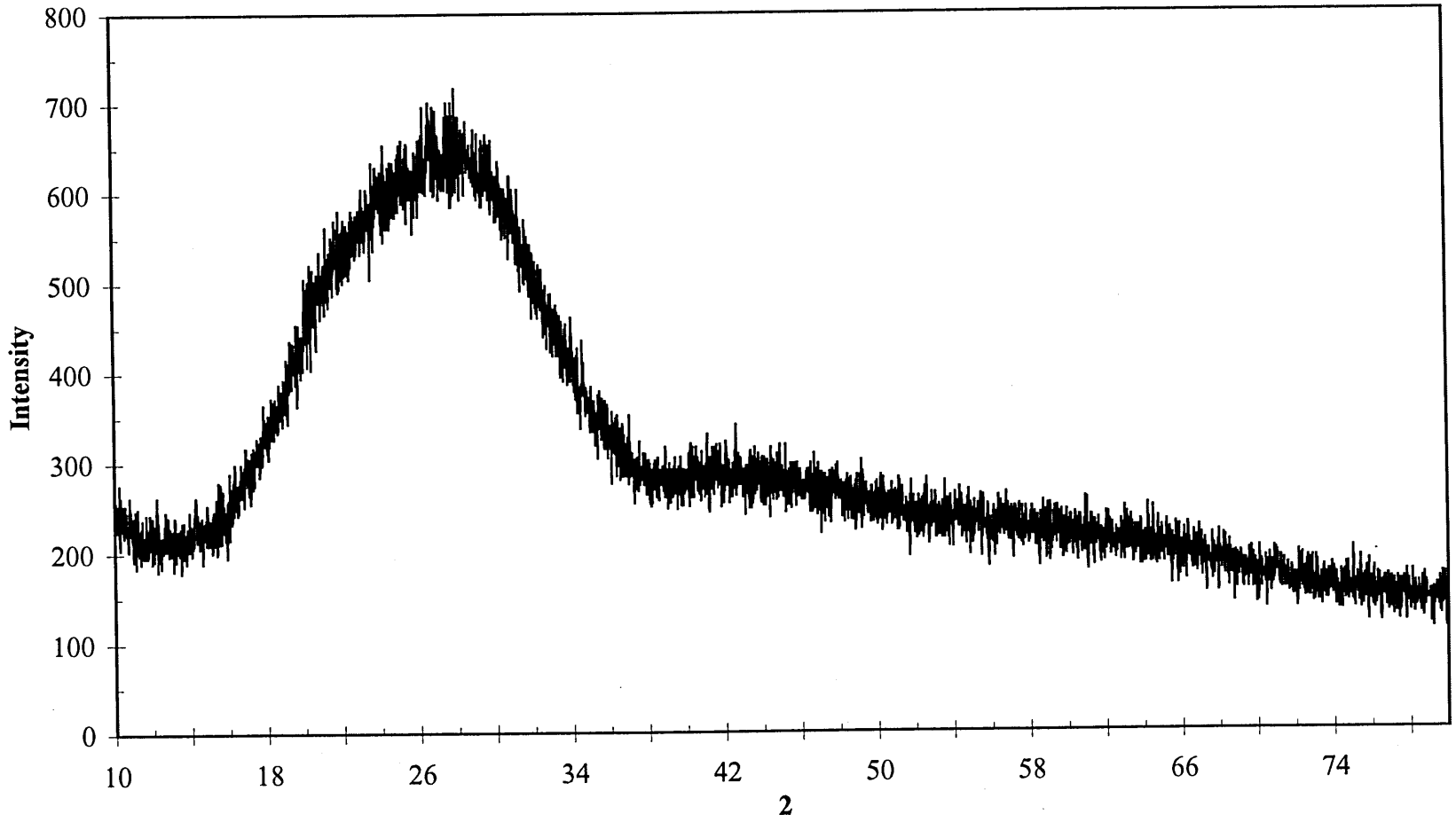

Figure 4-1 X-ray powder diffraction pattern of ground as-manufactured fibre blanket.

Figure 4-2 As-manufactured Superwool blanket.

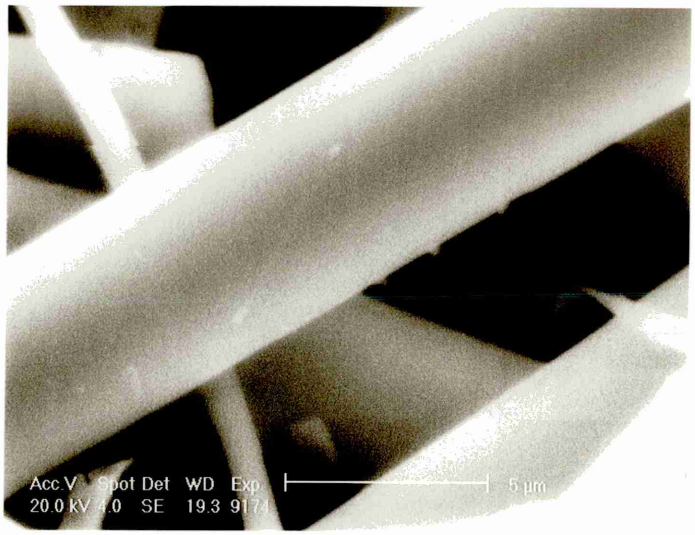

Figure 4-3 SEM micrograph of Superwool fibres.

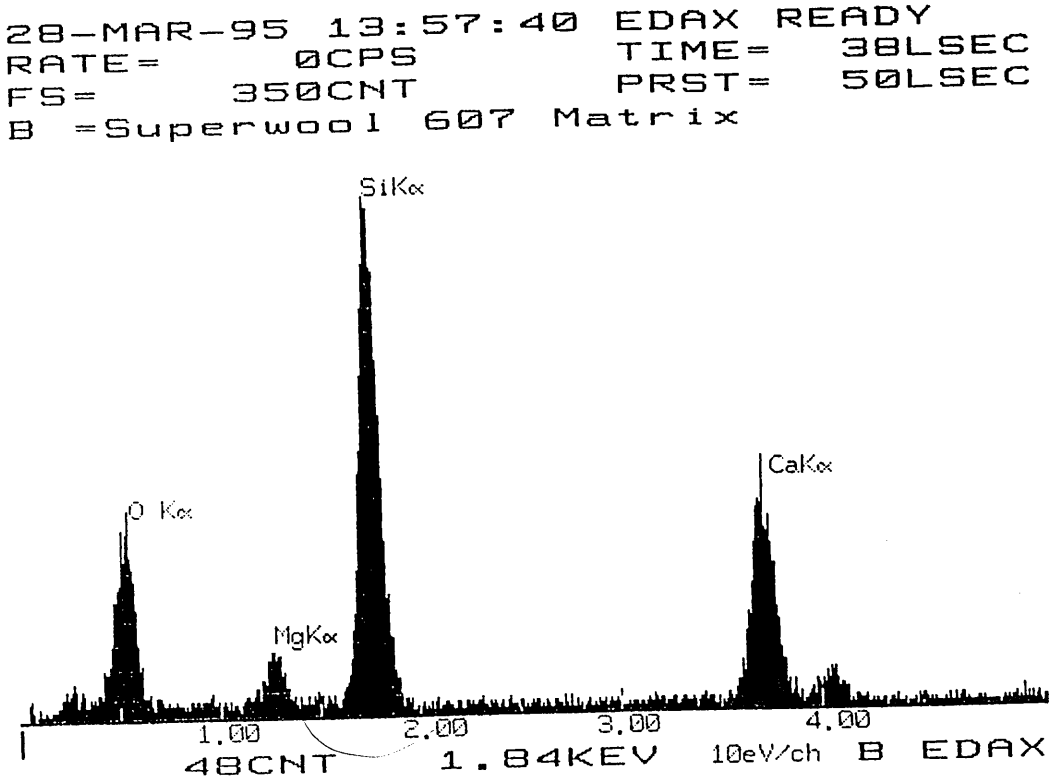

Figure 4-4 EDS of fibre matrix.

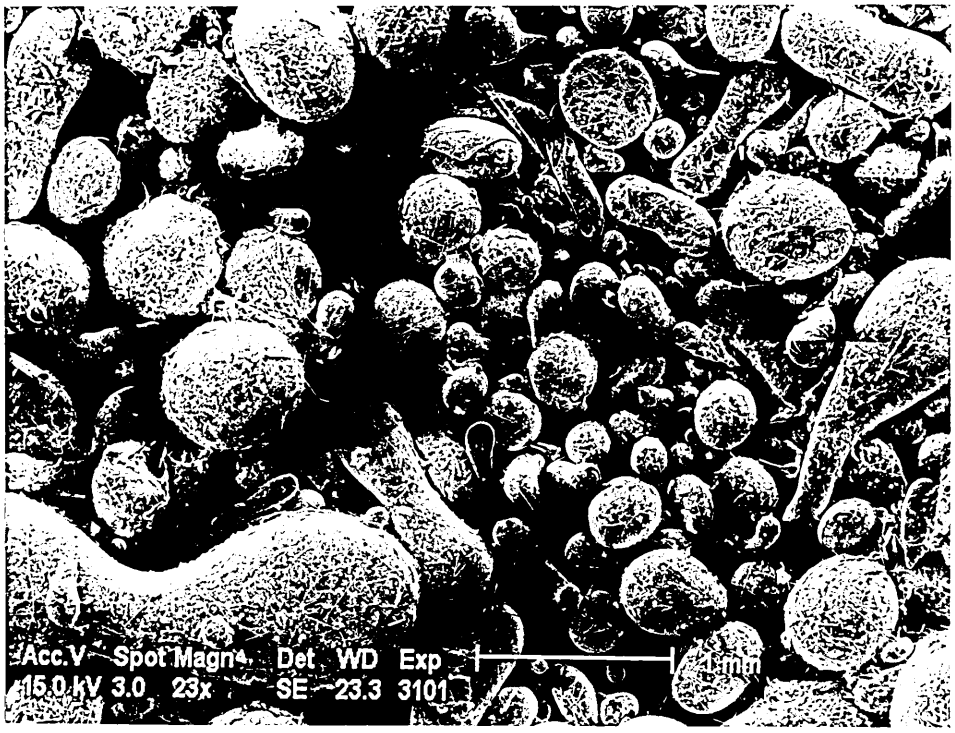

Figure 4-5 Shot particles showing a range of diameters.

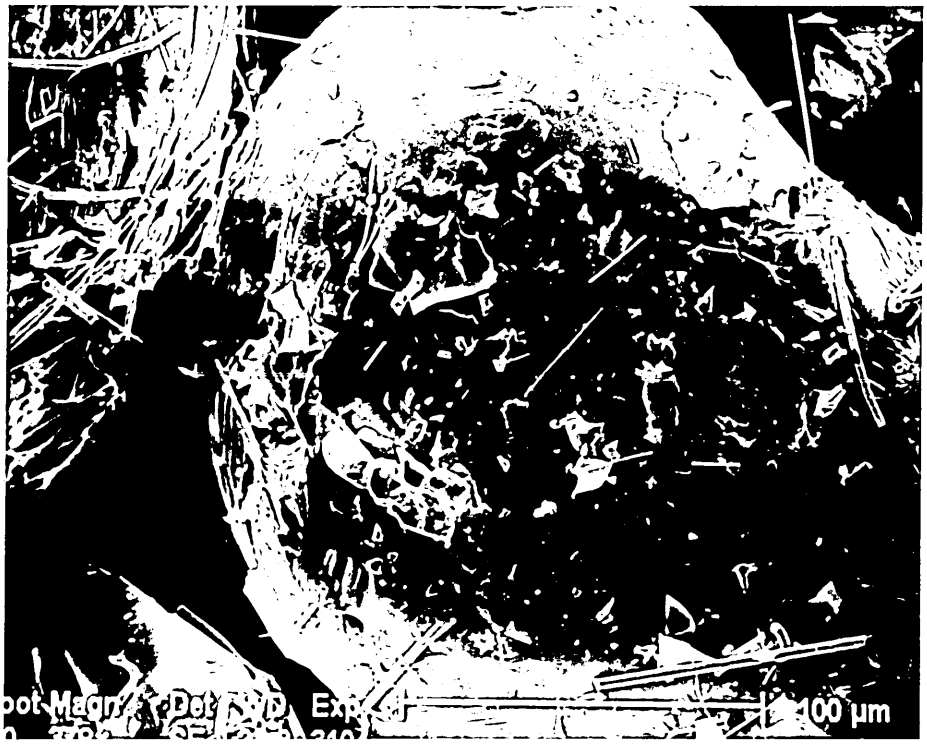

Figure 4-6 Surface of a shot particle before thermal exposure.

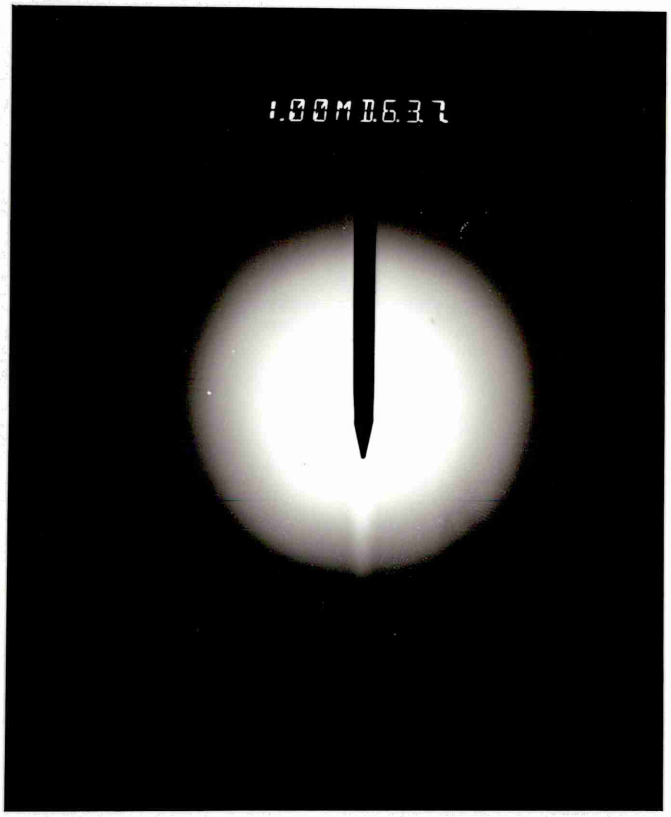

Figure 4-8 Electron diffraction pattern of alkaline-earth ions riched area.

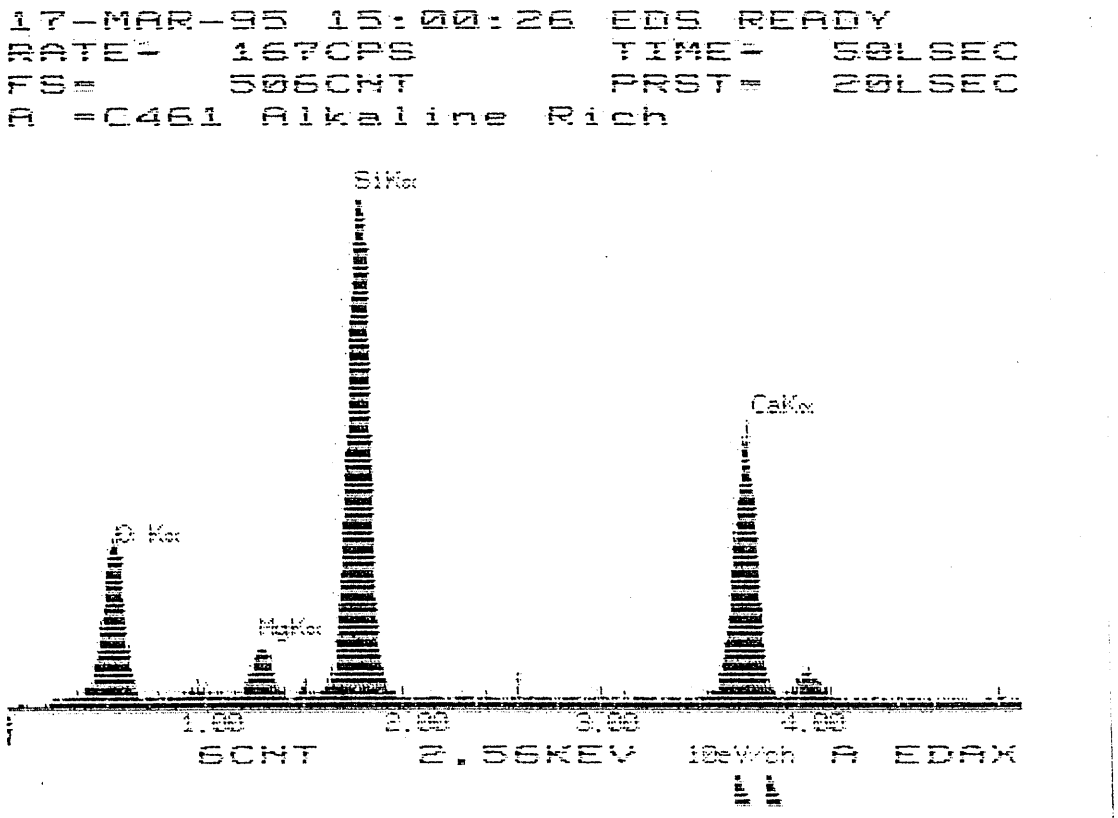

Figure 4-9a EDS in the alkaline-earth ions riched area.

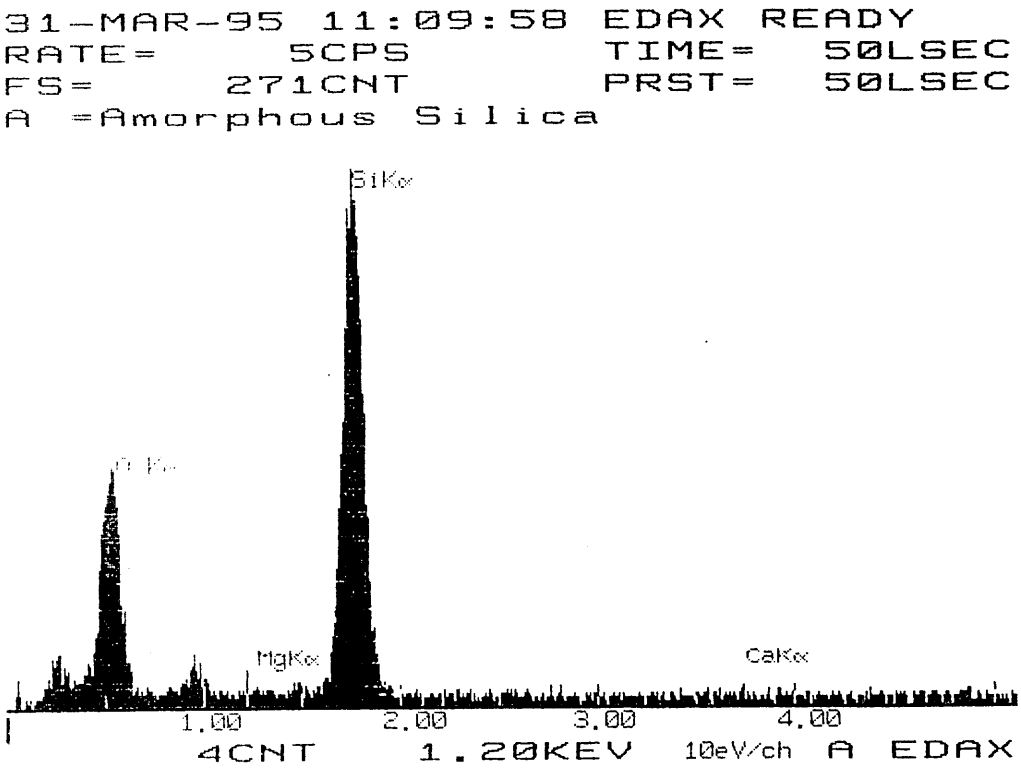

Figure 4-9b EDS of silica riched area.

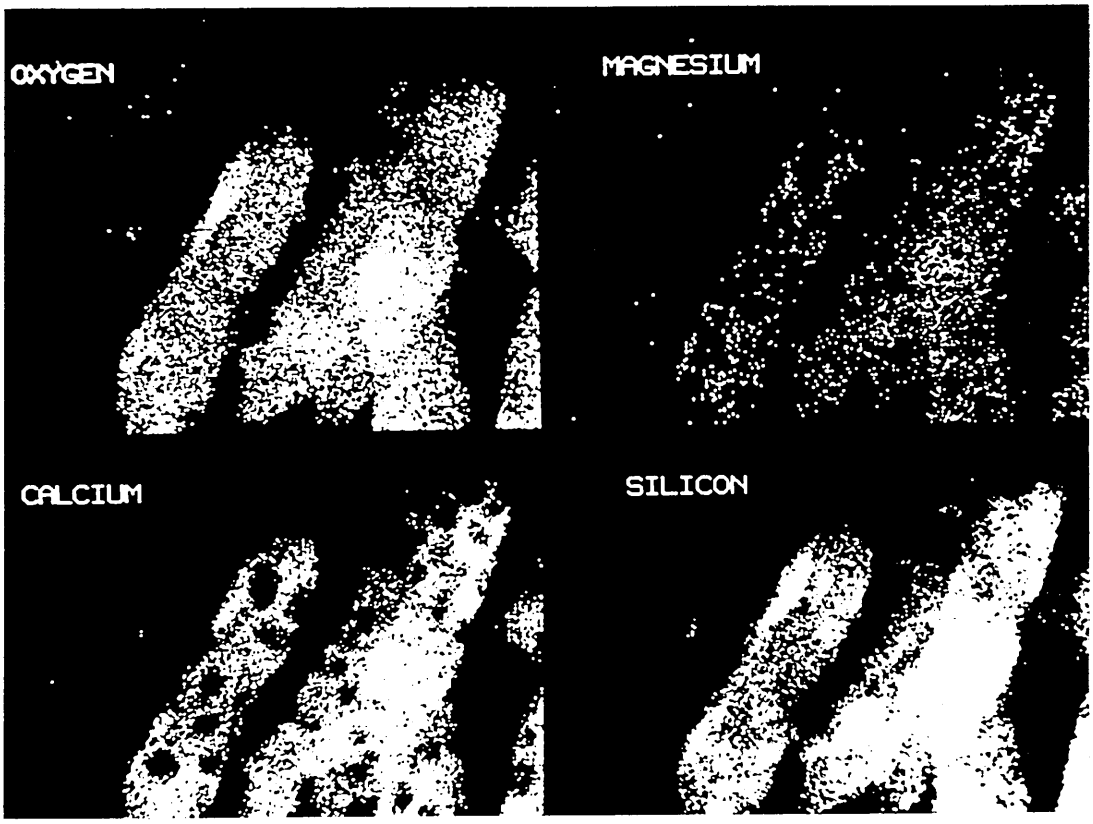

Figure 4-10 X-ray mapping of O, Si, Ca and Mg in phase separated shot particle.

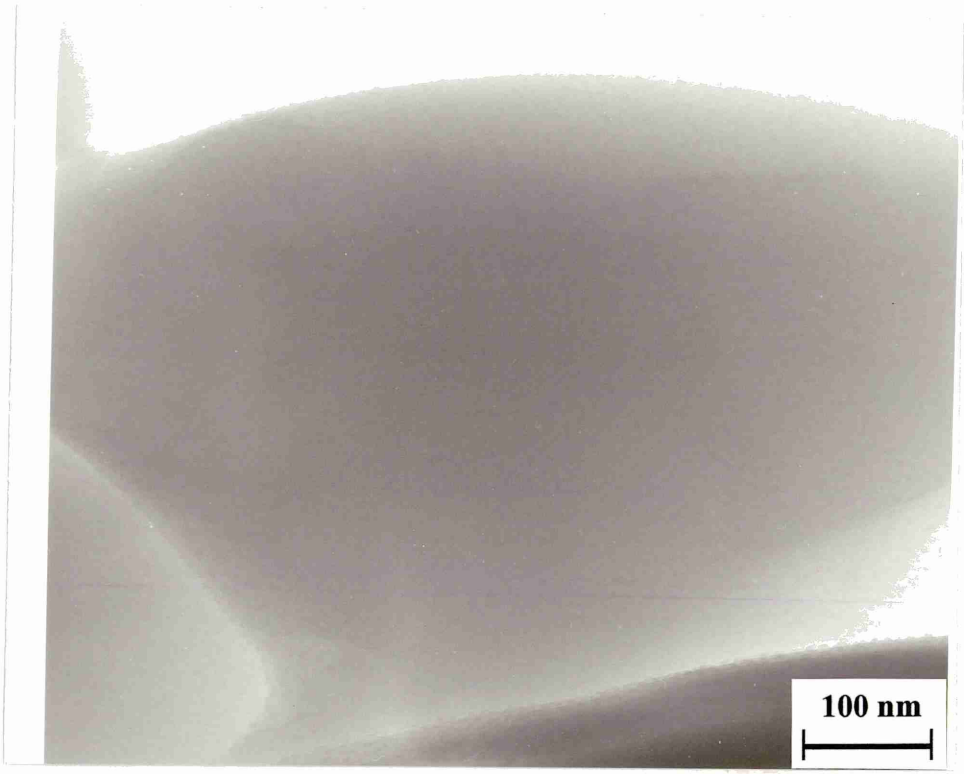

Figure 4-11 TEM micrograph of fibre cross section showing homogeneous structure of Superwool fibre before exposure.

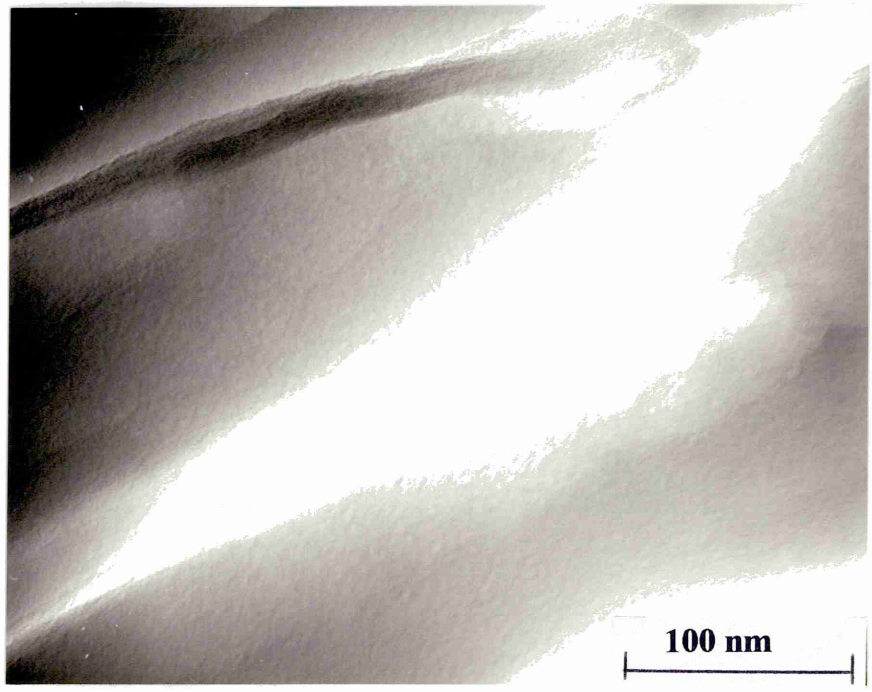

Figure 4-12 Microstructure of as-manufactured A2 fibre.

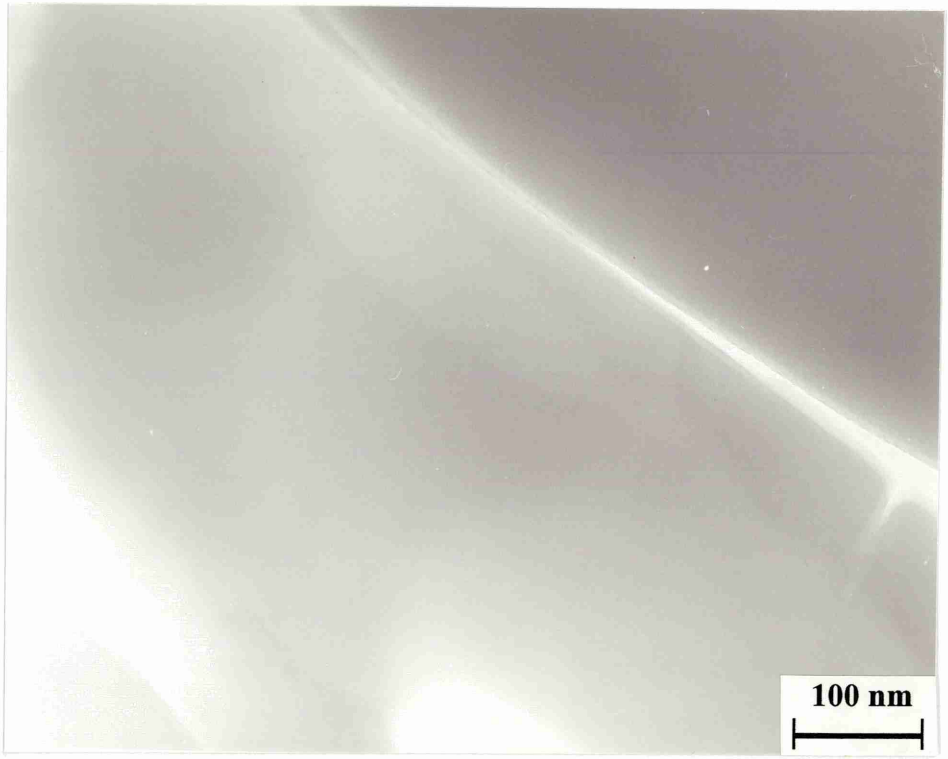

Figure 4-13 Microstructure of as-manufactured B3 fibre.

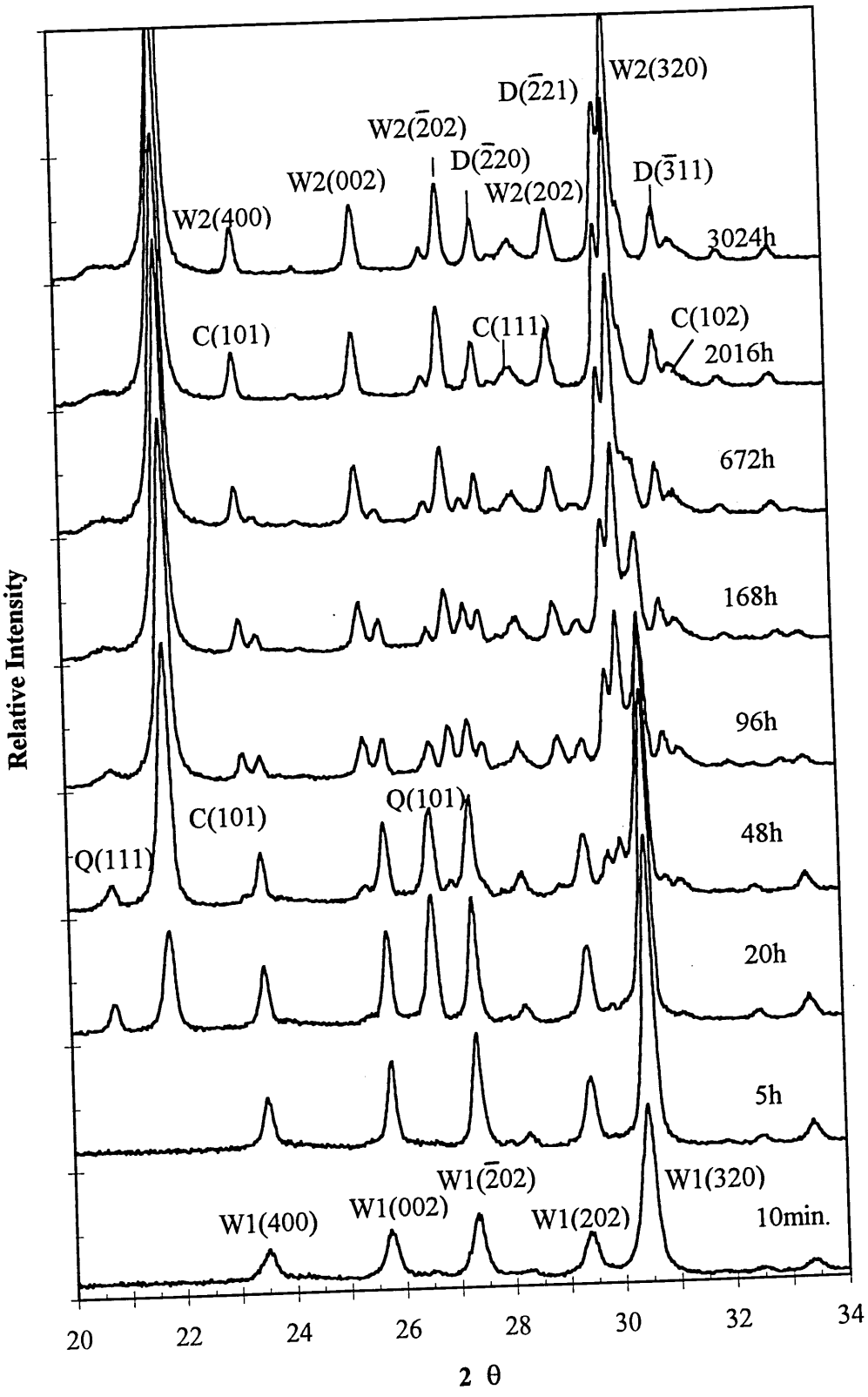

Figure 4-14 X-ray powder diffraction patterns for Superwool fibre after thermal exposure at 1100°C

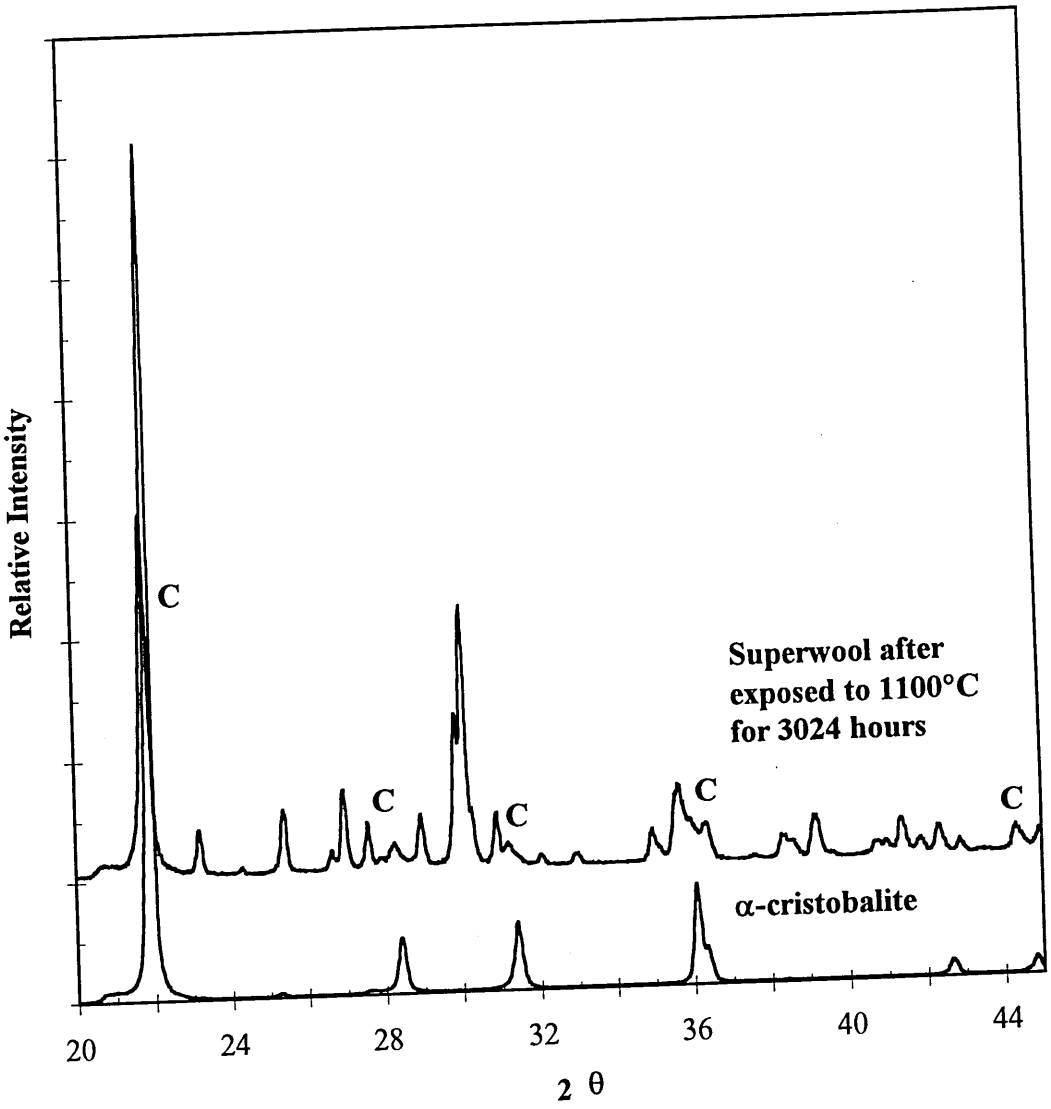

Figure 4-15 XRD patterns showing d-spacing shifts in α-cristobalite identified in devitrified fibres.

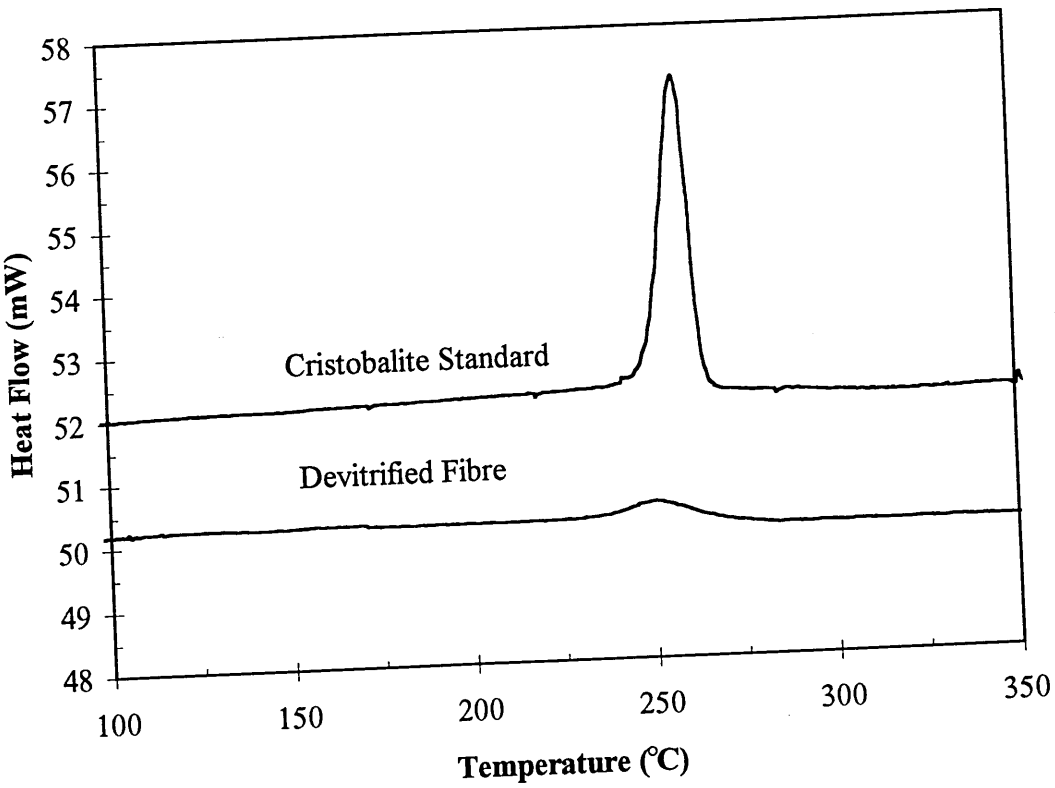

Figure 4-16 DSC traces of standard cristobalite and devitrified Superwool fibre.

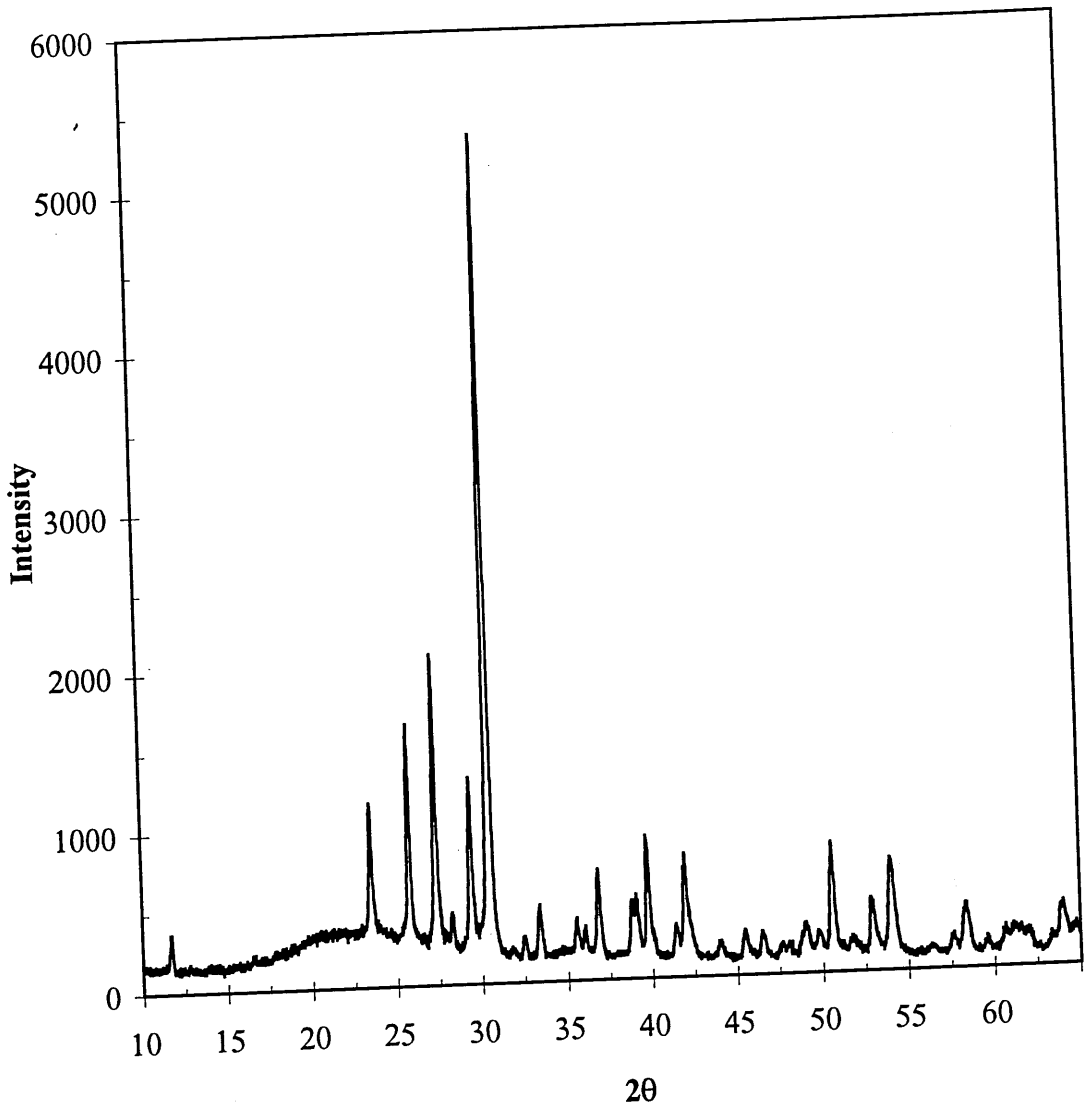

Figure 4-17 X-ray diffraction pattern for Superwool devitrified at 1100°C for 5 hours.

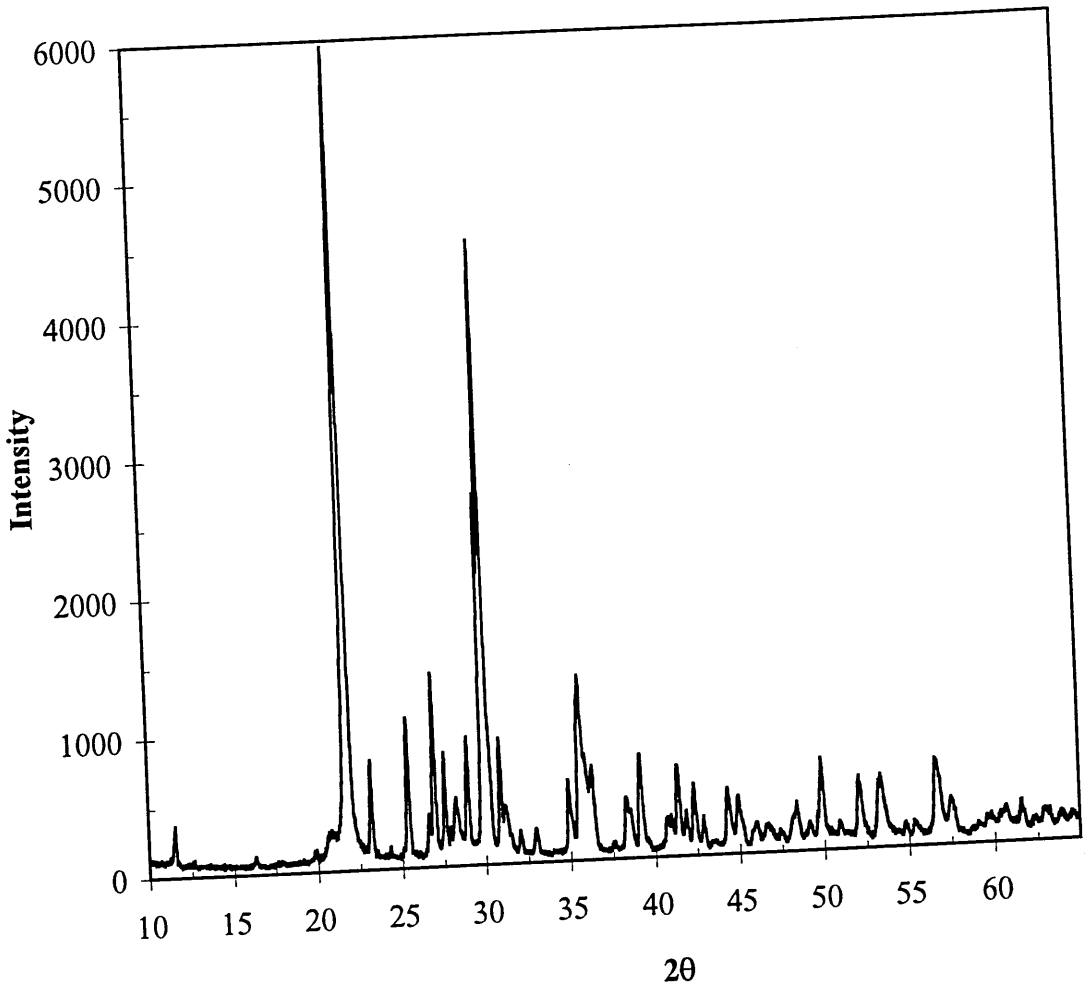

Figure 4-18 X-ray powder diffraction pattern for Superwool fibre devitrified at 1100°C for 3024 hours.

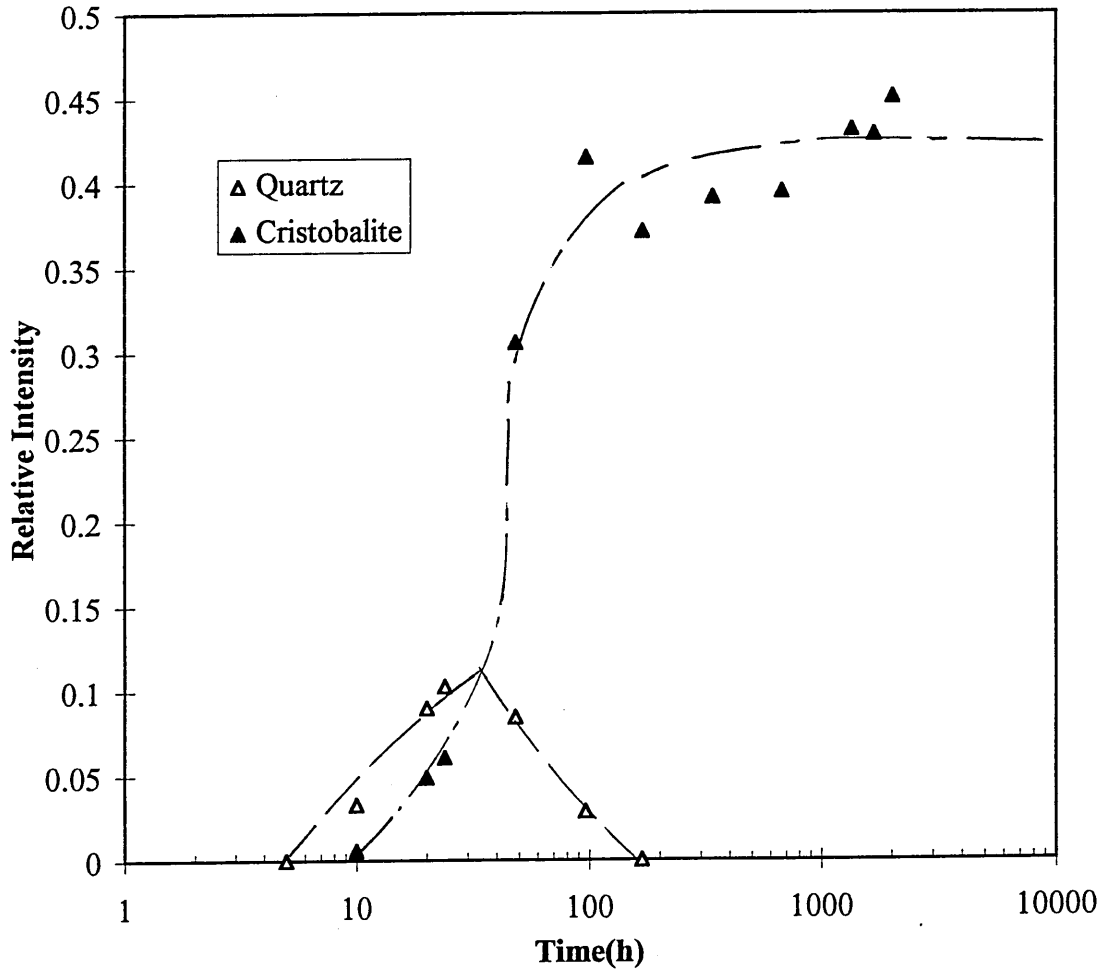

Figure 4-19 Development of X-ray peak intensities of quartz and cristobalite in Superwool fibre devitrified at 1100°C.

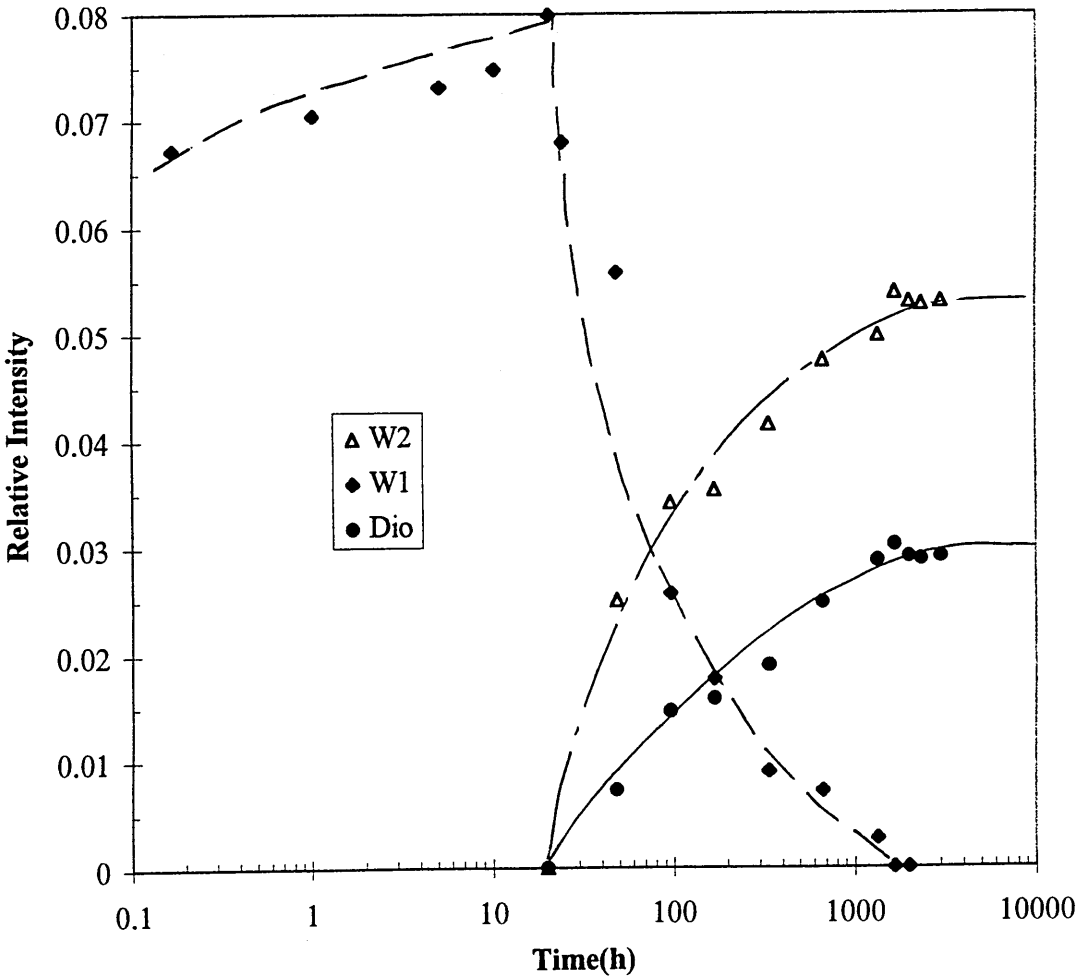

Figure 4-20 Development of X-ray peak intensities of wollastonite 1, wollastonite 2 and diopside in Superwool fibre devitrified at 1100°C.

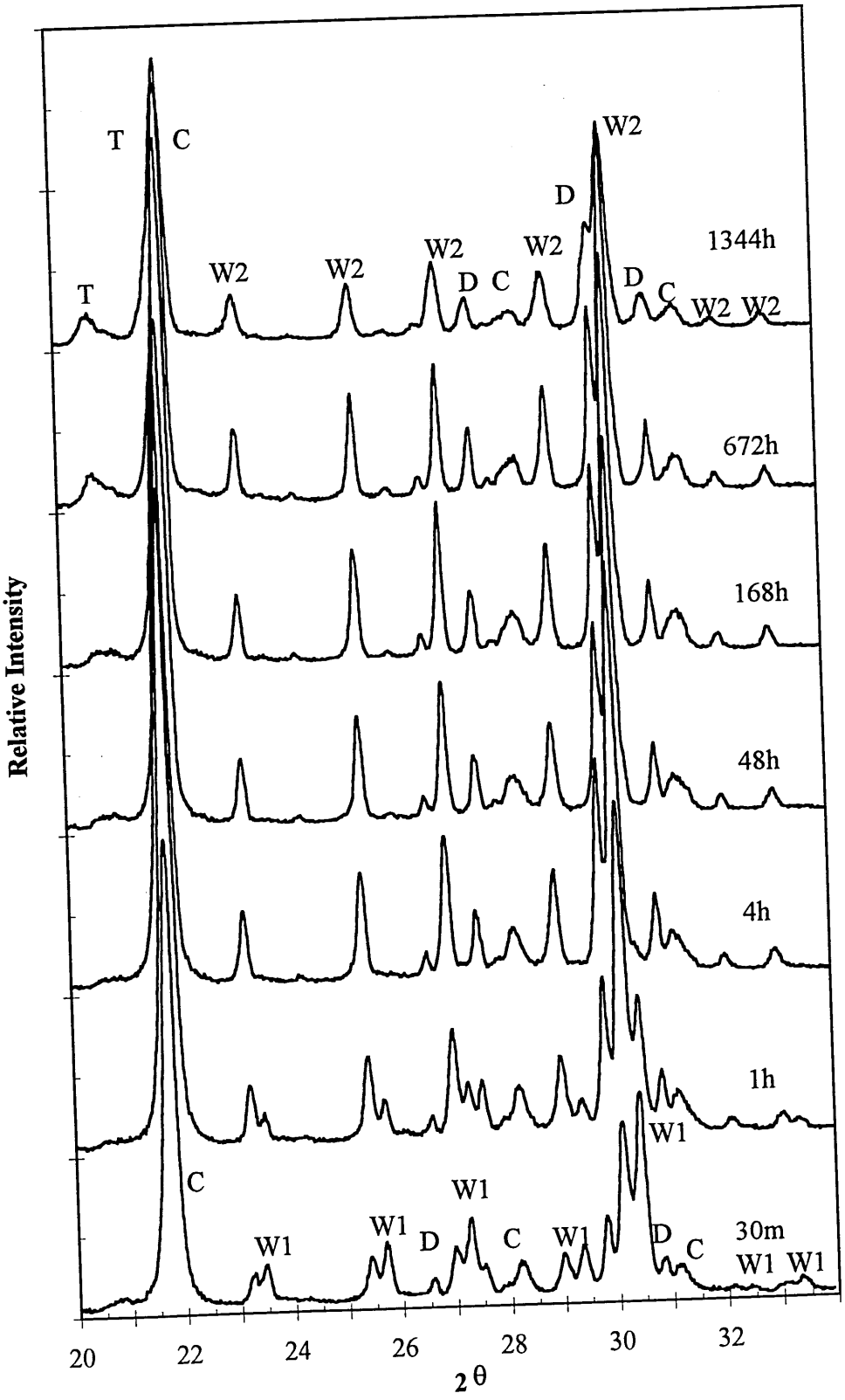

Figure 4-21 X-ray powder diffraction patterns of Superwool fibre devitrified at 1250°C.

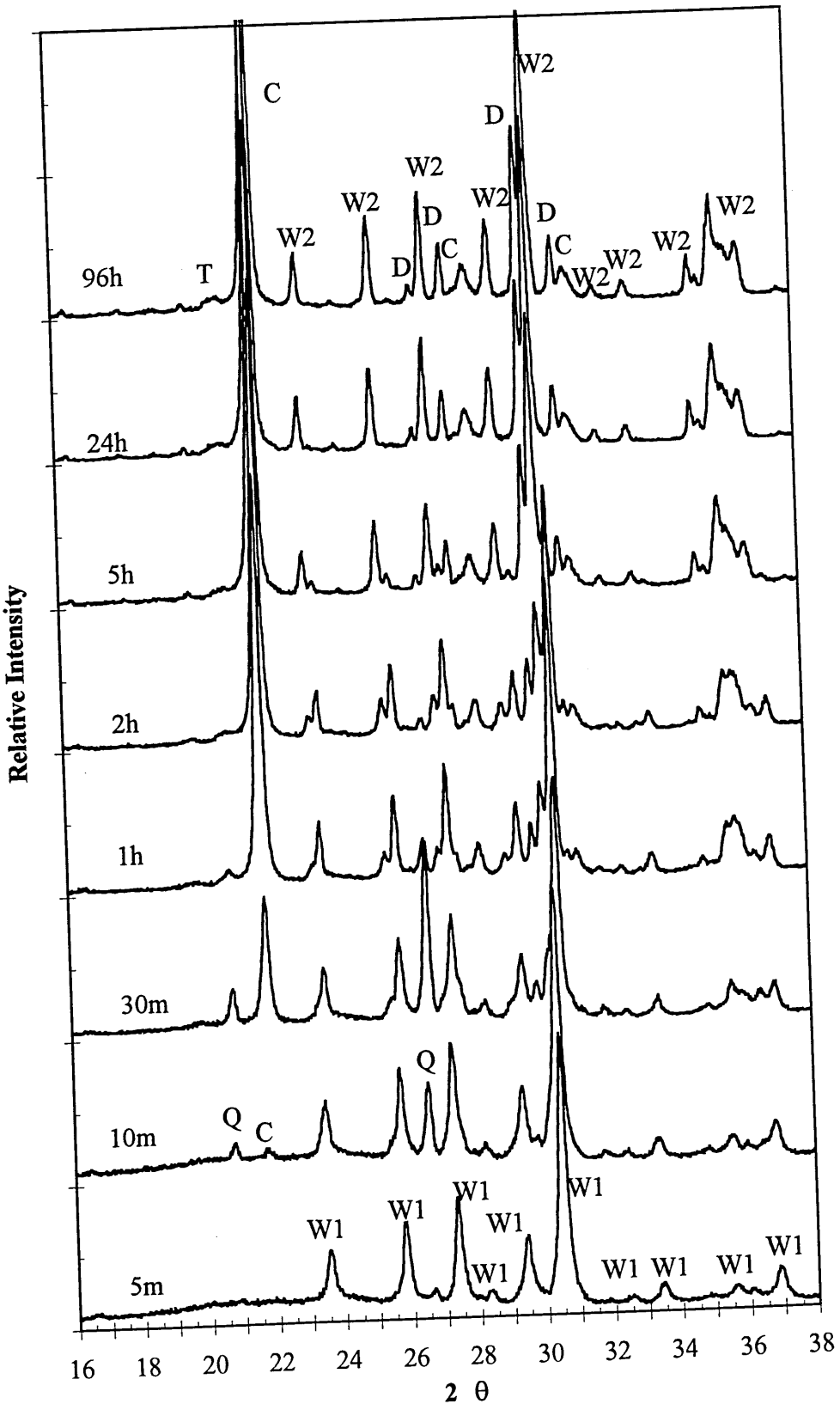

Figure 4-22 X-ray powder diffraction patterns of Superwool fibre devitrified at 1200°C.

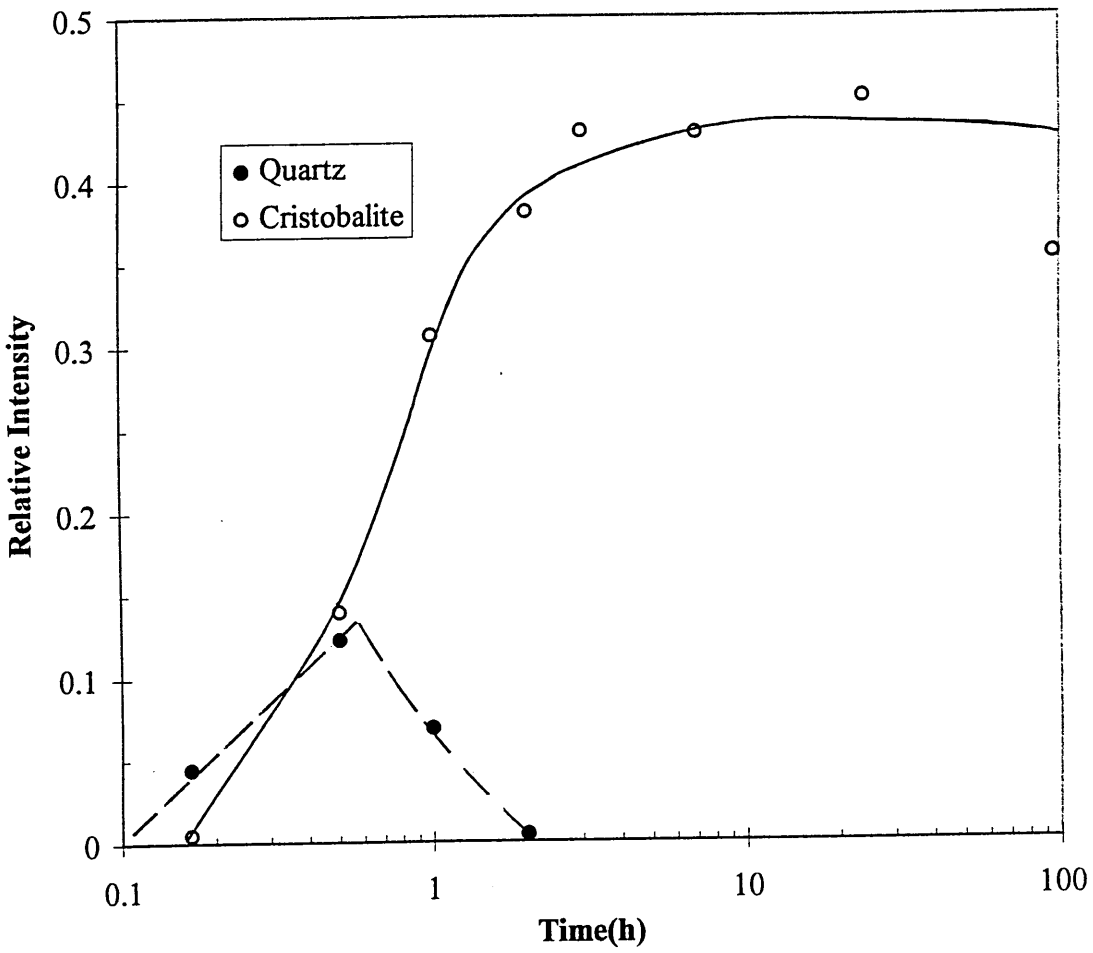

Figure 4-23 Development of X-ray peak intensities of quartz and cristobalite in Superwool fibre devitrified at 1200°C

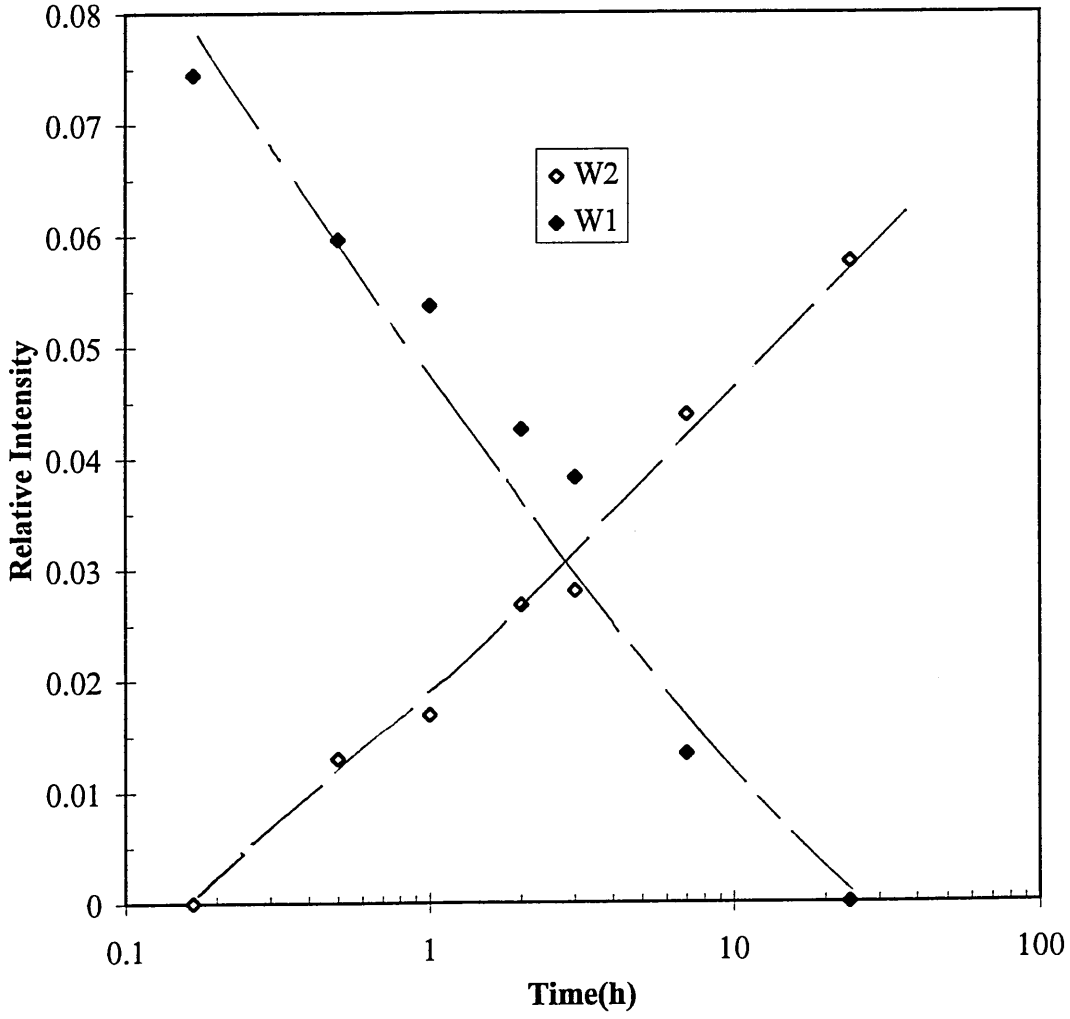

Figure 4-24 Development of wollastonite 1 and wollastonite 2 in Superwool fibre devitrified at 1200°C.

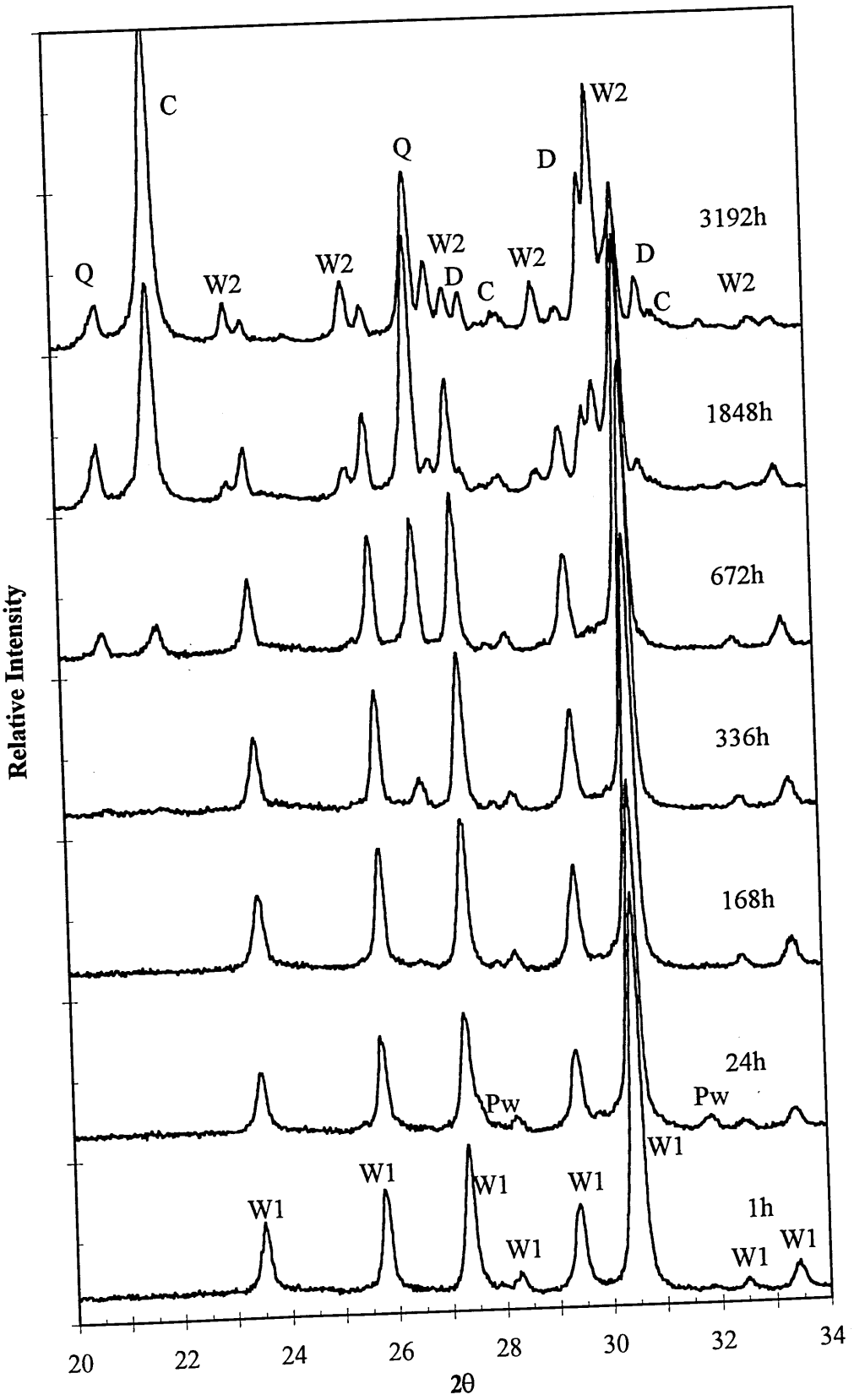

Figure 4-25 X-ray powder diffraction patterns for Superwool fibre devitrified at 1000°C.

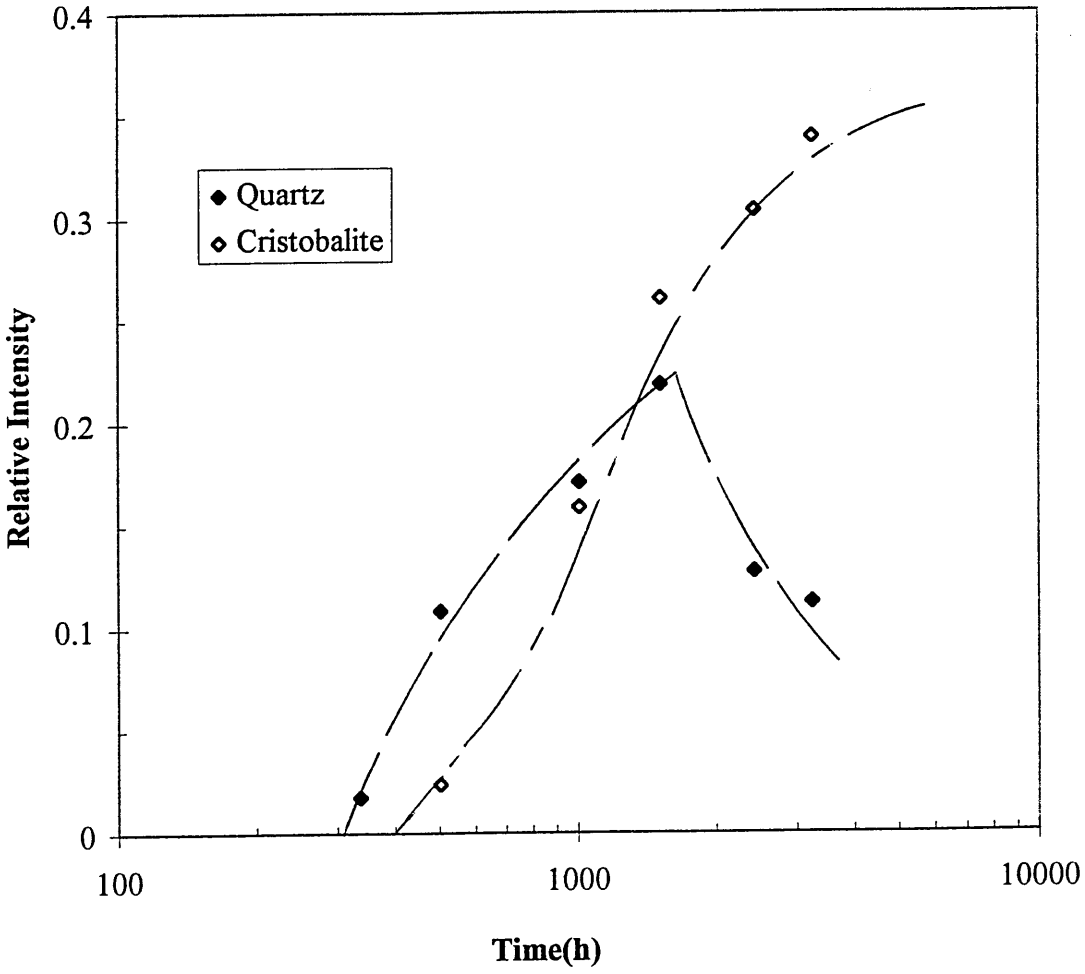

Figure 4-26 Development of X-ray peak intensities of quartz and cristobalite in Superwool fibre devitrified at 1000°C.

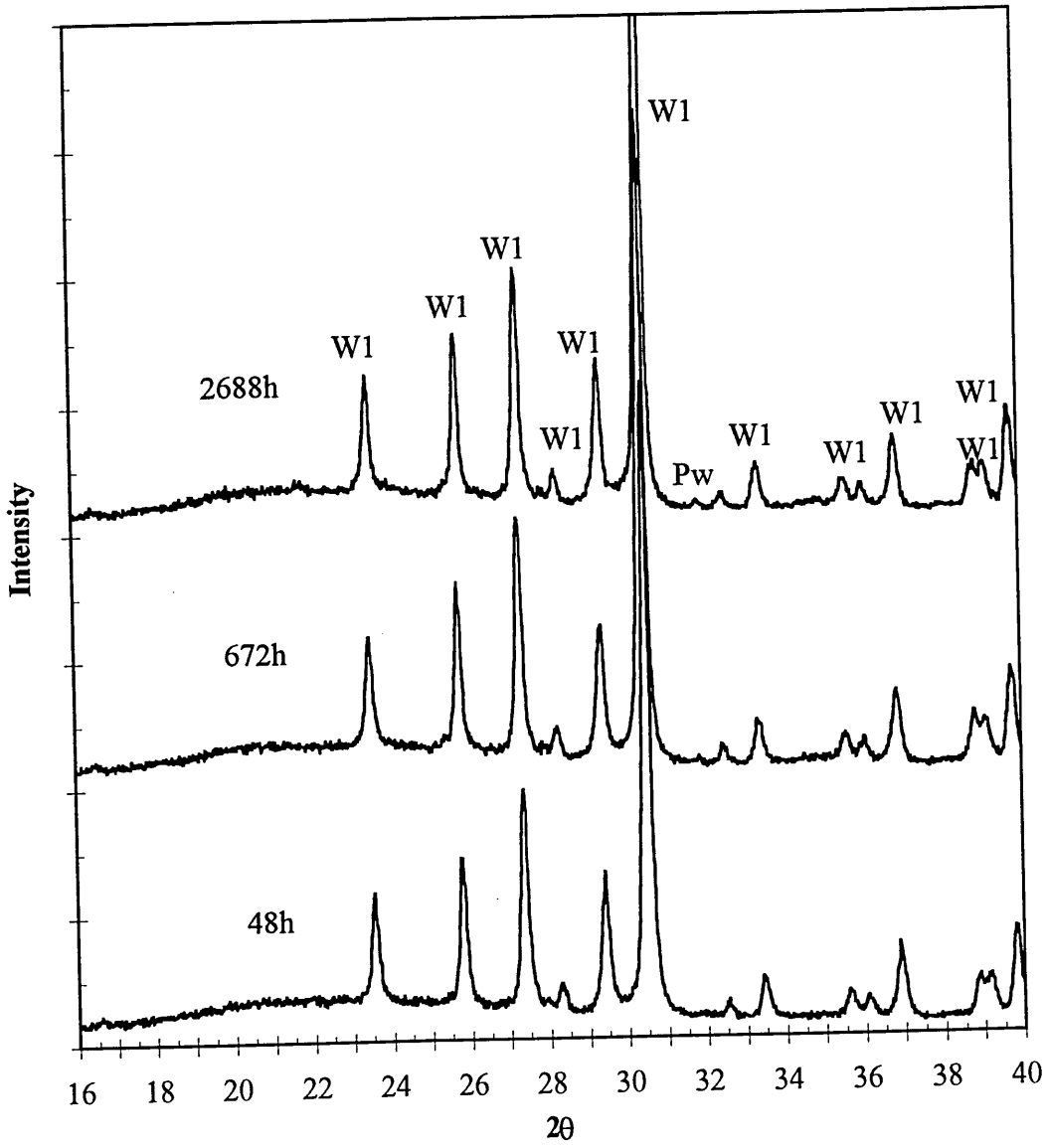

Figure 4-27 X-ray powder diffraction patterns for Superwool fibre devitrified at 900°C.

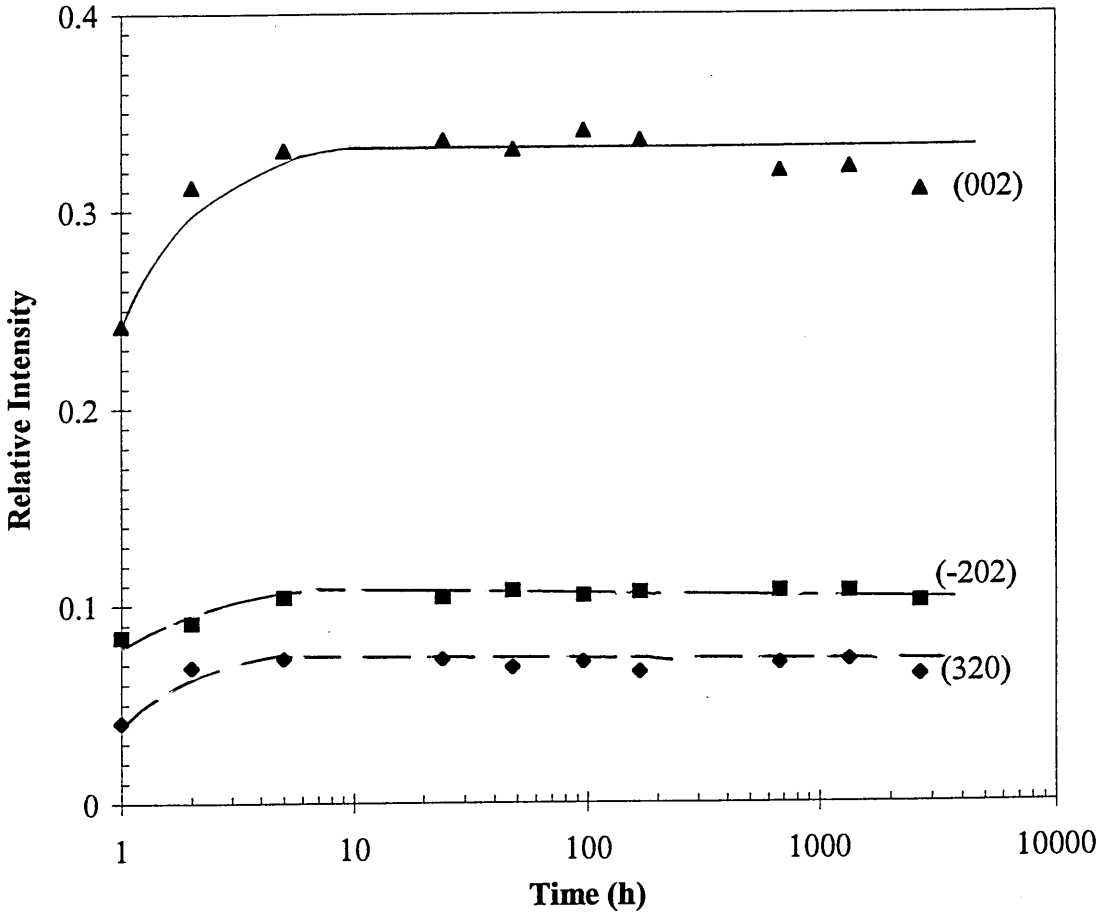

Figure 4-28 Development of intensities of X-ray peaks of wollastonite 1 at 900°C.

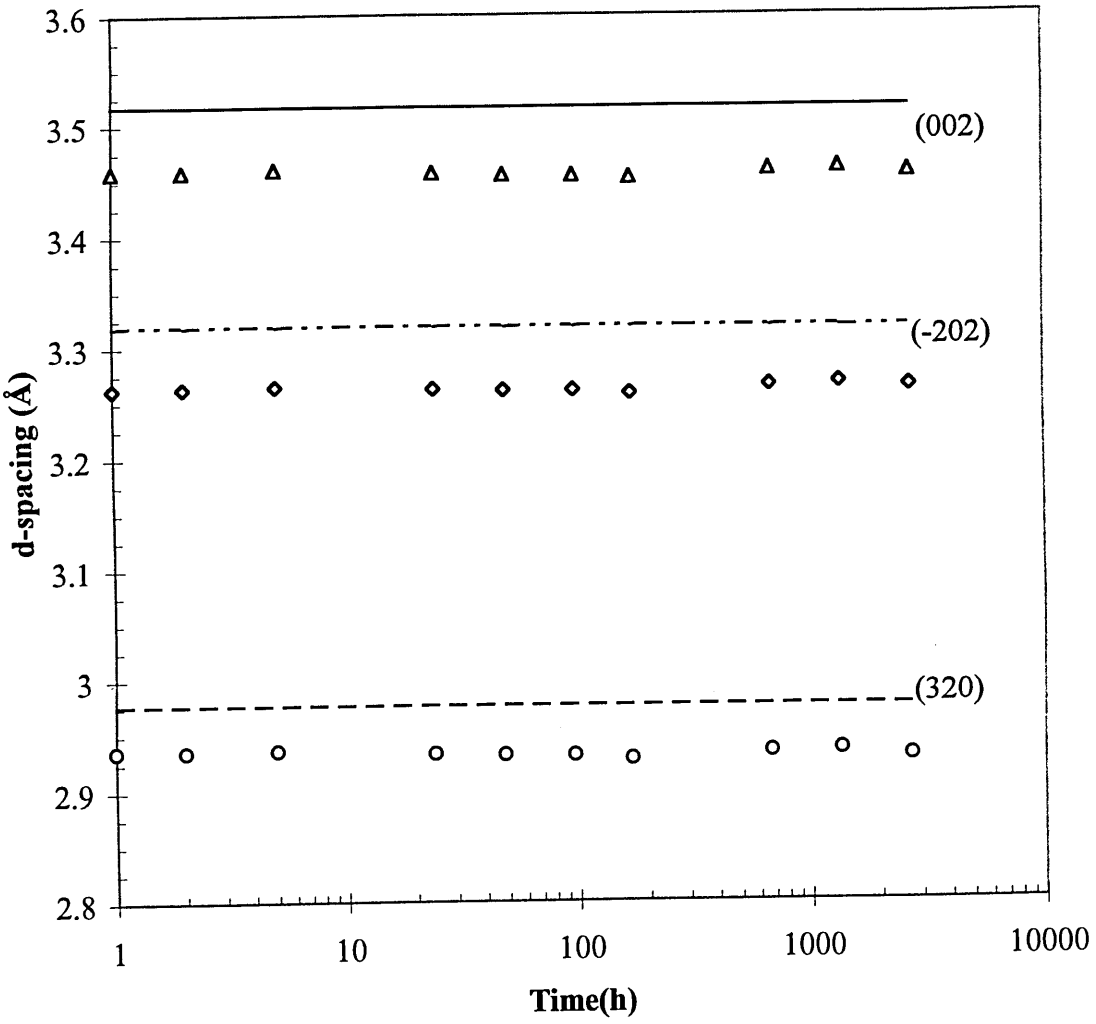

Figure 4-29 Development of d-spacings of wollastonite 1 in Superwool fibre at 900°C with increase time.

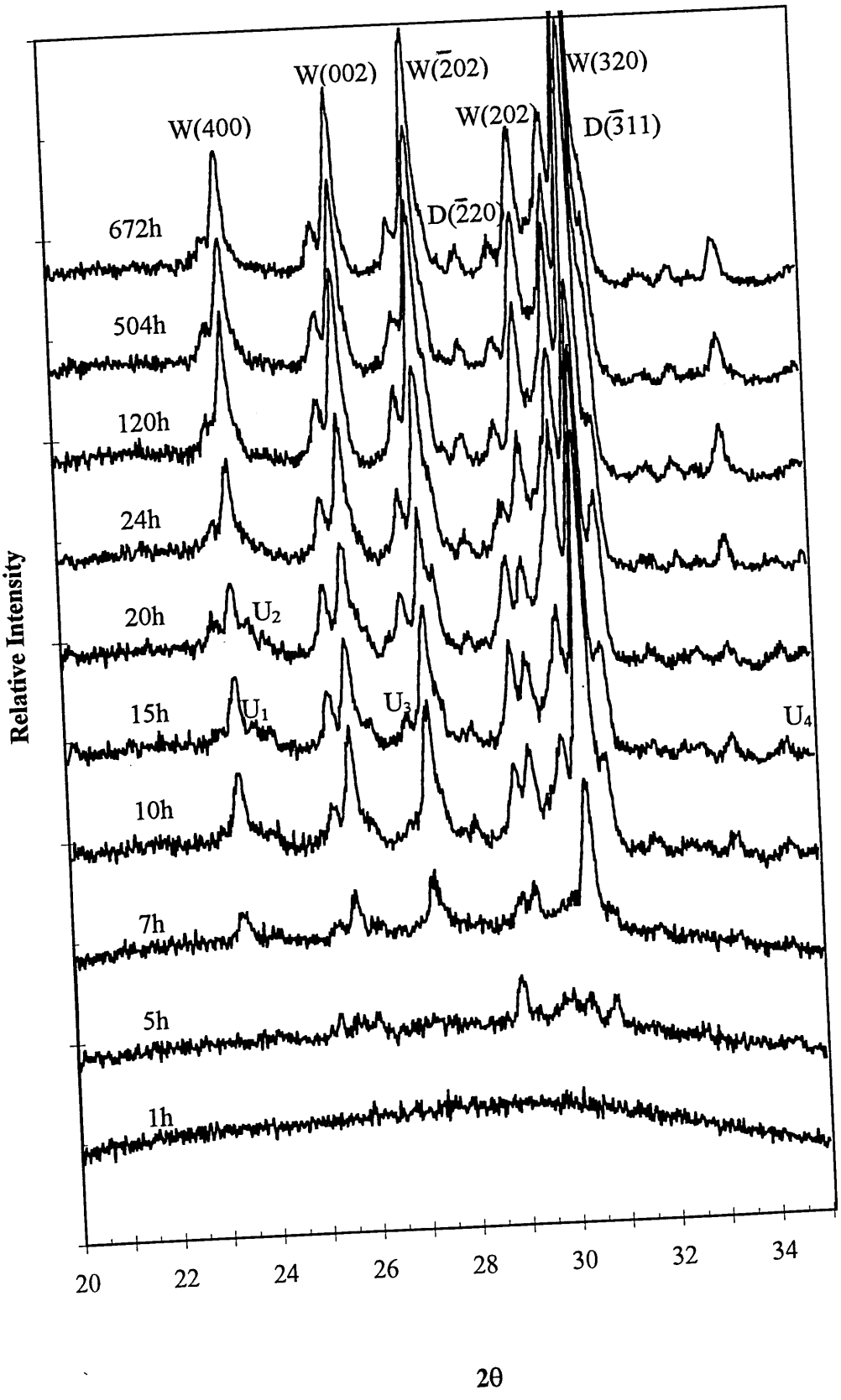

Figure 4-30 X-ray diffraction patterns for Superwool fibre devitrified at 850°C.

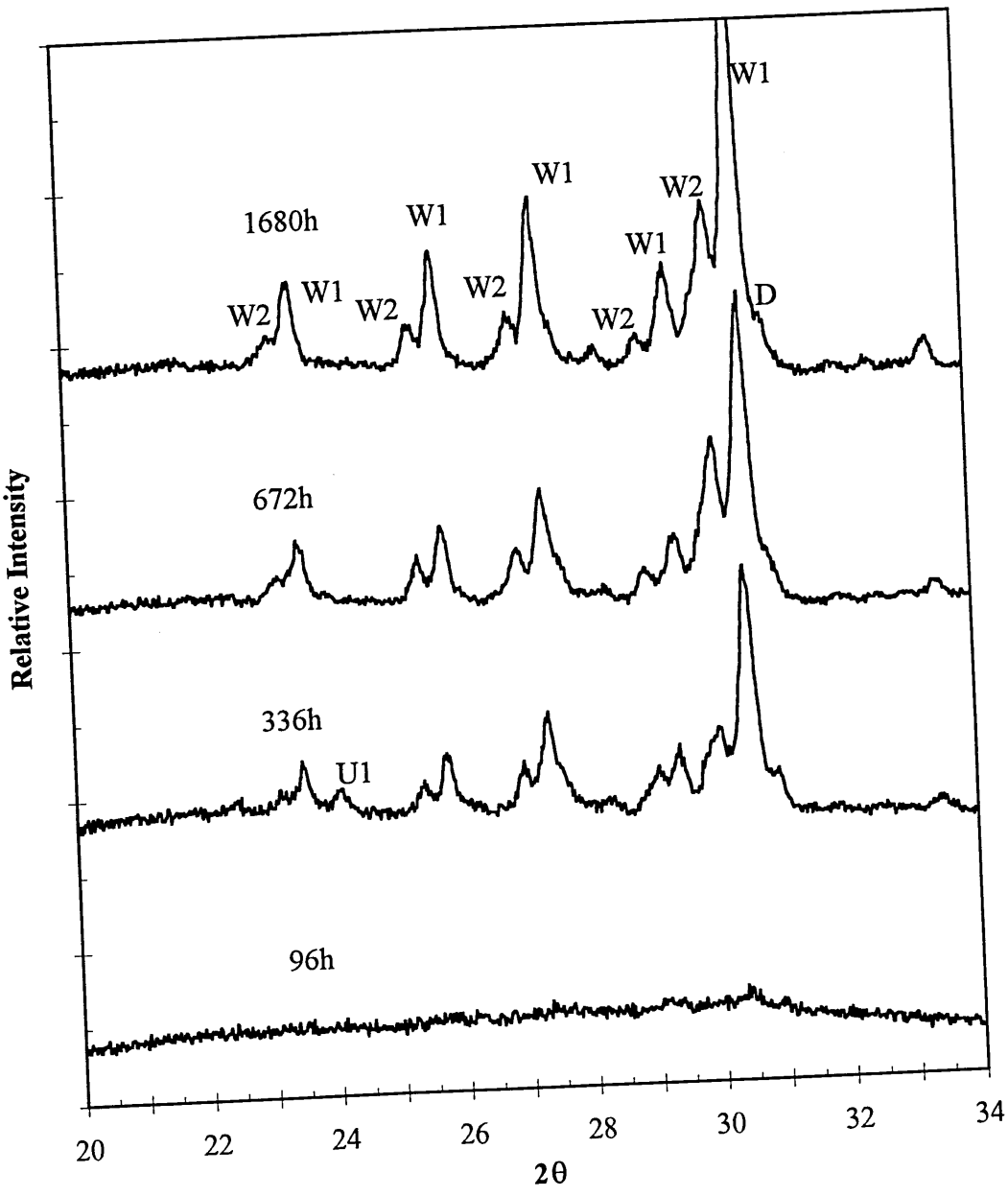

Figure 4-31 X-ray diffraction patterns for Superwool fibre devitrified at 800°C.

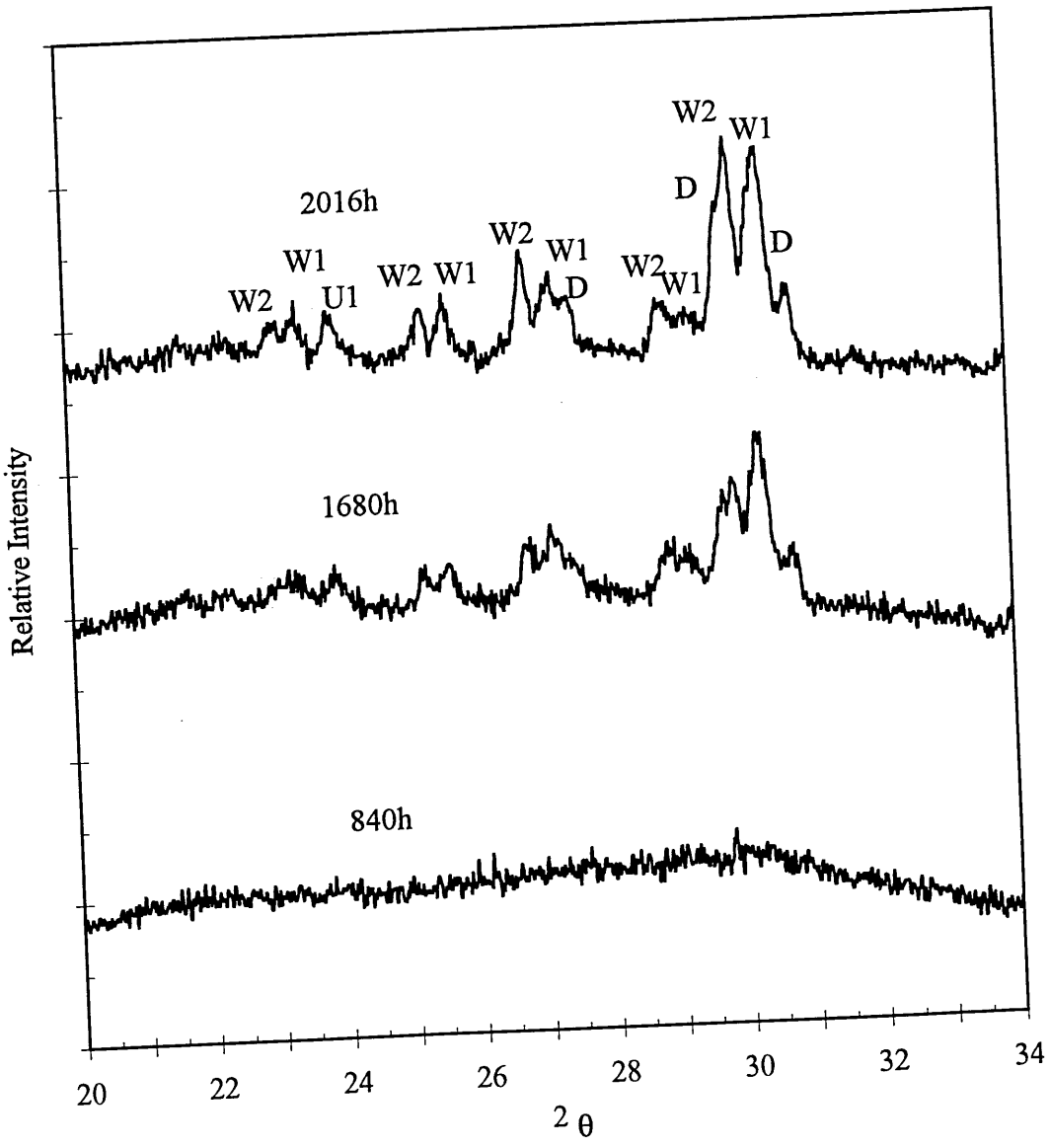

Figure 4-32 X-ray diffraction patterns for Superwool fibre devitrified at 750°C.

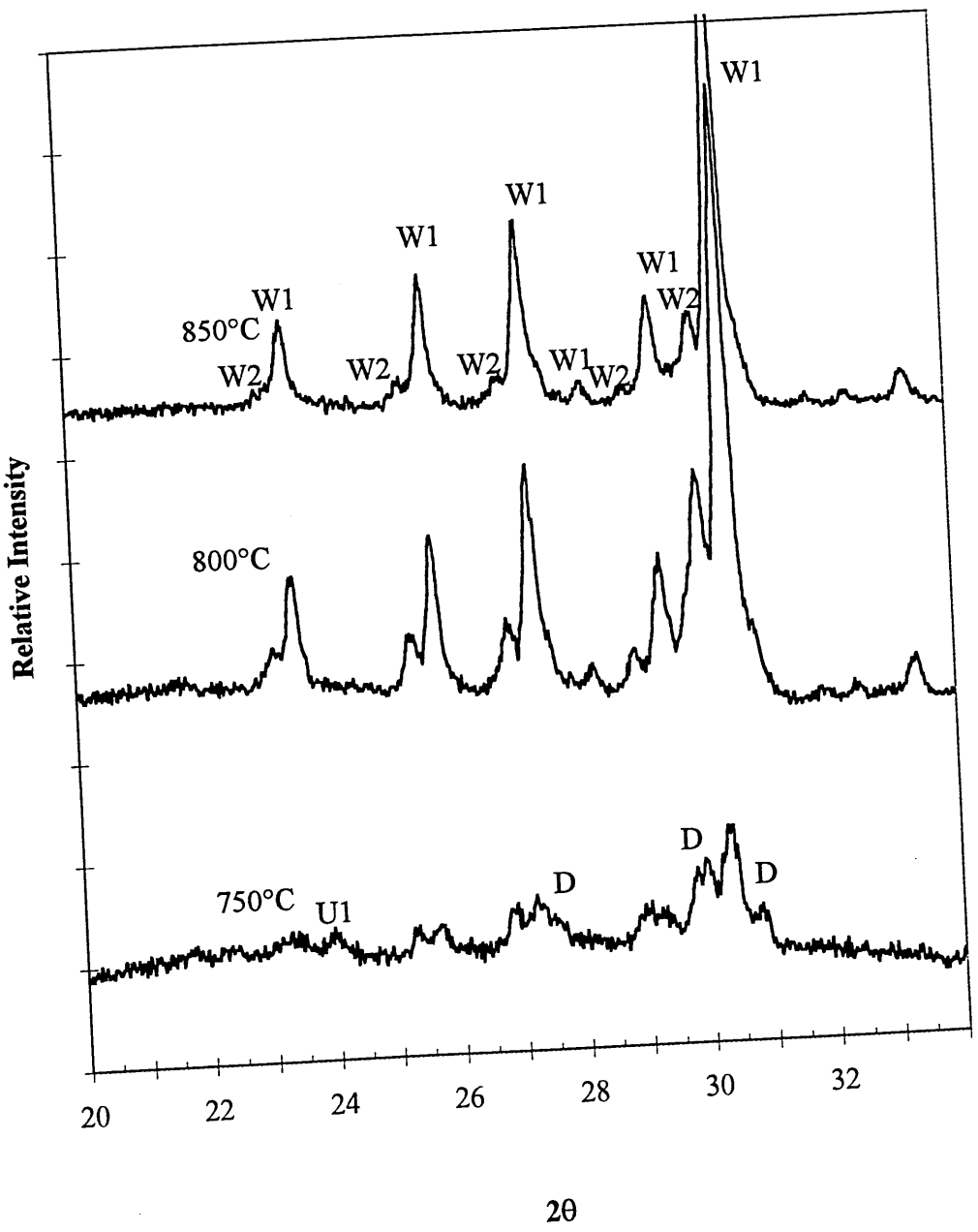

Figure 4-33 X-ray powder diffraction patterns for Superwool fibre devitrified for 1680 hours at 750°C, 800°C and 850°C respectively.

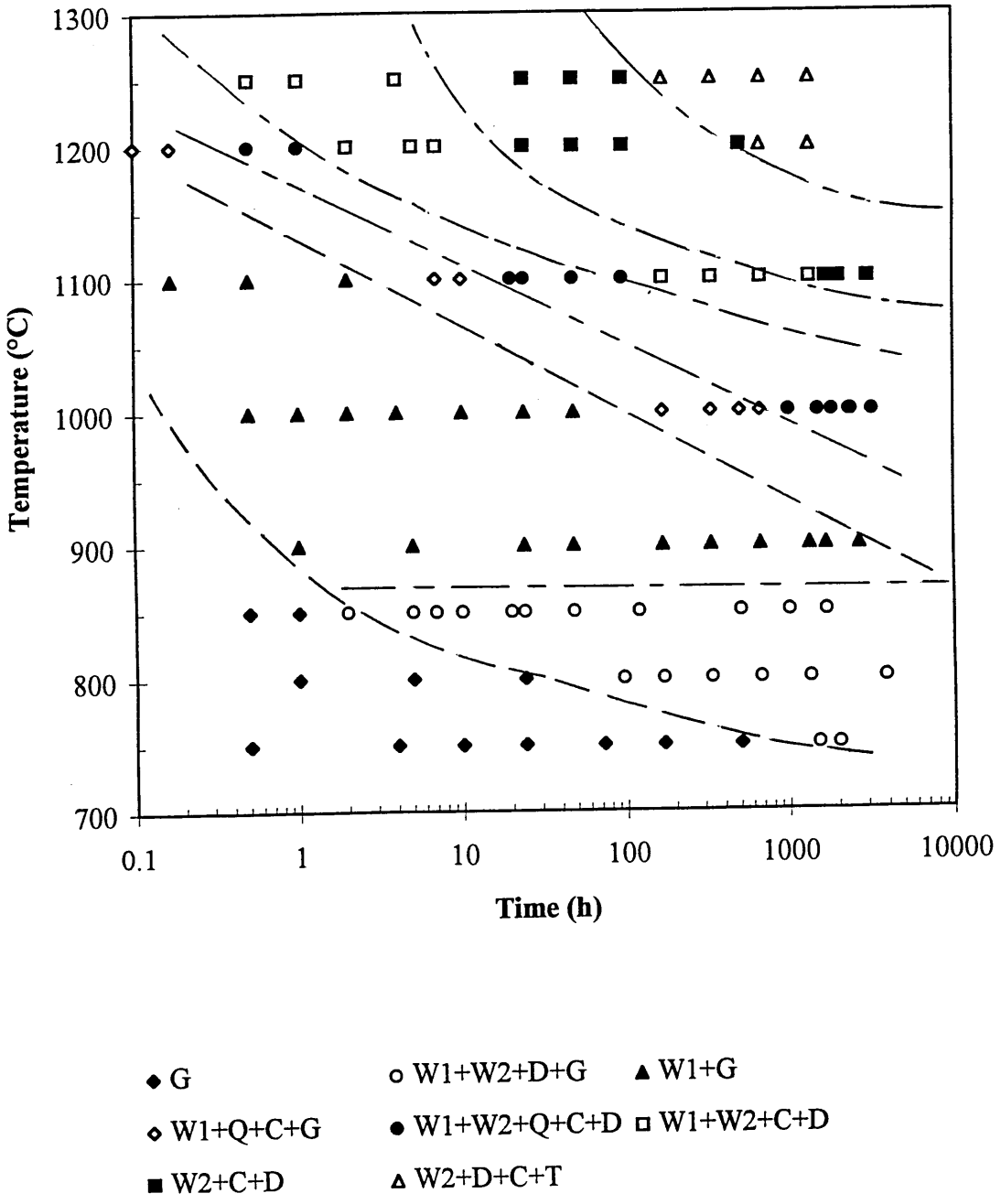

Figure 4-34 Exposure dependence of formation of devitrification products in Superwool fibre..

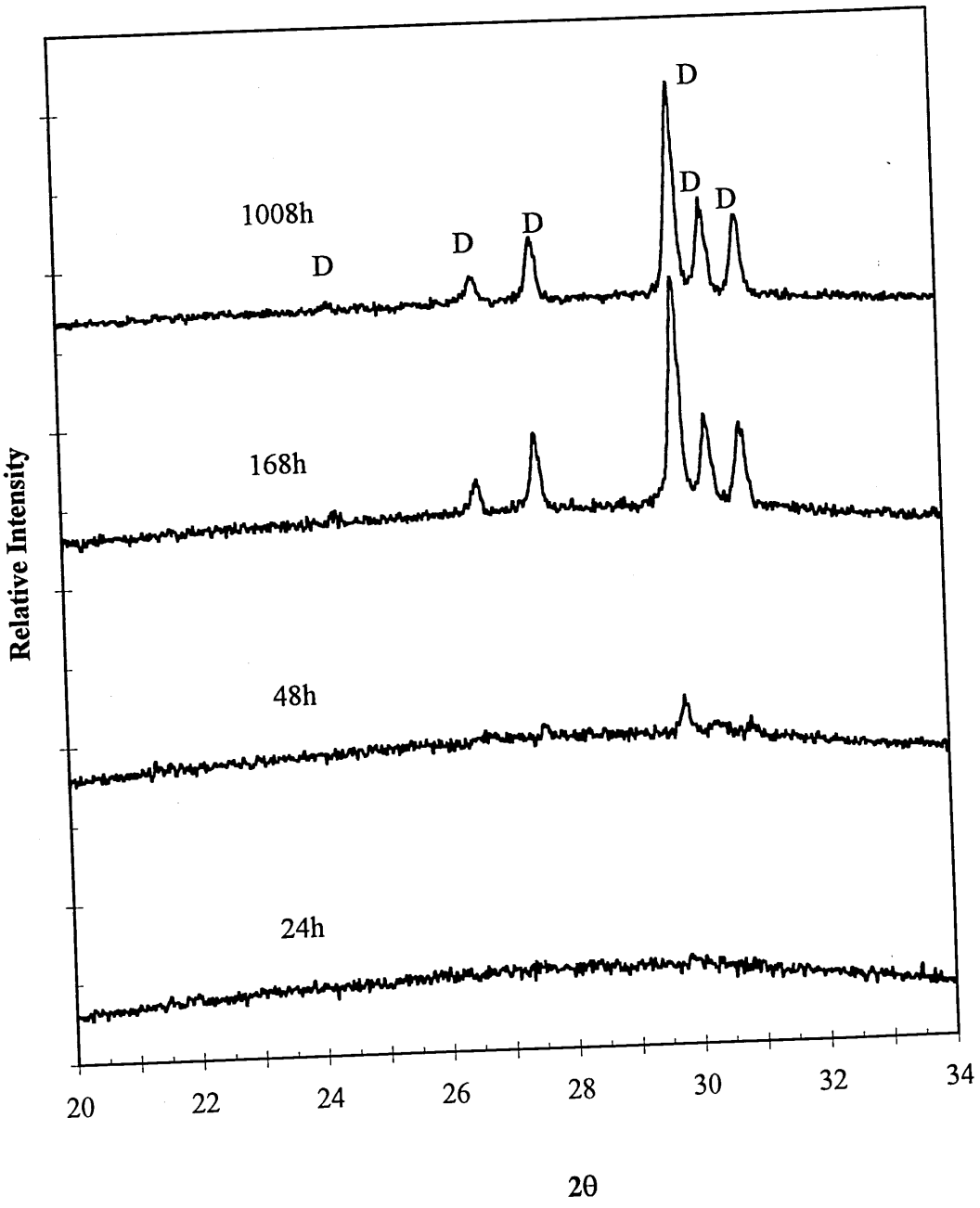

Figure 4-35 X-ray diffraction patterns for A2 fibres devitrified at 750°C for 24, 48, 168 and 1008 hours respectively

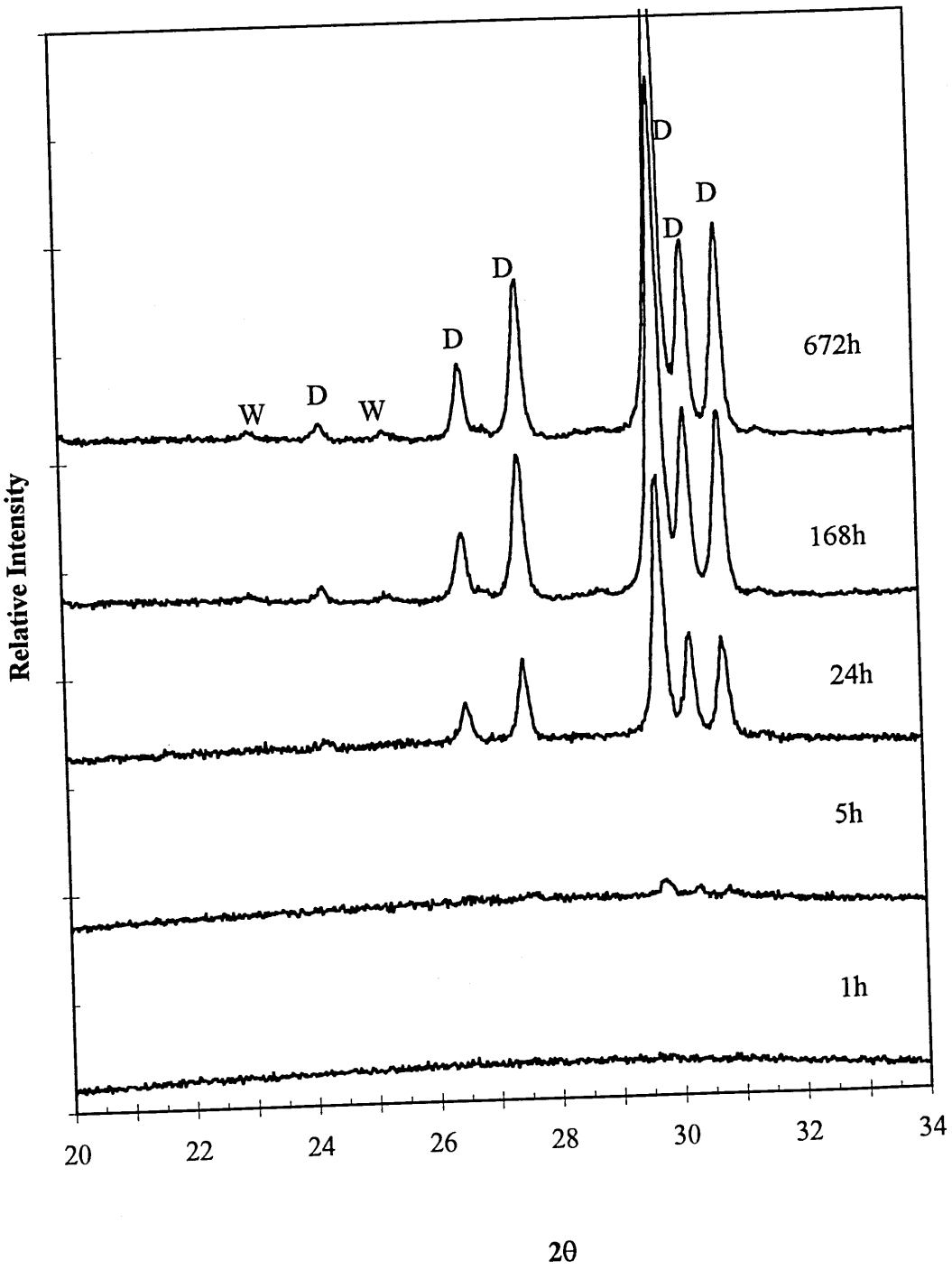

Figure 4-36 X-ray diffraction patterns for A2 fibre devitrified at 800°C for 1, 5, 24, 168 and 672 hours respectively.

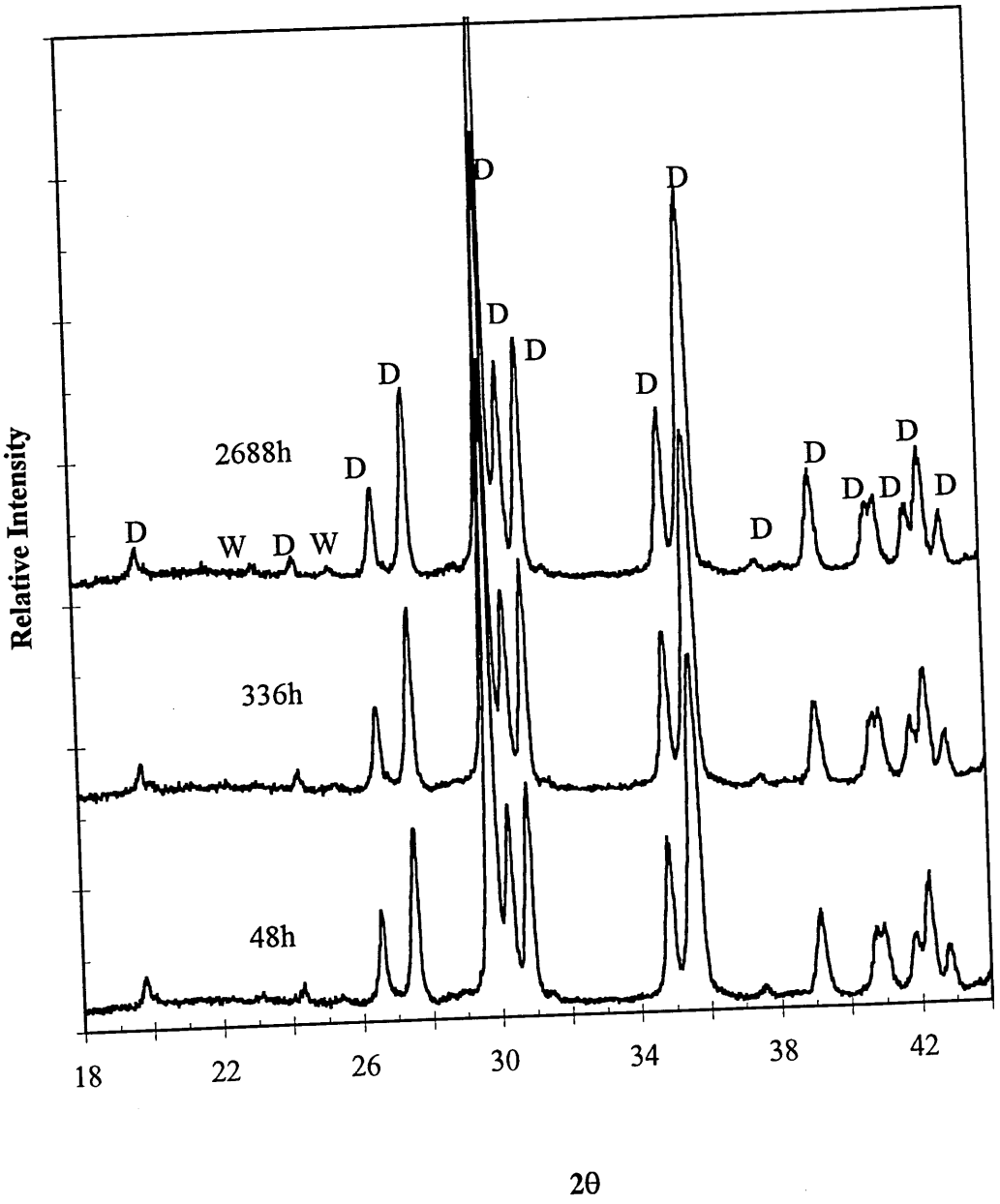

Figure 4-37 X-ray diffraction patterns for A2 fibres devitrified at 900°C for 48, 336 and 2688 hours.

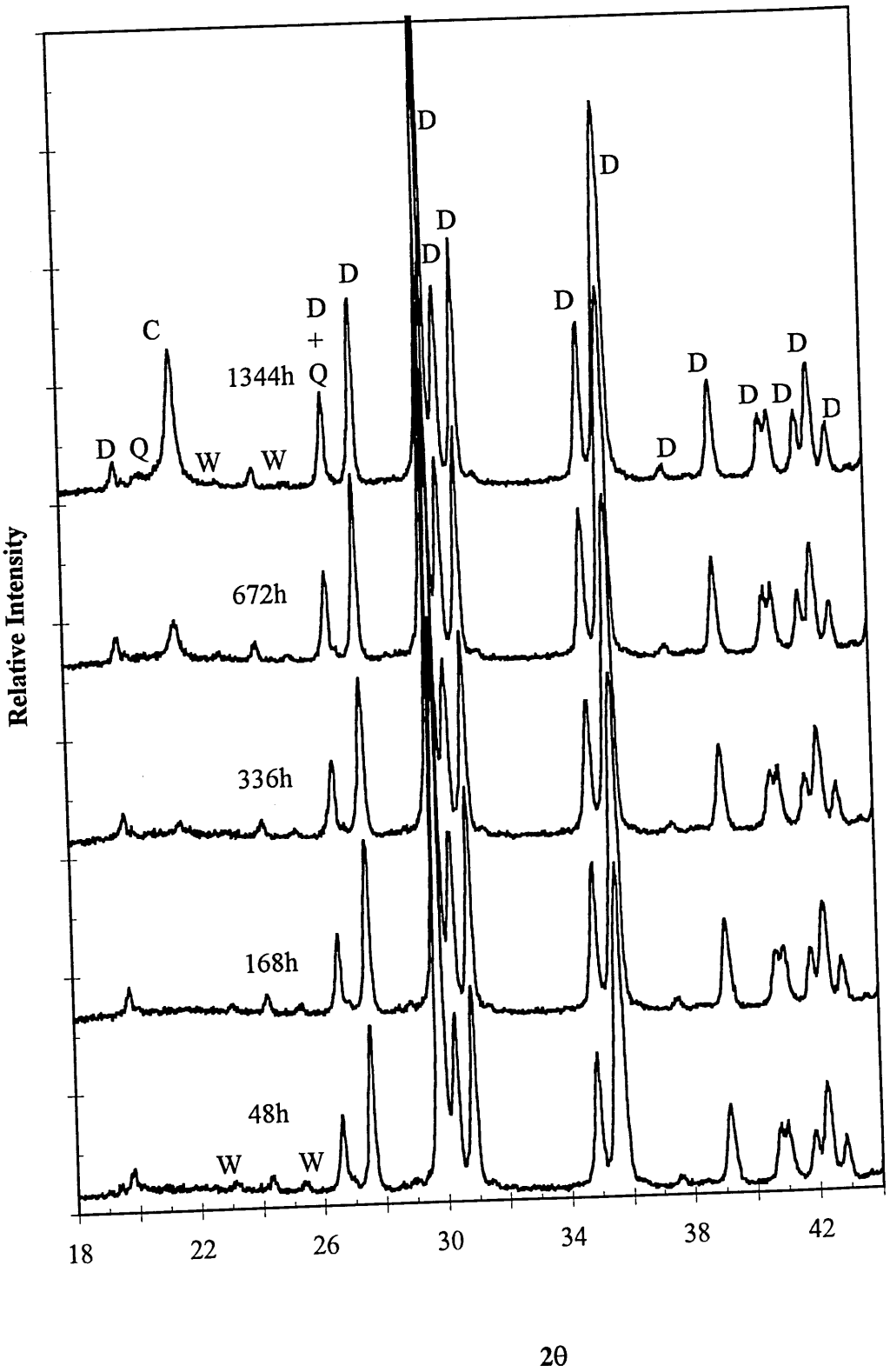

Figure 4-38 X-ray diffraction patterns for A2 fibres devitrified at 1000°C for 48, 168, 336, 672 and 1344 hours.

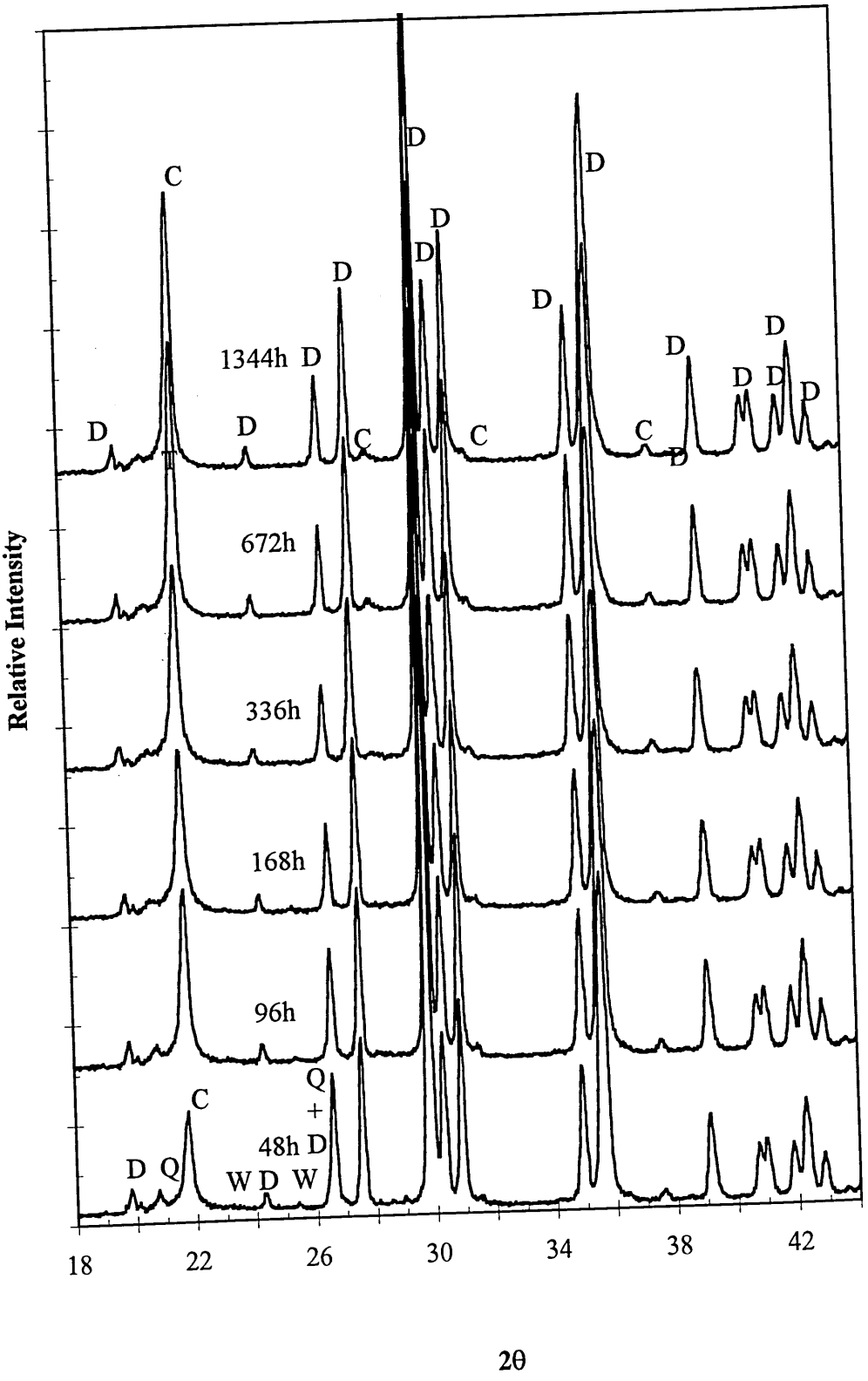

Figure 4-39 X-ray diffraction patterns for A2 fibres devitrified at 1100°C for 48, 96, 168, 336, 672 and 1344 hours.

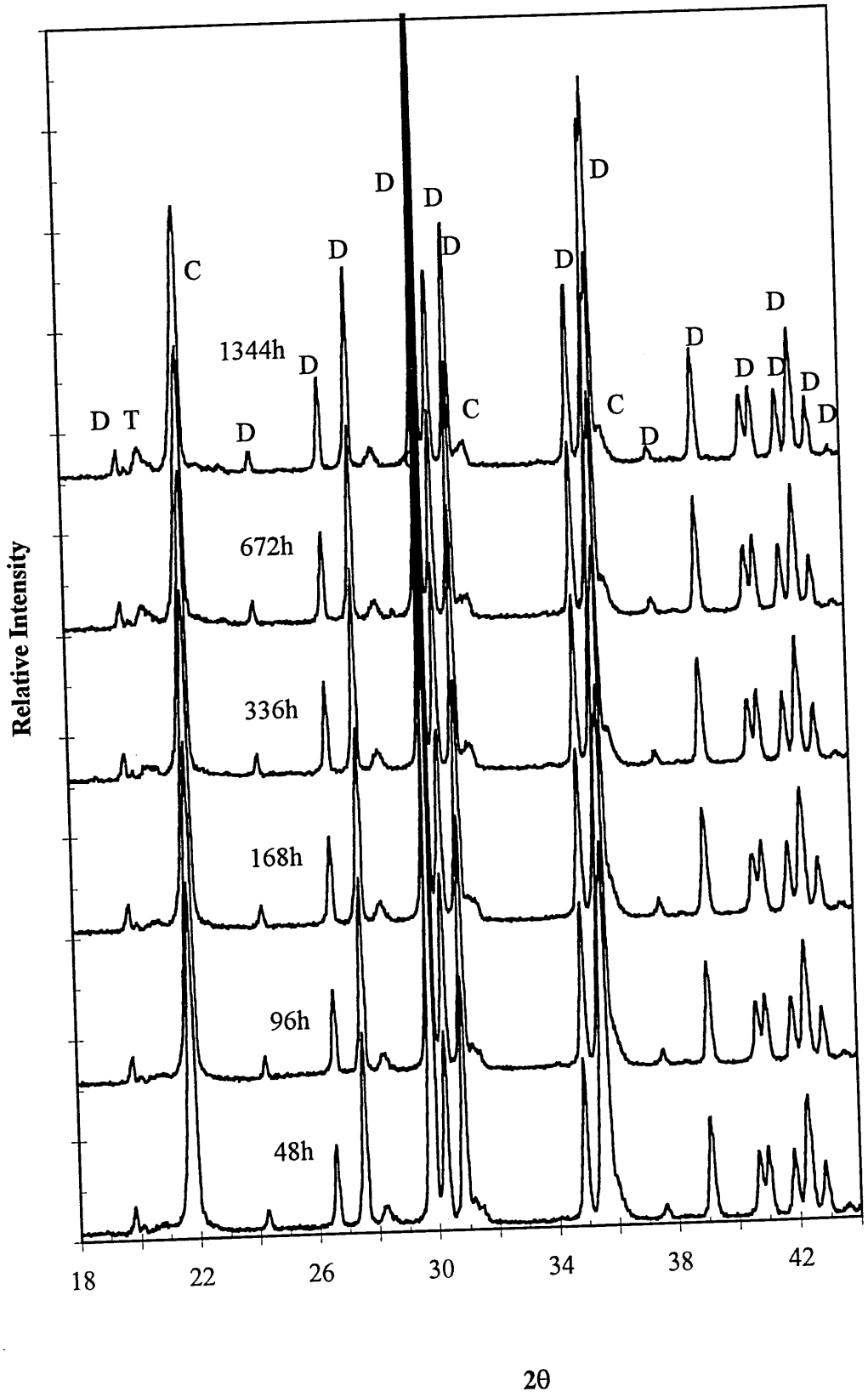

Figure 4-40 X-ray diffraction patterns for A2 fibres devitrified at 1250°C for 48, 96, 168, 336, 672 and 1344 hours.

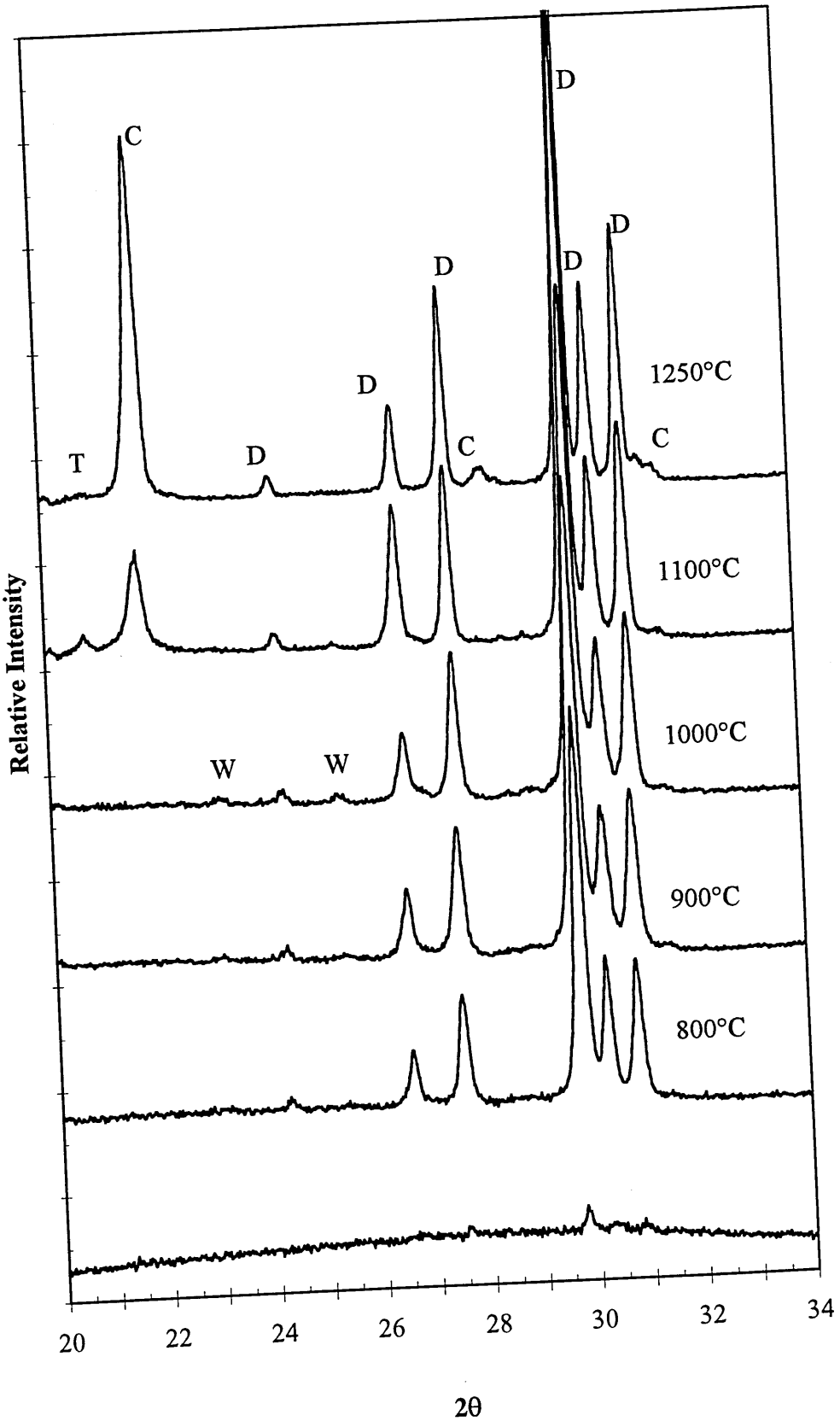

Figure 4-41 X-ray diffraction patterns for A2 fibres devitrified at 750°C, 800°C, 900°C, 1000°C, 1100°C and 1250°C for 48 hours.

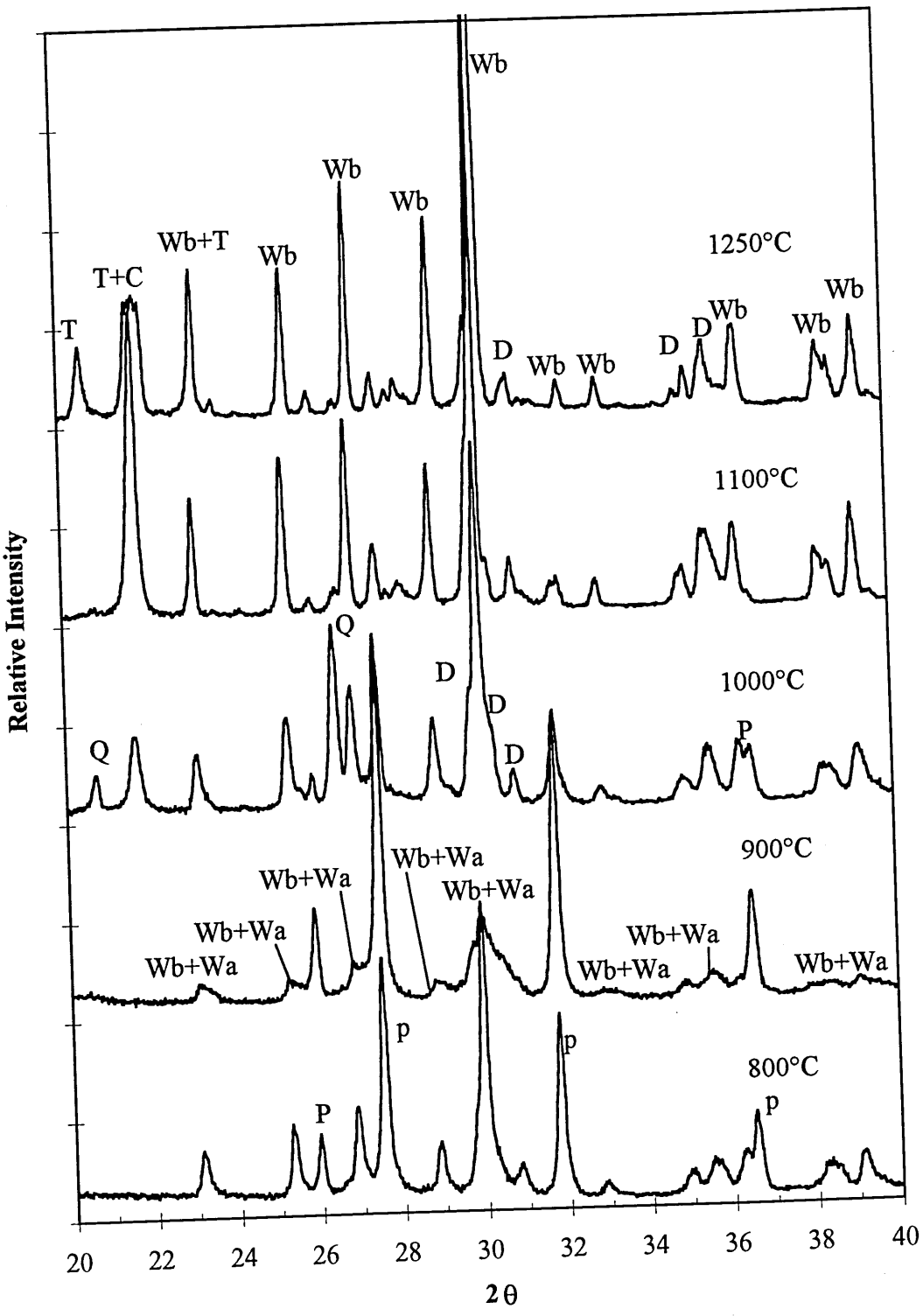

Figure 4-43 X-ray diffraction patterns for B3 fibres devitrified for 672 hours at 800°C, 900°C, 1000°C, 1100°C and 1250°C.

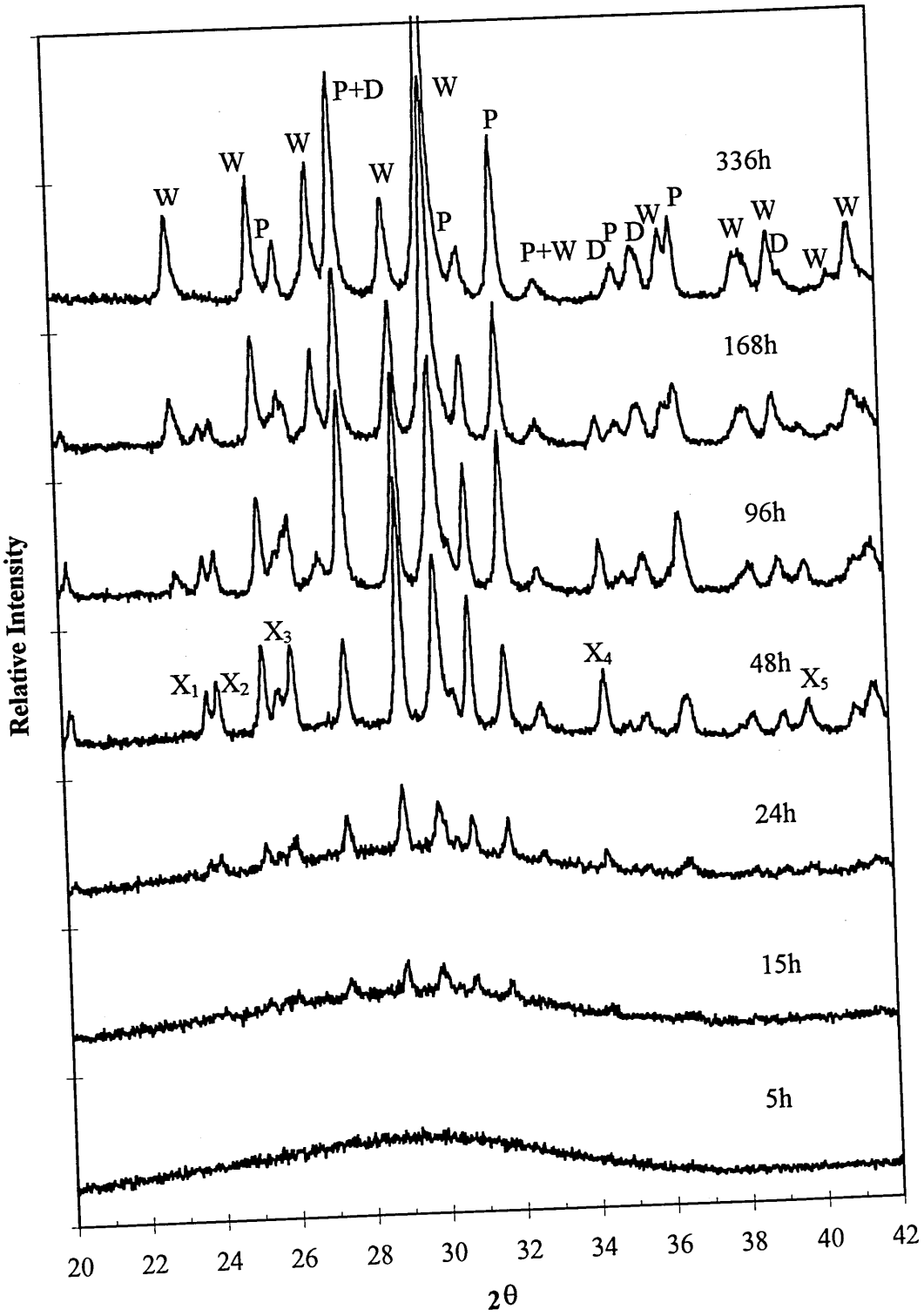

Figure 4-44 X-ray diffraction patterns for B3 fibres devitrified at 800°C for 5, 15, 24, 48, 96, 168 and 336 hours.

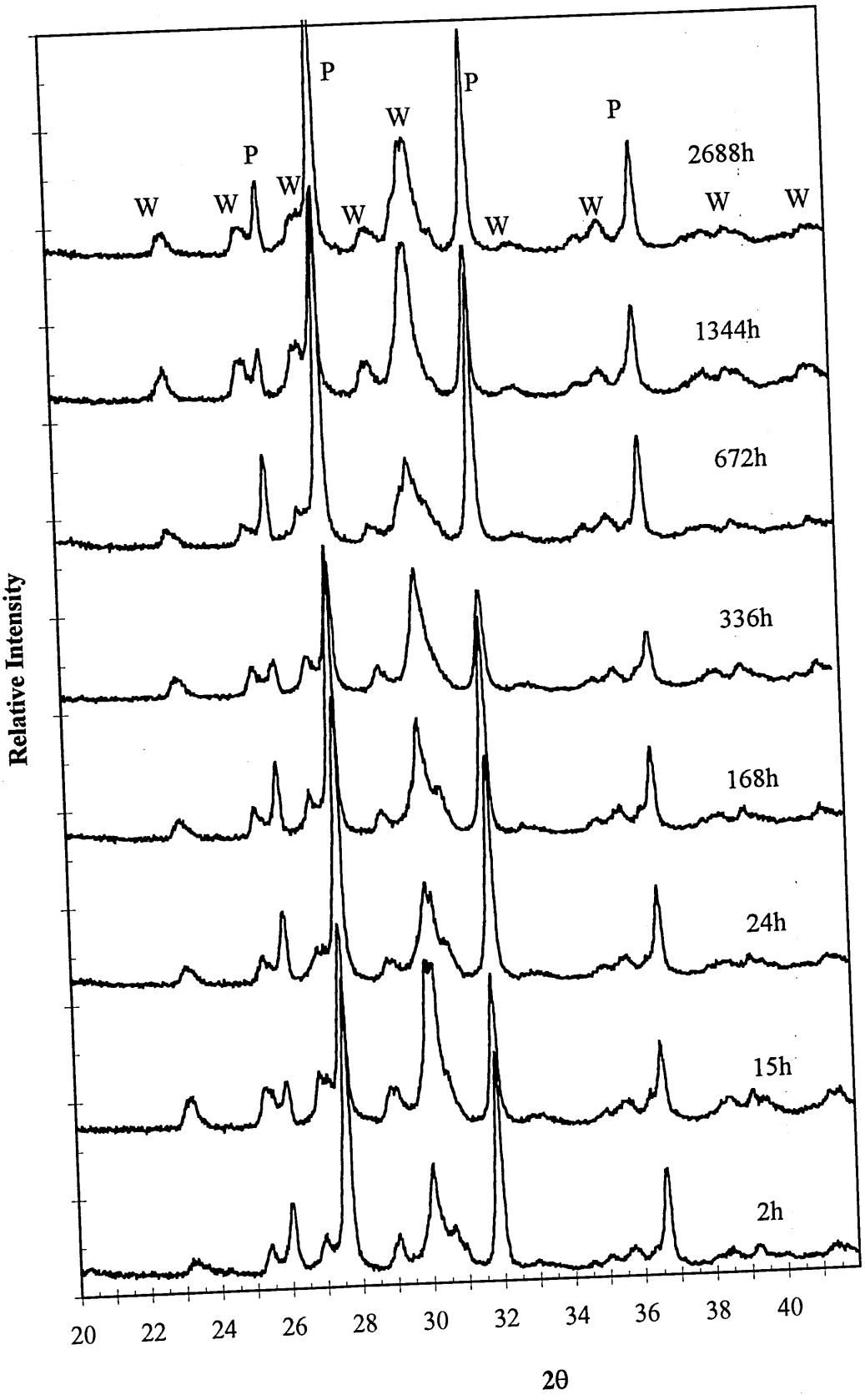

Figure 4-44 X-ray diffraction patterns for B3 fibres devitrified at 900°C.

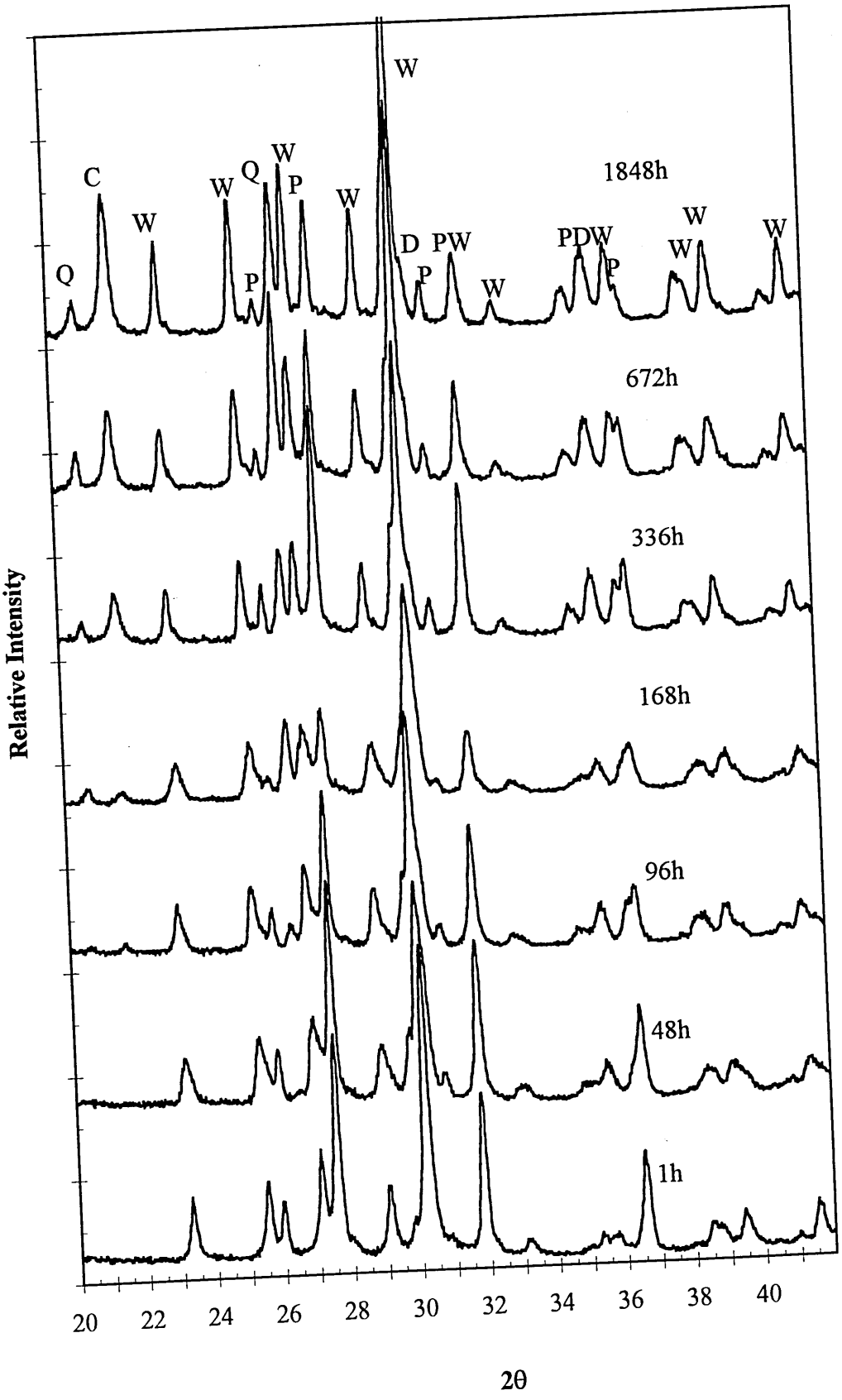

Figure 4-46 X-ray diffraction patterns for B3 fibres after exposed at 1000°C

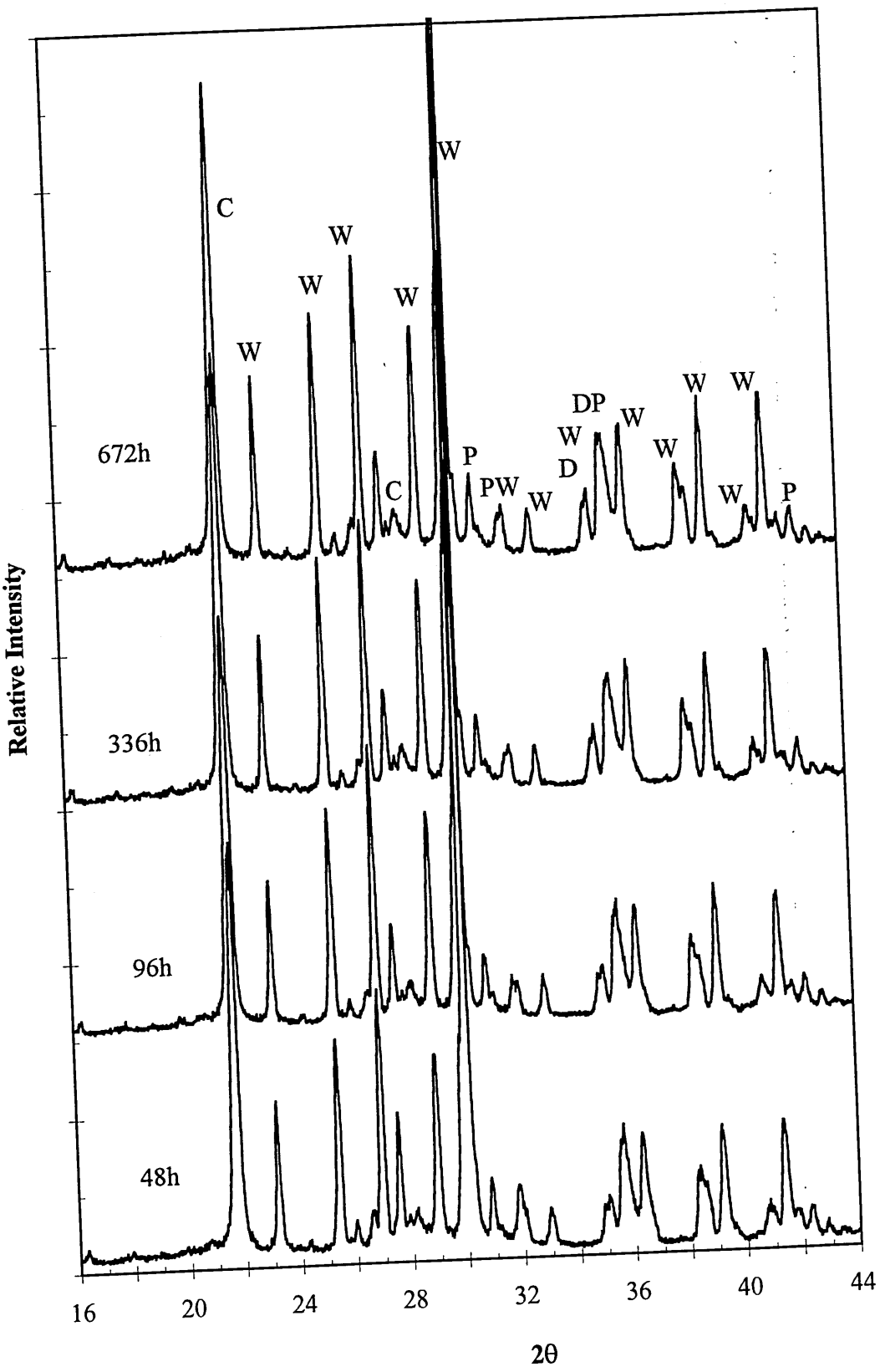

Figure 4-47 X-ray diffraction patterns of B3 fibres after exposed at 1100°C.

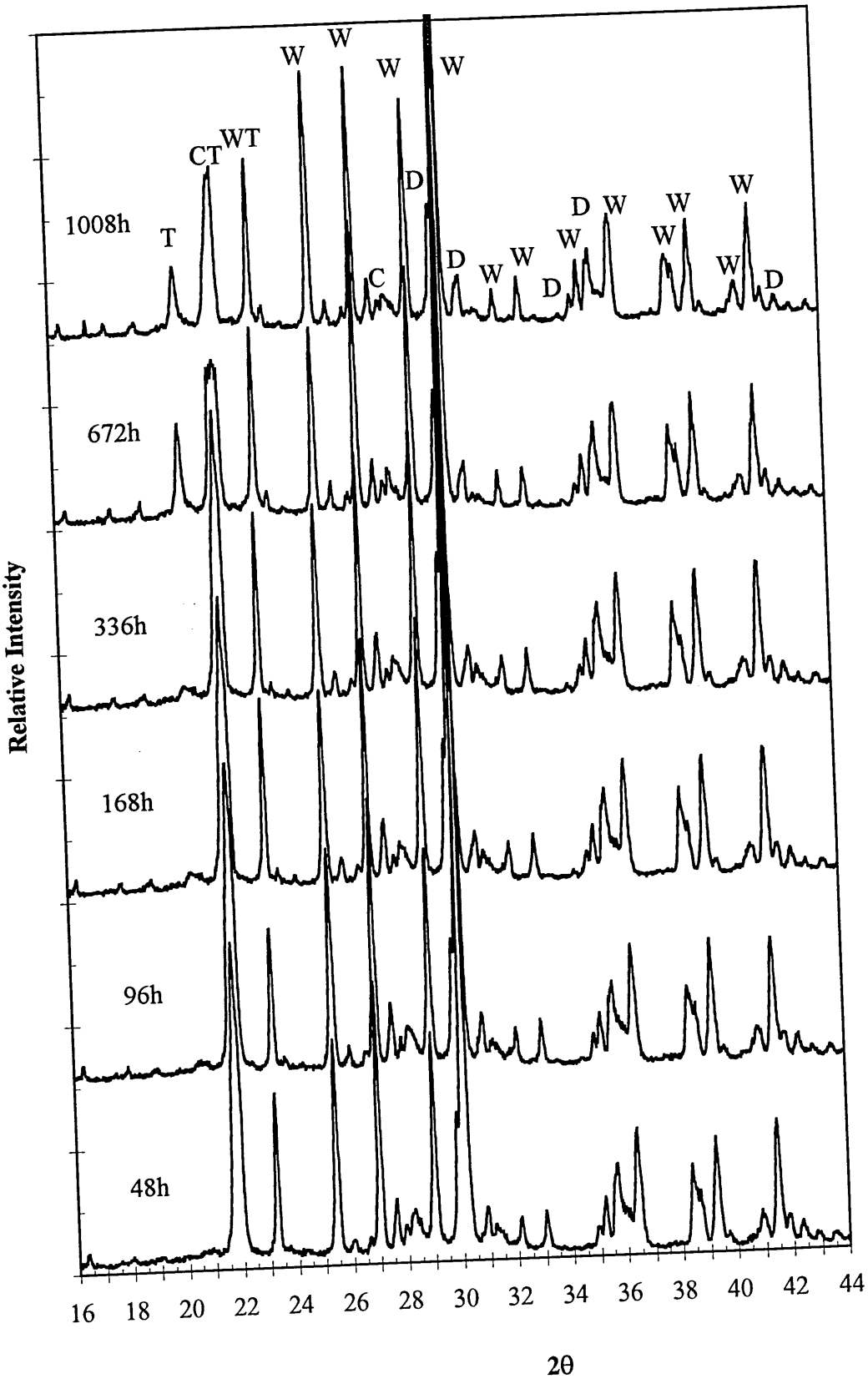

Figure 4-48 X-ray diffraction patterns for fibre B3 after exposed at 1250°C

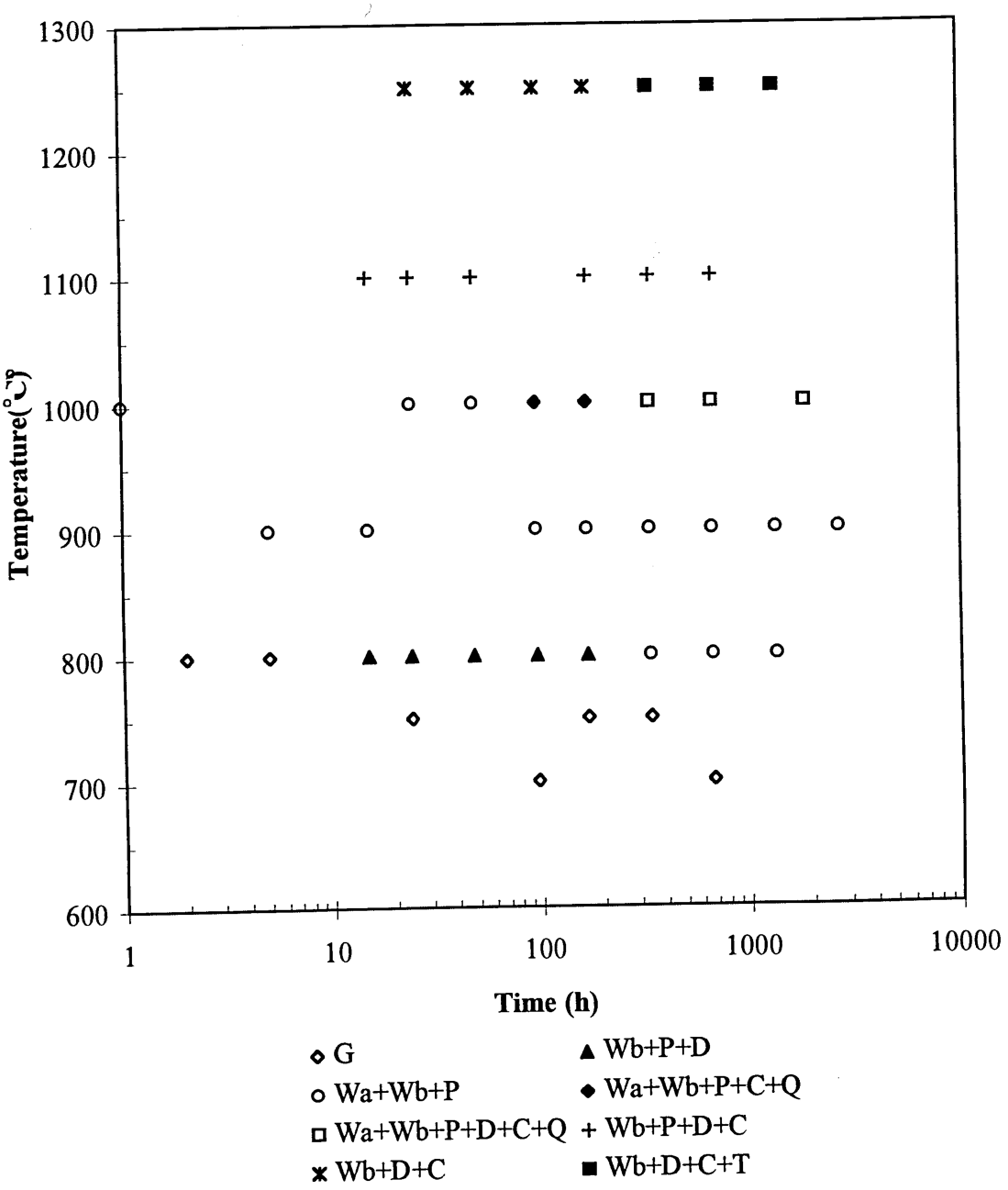

Figure 4-49 Exposure conditions dependence of formation of crystalline phases in B3 fibre.

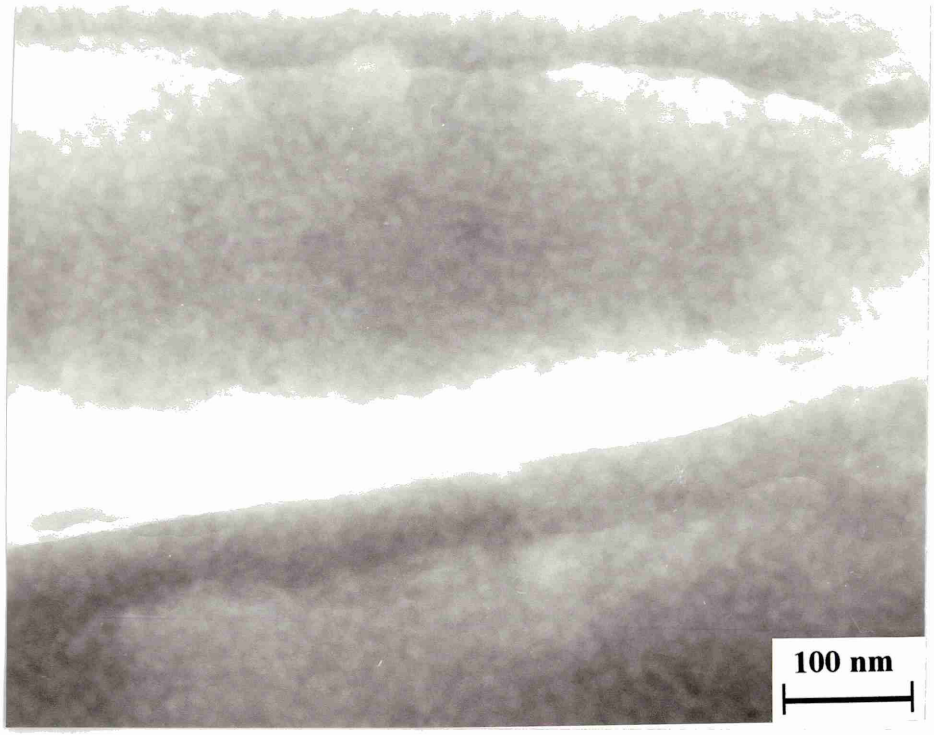

Figure 4-50a. Microstructure of Superwool fibre devitrified at 750°C for 4 hours.

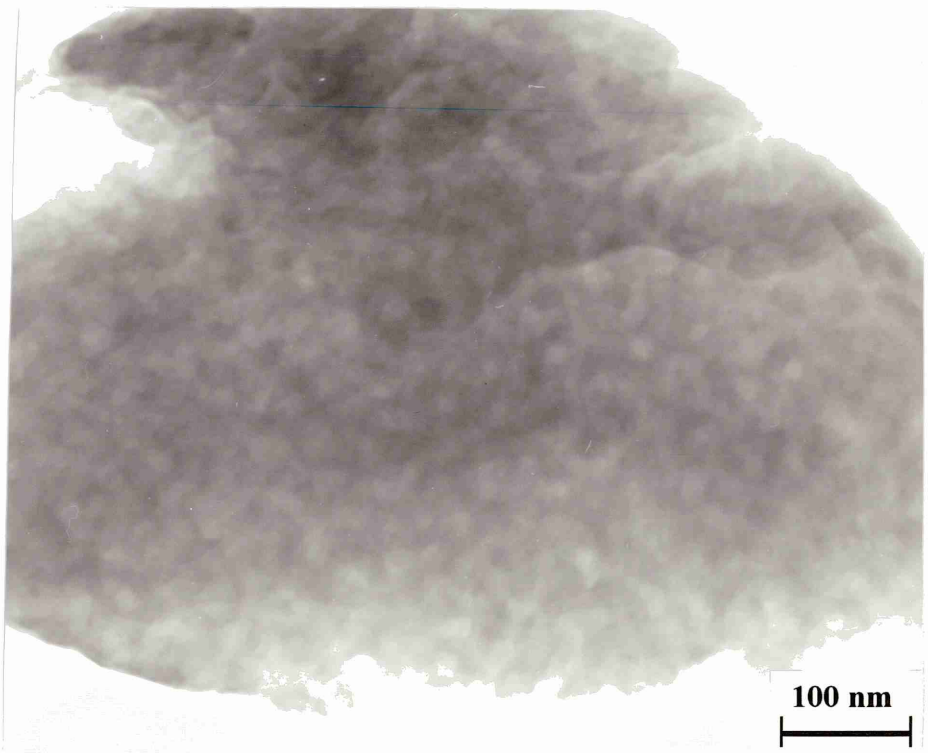

Figure 4-50b. Microstructure of Superwool fibre devitrified at 750°C for 24 hours.

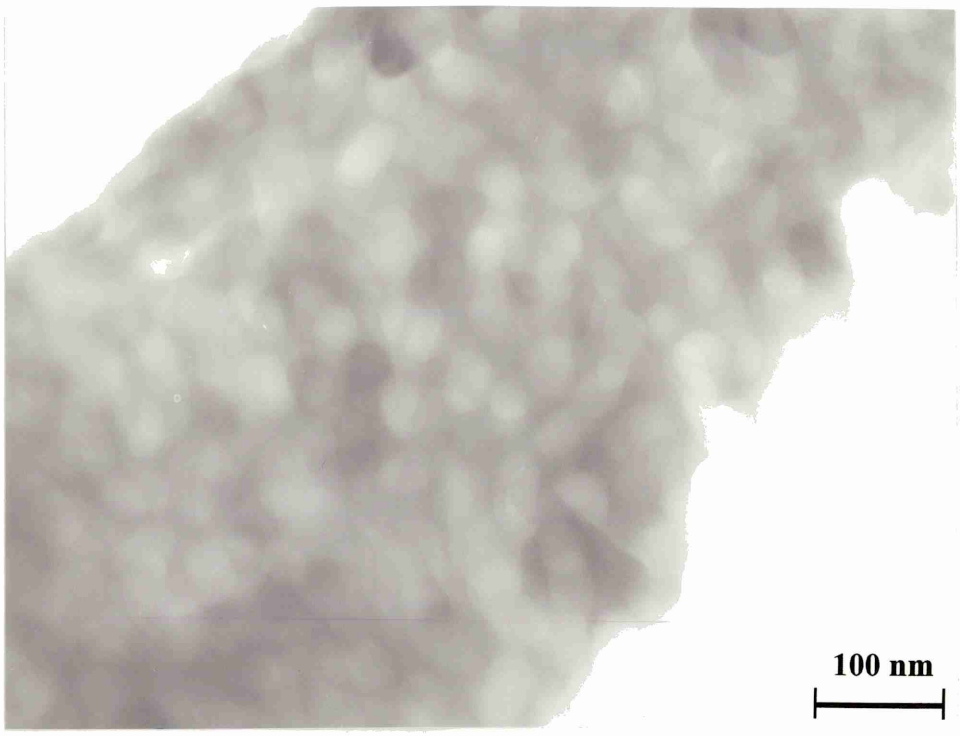

Figure 4-50c. Microstructure of Superwool fibre devitrified at 750°C for 168 hours.

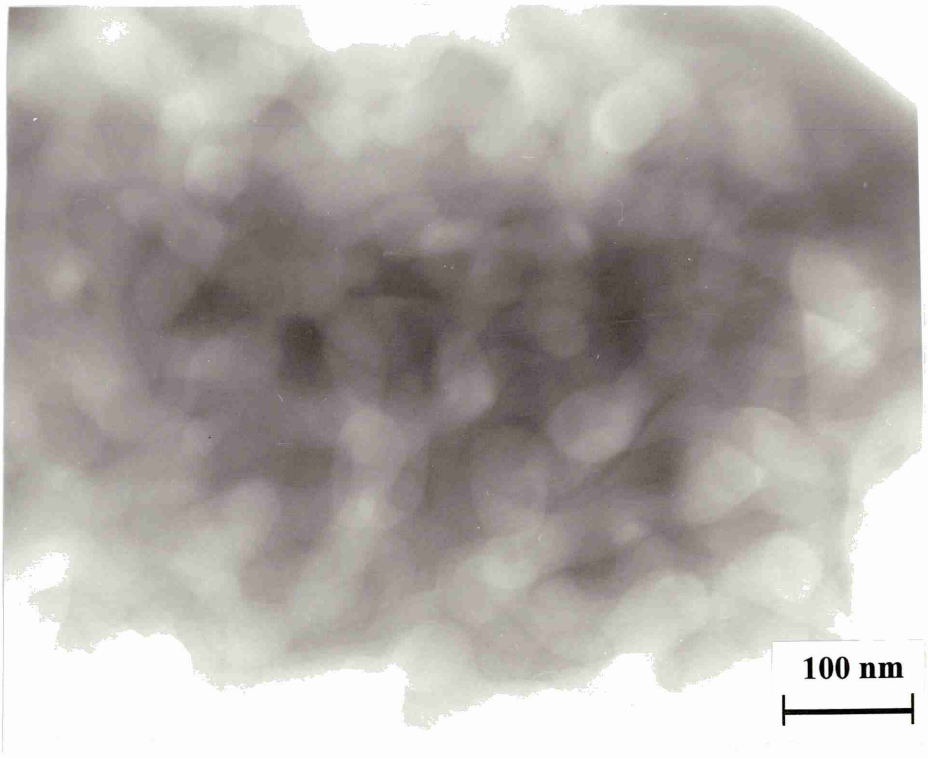

Figure 4-50d. Microstructure of Superwool fibre devitrified at 750°C for 336 hours.

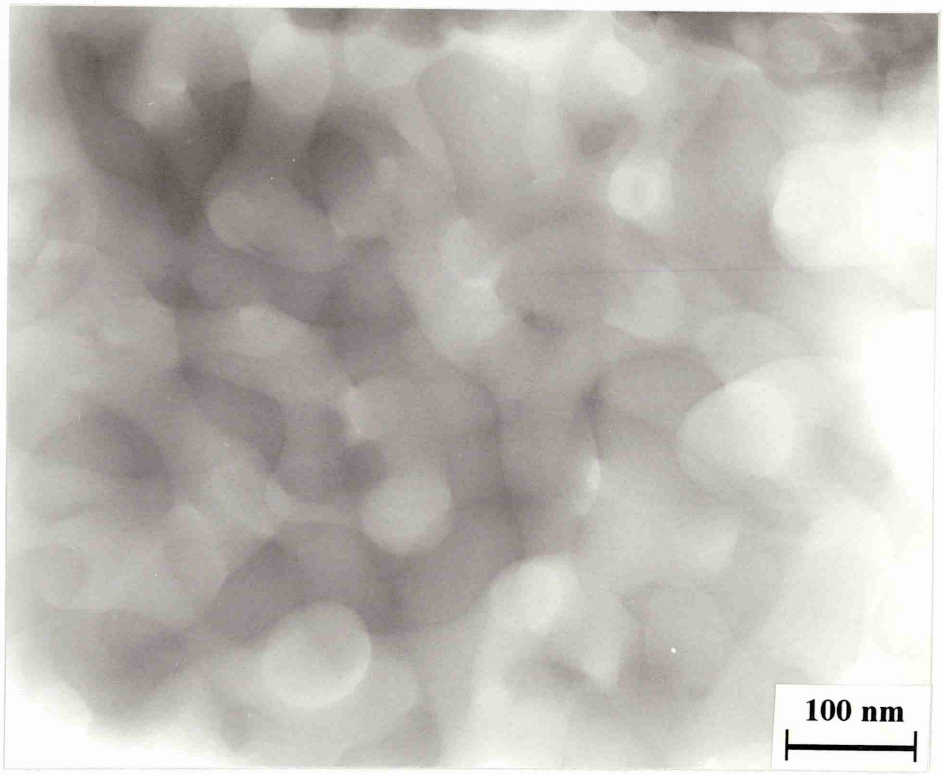

Figure 4-50e. Microstructure of Superwool fibre devitrified at 750°C for 504 hours.

Figure 4-50. Development of microstructure with time in Superwool fibres at 750°C.

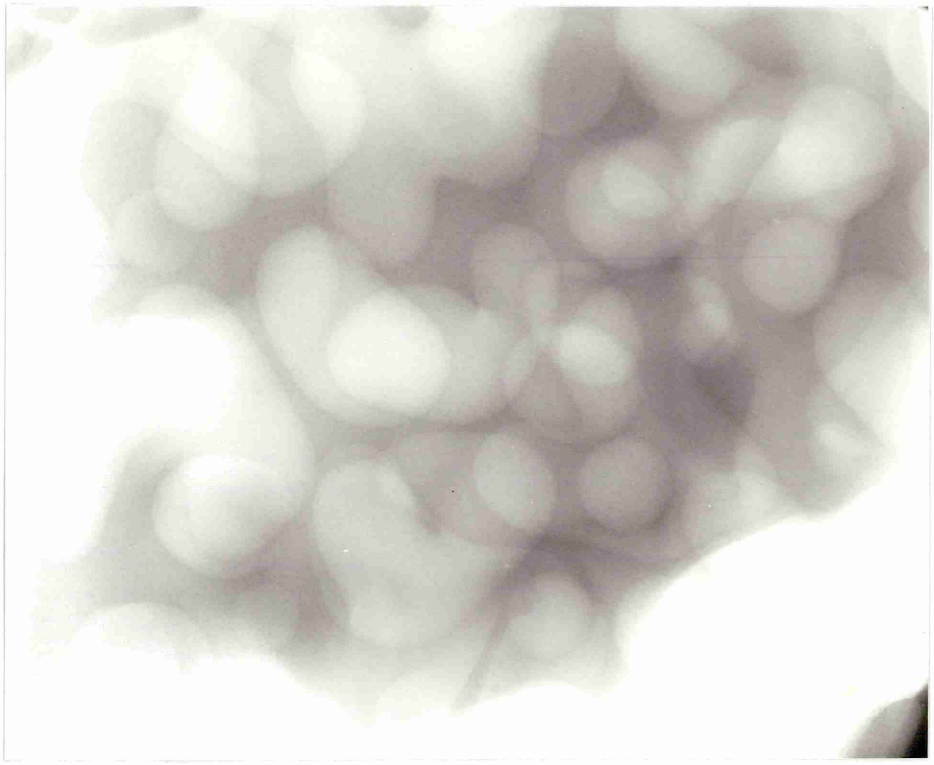

Figure 4-51. Microstructure of a shot particle devitrified at 750°C for 504 hours.

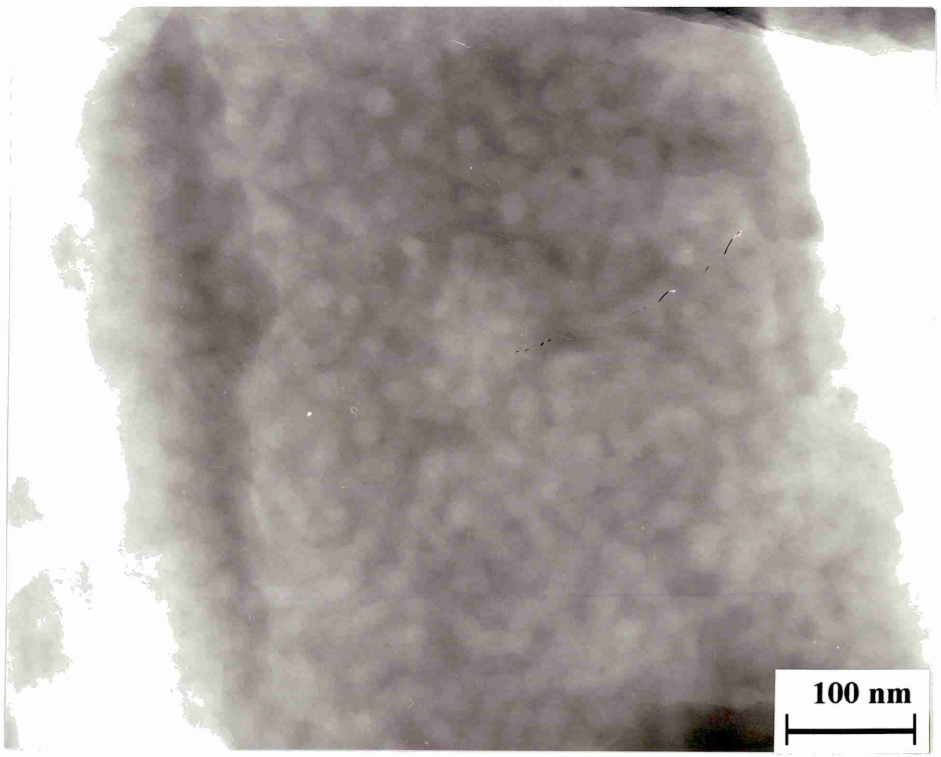

Figure 4-52a. Microstructure of Superwool fibre devitrified at 800°C for 1 hour.

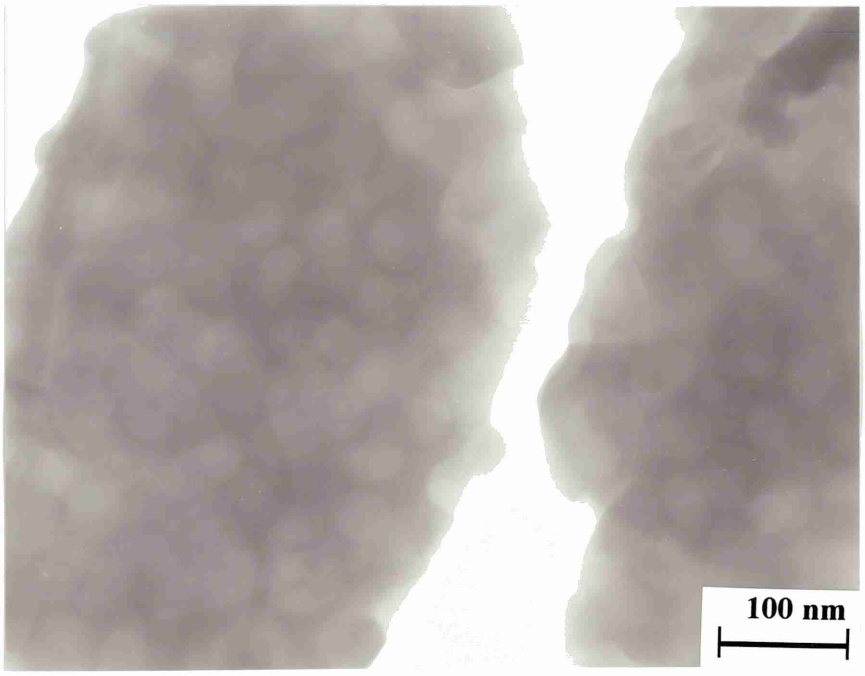

Figure 4-52b. Microstructure of Superwool fibre devitrified at 800°C for 5 hours

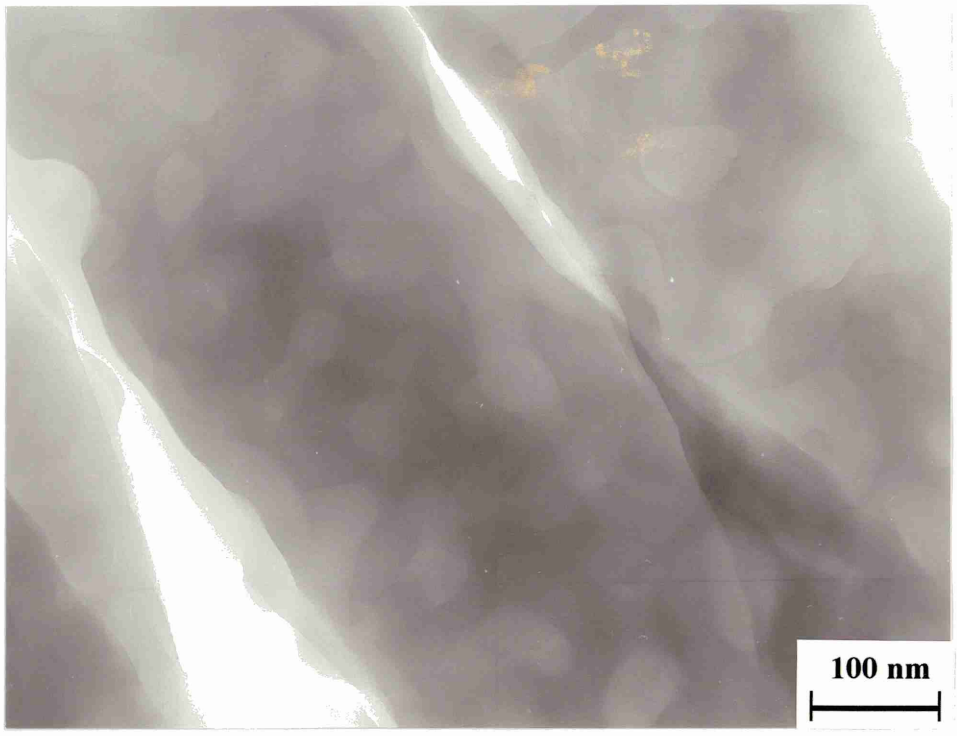

Figure 4-52c. Microstructure of Superwool fibre devitrified at 800°C for 24 hours.

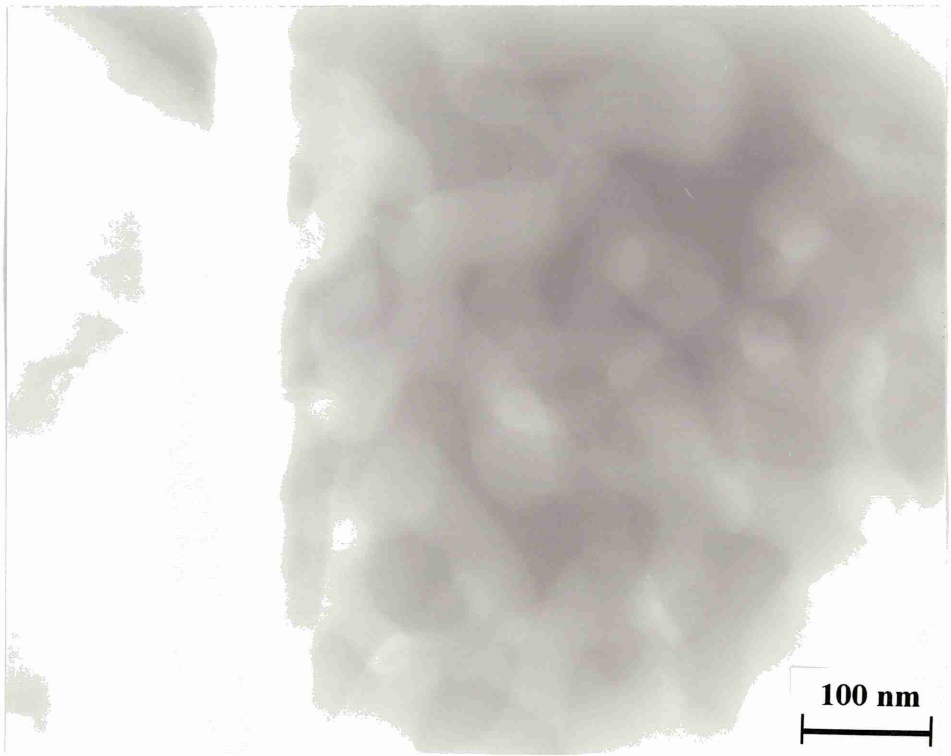

Figure 4-52d. Microstructure of Superwool fibre devitrified at 800°C for 48 hours.

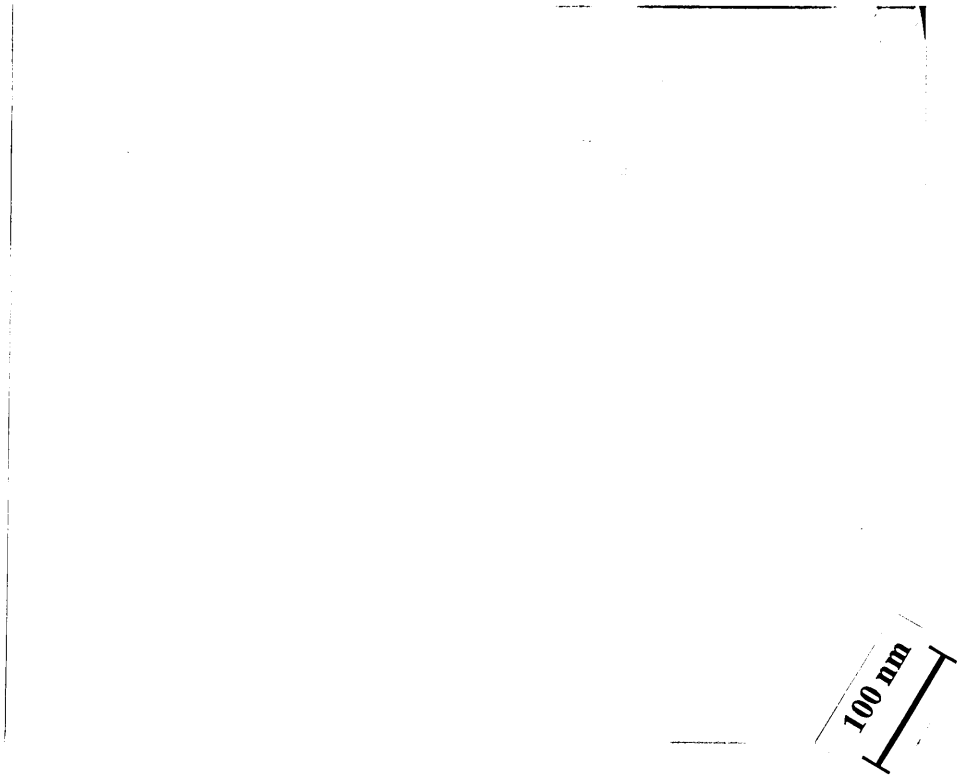

Figure 4-52e Skeleton structure found in the exposed Superwool fibre.

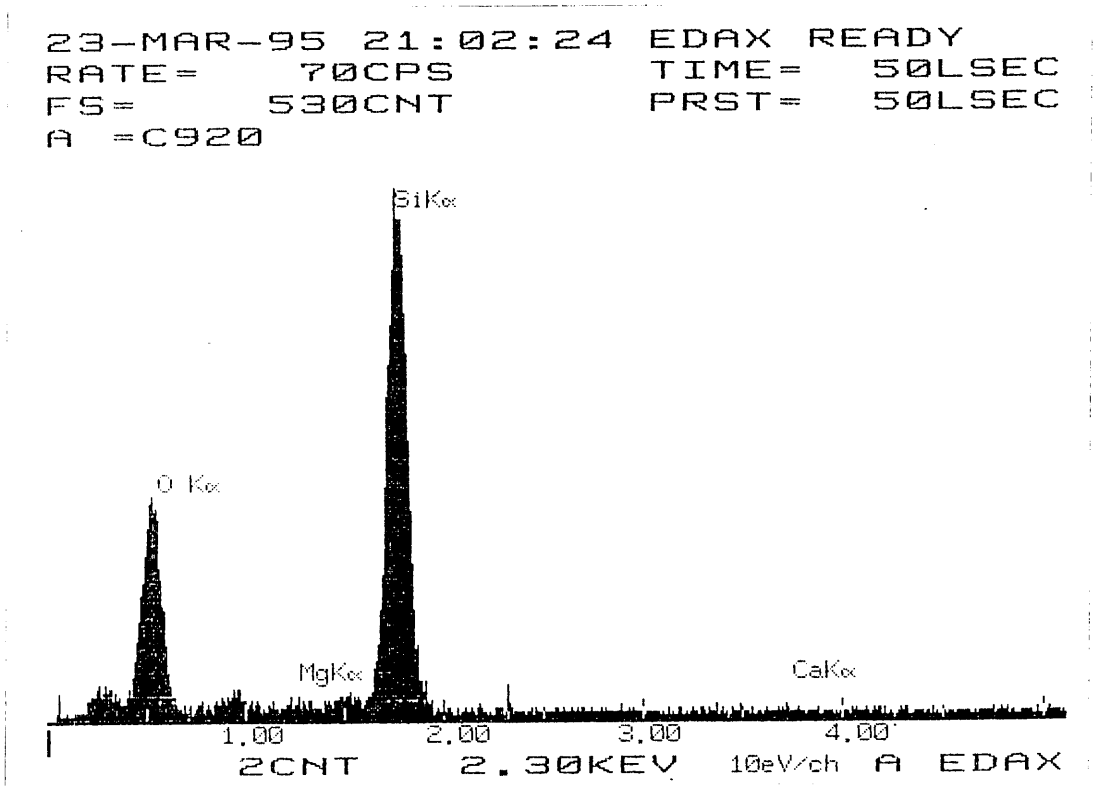

Figure 4-52f EDS spectrum corresponding to the phase shown in figure e.

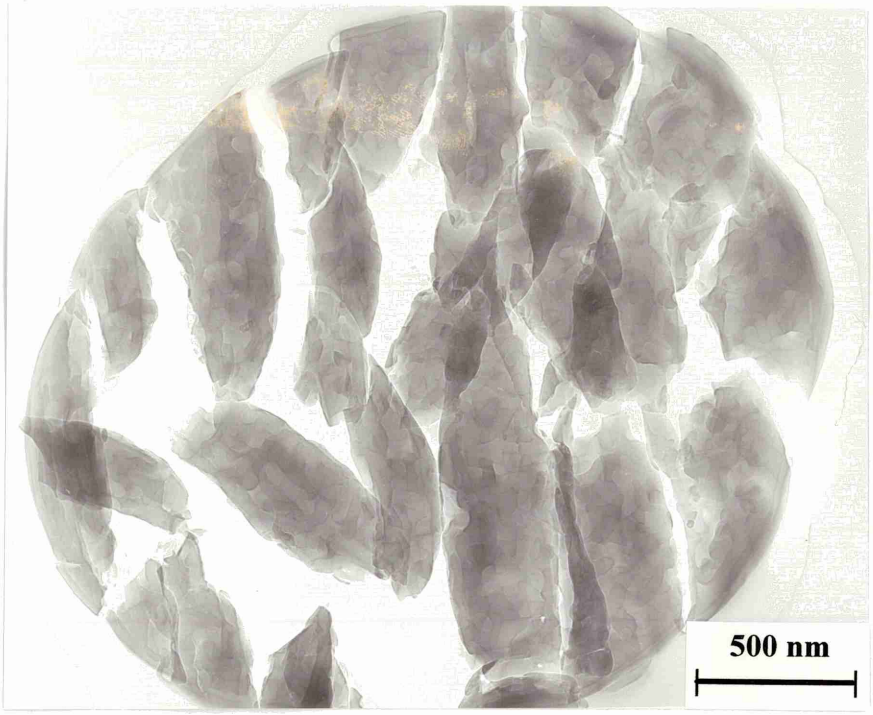

Figure 4-52g Cross section of a fibre devitrified at 800°C for 96 hours.

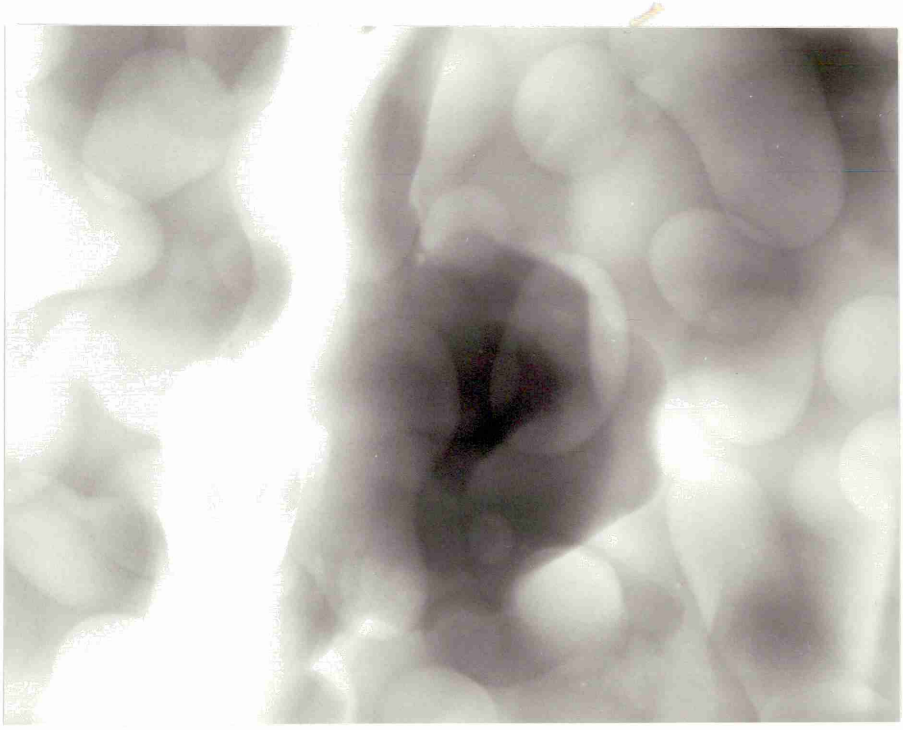

Figure 4-52h Microstructure of Superwool fibre devitrified at 800°C for 96 hours.

Figure 52 Development of phase separation with time in Superwool fibre at 800°C.

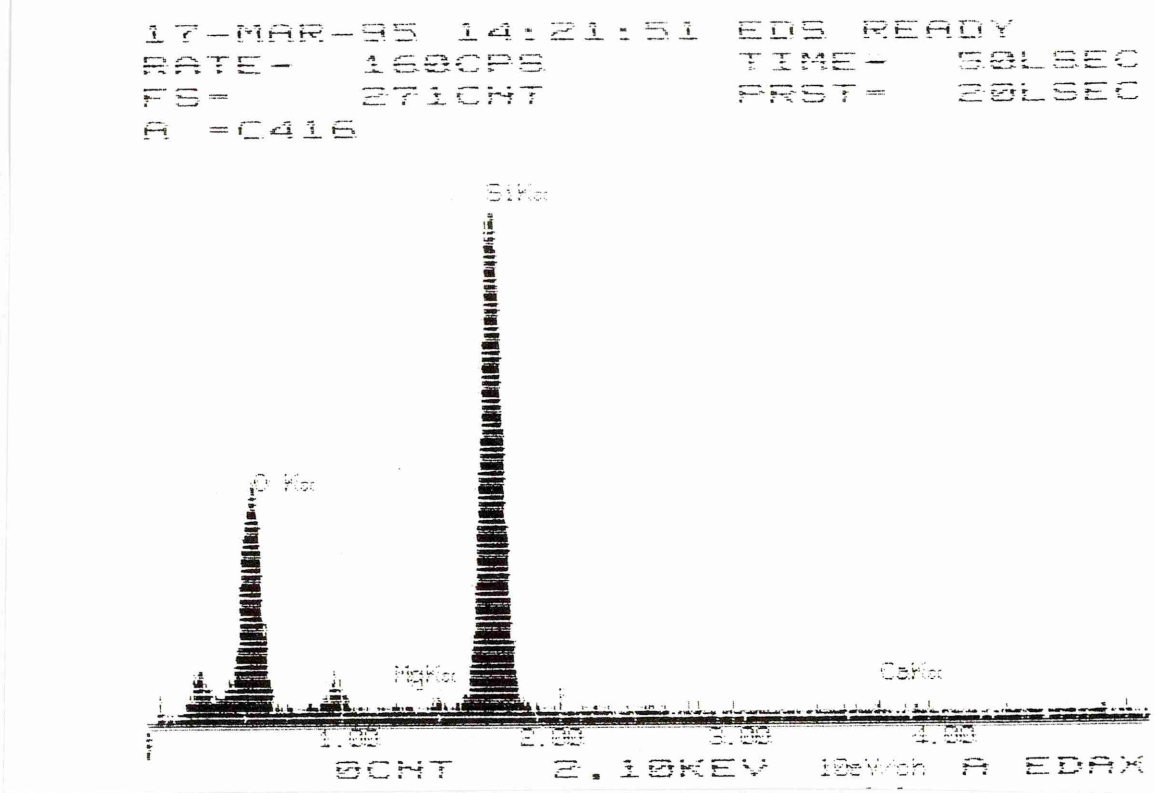

Figure 4-53a EDS of the brighter separated phase in figure 52h.

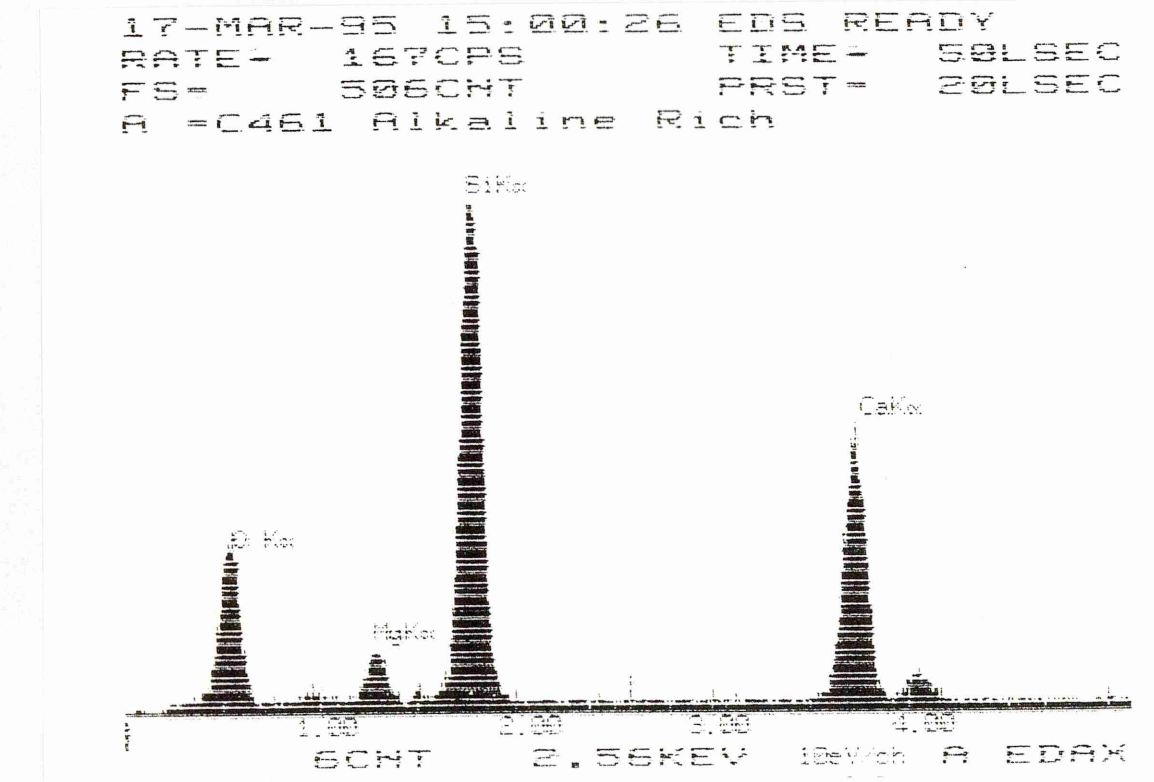

Figure 4-53b EDS of the darker separated phase in figure 4-52h.

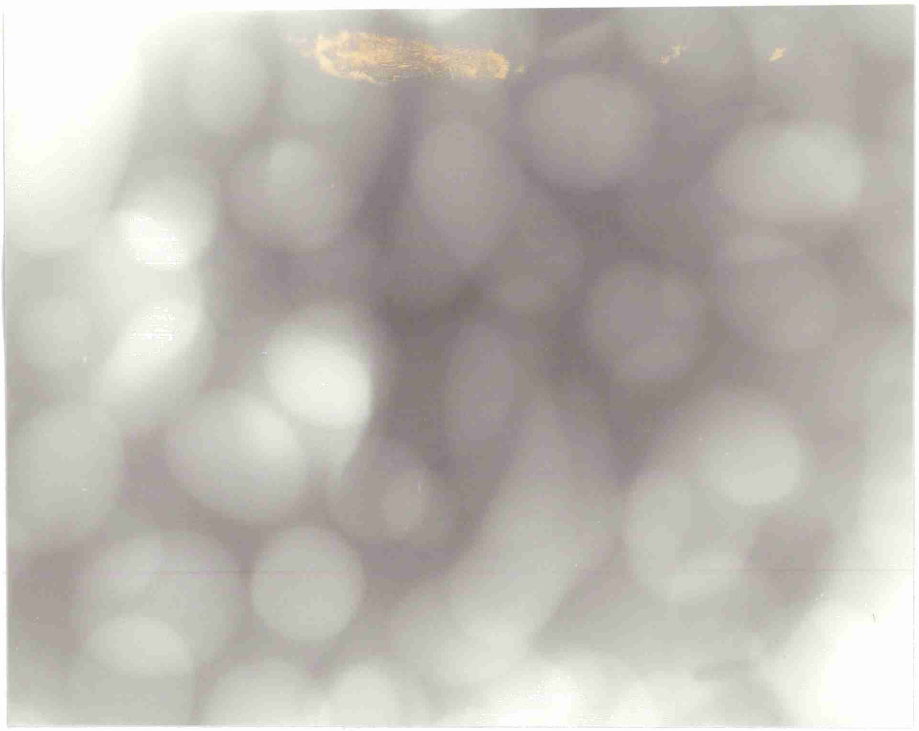

Figure 4-54 Microstructure of a shot particle devitrified at 800°C for 48 hours.

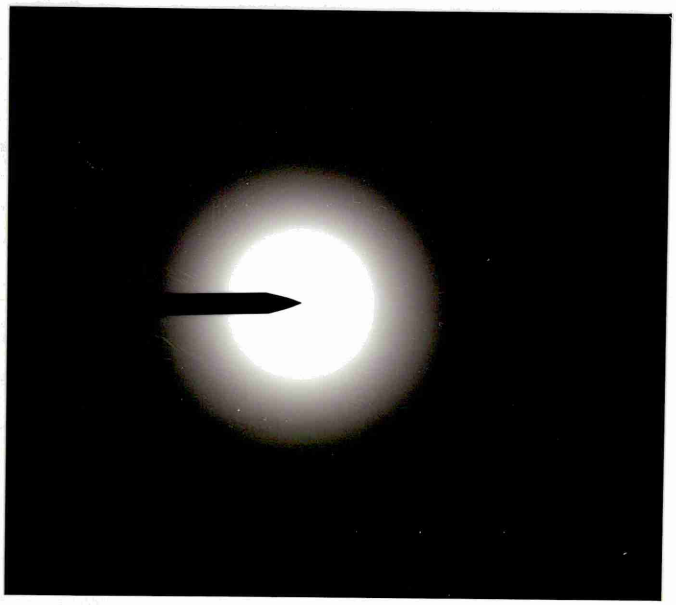

Figure 4-55 SAED patterns of the separated phases in figure 4-52h.

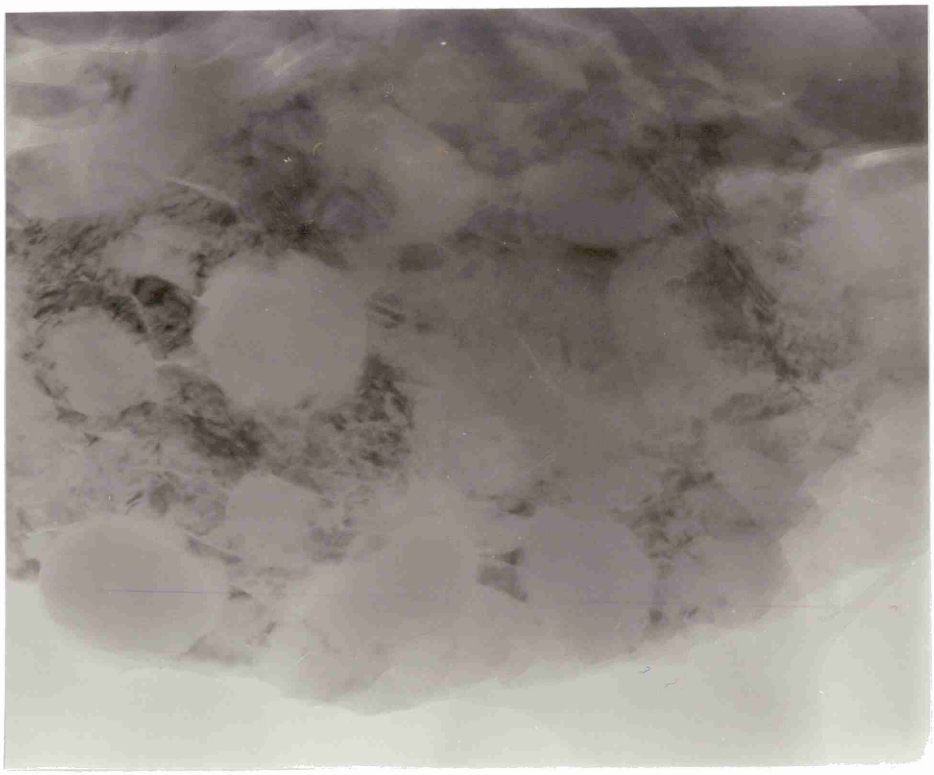

Figure 4-56 Microstructure of Superwool fibre devitrified at 800°C for 168 hours.

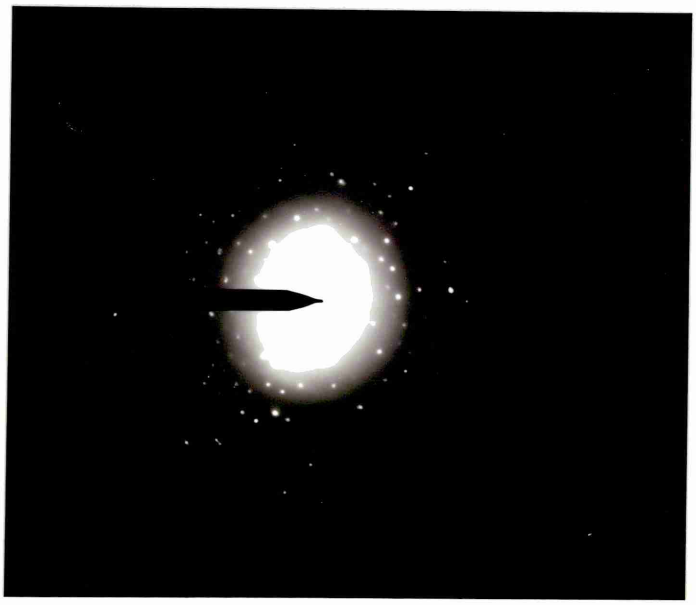

Figure 4-57 SAED pattern corresponding to the crystalline phase in figure 4-56.

Figure 4-58a Cross section of Superwool fibre devitrified at 900°C for 168 hours.

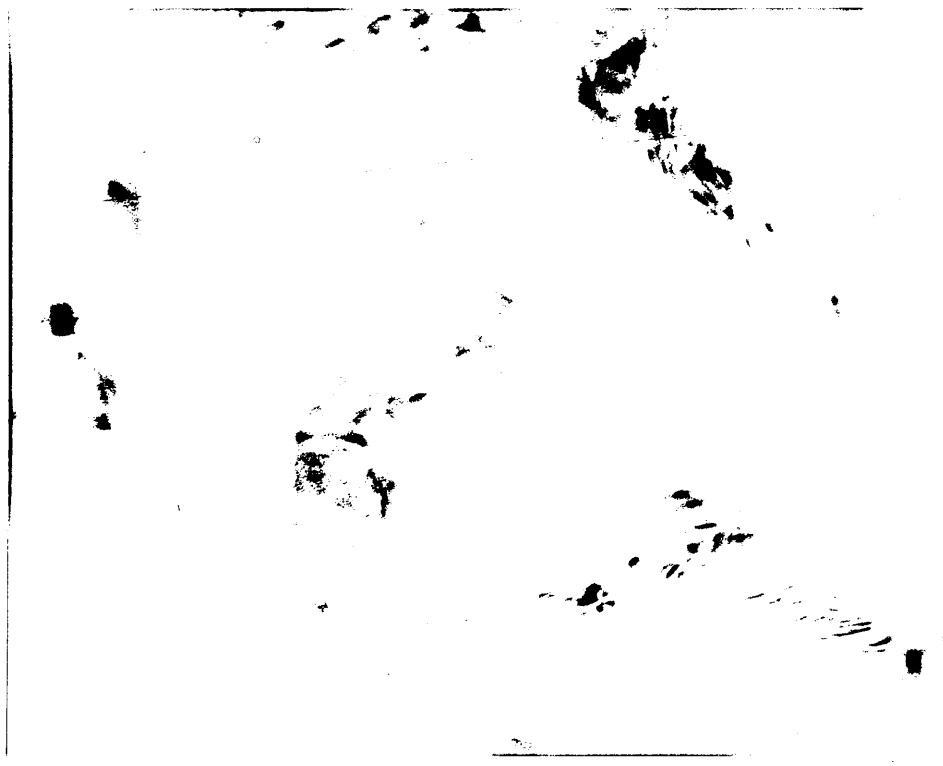

Figure 4-58b Microstructure of Superwool fibre devitrified at 900°C for 168 hours.

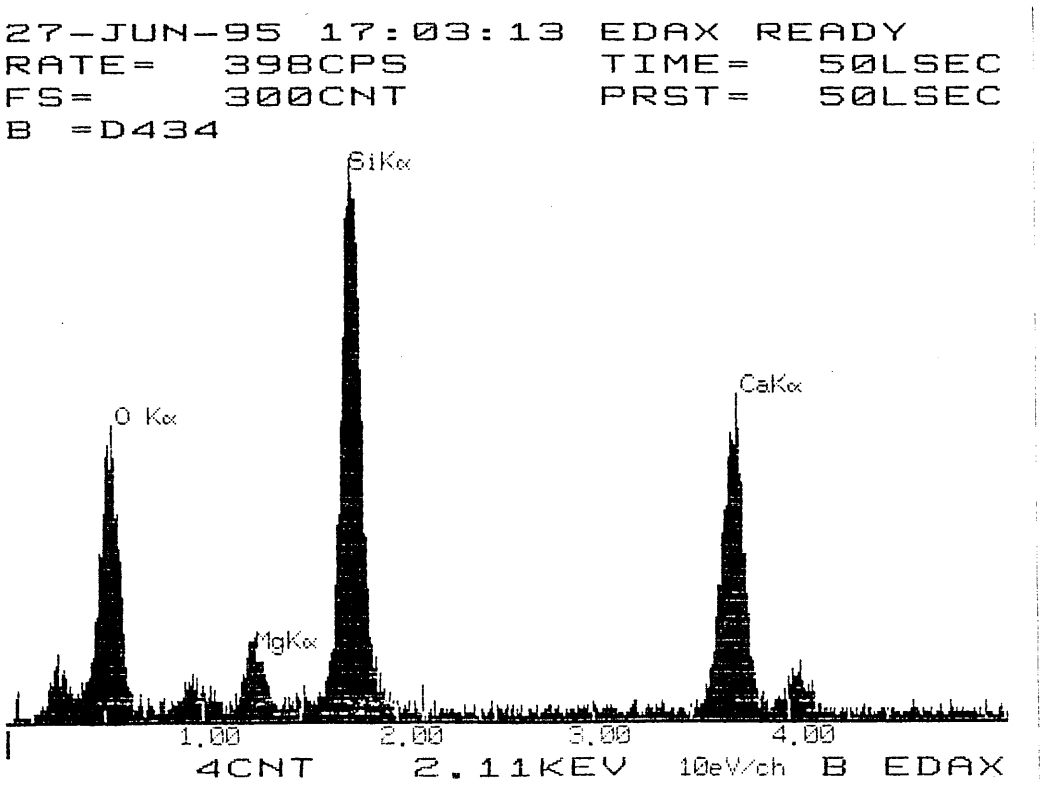

Figure 4-59a EDS of the crystallised area in figure 4-58b

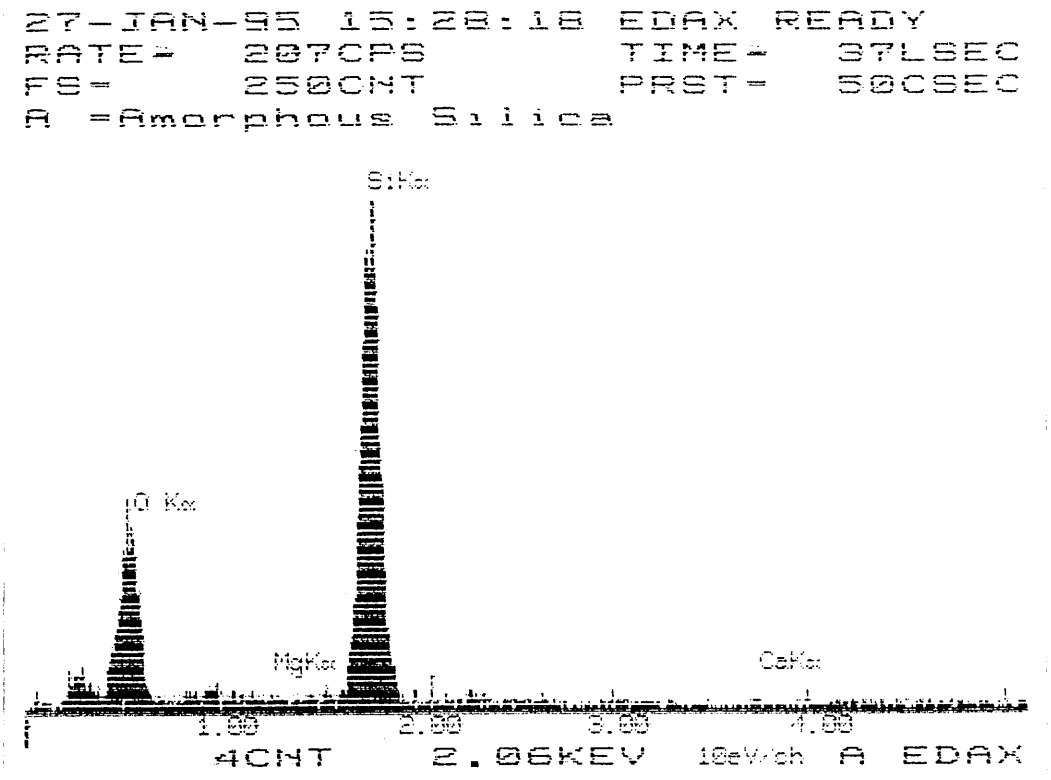

Figure 4-59b EDS of the amorphous area in figure 58b.

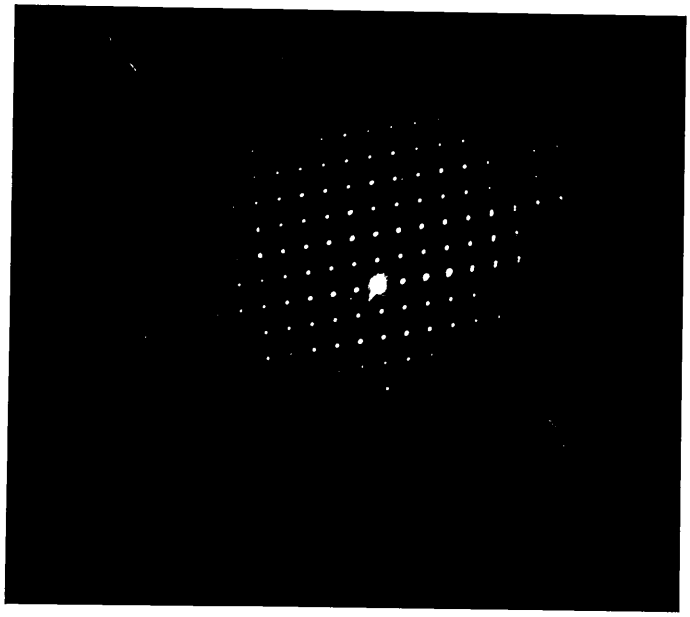

Figure 4-60 SAED patterns of the crystalline phase in figure 4-58b.

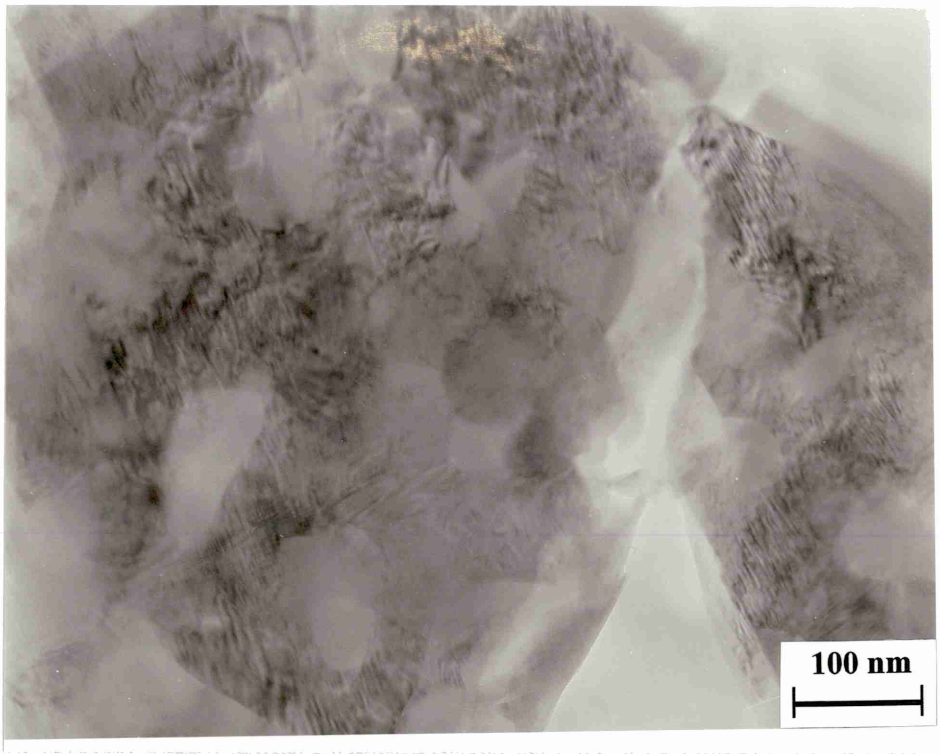

Figure 4-61 Microstructure of Superwool fibre devitrified at 900°C for 1344 hours.

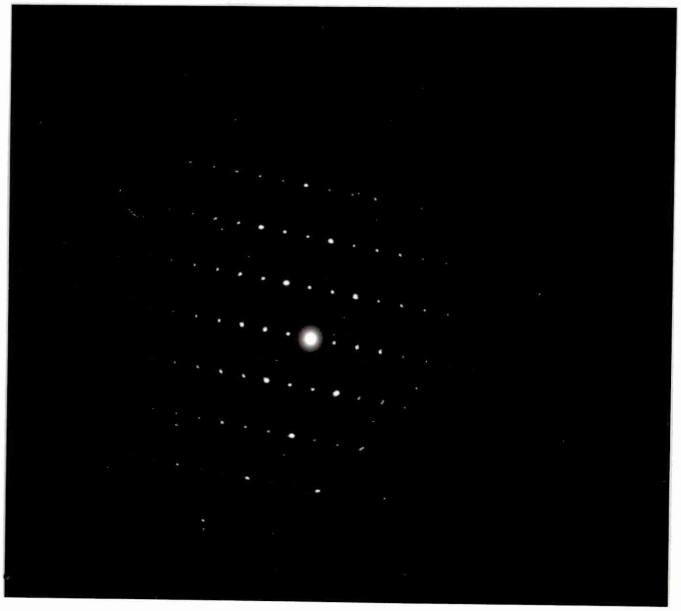

Figure 62 SAED pattern of the crystalline phase in figure 61.

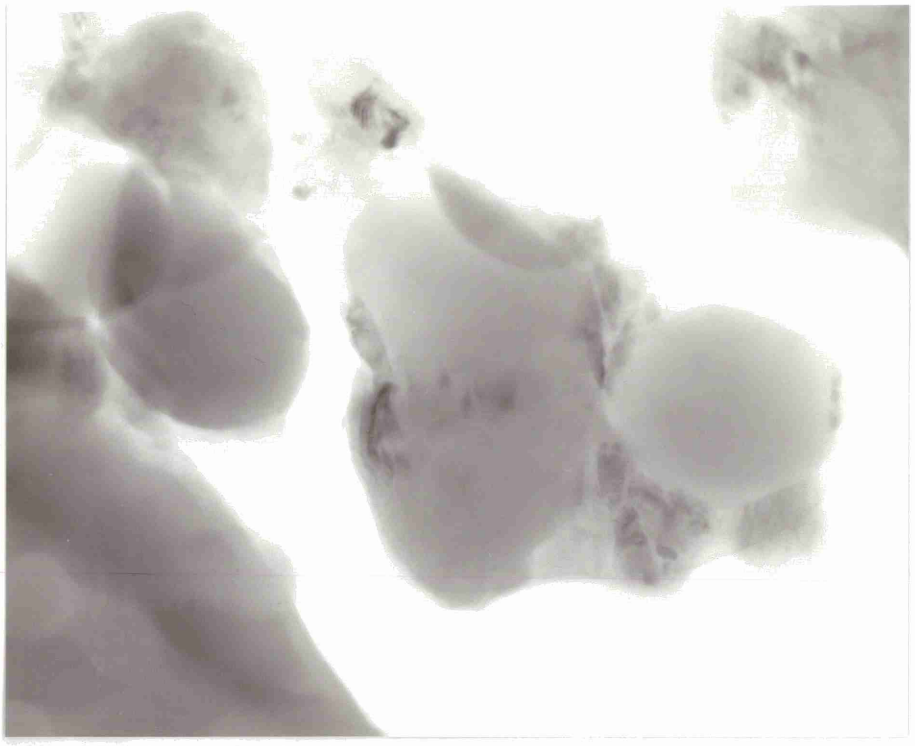

Figure 63 A cross section of Superwool fibre devitrified at 900°C for 1344 hours.

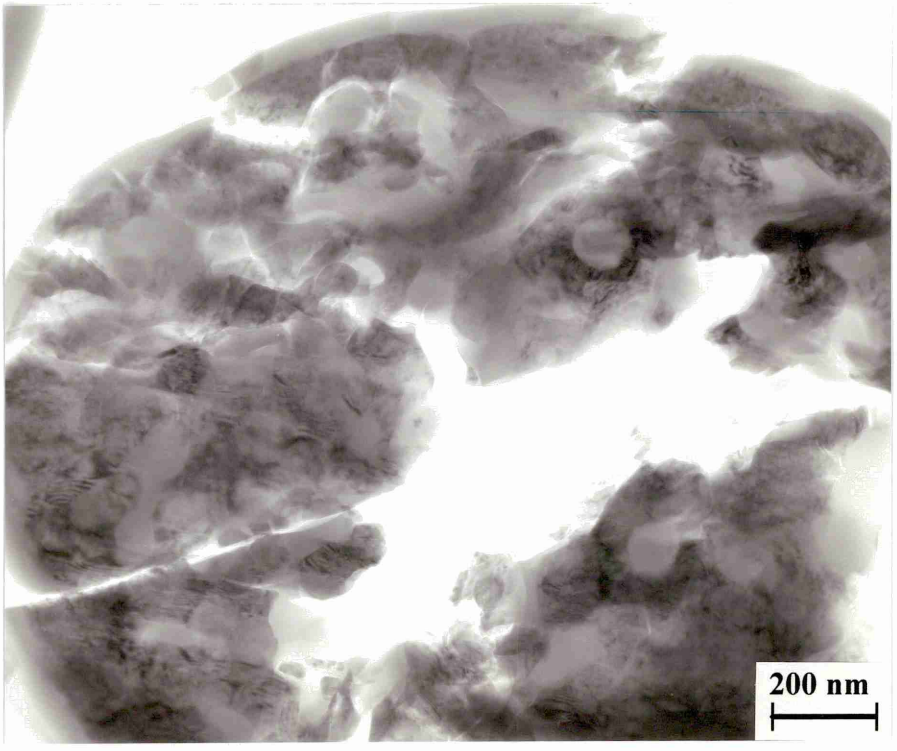

Figure 4-64 Microstructure of Superwool fibre devitrified at 1000°C for 168 hours.

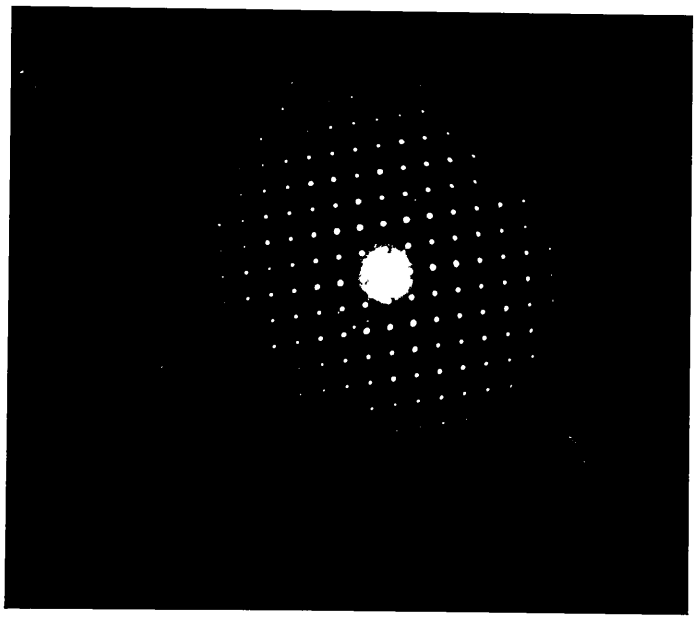

Figure 4-65 SAED pattern of the crystalline phase in figure 4-64.

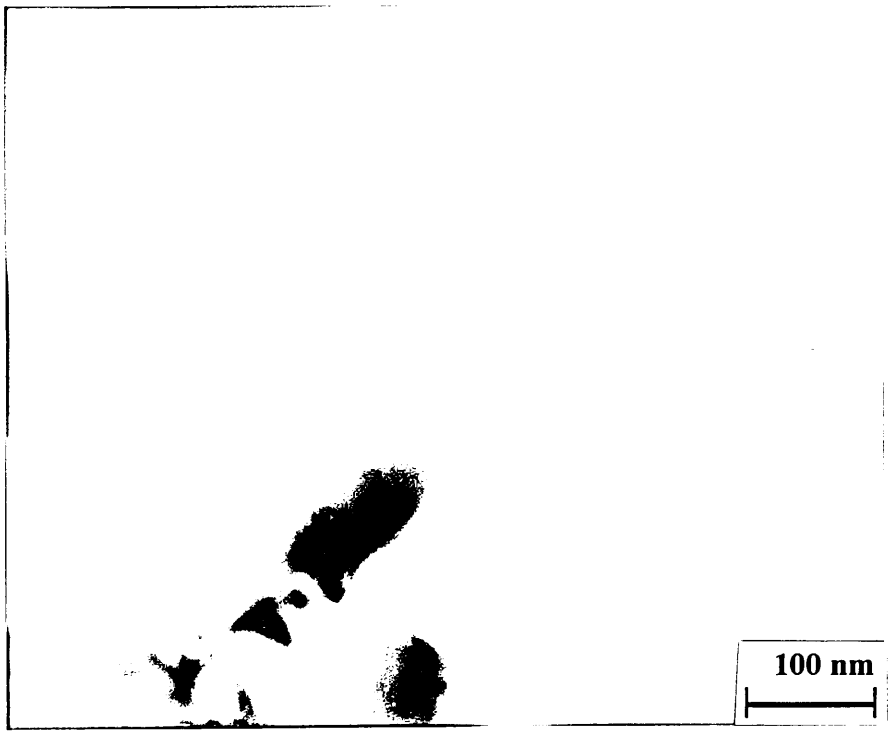

Figure 4-66 Microstructure of a broken cross section.

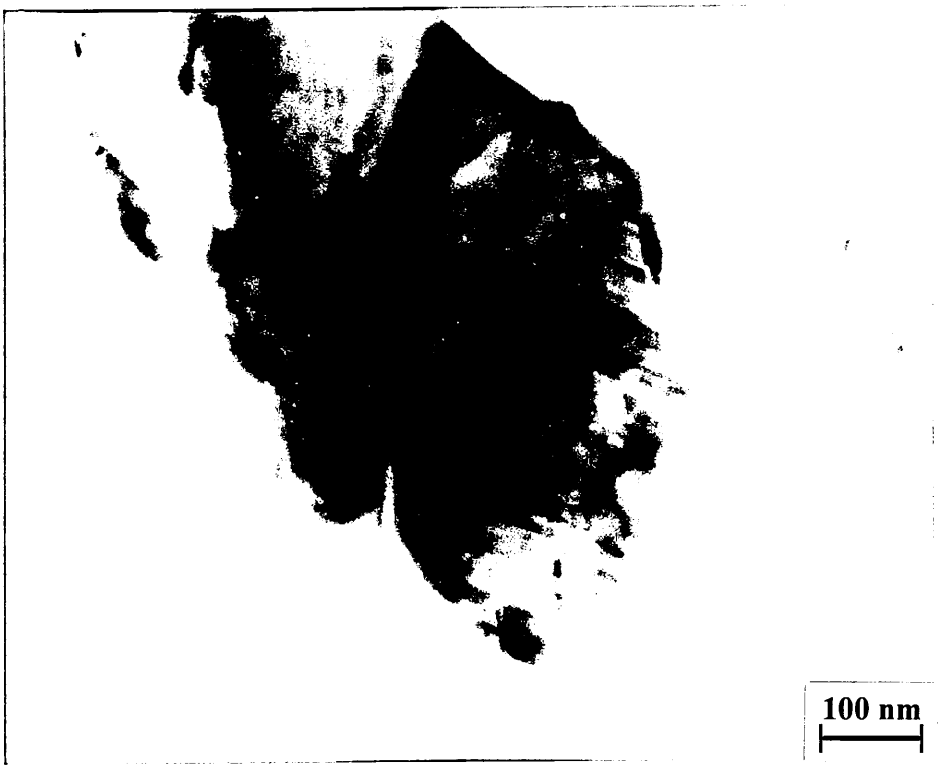

Figure 4-67a Bright field image of crystalline particle in devitrified Superwool fibre.

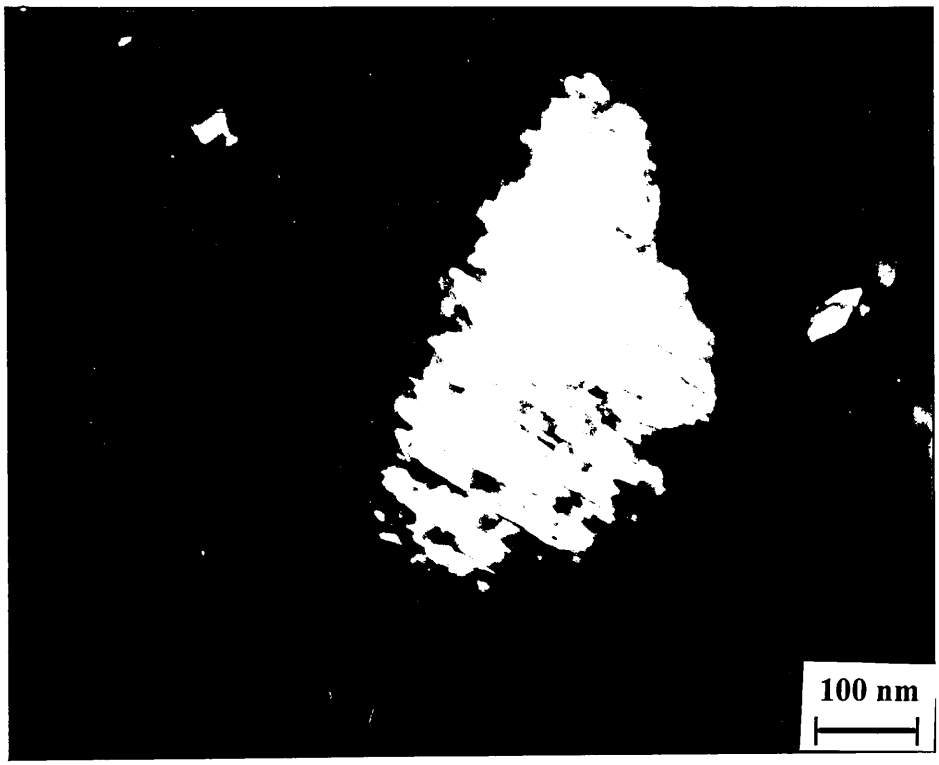

Figure 4-67b Dark field image of the crystalline particle in figure 4-67a.

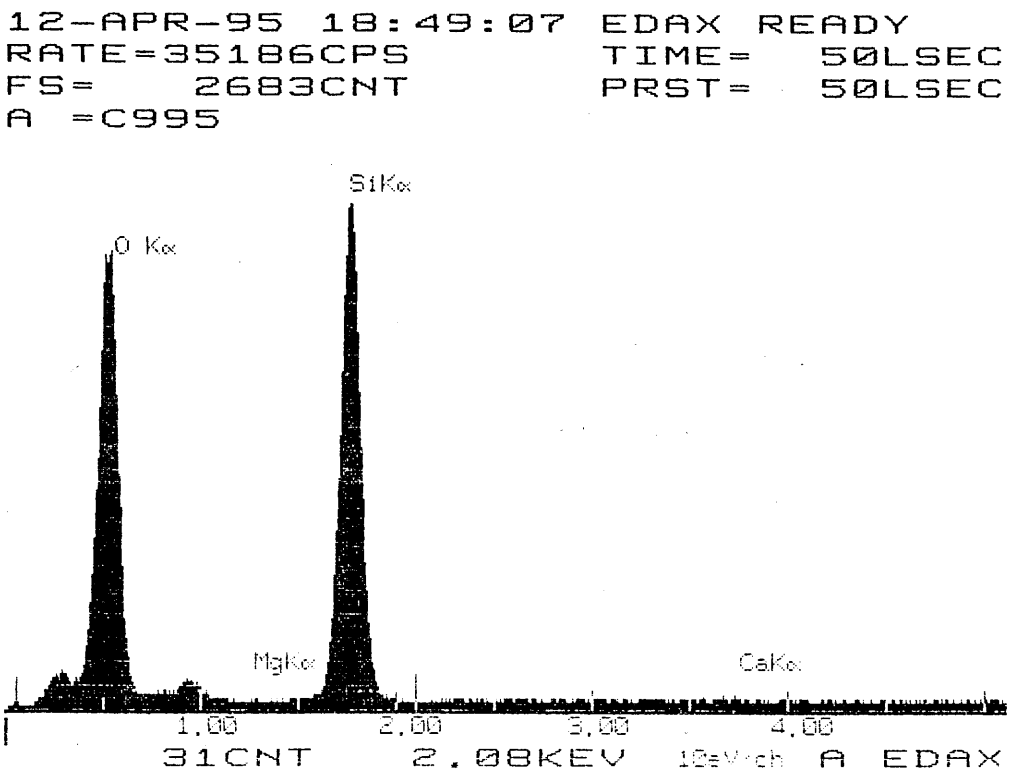

Figure 4-68 EDS corresponding to the particle in figure 4-67.

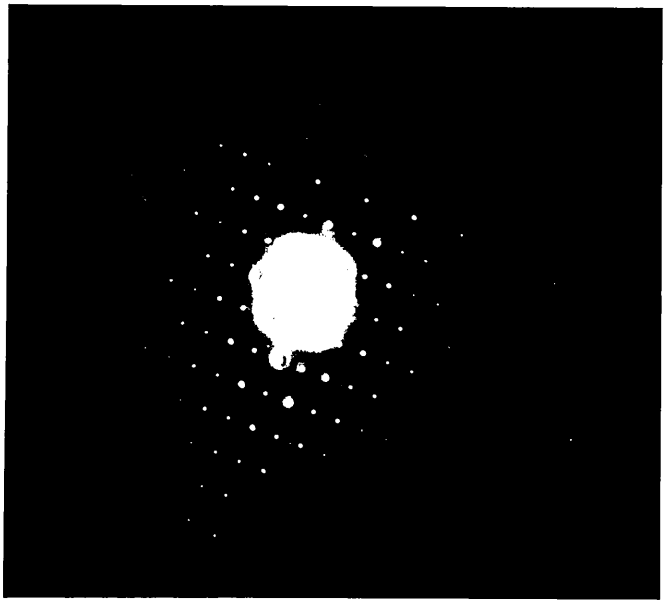

Figure 4-69 SAED patterns corresponding to the particle in figure 4-67.

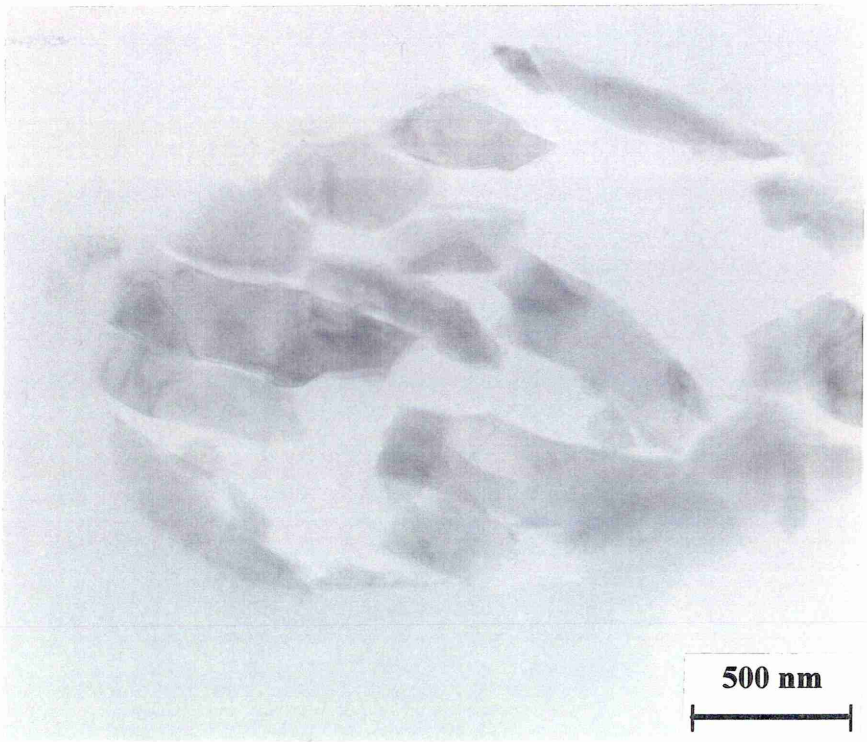

Figure 4-70 Cristobalite particles in fibre devitrified at 1250°C for 168 hours.

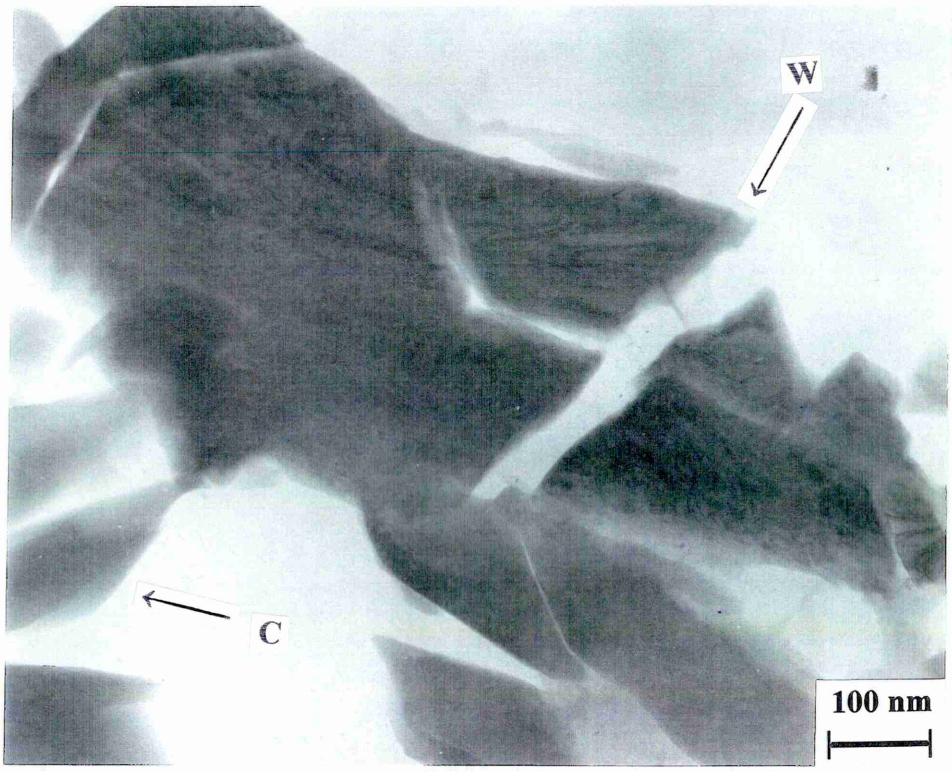

Figure 4-71 Crystalline particles in the fibre devitrified at 1250°C for 168 hours.

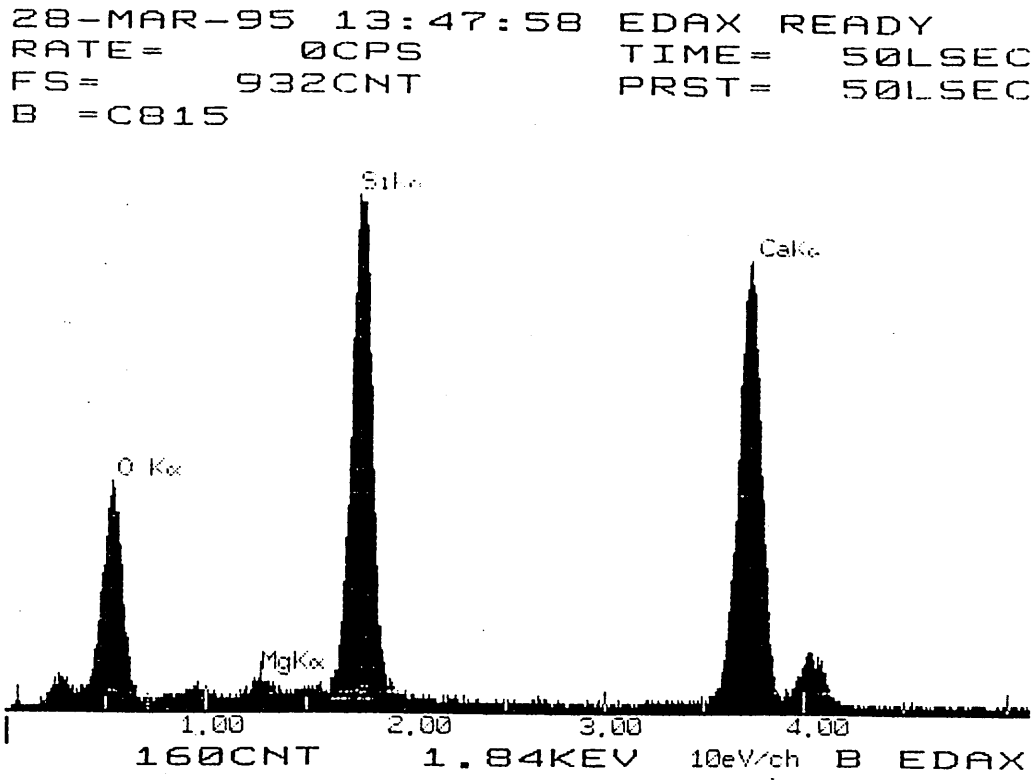

Figure 4-72 EDS of the particle w in figure 4-71.

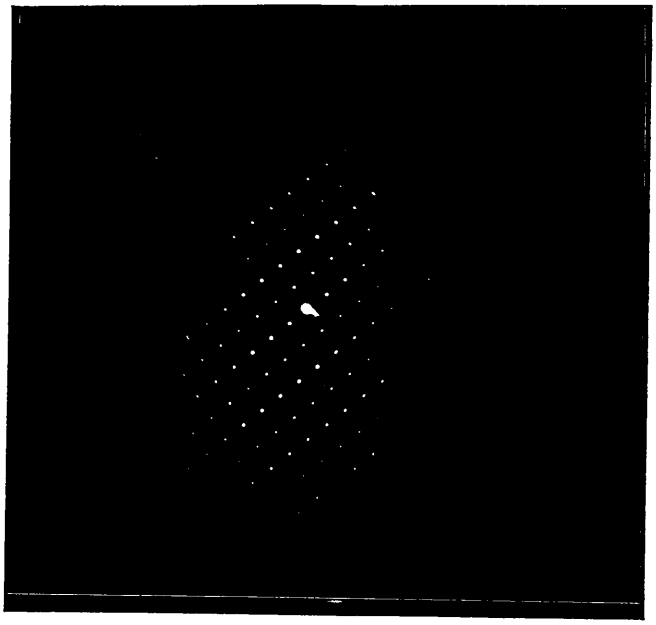

Figure 4-73 SAED patterns of the particles marked as w in figure 4-71.

Figure 4-74 Crystalline particles in the fibre devitrified at 1250°C for 168 hours.

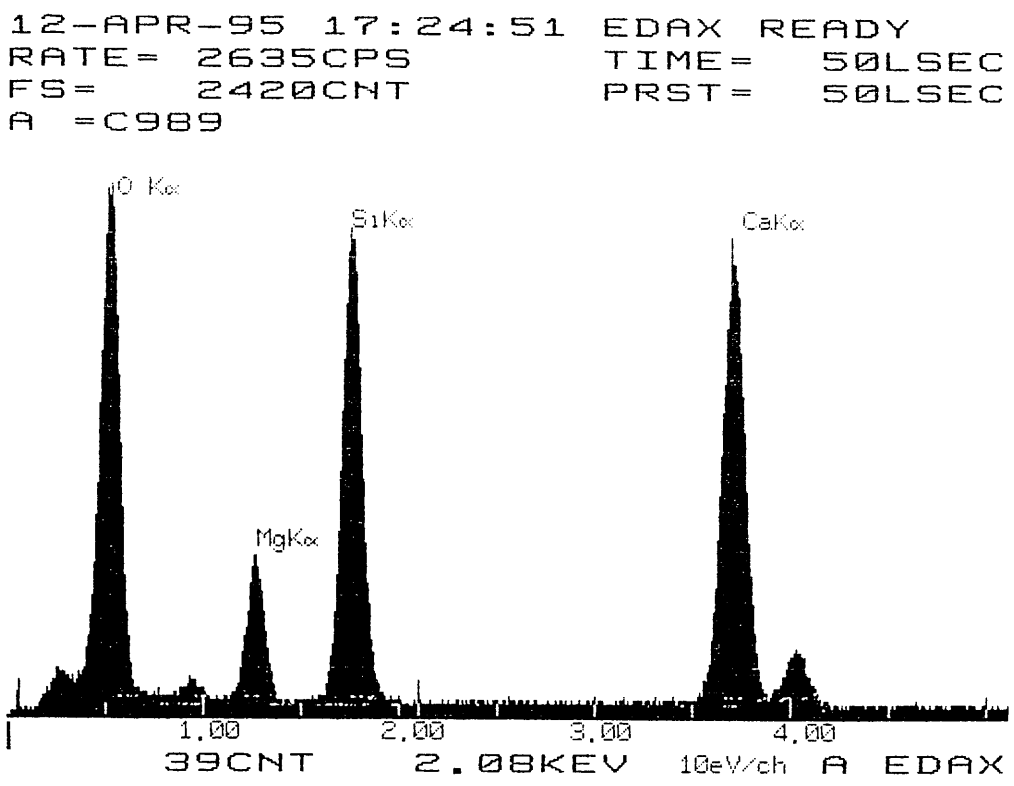

Figure 4-75 EDS of the particle w in figure 4-74.

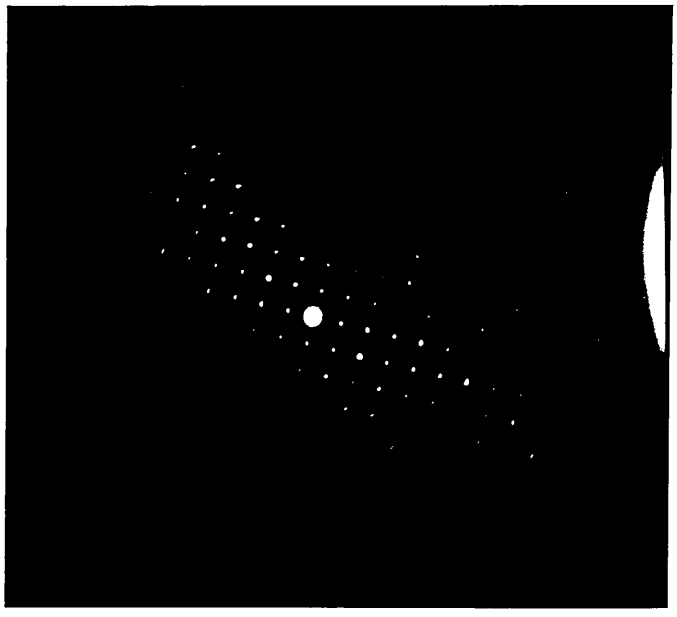

Figure 4-76 SAED patterns of the particle w in figure 4-74.

Figure 4-77a Bright image of tridymite crystals in the fibre.

Figure 4-77b Dark image of tridymite crystals in the fibre.

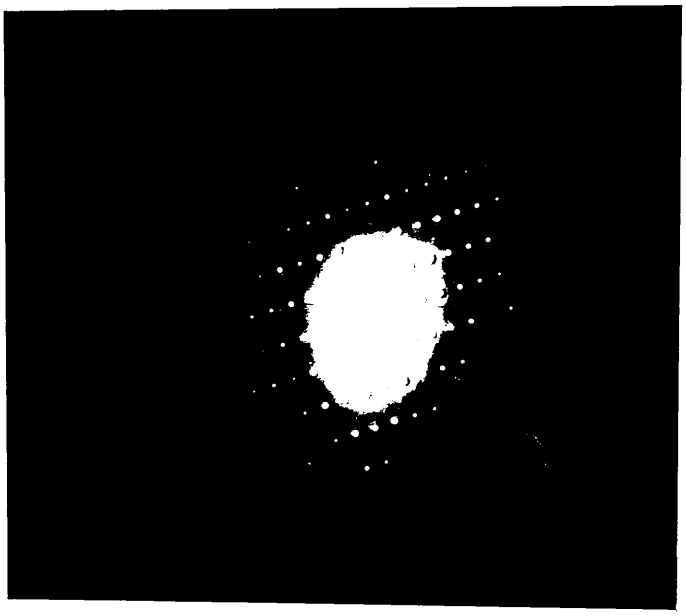

Figure 4-78 SAED patterns of tridymite.

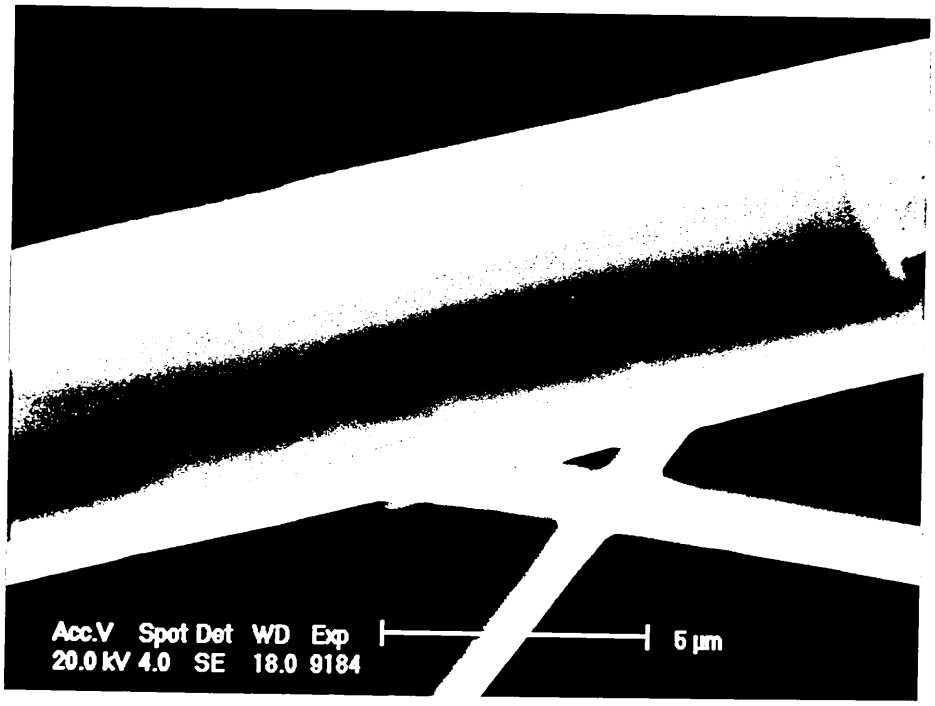

Figure 4-79 Fibre surface after devitrified at 800°C for 3864 hours.

Figure 4-80 Fibre surface after devitrified at 900°C for 1344 hours.

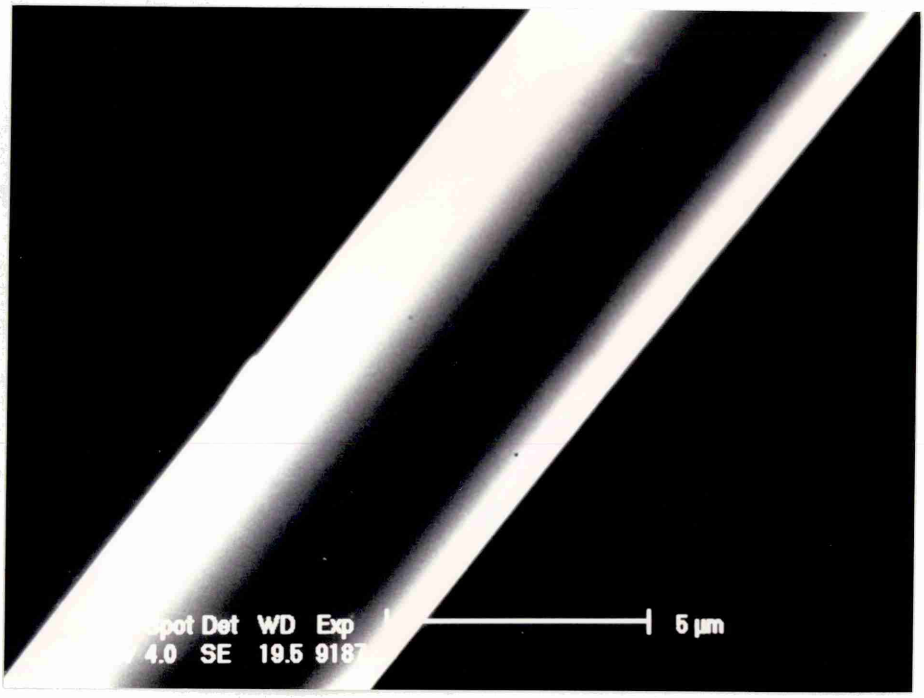

Figure 4-81 Fibre surface after devitrified at 1000°C for 672 hours.

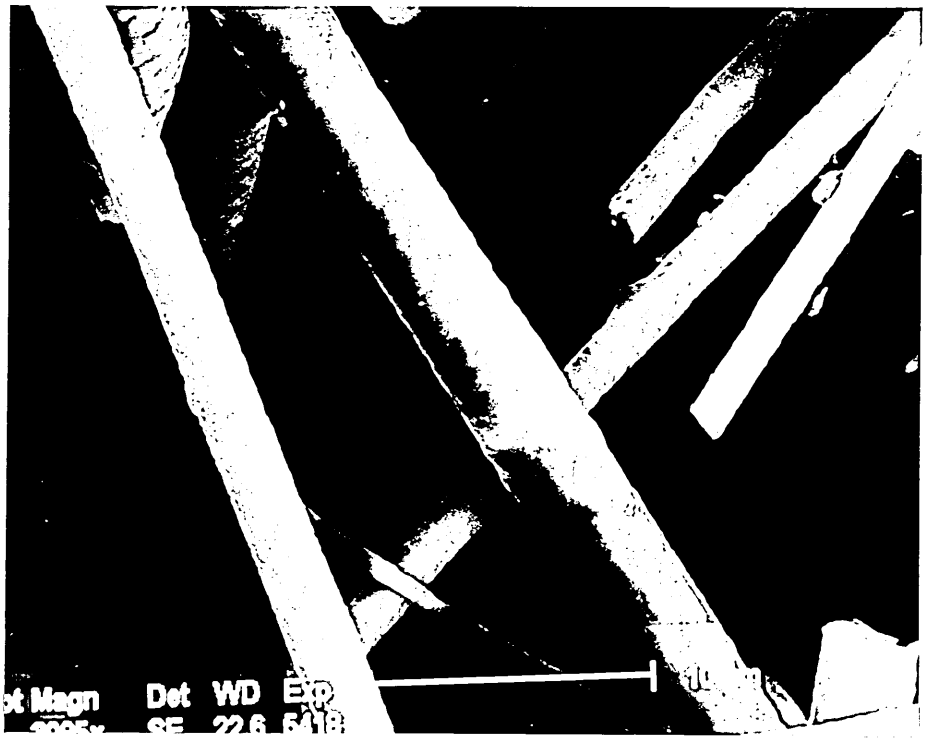

Figure 4-82 Fibre surface after devitrified at 1000°C for 2352 hours.

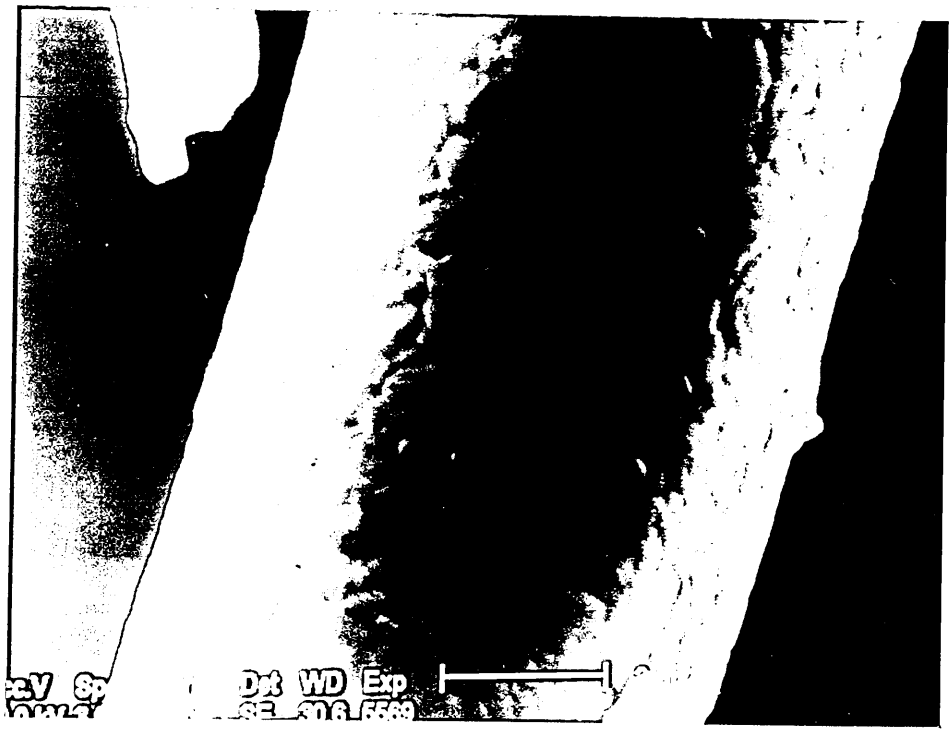

Figure 4-83 Fibre surface after devitrified at 1100°C for 336 hours.

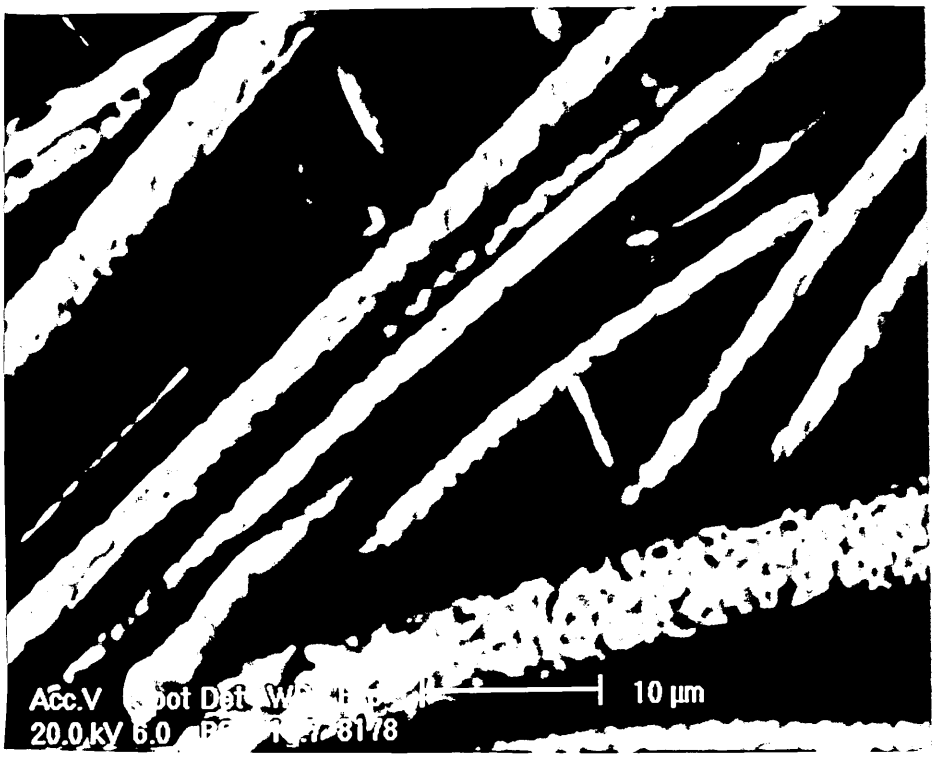

Figure 4-84a Fibre surface after devitrified at 1250°C for 0.5 hour.

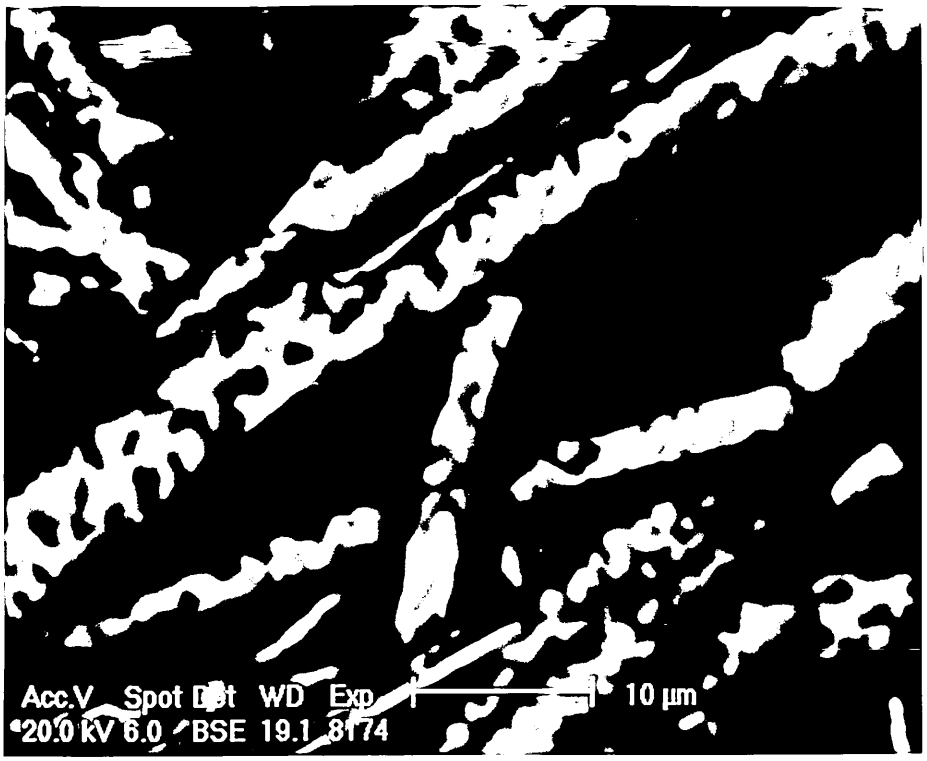

Figure 4-84b Fibre surface after devitrified at 1250°C for 24 hours.

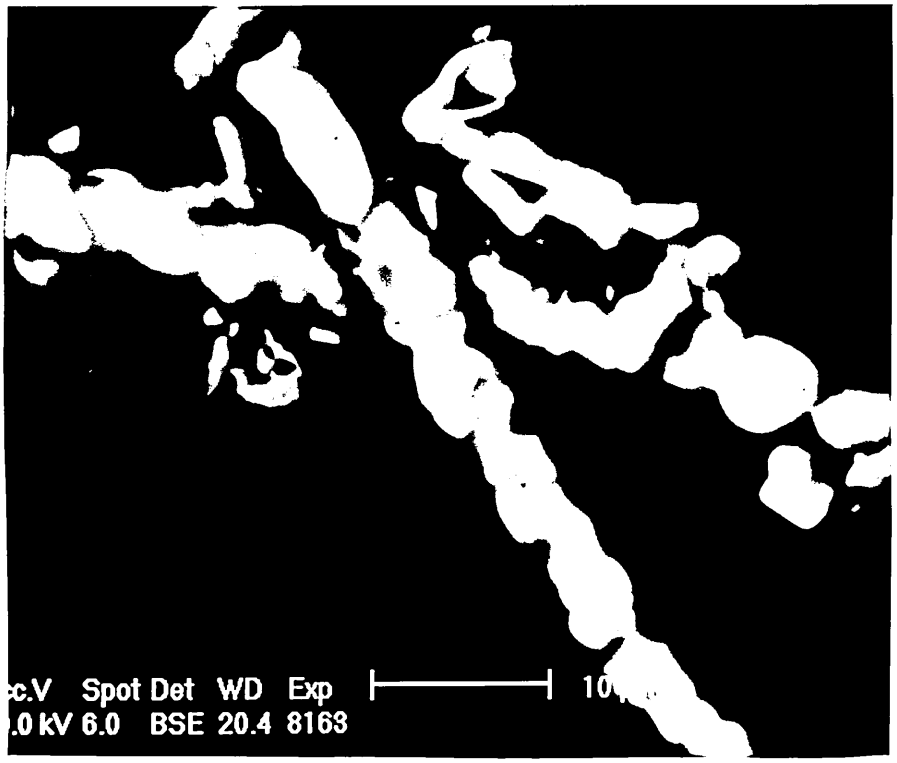

Figure 4-84c Fibre surface after devitrified at 1250°C for 168 hours.

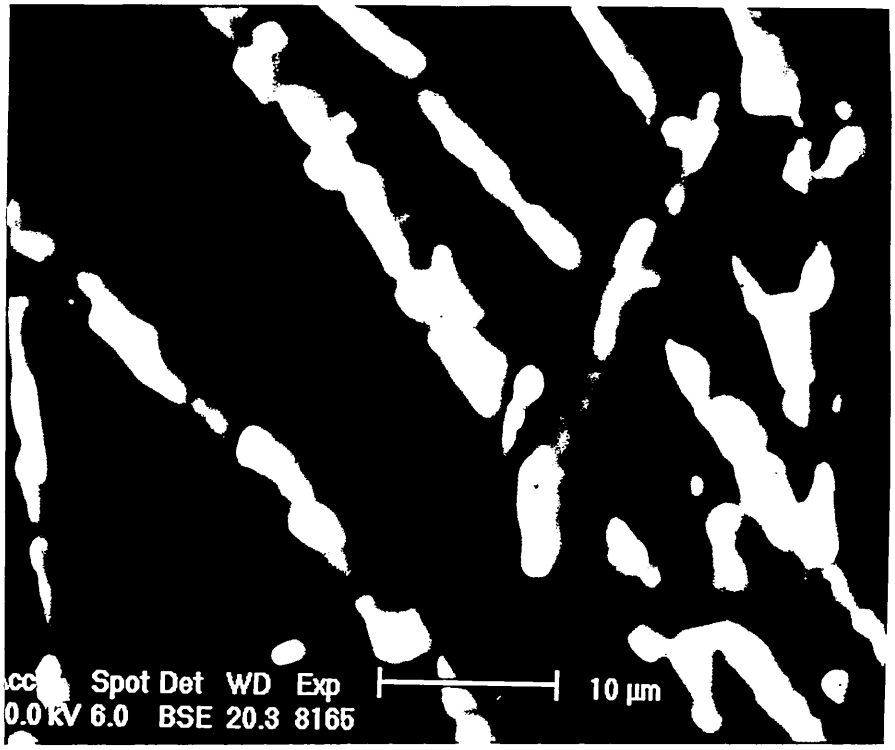

Figure 4-84d Fibre surface after devitrified at 1250°C for 672 hours.

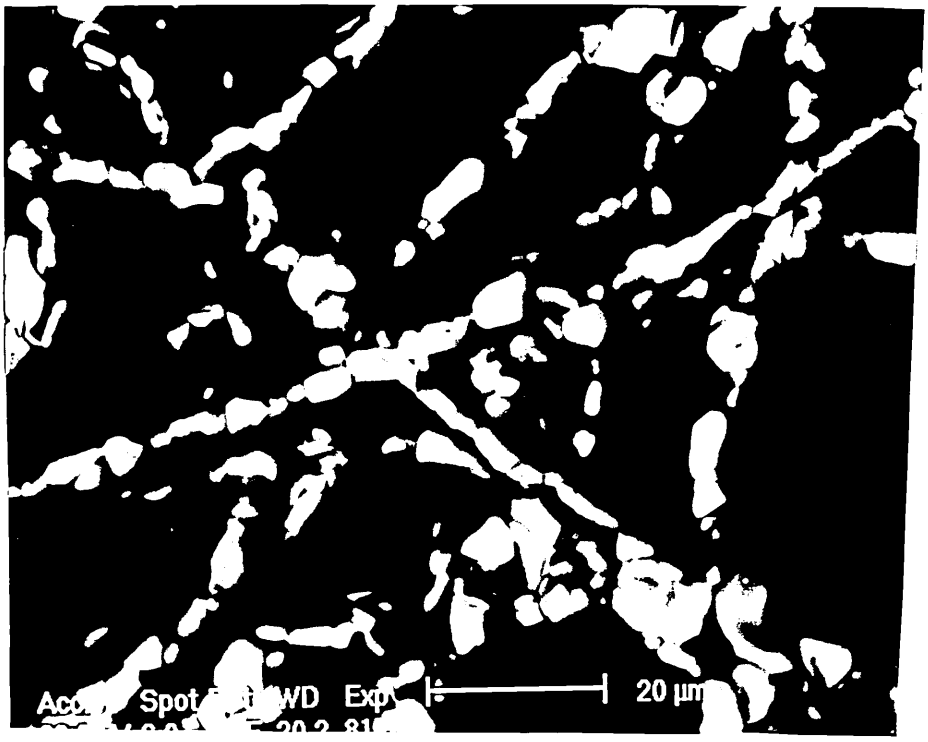

Figure 4-84e Fibre surface after devitrified at 1250°C for 1344 hours.

Figure 4-84 Development of fibre surface structure at 1250°C.

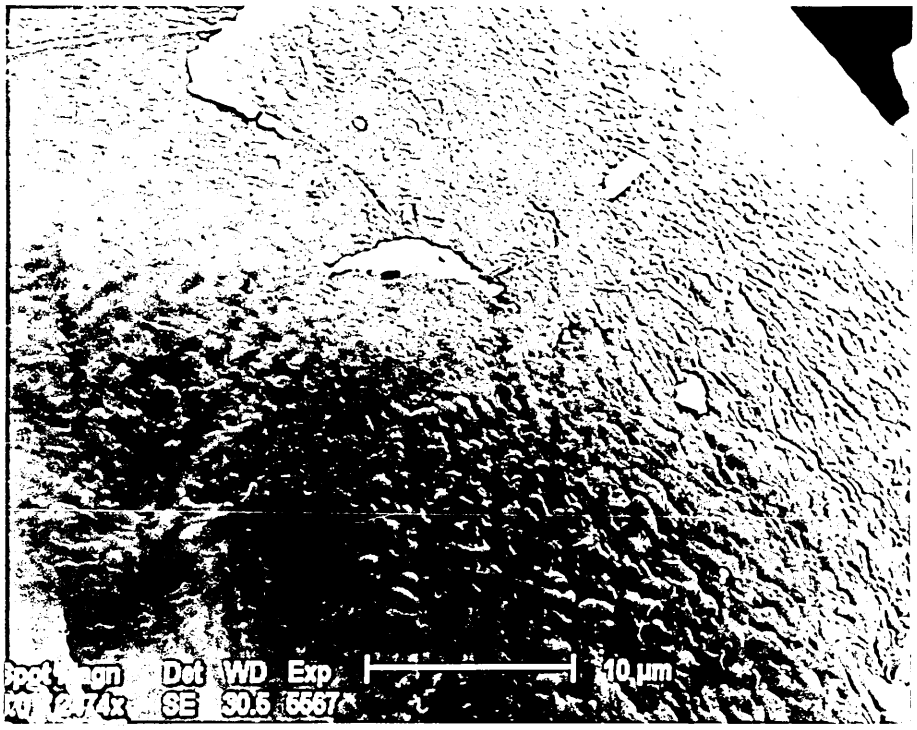

Figure 4-85 Surface of a shot particle after devitrified at 1100°C for 336 hours.

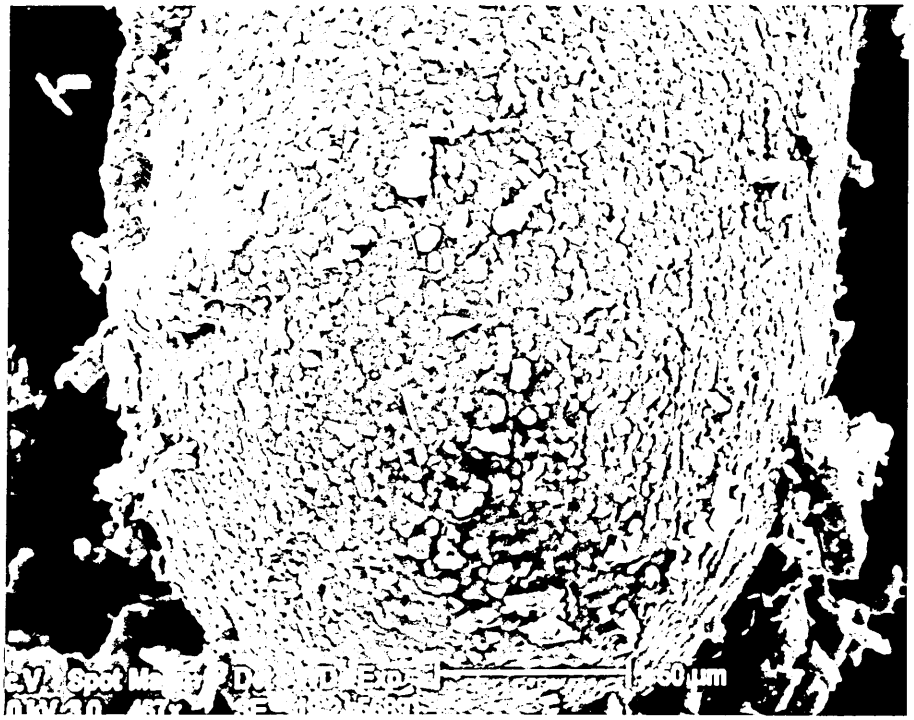

Figure 4-86 Surface of a shot particle after devitrified at 1200°C for 336 hours.

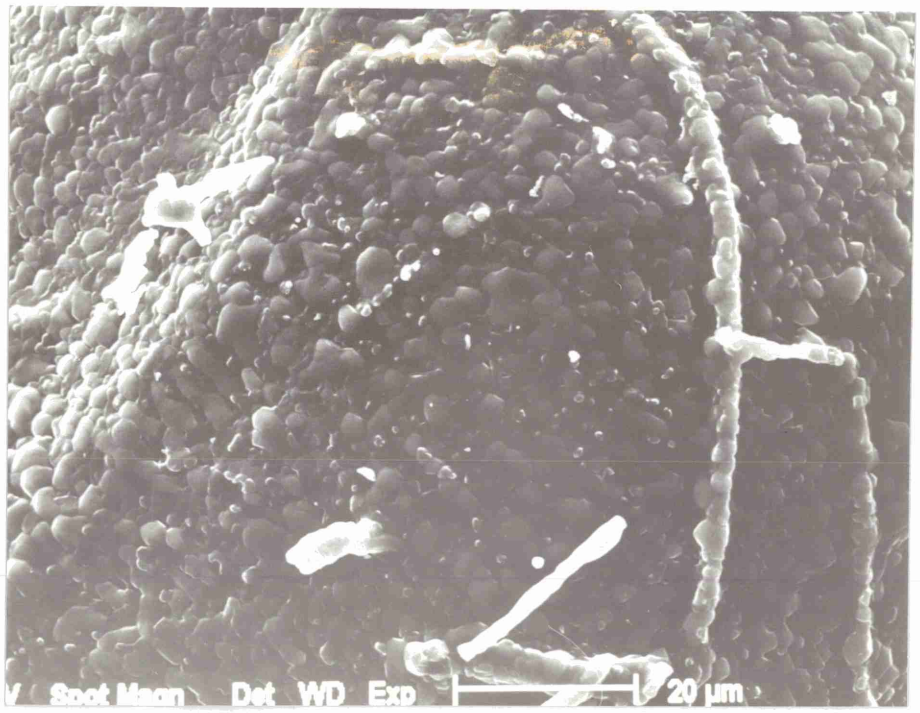

Figure 4-87a Surface of a shot particle after devitrified at 1250°C for 24 hours.

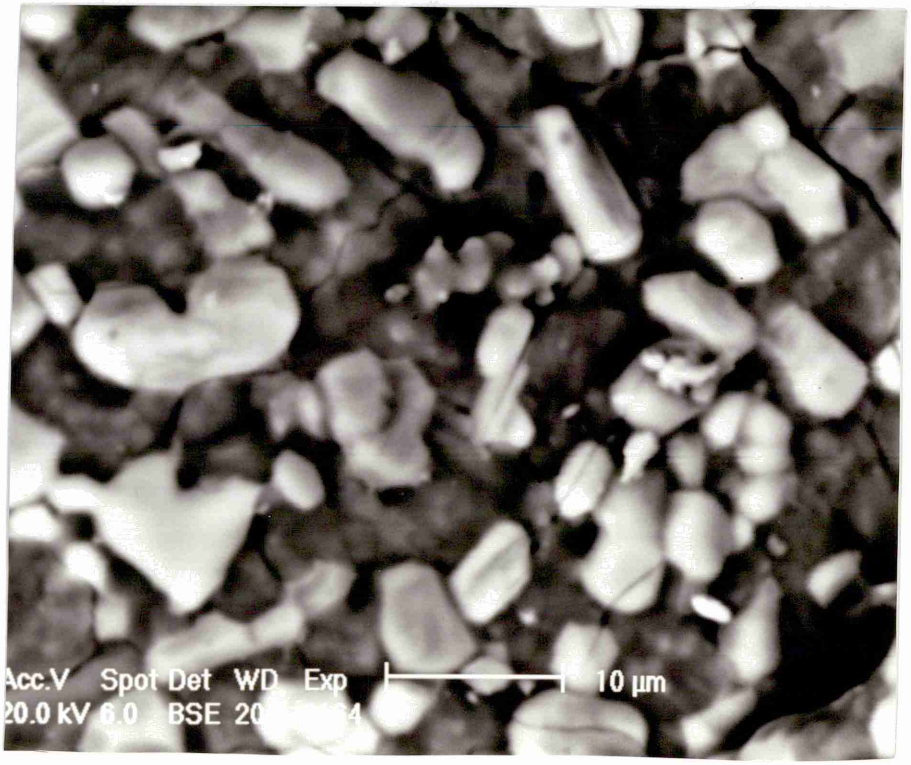

Figure 4-87b Surface of a shot particle after devitrified at 1250°C for 672 hours.

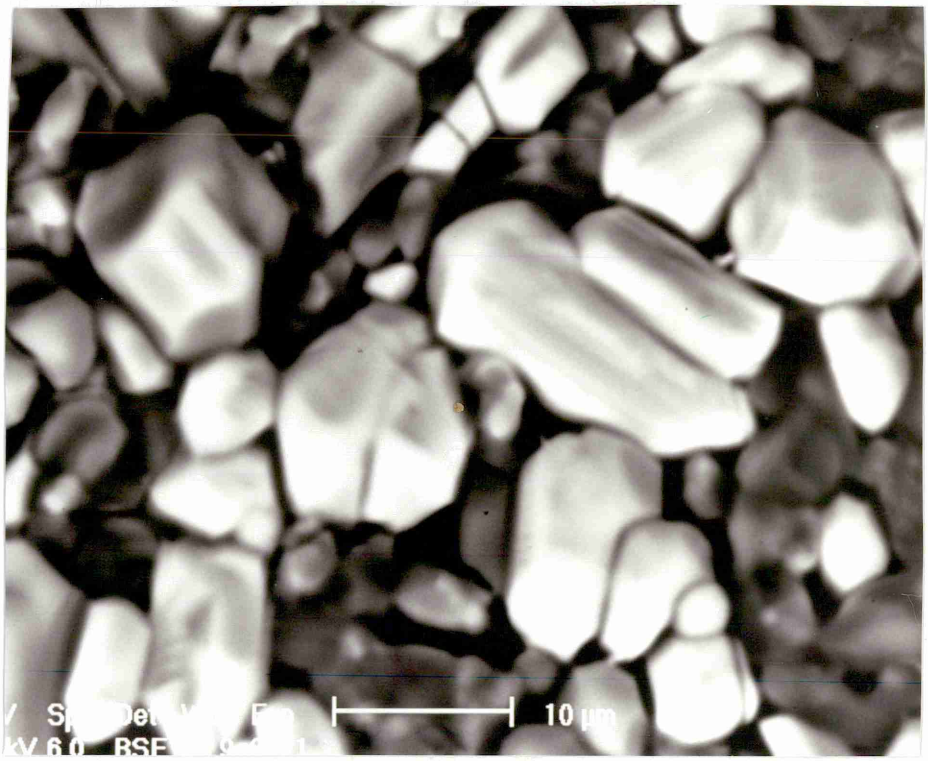

Figure 4-87c Surface of a shot particle after devitrified at 1250°C for 1344 hours.

Figure 4-87 Development of surface structure of shot particles at 1250°C.

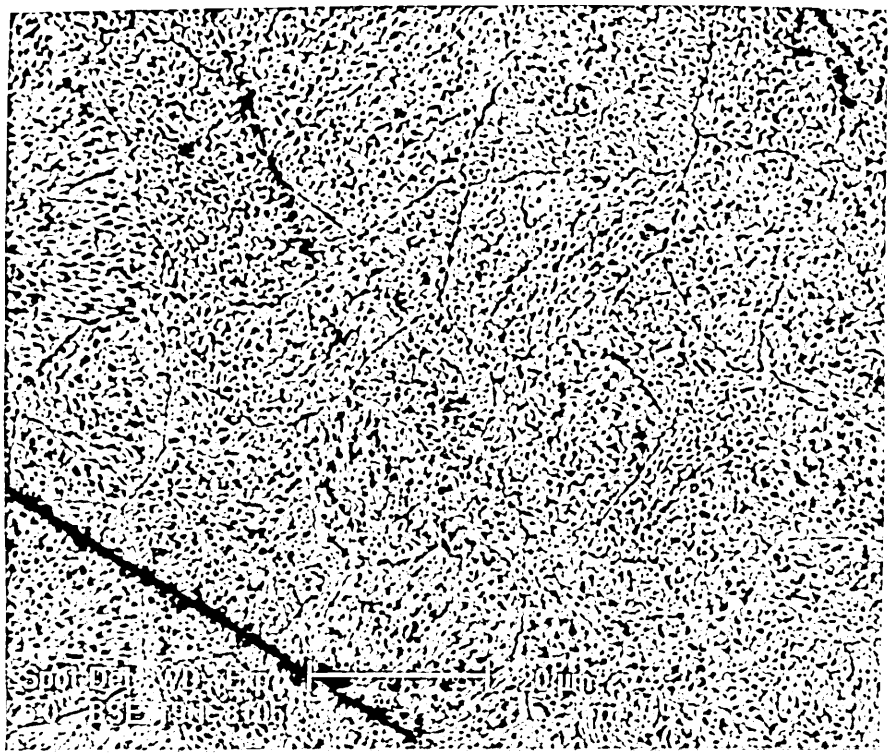

Figure 4-88 Microstructure of a shot particle devitrified at 1000°C for 3192 hours.

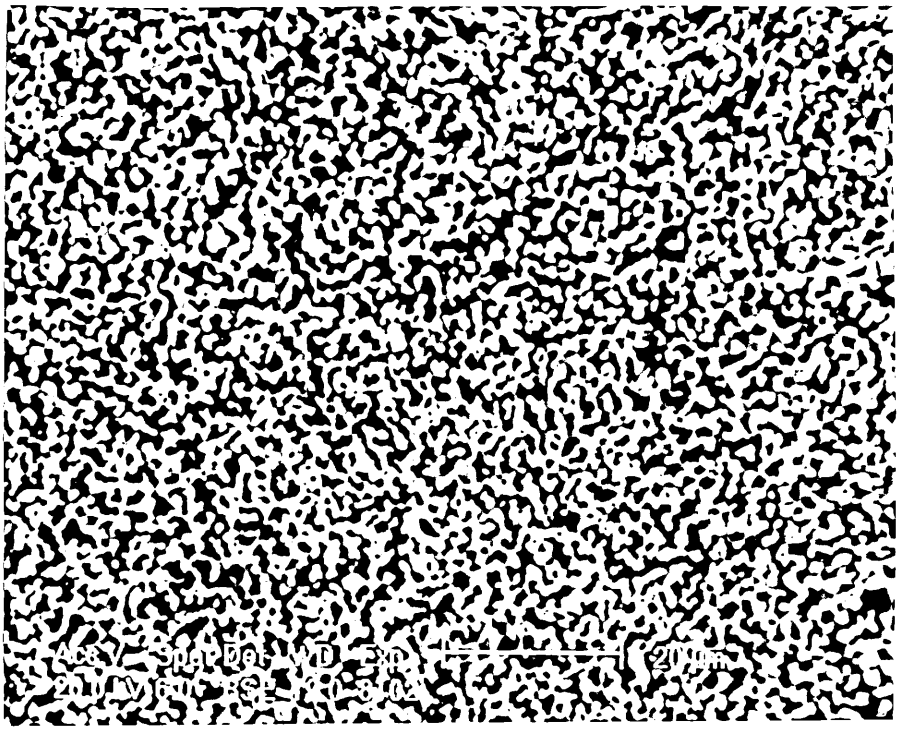

Figure 4-89 Microstructure of a shot particle devitrified at 1100°C for 3024 hours.

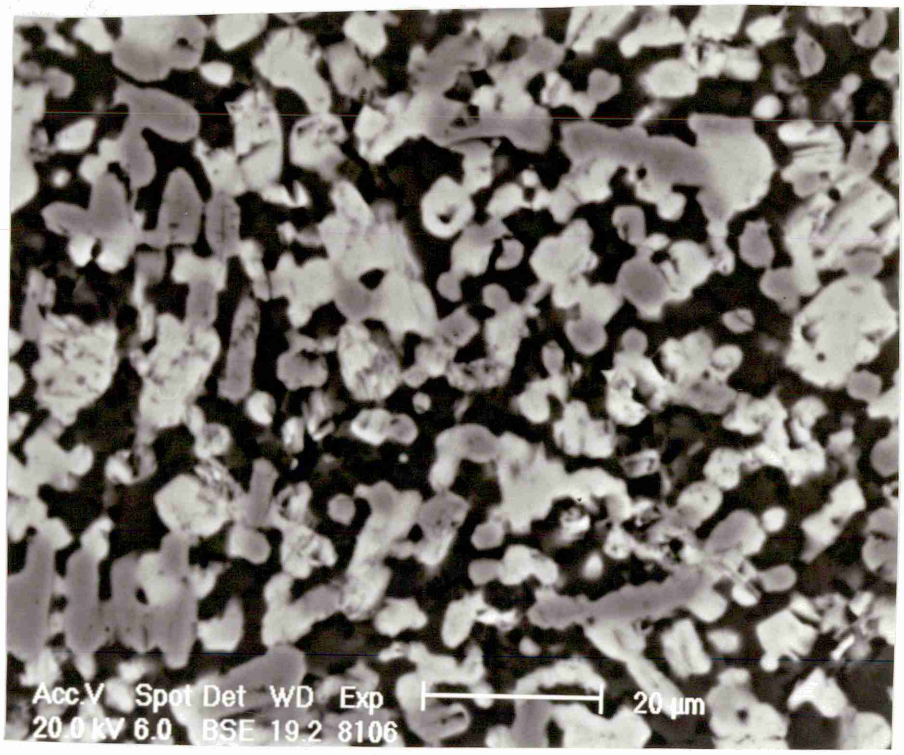

Figure 4-90 Microstructure of a shot particle devitrified at 1200°C for 672 hours.

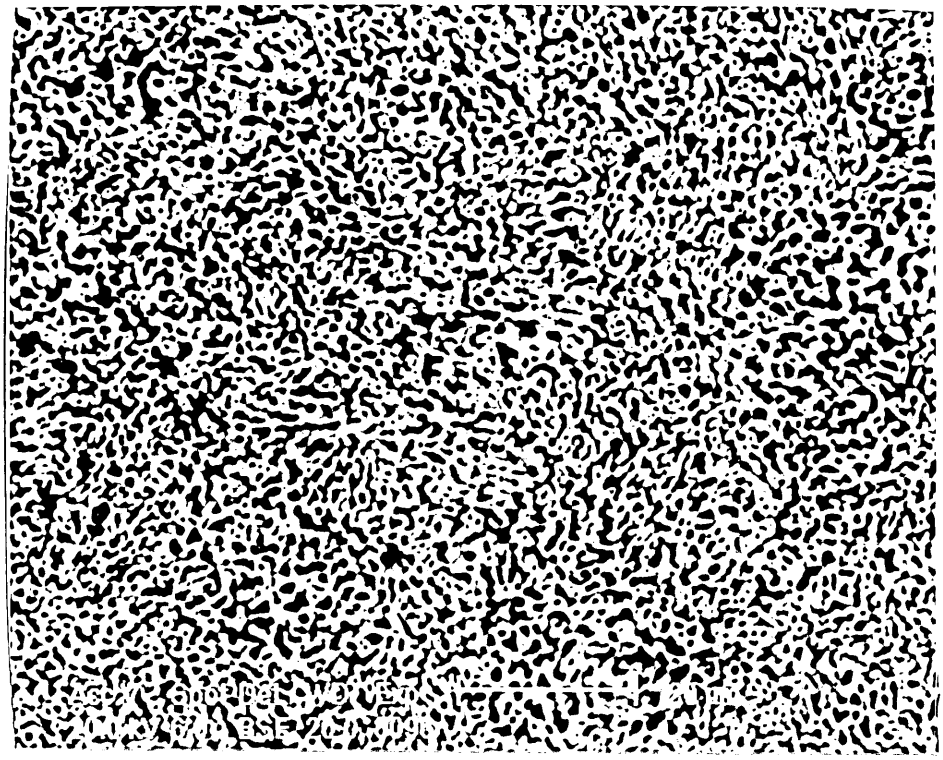

Figure 4-91a Microstructure of a shot particle devitrified at 1250°C for 0.5 hour.

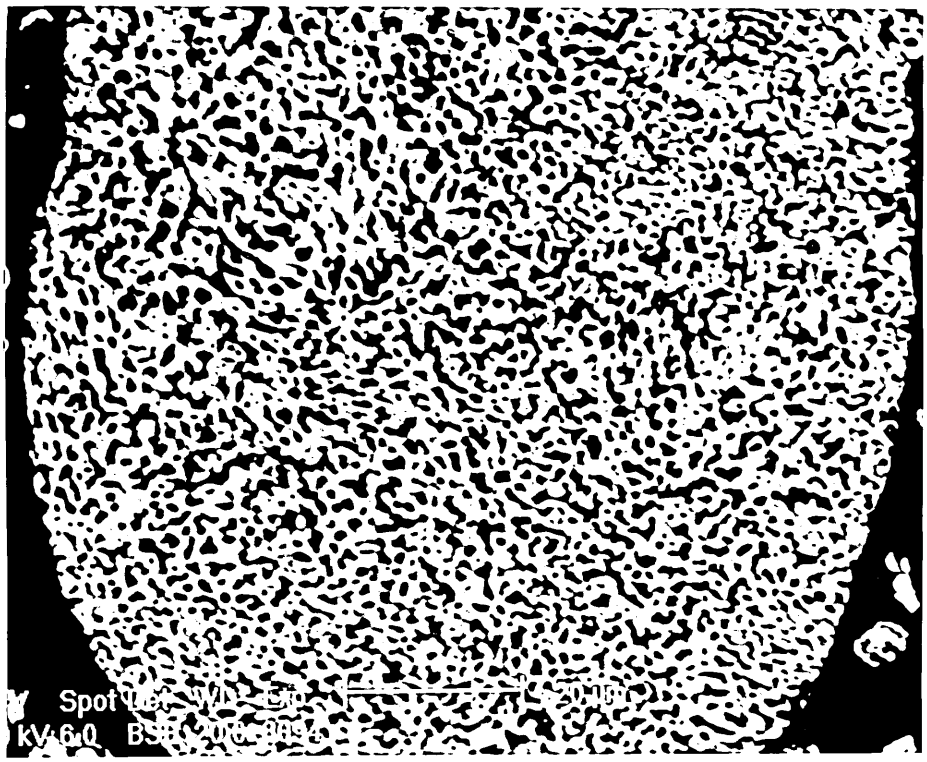

Figure 4-91b Microstructure of a shot particle devitrified at 1250°C for 1 hour.

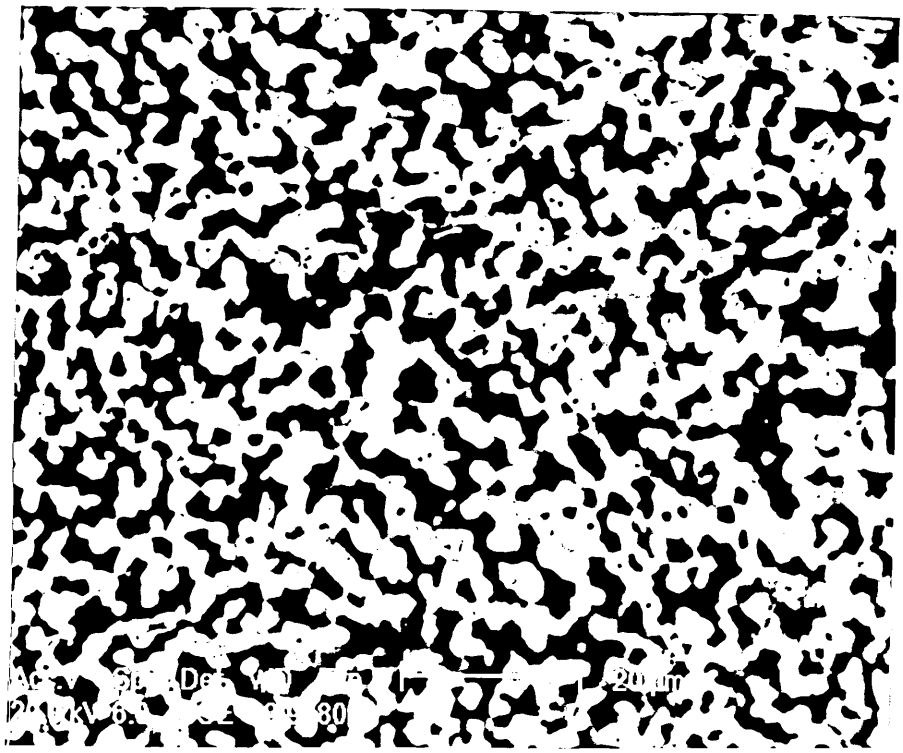

Figure 4-91c Microstructure of a shot particle devitrified at 1250°C for 24 hours.

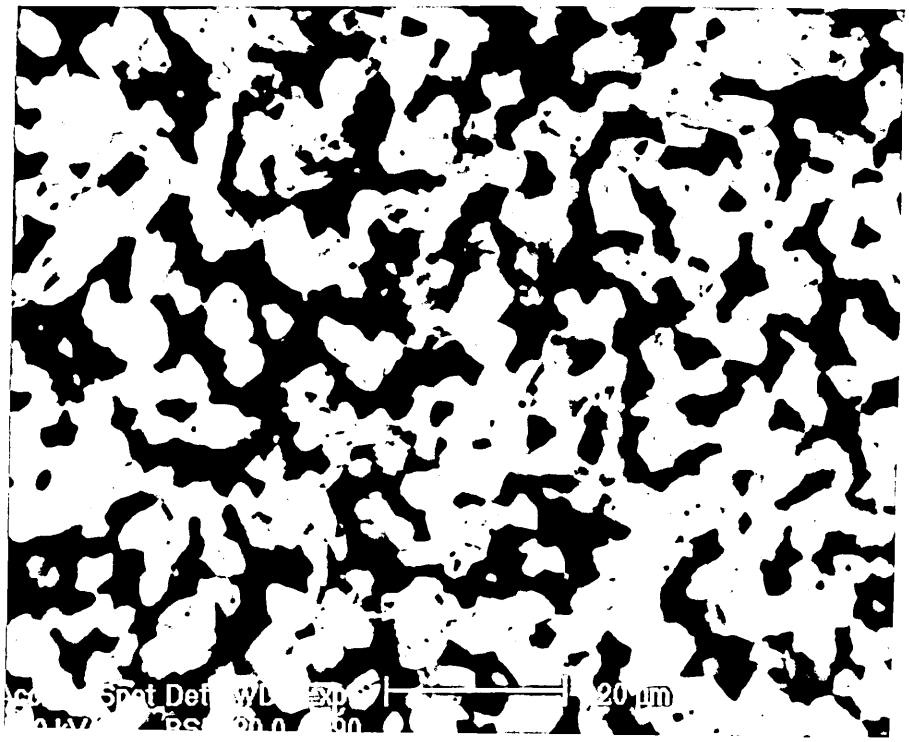

Figure 4-91d Microstructure of a shot particle devitrified at 1250°C for 168 hours.

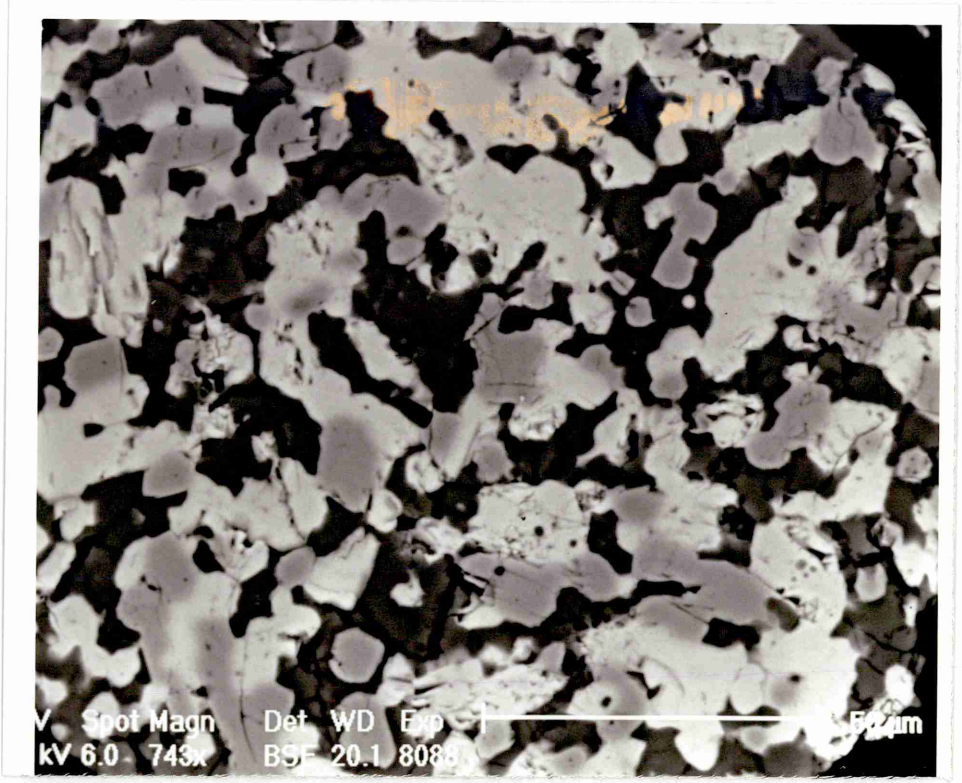

Figure 4-91e Microstructure of a shot particle devitrified at 1250°C for 672 hours.

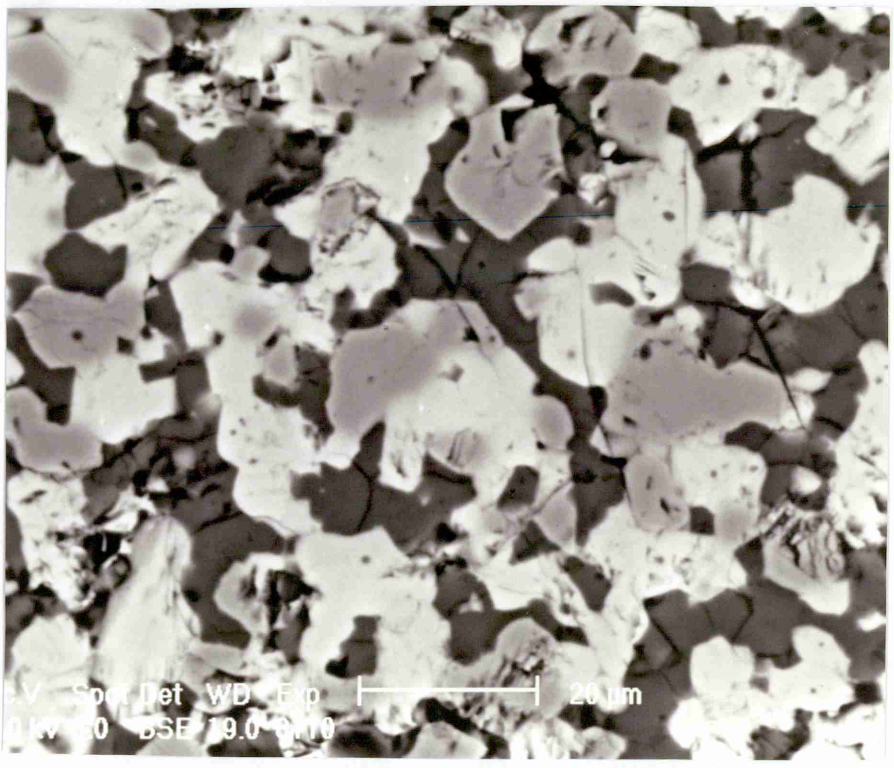

Figure 4-91f Microstructure of a shot particle devitrified at 1250°C for 1344 hours.

Figure 4-91 Development of microstructure of shot particles at 1250°C.

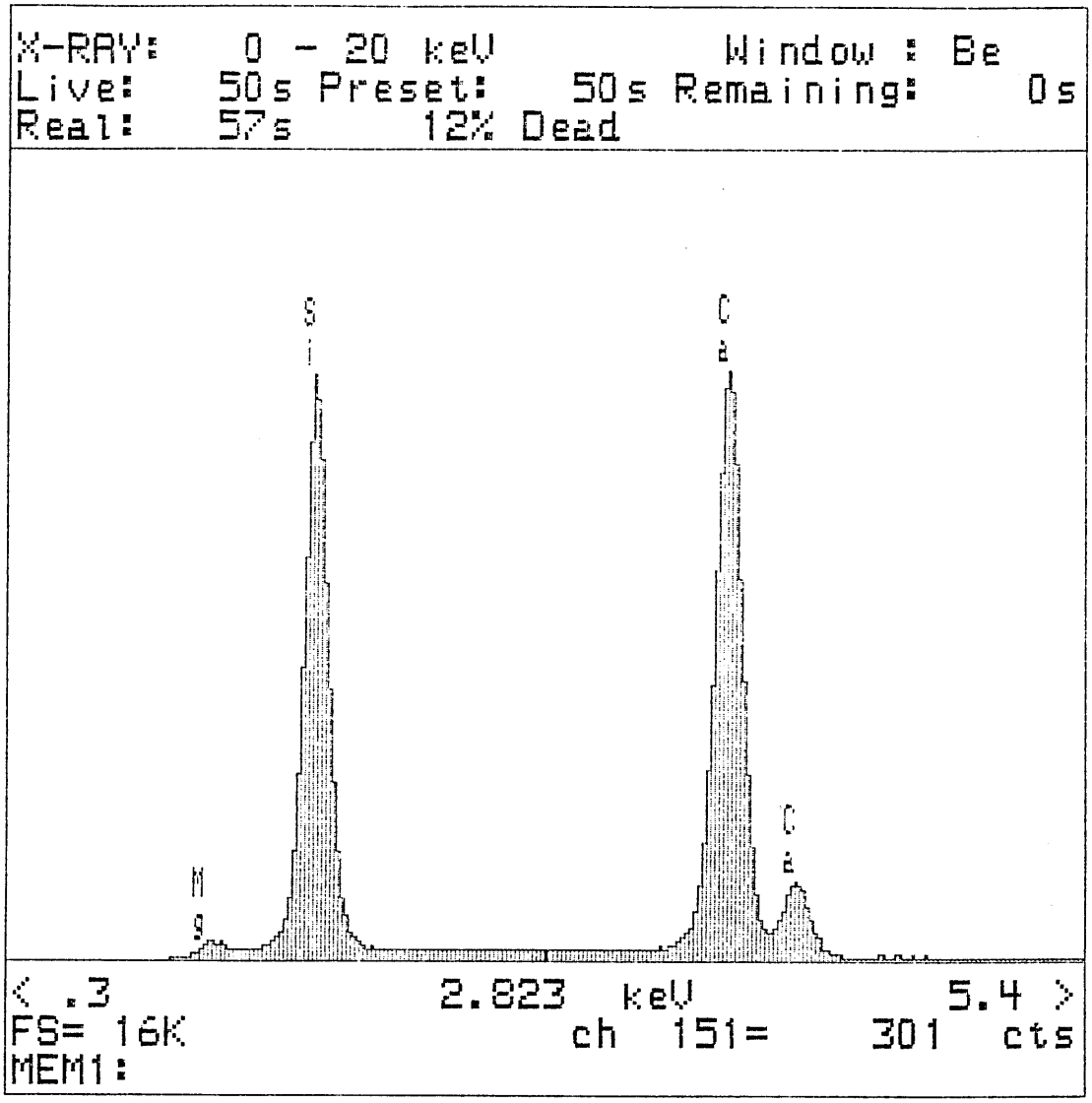

Figure 4-92a EDS spectrum of the brightest regions in figure 4-91f.

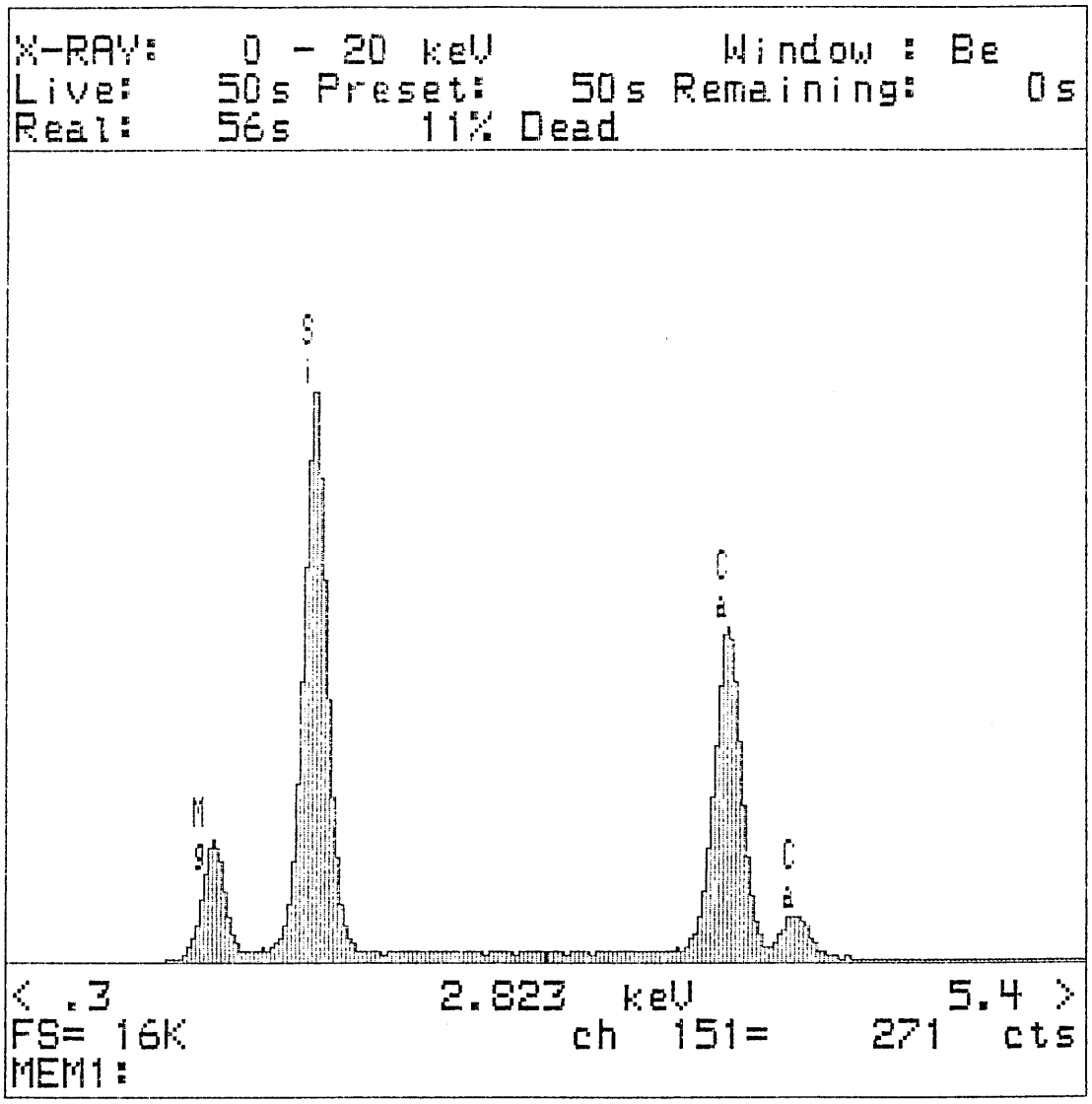

Figure 4-92b EDS spectrum of the brightest regions in figure 4-91f.

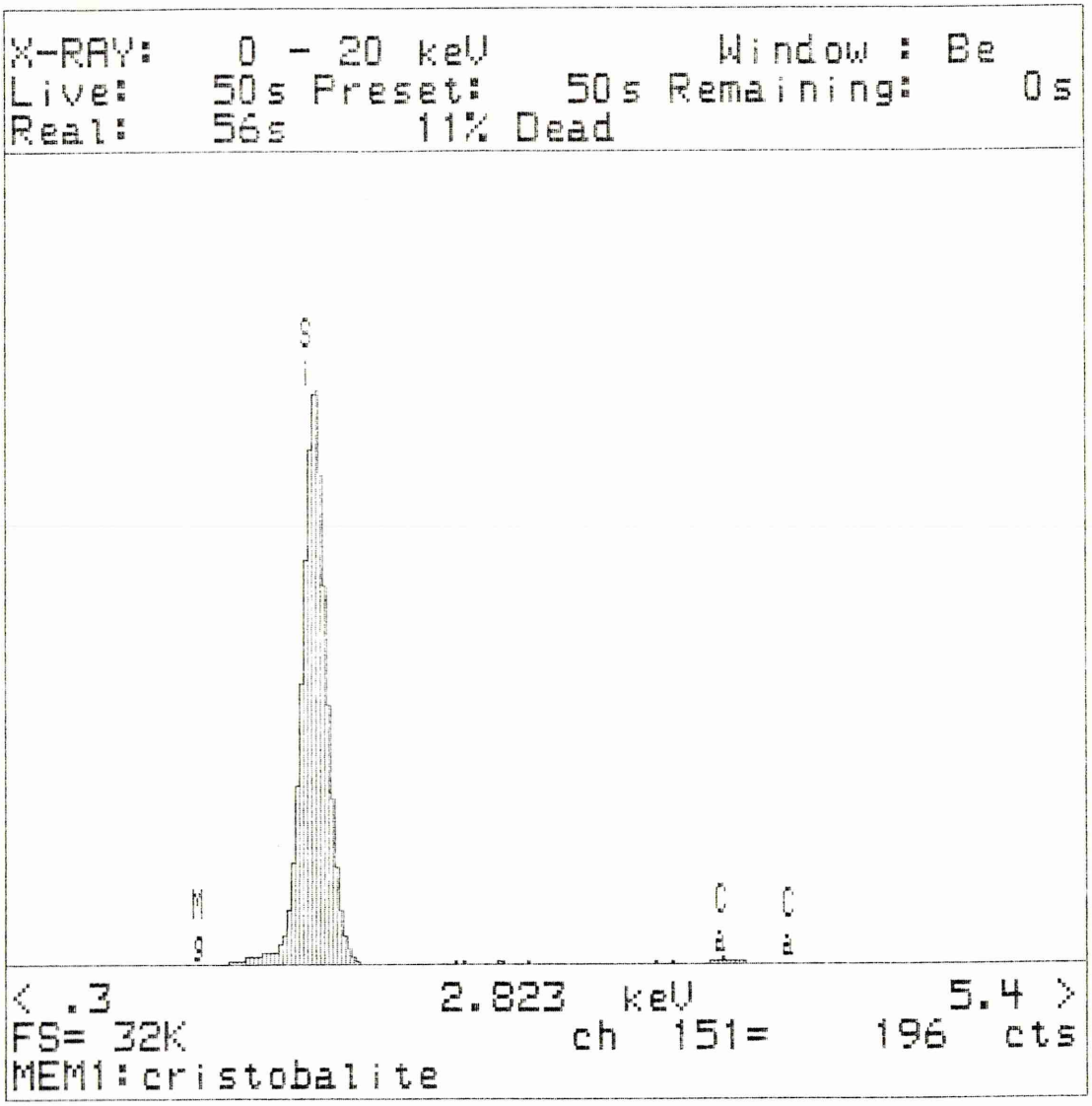

Figure 4-92c EDS spectrum of the darkest regions in figure 4-91f.

Figure 4-92 EDS spectra corresponding to different regions in figure 4-91f.

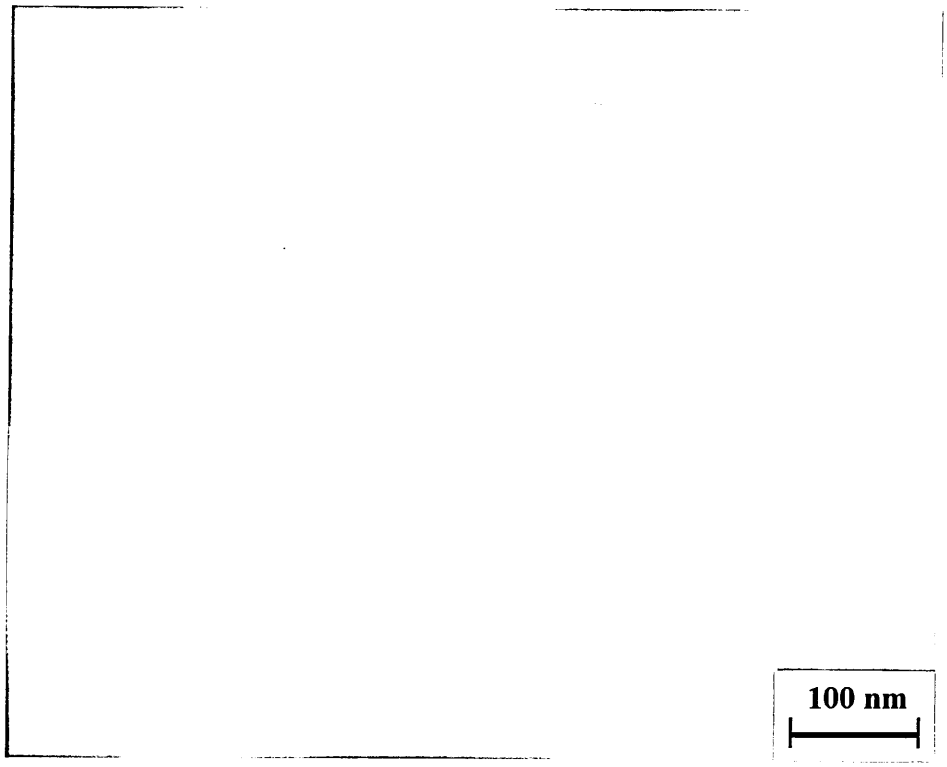

Figure 4-93 Microstructure of A2 fibre devitrified at 750°C for 24 hours.

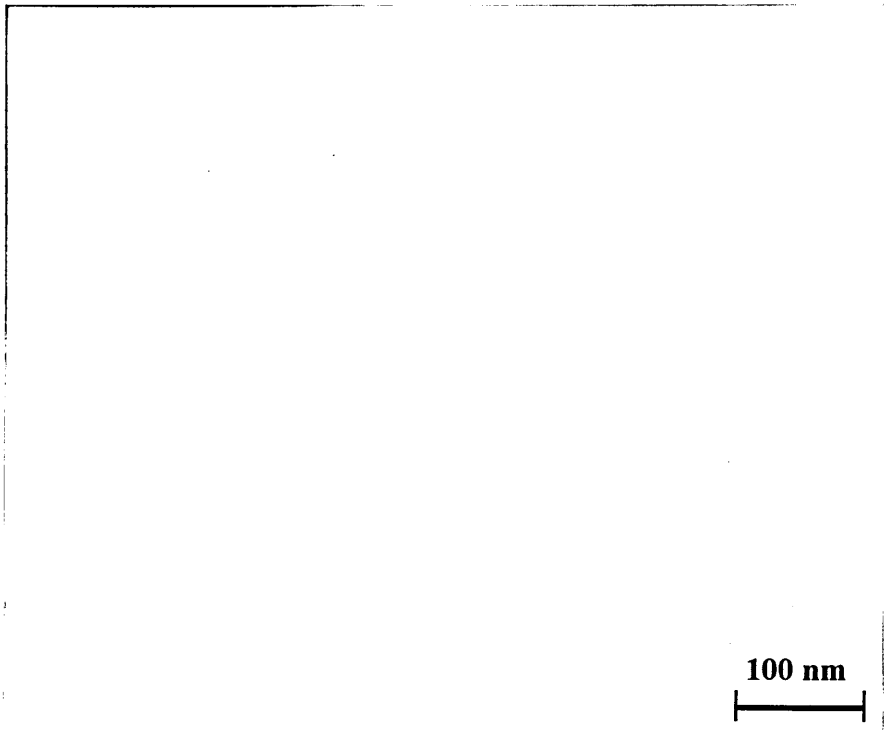

Figure 4-94 Microstructure of A2 fibre devitrified at 750°C for 48 hours.

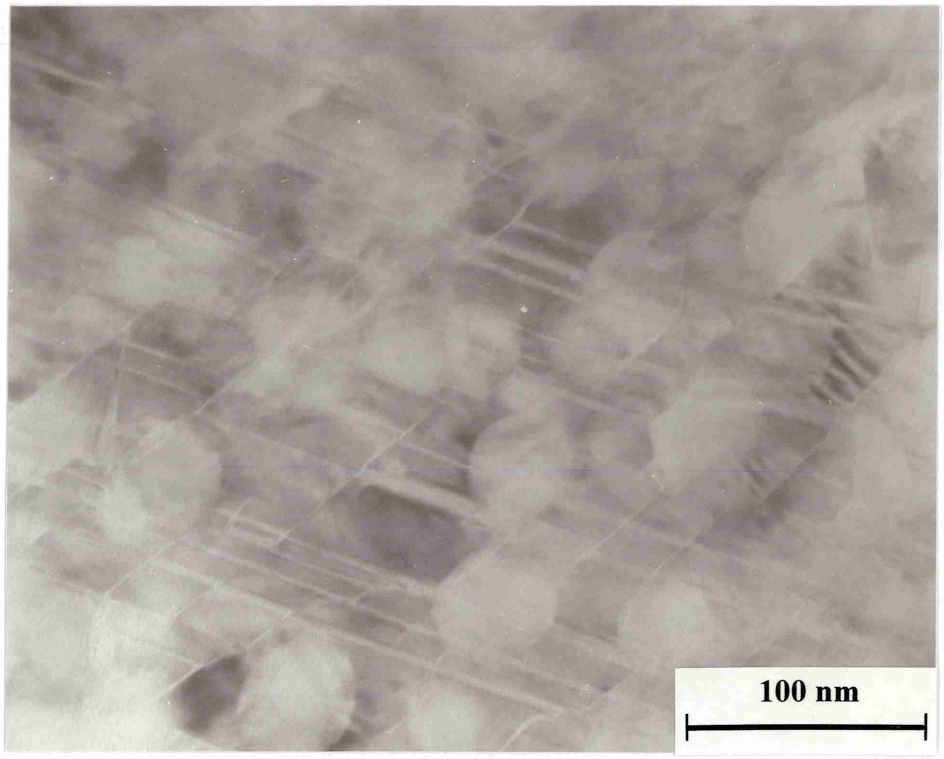

Figure 4-95 Microstructure of fibre A2 devitrified at 800°C for 48 hours.

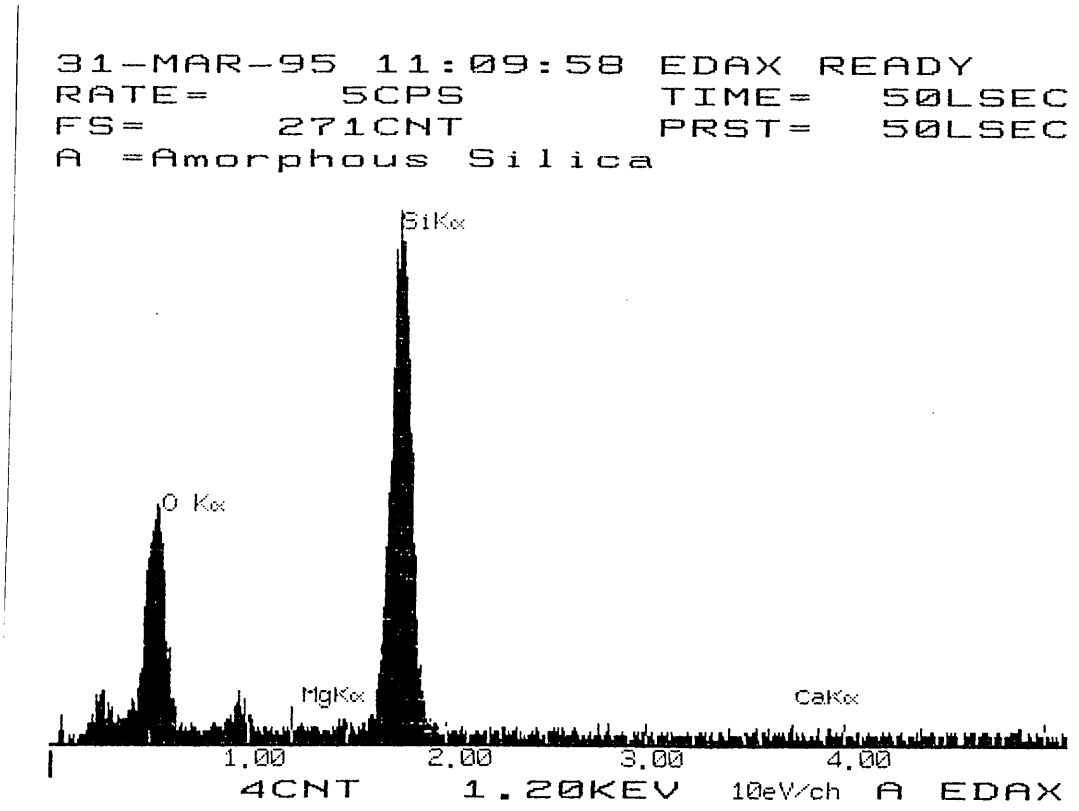

Figure 4-96 EDS spectrum of the circular particles in figure 4-95.

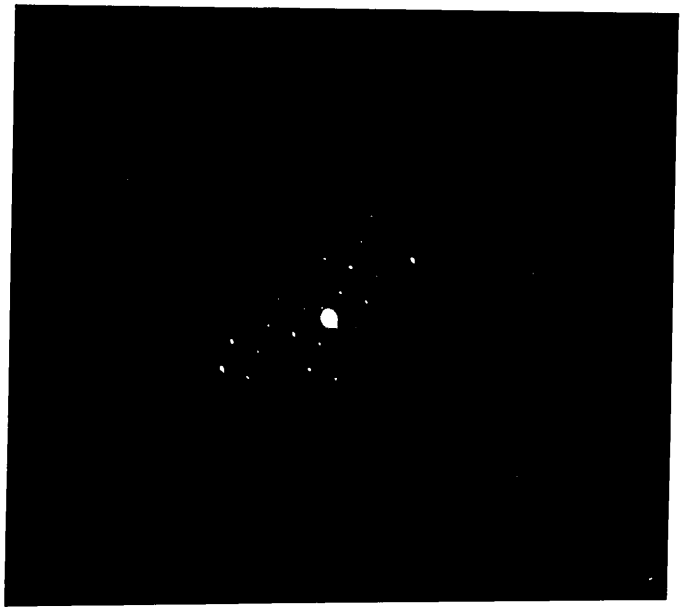

Figure 4-97 SAED pattern of the crystalline phase in figure 4-95

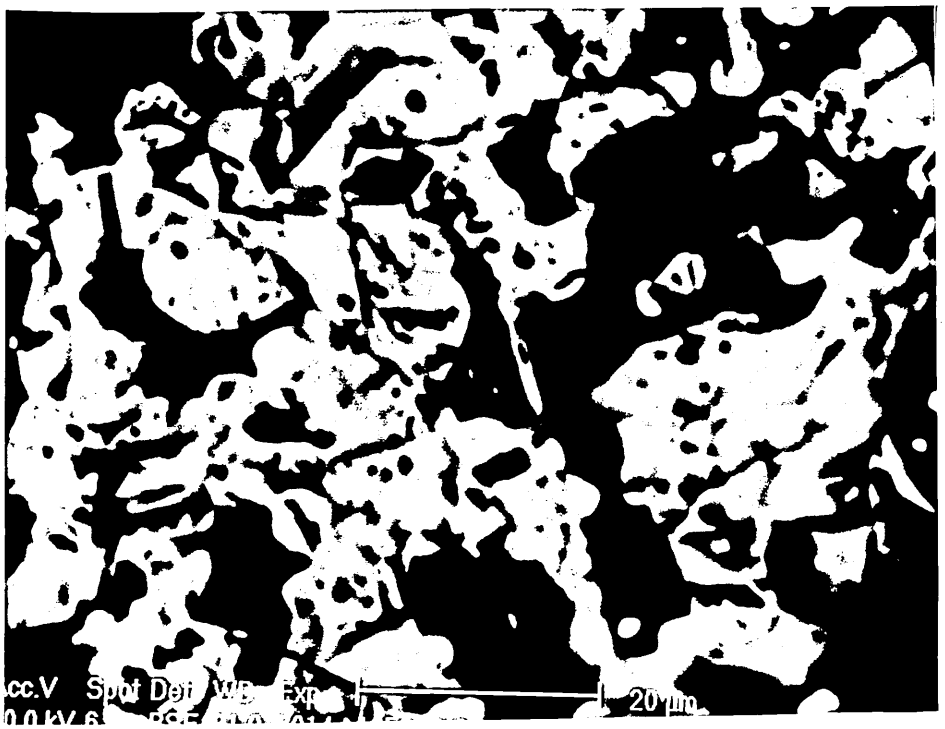

Figure 4-98 Microstructure of the shot particle devitrified at 1250°C for 1344 hours.

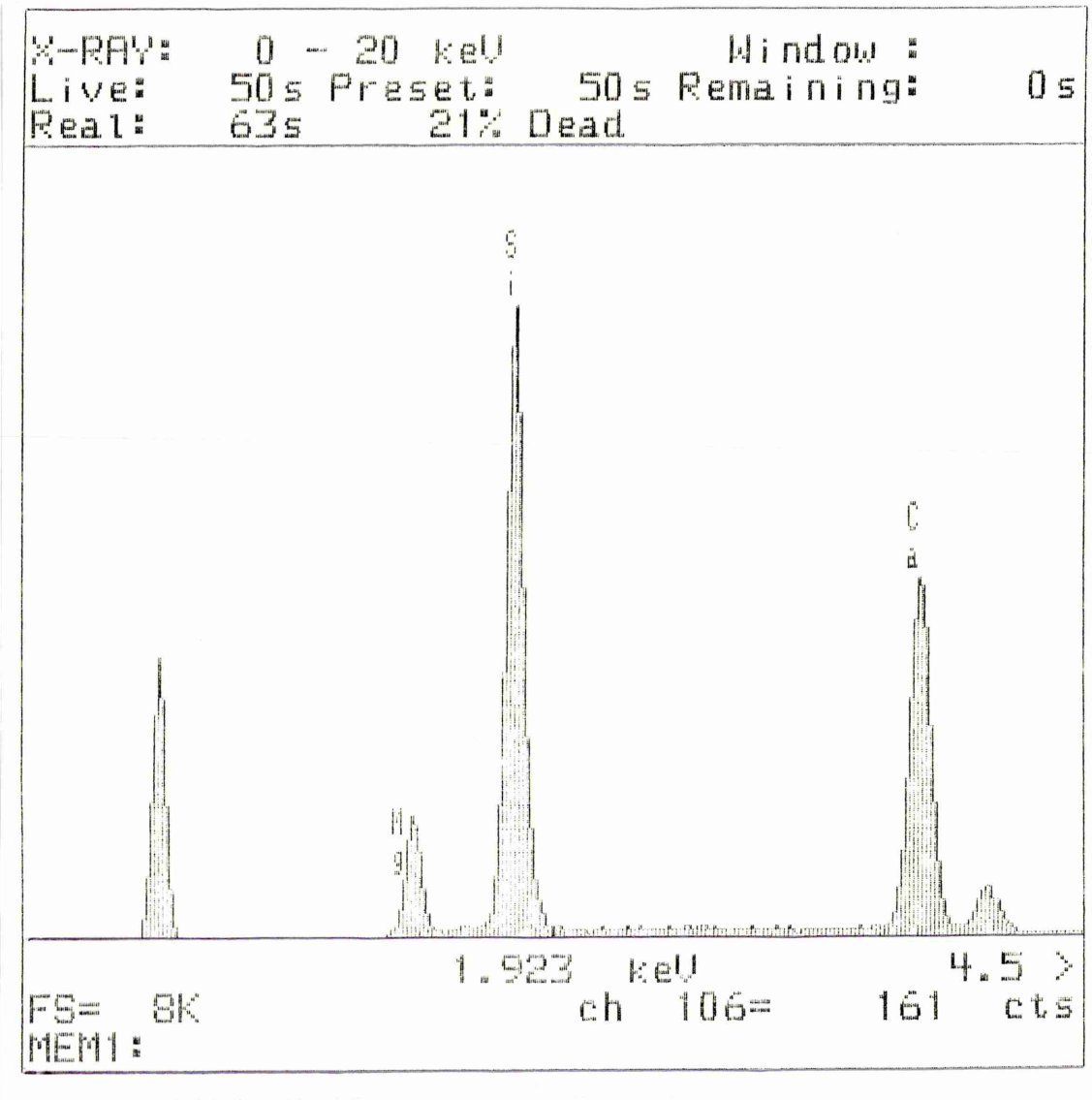

Figure 4-99a EDS spectrum of the brighter phase in figure 4-98.

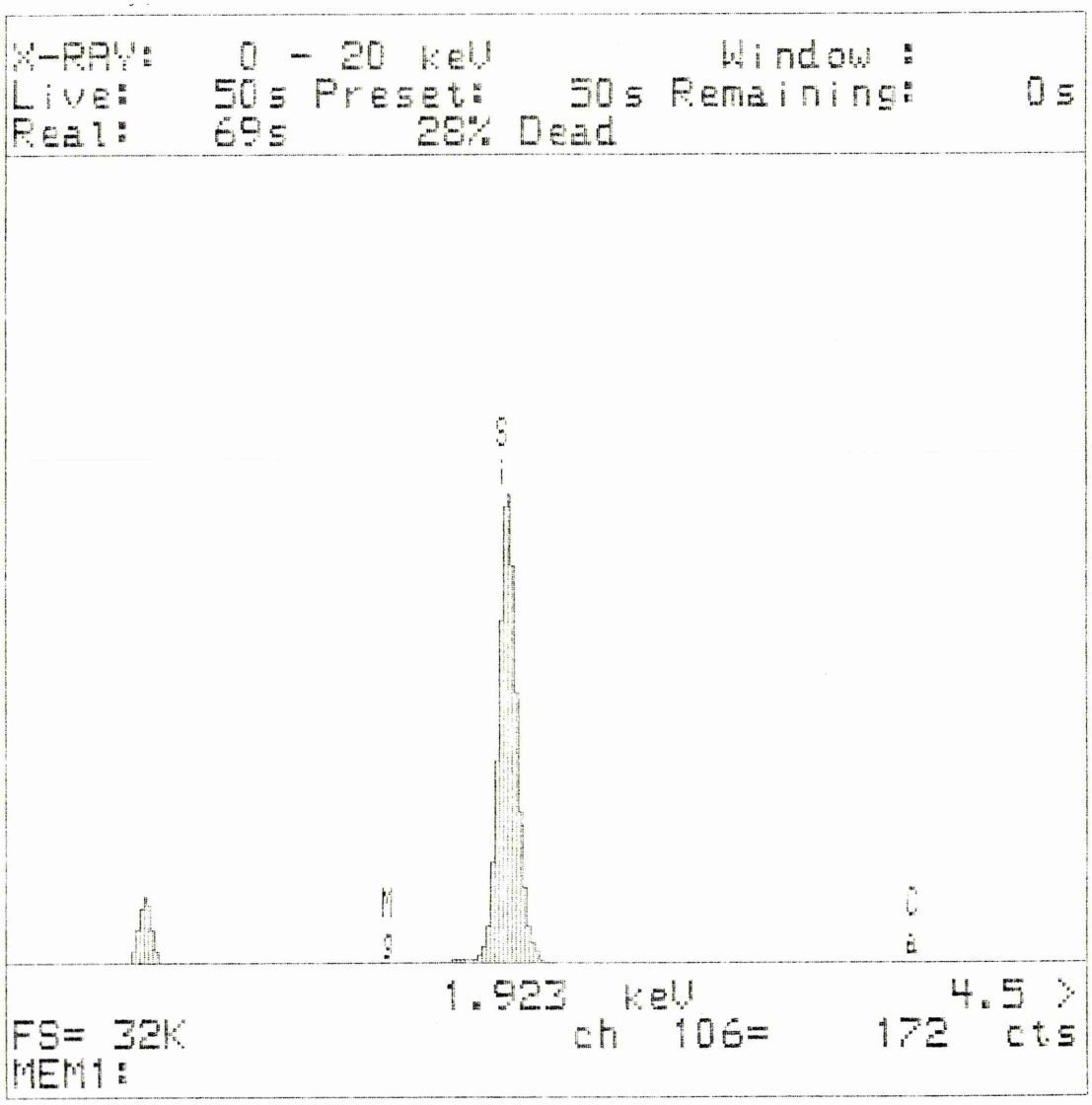

Figure 4-99b EDS spectrum of the darker phase in figure 4-98.

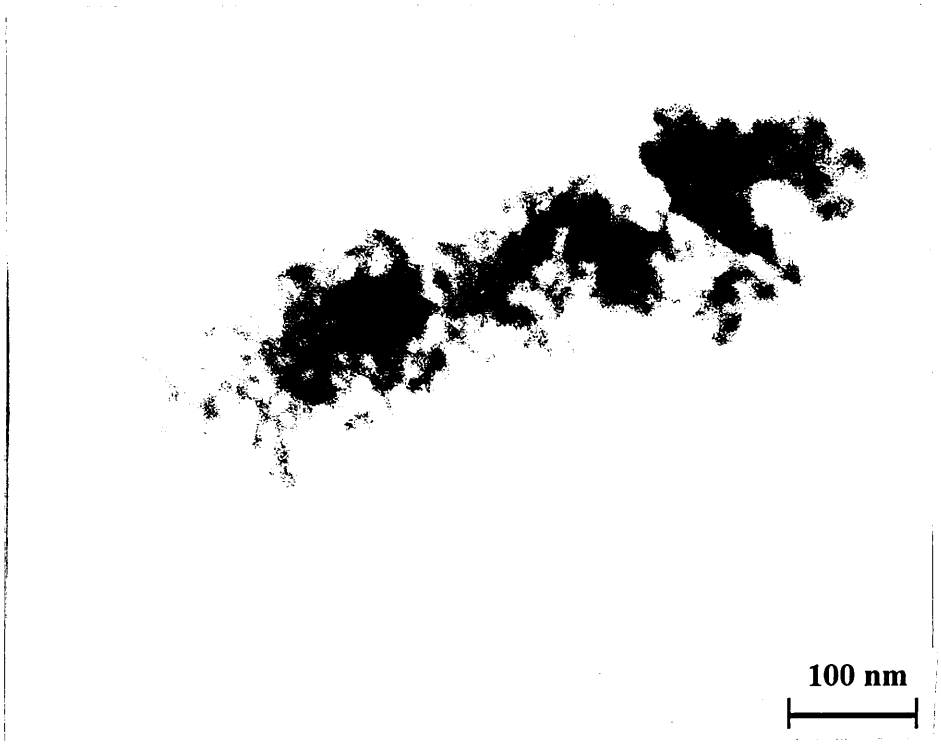

Figure 4-100 Microstructure of B3 fibre devitrified at 750°C for 24 hours.

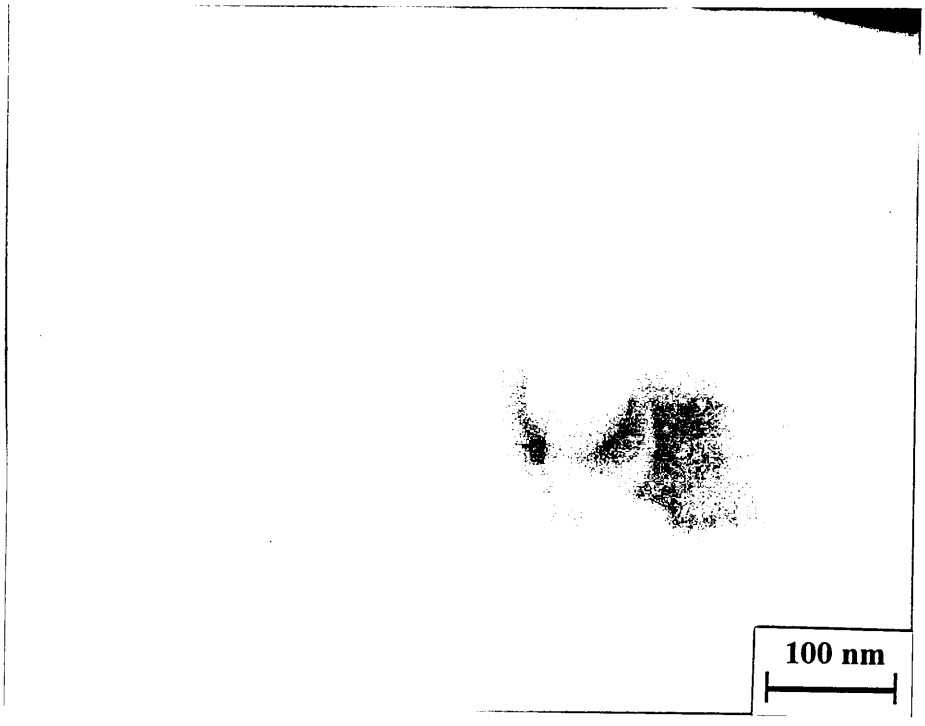

Figure 4-101 Microstructure of B3 fibre devitrified at 750°C for 336 hours

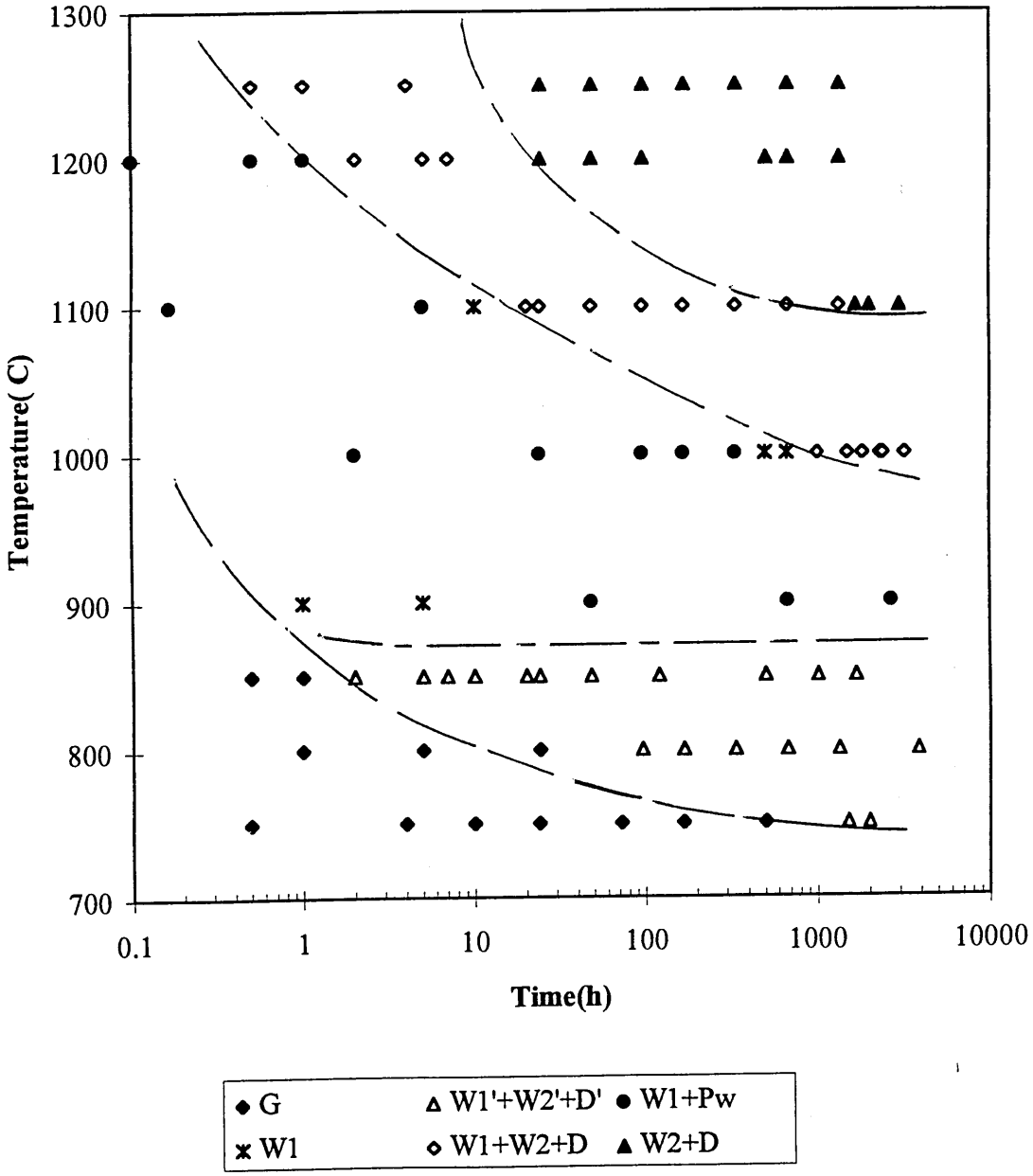

Figure 5-1 The development of alkaline-earth silicate phases in devitrified Superwool fibre.

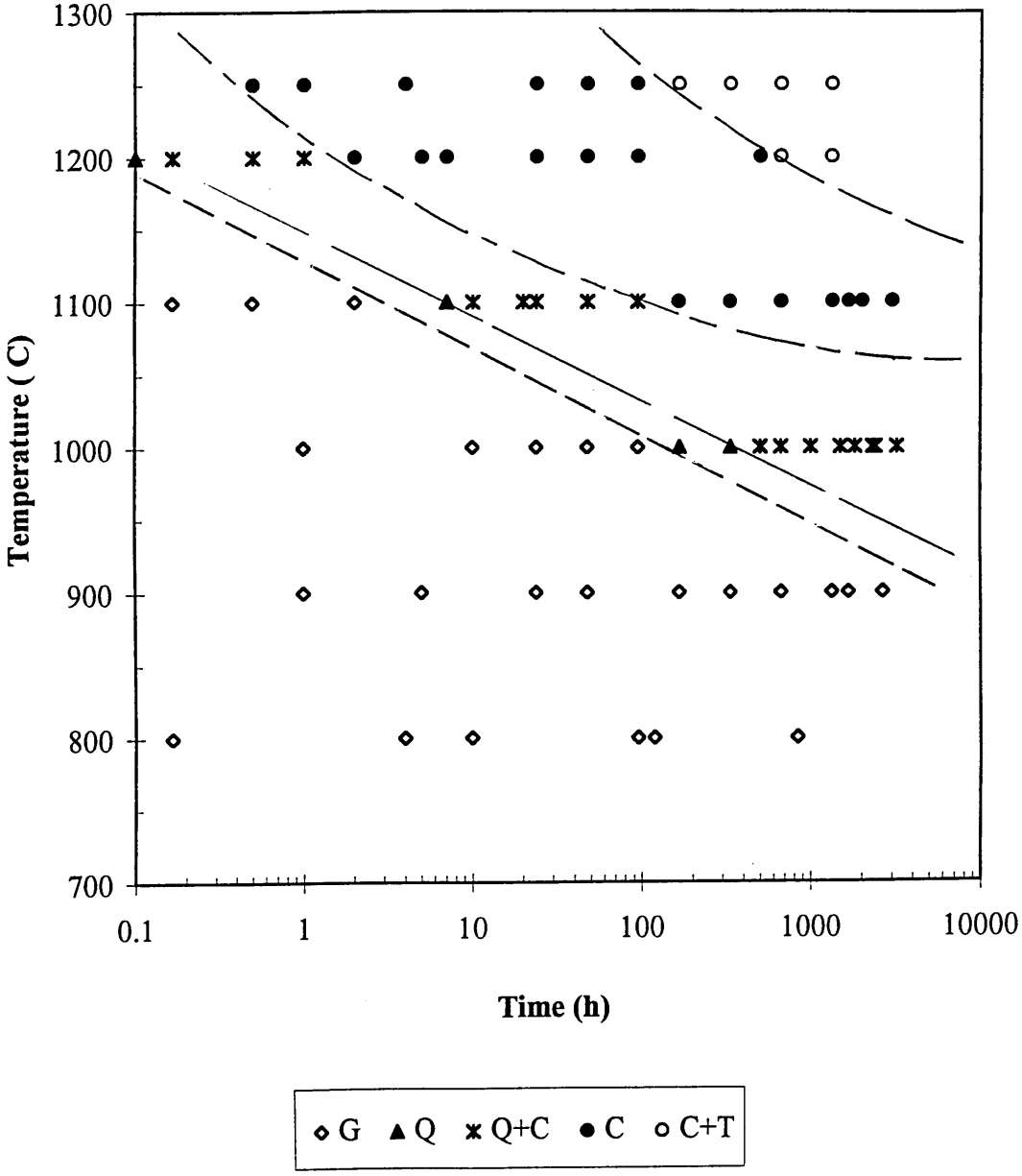

Figure 5-2 The development of silica phases in devitrified Superwool fibre.

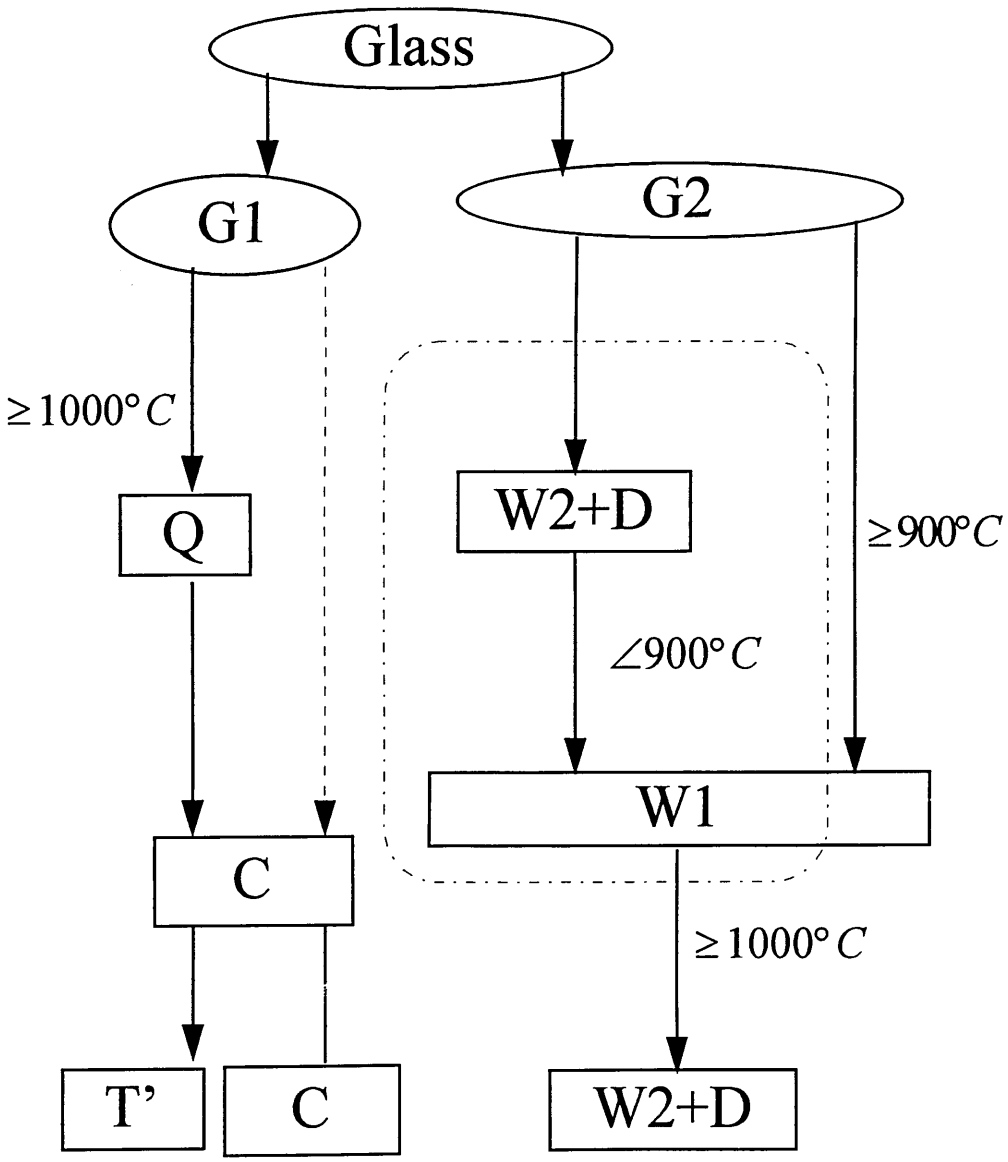

Figure 5-3 Devitrification process of Superwool fibre.

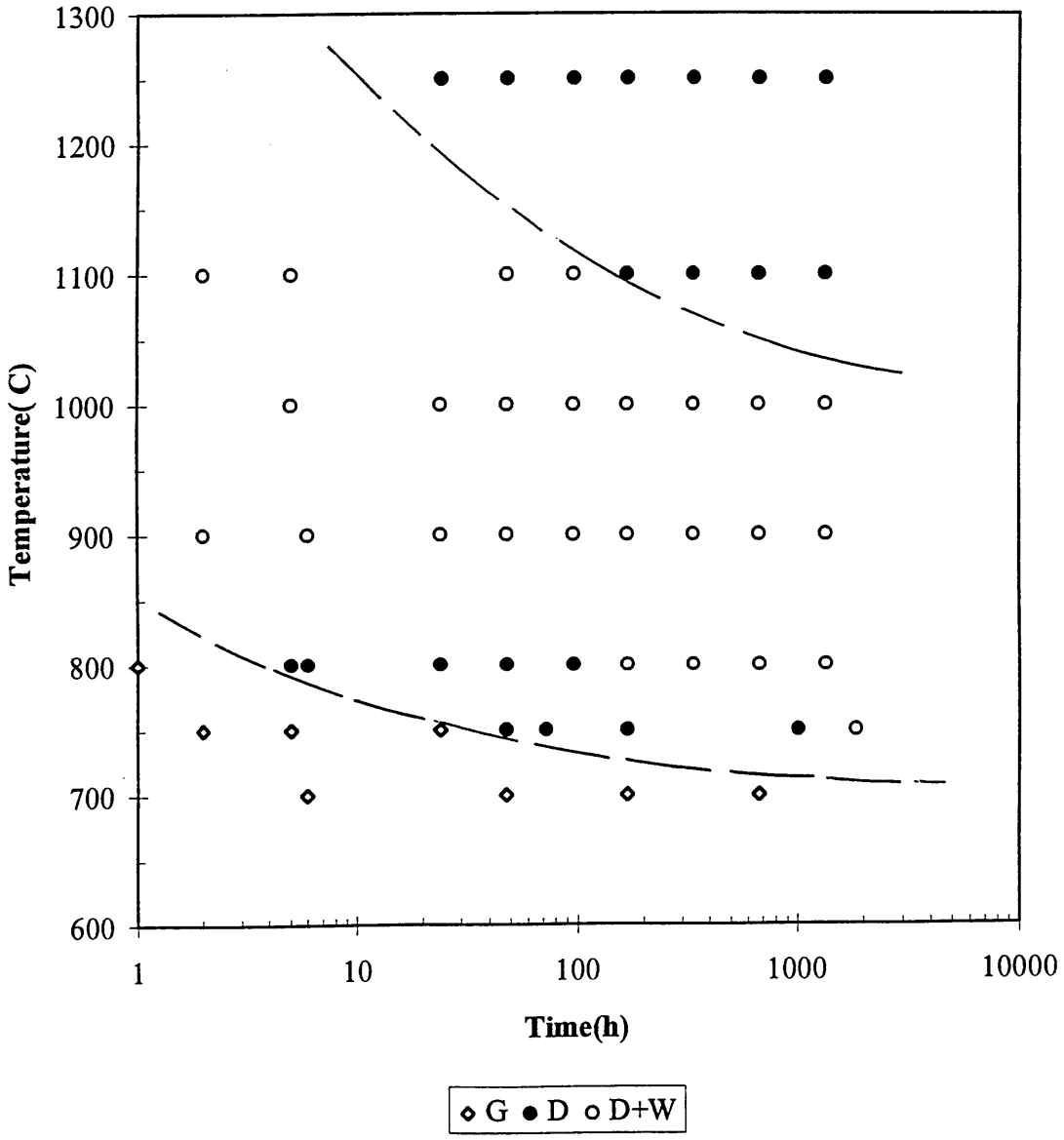

Figure 5-4 The development of alkaline-earth silicate phases in devitrified A2 fibre.

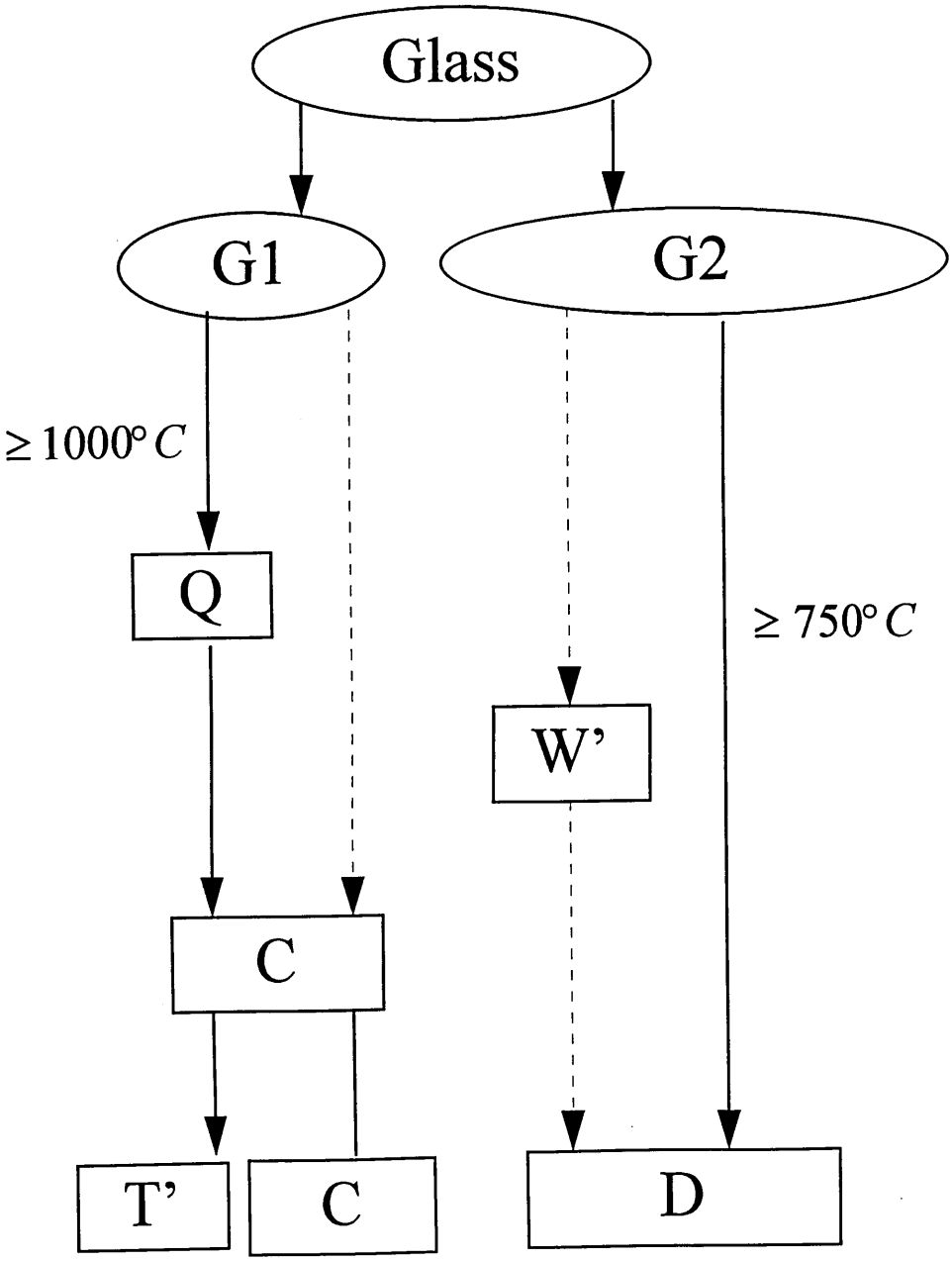

Figure 5-5 Devitrification process of A2 fibre.

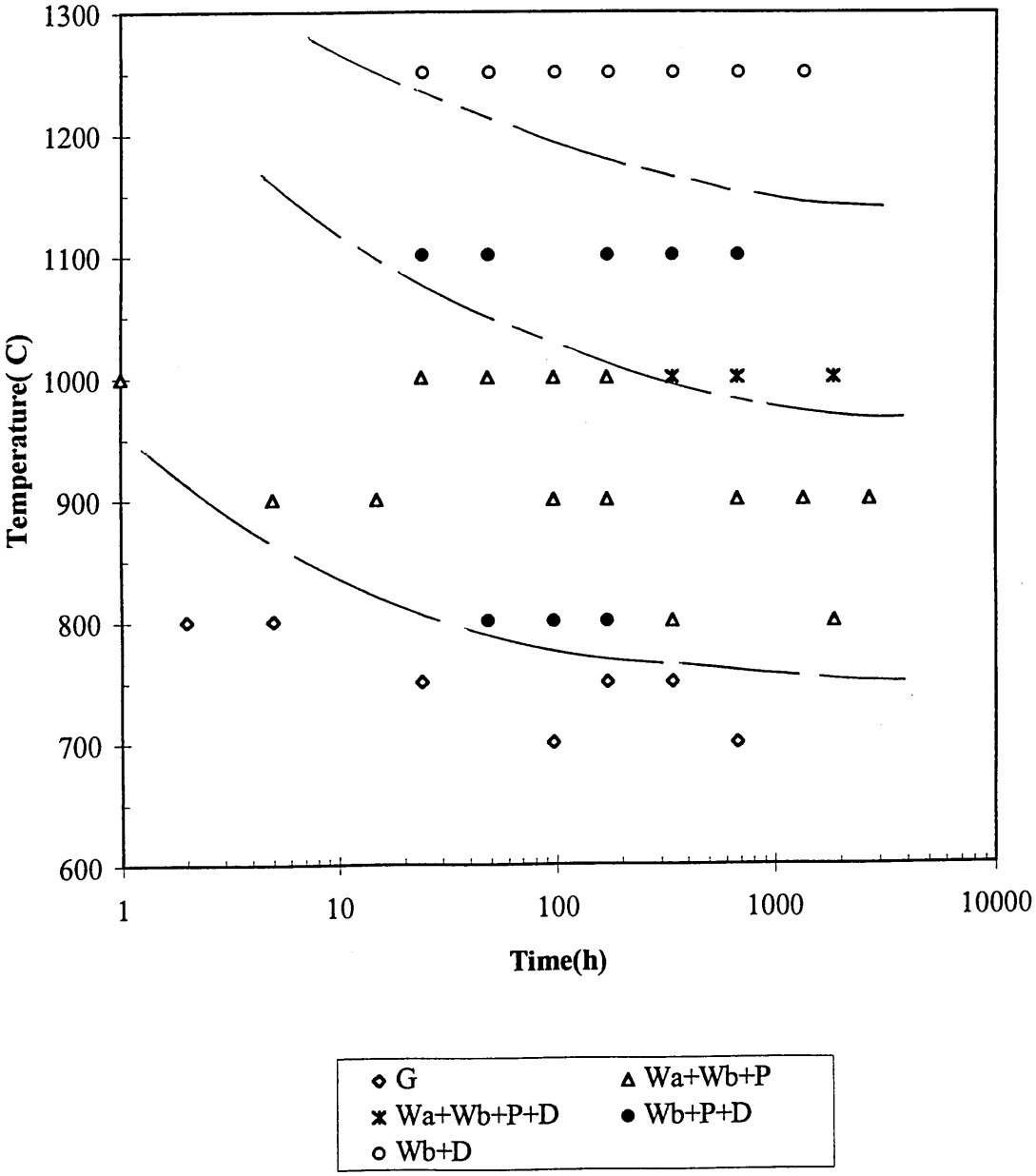

Figure 5-6 The development of alkaline-earth silicate phases in devitrified B3 fibre.

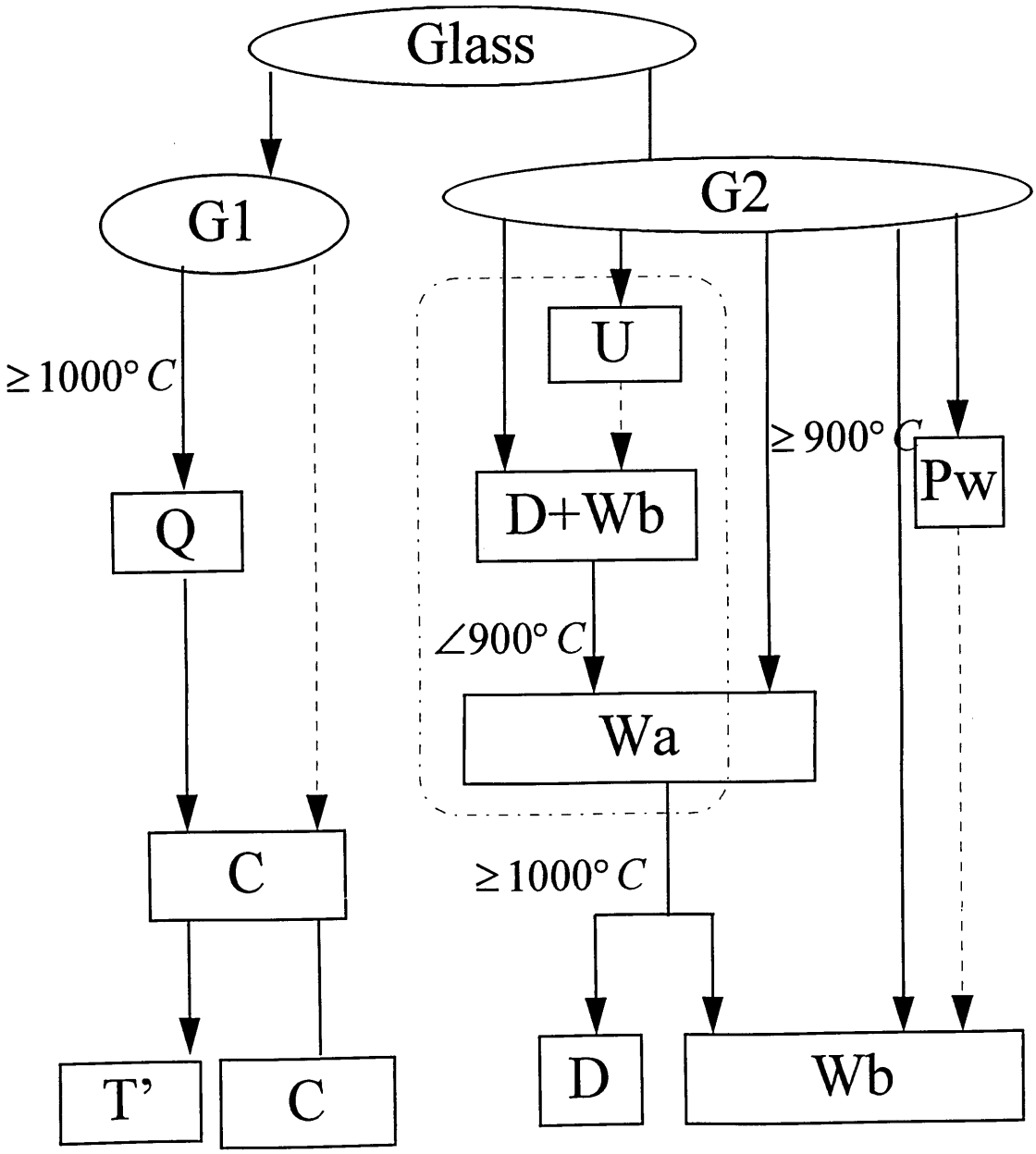

Figure 5-7 Devitrification process of Superwool fibre.

Journal of Microscopy, Vol. 184, Pt 1, October 1996, pp. 62–66.
Received 12 January 1996; accepted 10 May 1996

SHORT TECHNICAL NOTE

Preparation of ceramic fibre TEM cross-sections using ultramicrotomy and ion beam thinning methods

R. LI,* I. WADSWORTH,* J. YOUNG† & R. ACHESON‡
**Materials Research Institute, †School of Science and Mathematics, and ‡School of Engineering, Sheffield Hallam University, Sheffield S1 1WB, U.K.*

Key words. Ceramic fibre, fibre cross-sections, ion beam thinning, TEM specimen preparation, ultramicrotomy.

Summary

The preparation of specimens for detailed TEM micro-analysis of micrometre-diameter, ceramic fibre cross-sections is described. The starter material is ceramic fibre in powder form and both ultramicrotomy-based and ion beam thinning-based methods are described. Requirements for specimens of uniform and adequate thinness, for easy selection of representative fibre cross-sections within the same specimen and for a reliable and time-efficient preparation method, resulted in choice of the ultramicrotomy-based method and the associated development of a novel extrusion and sedimentation technique of embedding the fibres to provide necessary pre-alignment and packing.

Introduction

Detailed investigation of as-manufactured and heat-exposed microstructures of ceramic fibres is important to the understanding of their in-service behaviour and their interaction with the respiratory system (Young, 1991; Brown *et al.*, 1992). Our studies (to be reported) required the determination of these microstructures, using analytical transmission electron microscopy, in cross-sections of micrometre-diameter, as-manufactured and heat-exposed aluminosilicate and alkaline-earth silicate fibres.

The as-manufactured starter material is normally in the form of a wool and comprises a loose network of smooth-surfaced fibres (Fig. 1). Typically, aluminosilicate fibres have an arithmetic mean diameter of 2–3 μm whereas alkaline-earth silicate fibres have an arithmetic mean diameter of 4–5 μm (manufacturer's data). Devitrification at elevated exposure temperatures can roughen fibre surfaces and fibre networks can become bonded and brittle (Young, 1991).

The TEM work necessitated preparation of specimens which would allow the detailed microstructural analysis of fibre cross-sections. The specimens had to be uniformly and adequately thin (a) to allow representative cross-sections to be selected from a number of sections viewed in the specimen and (b) to enable the separate identification and analysis of single grains or phase-separated regions in selected fibre cross-sections. Requirement (b) was particularly stringent as the dimensions of individual grains or phase separated regions could be less than 100 nm. Too great a specimen thickness thus (i) made it difficult to isolate and analyse distinct phase regions due to the tendency for grains or phase-separated regions to overlap through the depth of the specimen and (ii) degraded the spatial resolution, especially for energy dispersive X-ray analysis, which again limited the ability to analyse distinct regions in the selected fibre cross-sections. Requirement (a) demanded pre-alignment and parallel packing of fibres and the preparation method chosen had to be reliable and time efficient to cope with the number of specimens required by our investigation.

Ion beam thinning method

The first stage was to make a 3-mm-diameter fibre/resin disc having a high fibre packing density and low porosity. The fibre starter material was crushed to fine powder with a pestle and mortar and then mixed on a glass slide with Gatan's G-1 epoxy resin and hardener. The mixture was vacuum degassed for 30 min, packed into a 3-mm inside-diameter stainless steel tube and again vacuum degassed. The epoxy was cured for 30 min at 100 °C and the tube was sliced into a series of 250–500-μm-thick discs using a

Correspondence to: J. Young: Tel. (0114) 2533001; Fax (0114) 2533066; E-mail: j.young@shu.ac.uk

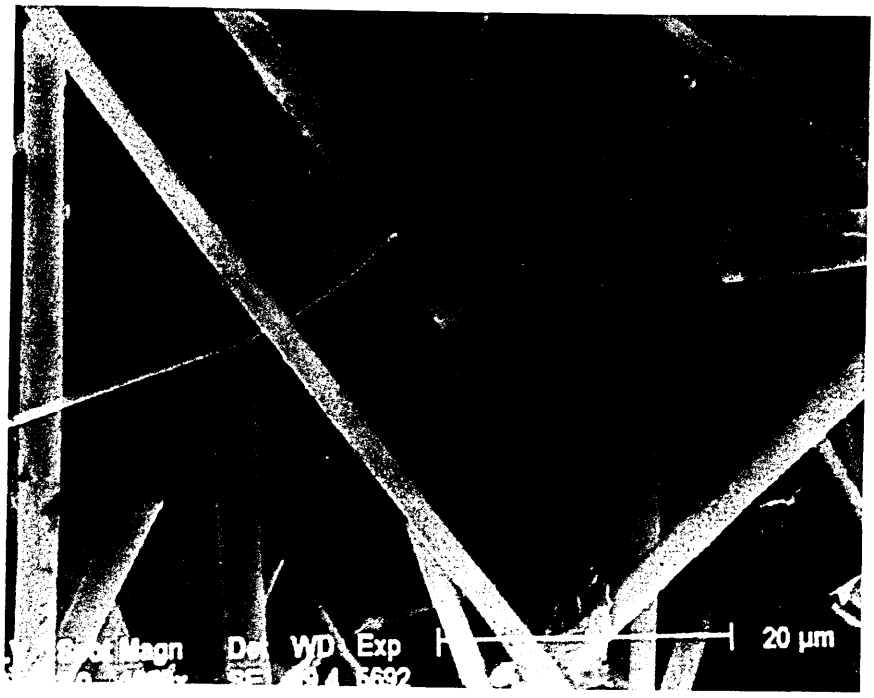

Fig. 1. TEM image showing a representative network of as-manufactured aluminosilicate refractory ceramic fibres.

wiresaw. The discs were ground to a thickness of about 50 μm and one side polished with 0·25-μm-grade diamond paste.

Dimpling of the discs was achieved by grinding, coarse polishing and then fine polishing using a Gatan model 656 Dimple Grinder. Six-micrometre diamond paste was used to coarse grind the disc to a central thickness of 20 μm; 1-μm diamond paste was used to coarse polish the sample to a central thickness of 15 μm, and fine polishing required a felt polishing wheel and 0·05-μm γ-alumina suspension. The sample was cleaned in methanol in an ultrasonic bath after each stage of the polishing operation.

Ion beam thinning of the discs was achieved using the Gatan model 691 Precision Ion Polisher (PIPS^{TM}). This system overcomes the problem of preferential ion etching of the resin by allowing the incident argon ion beam to strike the sample at near grazing incidence thus allowing the fibres to shield the resin and minimize the rate of resin removal. The dimpled discs were ion thinned, dimple downwards, using a 3-keV argon ion beam. The specimen was continuously observed with the attached microscope and the thinning was terminated manually as soon as the perforation was first seen. The perforated disc was then reloaded with dimple upwards and ion-beam polished for 5 min at 2 keV. The disc was carbon coated before analysis in the electron microscope.

Figure 2 illustrates the packing and alignment of fibres in an ion beam thinned specimen. The resulting specimens showed (a) only limited preferential thinning of the resin matrix, (b) full views of fibre cross-sections with no fragmentation and (c) good adhesion of cross-sections to the resin matrix. Drawbacks were (a) increasing specimen thickness with distance from the perforation with the associated loss in the ability to resolve and analyse individual grains and phase-separated regions in selected fibre cross-sections, (b) random alignment of fibres which made it difficult to obtain sufficient well-aligned cross-sections sufficiently close to the perforation for analysis, and (c) the length and complexity of the process to prepare a single specimen from an initial sawn disc.

Ultramicrotomy method

Ultramicrotomy has been extensively used for the preparation of TEM specimens from biological materials and increasingly from a wider range of materials including polymers (Sawyer & Grubb, 1987), metals (Thomas, 1962), surface coatings (Swab & Linger, 1988), metal multilayers (Howell *et al.*, 1995), particles (Chowdhury *et al.*, 1990) and whiskers (Ulan *et al.*, 1990). The challenge and uniqueness of our work was to develop the method, as described by Reid (1974), to meet our analytical requirements for fibre alignment, high fibre packing density and specimen uniformity and thinness.

The crushed fibres were initially wetted in an epoxy resin primer solution of 1% γ-glycidoxypropyl trimethoxysilane in 50% methanol and 50% water and then dried. This process, reported by Swab & Klinger (1988) for multilayer optical coatings, strengthened the interfacial bond between fibres and resin and limited fibre pullout during ultramicrotomy.

An important consideration concerning embedding was the need for parallel alignment and close packing of fibres to

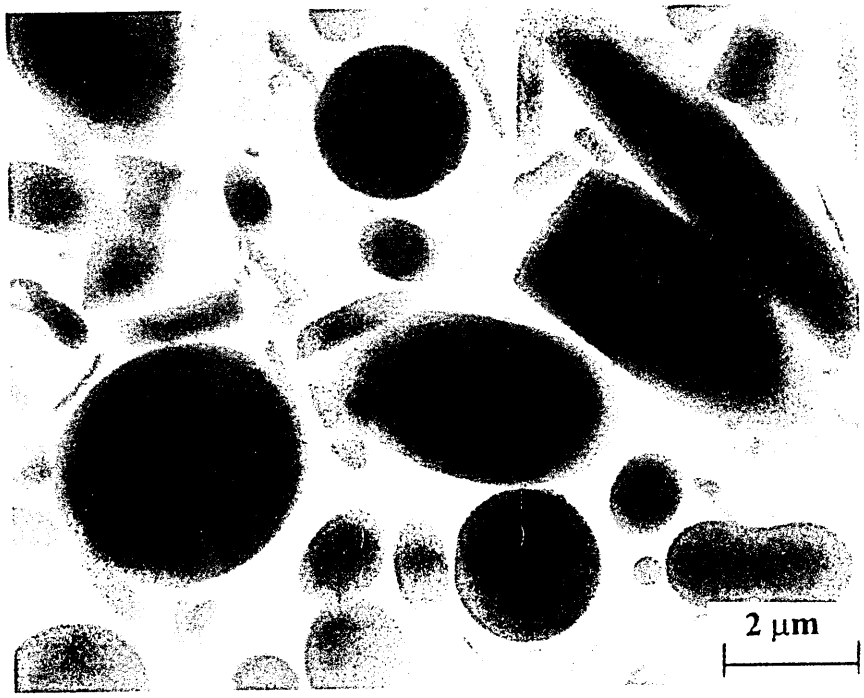

Fig. 2. TEM image showing fibre packing and alignment in a specimen of aluminosilicate fibres prepared by the ion beam thinning method.

ensure that as many as possible would appear in the TEM specimen with cross-sections parallel to the specimen surface. To this end, typically 20% by mass of fibre powder was added and dispersed in a fresh mixture of four-component Spurr's resin (Agar Scientific Ltd). This resin was chosen for its low initial viscosity and good sectioning properties after polymerization and the proportions of the four components were chosen to produce a block of suitable hardness. Generally, the harder the block the better the results, although too much hardener reduces the lifetime of the resin. The following embedding process was followed.

A Pasteur pipette was used to extrude and inject the fibre/resin mixture into a plastic tube of 1 mm internal diameter and then the loaded tube was laid horizontally and left for 30 min before curing the fibre/resin mixture in an oven for 8 h at 70 C. The extrusion process produced initial fibre

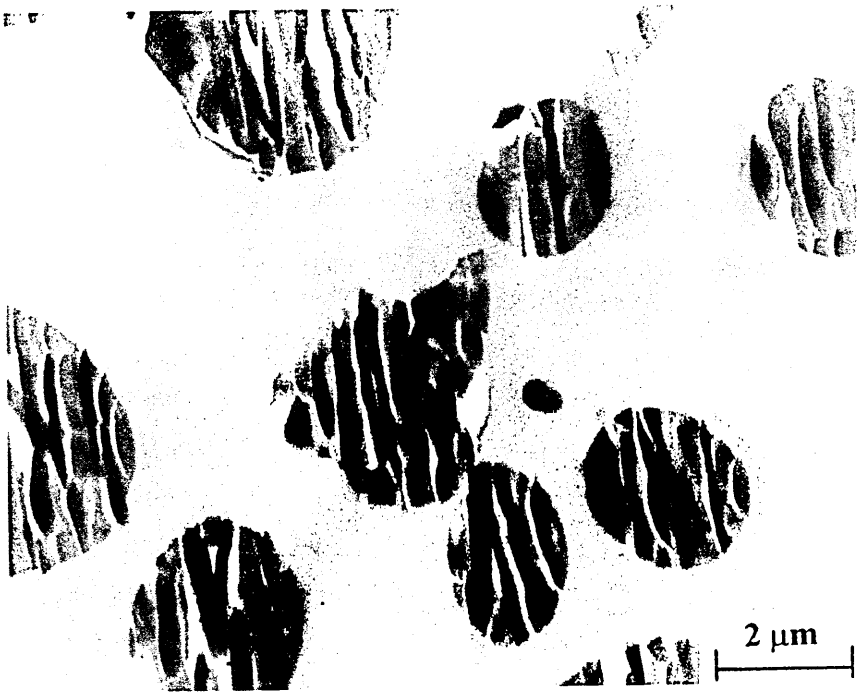

Fig. 3. TEM image showing fibre cross-sections in a specimen of aluminosilicate fibres prepared by the ultramicrotomy method.

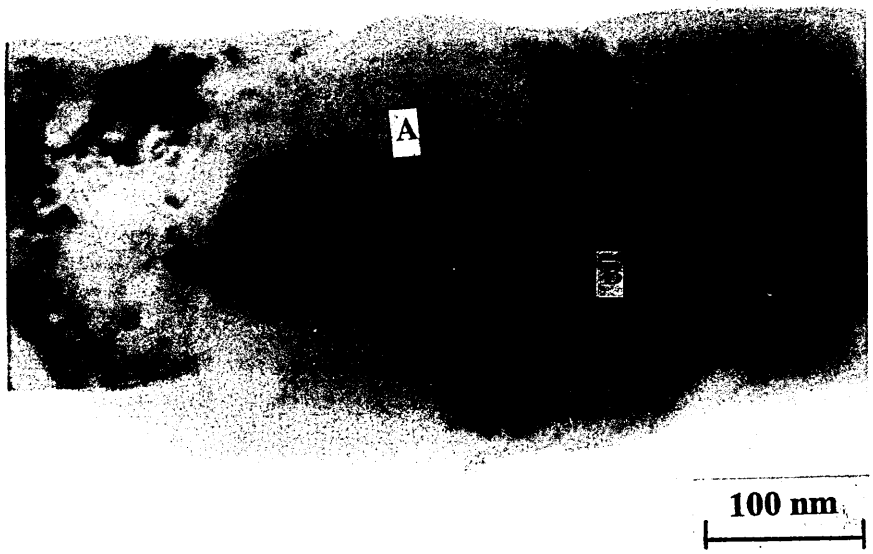

Fig. 4. TEM image showing a typical devitrified microstructure for furnace-exposed alkaline-earth silicate fibres. Regions shown as A are vitreous silica and regions shown as B comprise grains of wollastonite.

alignment, horizontal resting of the loaded tube enhanced fibre packing and produced further alignment due to sedimentation, and the subsequent curing of the loaded tube and removal of the outer plastic sheath resulted in a solid fibre/resin cylinder. The cured fibre/resin cylinder was then vertically positioned with its end up to the mould face of a standard specimen mould (Agar Scientific Ltd) which was then filled with fresh resin and cured at 70 °C for 8 h.

A Reichert OmU3 ultramicrotome fitted with a freshly made glass knife was used to trim down the cutting face of the block to a taper which would provide a suitable cutting area to the knife and maximize the cutting force per unit length. Ultrathin sectioning was achieved by replacing the glass knife by a 45° diamond knife fitted with a collecting trough filled with distilled water. The rate of thermal feed, the cutting speed and the knife returning speed were carefully controlled to collect ribbons of sections which were grey in colour and had a section thickness of about 60 nm (Peachey, 1958). The sections were collected onto carbon films on 200-mesh copper grids from the distilled water surface of the collecting trough and dried prior to viewing in the Philips CM20 analytical transmission electron microscope.

Figure 3 shows a typical electron micrograph of cross-sections of as-manufactured aluminosilicate fibres from a specimen prepared by this ultramicrotomy method. Extensive electron-transparent regions of uniform and adequate thinness were obtained and the good alignment and adequate packing density of fibres enabled the easy selection of fibre cross-sections for analysis. The fibre cross-sections tended to crack and fragment during sectioning but this did not prove a problem in analysis as the microstructures in fragments could be individually analysed and the spatial arrangement of fragments relative to the original fibre cross-section was preserved. Fibre sections were firmly adhered to the resin and no pullout of fibres was observed. Figure 4 illustrates a typical devitrified microstructure for furnace-exposed, alkaline-earth silicate fibres; the regions shown as B comprise grains of wollastonite whereas the regions shown as A are vitreous silica. Specimens produced routinely by the ultramicrotomy method were thin enough to allow the detailed identification and analysis of the various components of the microstructures by analytical transmission electron microscopy and, once the resin block was made for a particular starter powder, further TEM specimens could be quickly prepared.

Conclusion

While the ion beam thinning method was capable of providing TEM specimens of fibre cross-sections, the ultramicrotomy method, with the associated development of embedding to provide pre-alignment and closer fibre packing, offered major advantages in terms of fibre alignment and packing, uniform and adequate thinness of specimens and reliability and time efficiency of operation.

References

Brown, R.C., Sara, E.A., Hoskins, J.A., Evans, C.E., Young, J., Laskowski, J.J., Acheson, R., Forder, S.D. & Rood, A.P. (1992) The effects of heating and devitrification on the structure and biological activity of aluminosilicate refractory ceramic fibres. *Ann. Occup. Hyg.* **36**, 115–129.

Chowdhury, A.J.S., Freundlich, A. & Sheppard, T. (1990) The role of ultramicrotomy in the microstructural studies of rapidly solidified aluminium alloy powders. *Mater. Res. Soc. Symp. Proc.* **199**, 181–188.

Howell, D.A., Heckman, J.W. & Crimp, M.A. (1995) Preparation of metal multilayer TEM cross-sections using ultramicrotomy. *J. Microsc.* **180**, 182–185.

Peachey, L.D. (1958) Thin sections. I. A study of section thickness and physical distortion produced during microtomy. *J. Biophys. Biochem. Cytol.* **4**, 233.

Reid, N. (1974) Ultramicrotomy. *Practical Methods in Electron Microscopy*, Vol. 3 (ed. by A. M. Glauert), pp. 273–323. Elsevier, Amsterdam.

Sawyer, L.C. & Grubb, D.T. (1987) *Polymer Microscopy*. Chapman and Hall, London, pp. 85–95.

Swab, P. & Linger, R.E. (1988) Preparation of multilayer optical coatings for TEM cross-sectional microanalysis by ultramicrotomy. *Mater. Res. Soc. Symp. Proc.* **115**, 229–234.

Thomas, G. (1962) *Transmission Electron Microscopy of Metals*. Wiley, New York, p. 182.

Ulan, J.G., Schooley, C. & Gronsky, R. (1990) Microtomy of large particle zeolites for TEM. *Mater. Res. Soc. Symp. Proc.* **199**, 153–156.

Young, J. (1991) Properties, applications and manufacture of man-made mineral fibres. *Mineral Fibres and Health* (ed. by D. Liddell and K. Miller), pp. 38–53. CRC Press, Florida.